

Regulatory post-translational modifications and protein-protein interactions involved in function and proteostasis of aromatic amino acid hydroxylases



Kunwar Jung K C

Thesis for the degree of Philosophiae Doctor (PhD)
University of Bergen, Norway
2021

UNIVERSITY OF BERGEN



**Regulatory post-translational modifications and
protein-protein interactions involved in function and
proteostasis of aromatic amino acid hydroxylases**

Kunwar Jung K C



Thesis for the degree of Philosophiae Doctor (PhD)
at the University of Bergen

Date of defense: 16.09.2021

© Copyright Kunwar Jung K C

The material in this publication is covered by the provisions of the Copyright Act.

Year: 2021

Title: Regulatory post-translational modifications and protein-protein interactions involved in function and proteostasis of aromatic amino acid hydroxylases

Name: Kunwar Jung K C

Print: Skipnes Kommunikasjon / University of Bergen

*In loving memory of my beautiful grandmother, Balikadevi K C (Ama).
Ama, I wish I inherited your storytelling finesse.*

ABSTRACT

The non-heme iron and (6R)-L-erythro-5,6,7,8-tetrahydrobiopterin (BH₄) dependent aromatic amino acid hydroxylases (AAAHs) family of enzymes include phenylalanine hydroxylase (PAH), tyrosine hydroxylase (TH), and tryptophan hydroxylase 1 and 2 (TPH1 and TPH2). PAH catalyses the rate-limiting step in the catabolism of phenylalanine (L-Phe) that mainly takes place in the liver. TH catalyses the first and rate-limiting step in the biosynthesis of catecholamine neurotransmitters and hormones dopamine, norepinephrine and epinephrine in the brain and periphery. TPHs catalyse the first and rate-limiting step in the biosynthesis of serotonin in the peripheral (TPH1) and the central (TPH2) nervous systems. The AAAHs are of physiological and clinical importance. Dysfunctional PAH results in phenylketonuria (PKU), characterised by elevated levels of L-Phe in the blood, which can lead to brain damage. Catecholamine deficiency, due to dysfunctional TH, leads to motor dysfunction and neuropsychiatric disorders, such as TH deficiency (THD) and Parkinson's disease. Reduced level of serotonin has been linked to anxiety disorder, depression, posttraumatic stress disorder and attention deficit hyperactivity disorder. Hence, the reactions catalysed by the AAAHs are important and tightly regulated. The aim of this thesis was to study the regulation of the AAAHs PAH and TH both in physiological and pathological states. We focused on regulatory mechanisms by selected post-translational modifications and protein-protein interactions and phosphorylation, investigating their role in the function, localisation and proteostasis of these enzymes using cellular and animal models.

We investigated the role of DNAJC12, a type III member of the HSP40/DNAJ family, in the folding and degradation of wild-type (Wt) and mutant PAH. We observed a positive correlation between DNAJC12 and Wt and mutant PAH protein levels in the soluble cellular fractions. Detailed characterisations in liver lysates of the

hyperphenylalaninemic *Enul* mouse (p.V106A-PAH mutation) revealed increased ubiquitination, instability, and aggregation of mutant PAH compared with Wt PAH. Furthermore, we showed that in the liver lysates, DNAJC12 interacts with both Wt and mono-ubiquitinated PAH; also, PAH mutation did not alter mRNA expression of *DNAJC12*. Our results support the role of DNAJC12 not only in proper folding but also in the processing of misfolded ubiquitinated PAH.

We characterised a new custom-made *Pah-R261Q* knock-in mouse carrying mutation c.782G>A in the *Pah* gene. The homozygous *Pah-R261Q* mice exhibited reduced PAH activity and BH₄ responsive hyperphenylalaninemia. Moreover, the mutant mice presented a reduced BH₄ content in the liver, altered lipid metabolism, and increased oxidative stress, including increased mRNA expression of *DNAJC12*. Furthermore, the *Pah-R261Q* mice displayed large amyloid-like ubiquitinated PAH aggregates. The colocalisation of mutant PAH with selective autophagy markers indicated the involvement of the autophagic pathway in the clearance of mutant aggregates. These findings indicate a paradigm shift from a loss-of-function disorder to a toxic gain-of-function in PKU pathology.

We next investigated the functional role of Ser31 phosphorylation in the regulation of TH in the cellular models. We observed that the perinuclear distribution of THpSer31 was concomitant with Golgi complex and synaptic vesicle marker in rat and human dopaminergic cells. The co-distribution of THpSer31 with vesicular monoamine transporter 2 (VMAT2) and α -synuclein (α -syn) in cells and their detection as co-immunoprecipitant in mouse brain lysate indicated an association of TH with vesicles. Furthermore, disruption of the microtubules caused accumulation of TH in the cell soma. Our study revealed that Ser31 phosphorylation regulates the subcellular localisation of TH by facilitating protein-protein interaction with VMAT2 and α -syn and enabling its transport toward axon terminals along microtubules.

Finally, using SH-SY5Y cells, we sought to investigate the relationship between phosphorylation at different phosphosites and the nuclear distribution of TH, which

was earlier proposed to be associated with Ser19 phosphorylation. We indeed observed that THpSer19 was predominantly nuclear, yet the phospho-null mutant of Ser19 (V5-TH-S19A) surprisingly accumulated significantly higher in the nuclear fraction when compared to Wt. Moreover, other phosphosites (Ser31 and Ser40) did not seem to influence the nuclear distribution of TH. When the phospho-null mutant of Thr8 (V5-TH-T8A) was expressed in SH-SY5Y cells, recombinant TH in the nuclear fraction was significantly reduced compared to Wt and the phospho-mimicking mutant V5-TH-T8E, indicating the potential role of Thr8 phosphorylation in the nuclear distribution of TH. In addition, inhibition of importin- β also reduced the amount of recombinant TH in the nucleus suggesting the involvement of the importin- β /RanGTP system in the nuclear localisation of TH in SH-SY5Y cells.

To conclude, this study has brought new insights on the short-term regulation of AAAHs (PAH and TH) in physiological and pathological conditions by interacting with partners and by post-translational modifications, such as ubiquitination and phosphorylation (for TH), which ultimately affect their abundance, function and availability in different compartments of cells. Thus, this study has shed light on some of the molecular mechanisms involved in the proteostasis of AAAHs. Together, these findings open new research avenues to better understand disorders associated with the AAAHs.

SCIENTIFIC ENVIRONMENT

The work presented in this thesis was carried out with the Biorecognition research group at the Department of Biomedicine, Faculty of Medicine, University of Bergen, during the period 2017-2021. The main supervisor of the doctoral education has been Professor Aurora Martinez (Department of Biomedicine, University of Bergen), with co-supervisor Dr. Ana Jorge-Finnigan (NHH, Norwegian School of Economics) and Dr. Rune Kleppe (Department of Occupational Medicine, Haukeland University Hospital).

The project was financially supported by the Faculty of Medicine, University of Bergen. Financial aid has also been provided by the Norwegian Biochemical Society (NBS), the Norwegian Graduate School in Biocatalysis (BioCat), the Norwegian Research School in Neuroscience (NRSN) and the Digital Life Norway for participation in scientific conferences and courses.

ACKNOWLEDGEMENTS

Life is a journey, and through the struggle, we reach a milestone. My journey was accidental or not. I happened to miss a class on the day we Master students were supposed to choose a research group to participate in the eight-week research activity. And the very next day, I was told, “oh! you missed the class, and nobody wanted to be in the Biorecognition group, so we put you there”. I said, “whatever”, but little did I know that that was the beginning of my journey toward a milestone, and I have many to express my gratitude for being part of the enriching experiences throughout.

Standing at the milestone when I look back, the first person I would like to wholeheartedly thank is my supervisor Prof. Aurora Martinez. It is unthinkable to achieve this goal without your never-ending support, guidance and opportunities that you provided. You are an extremely hardworking, positive, kind, insightful and strong person I know. After more than six-year of being part of the research group, I am still fascinated by your ability to motivate people in such an effective manner.

I would like to express my deepest gratitude to my co-supervisor Dr. Ana Jorge-Finnigan, for mentoring, shaping and believing in me. I learnt a lot from you, and thank you for giving me the scientific wings. You are an extremely diligent person, and I know you will excel no matter what you do. I would like to extend my gratitude to my second co-supervisor Dr. Rune Kleppe. Your guidance has been very crucial in the hour of need. Your sincere commitment and involvement in the thesis writing are appreciated immensely.

“No man is an island”. I feel fortunate to be surrounded by a highly supportive and fantastic group of people. Ming, you are one of the most organised people I know, and you are the backbone of the group, I have seen people panicking when you go on a long holiday. Fredrik and Maite, I appreciate you guys putting up with me and listening to all my bickering, and I know you guys will complete your PhD with flying colours. Ann Kari, really appreciate your feedback on the thesis writing. Marte, thank you for inviting me to co-supervise the master students, it was a great learning experience. Helene, we all are grateful to you for organising a continuous supply of coffee in the group. Thank you, Biorecognizers; Svein, Karina, Åge, Juha, Chimge, Trond-André, Sten, Knut, Dayne, Christer and Ali for all the collaboration and help I received throughout my PhD and for organising all the social events, of course. I would also like to thank my other colleagues in the BBB and the collaborators abroad.

A good friend is like a four-leaf clover, hard to find and lucky to have one. I would like to show my appreciation to my friends, some in Nepal and some abroad; Pakku, Nishu, Pradip, Motu, Anup, Pankaj, Sagar, Golu; you guys have given me some good memories to cherish for life. Some new friends in Norway that made my life easier; Sushil, you are not only my colleague but a friend as well. I have come to enjoy your company, be it a hike to Ulriken or a feet-numbing trip to Trolltunga. Stig, I really appreciate you as a person and thank you for everything you have done for me. TG, I really enjoy our training sessions and thank you for dragging me to the gym.

Finally, I would like to extend my love and appreciation to my family. Mom and dad, it is impossible to achieve this milestone without your support. Life is incomplete without the love and affection of siblings (which I have many); therefore, they deserve appreciation as well. Ama and Buwa (grandparents), your blessings were always with me. I do not want to miss out on any of my relatives, so thank you all for believing in me.

अन्तमा, म मेरो परिवारलाई माया र प्रसंसा देखाउन चाहन्छ। आमा र बुबा, तपाईंको समर्थन बिना यो लक्ष्य प्राप्त गर्न असम्भव थियो। भाइबहिनीहरू (जुन मसँग धेरै छन्) को माया र प्रिती बिना जीवन अधुरो हुन्छ, तेसैले मेरा सबै दाईं भाई प्रशंसाको योग्य छन्। हजुरआमा, बुवा, तपाईंका आशिष्हरू मसँग सधैं थिए। म मेरा कुनै पनि परिवारको सदस्यलाई छुटाउन चाहन्न; तेसैले म मा विश्वास राख्नुहुने सबै जनालाई धन्यवाद भन्न चाहन्छु।

Table of Contents

Abstract	i
Scientific environment	v
Acknowledgements	vii
Abbreviations	xi
List of Publications	xv
1 GENERAL INTRODUCTION	1
1.1 Protein homeostasis.....	1
1.1.1 Protein Folding	1
1.1.2 Chaperone System	4
1.1.3 Ubiquitin-Proteasome System	7
1.1.4 Autophagy.....	8
1.2 Aromatic amino acid hydroxylases	10
1.2.1 Background.....	10
1.2.2 AAAH _s Structure.....	14
1.2.3 Mechanism of Aromatic Amino Acid Hydroxylation and BH ₄ Synthesis	16
1.2.4 Regulation of Phenylalanine Hydroxylase	18
1.2.5 Regulation of Tyrosine Hydroxylase and Catecholamine Synthesis	19
1.3 Diseases associated with dysfunctional AAAHs.....	24
1.3.1 Phenylketonuria	24
1.3.2 Tyrosine Hydroxylase Deficiency	29
1.4 Protein-protein interaction in AAAHs	31
1.4.1 The 14-3-3 Proteins	31
1.4.2 DNAJC12	33
1.4.3 Alpha-Synuclein	34
1.4.4 VMAT2	36

2	AIMS.....	39
3	SUMMARY OF THE PAPERS.....	41
3.1	Paper I	42
3.2	Paper II	43
3.3	Paper III.....	46
3.4	Paper IV.....	47
4	DISCUSSION.....	49
4.1	Co-Chaperone DNAJC12: A Double Edged Sword?	49
4.2	Proteostasis regulation of Wt and Mutant PAH and TH; Degradation Systems.....	51
4.3	Regulatory Ser/Thr Phosphorylation of TH and Consequent PPI Formation.....	53
5	CONCLUSIONS AND FUTURE PERSPECTIVES.....	59
	REFERENCES.....	61

PAPER I

PAPER II

PAPER III

PAPER IV

ABBREVIATIONS

5-HIAA	5-hydroxyindolacetic acid
AAAH	aromatic amino acid hydroxylase
AADC	aromatic L-amino acid dopa decarboxylase
ACT	Aspartate kinase-Chorismate mutase-TyrA
Atg	autophagy-related
BH ₄	6R-L-erythro-5,6,7,8-tetrahydrobiopterin
CA	catecholamine
CDK	cyclin-dependent kinase
CaMKII	calcium/calmodulin-dependent protein kinase II
CNS	central nervous system
COP	coat protein complexes
CSF	cerebrospinal fluid
DA	dopamine
DAB	3,3'-diaminobenzidine
DAT	dopamine transporter
DBH	dopamine beta-hydroxylase
DRD	dopa-responsive dystonia
EM	electron microscopy
Enu	N-ethyl-N-nitrosourea
ERK	extracellular signal-regulated kinase
FDA	Food and Drug Administration
GABARAP	γ -aminobutyric acid receptor-associated protein
GATE-16	Golgi-associated ATPase enhancer of 16 kDa
GC	Golgi complex
GTP	guanosine triphosphate
HOPS	homotypic vacuole fusion and protein sorting
HPA	hyperphenylalaninaemia
HPD	histidine-proline-aspartate

HSC70	heat shock cognate 70
HSP	heat-shock proteins
hTH	human tyrosine hydroxylase
HVA	homovanillic acid
LC3	microtubule-associated protein light chain 3
L-DOPA	3,4-dihydroxyphenylalanine
L-Phe	phenylalanine
L-Tyr	tyrosine
MHPG	3-methoxy-4-hydroxyphenylethylene
mTORC1	mammalian target of rapamycin complex 1
NEF	nucleotide exchange factor
NGF	nerve growth factor
NLS	nuclear localisation signal
NMR	nuclear magnetic resonance
OMIM	online Mendelian Inheritance in Man
PAH	phenylalanine hydroxylase
PAL	phenylalanine ammonia lyase
PC	pharmacological chaperones
PC12	pheochromocytoma
PD	Parkinson's disease
PDB	protein data bank
PEG	polyethylene glycol
PIP3	phosphatidylinositol 3-phosphate
PKA	protein kinase A
PKC	protein kinase C
PKG	protein kinase G
PKU	phenylketonuria
PNMT	phenylethanolamine N-methyltransferase
PP	protein phosphatases
PPI	protein-protein interaction
Ran	RAs-related Nuclear protein
SLC18A2	solute carrier family 18 member 2

SNARE	soluble N-ethylmaleimide sensitive fusion protein receptor
TEM	transmission electron microscope
TH	tyrosine hydroxylase
THD	tyrosine hydroxylase deficiency
TPH	tryptophan hydroxylases
ULK1	unc-51-like kinase 1
UPS	ubiquitin-proteasome system
VMAT2	vesicular monoamine transporter 2
Vps34	vesicular protein sorting 34

LIST OF PUBLICATIONS

I Jung-KC K., Himmelreich N., Prestegård K.S., Shi T.J.S., Scherer T., Ying M., Jorge-Finnigan A., Thöny B., Blau N. & Martinez A. (2019) **Phenylalanine hydroxylase variants interact with the co-chaperone DNAJC12.** *Human Mutation* **40**(4):483-494. doi: 10.1002/humu.23712.*

II Aubi O., Prestegård K.S., Jung-KC K., Shi T.J.S., Ying M., Grindheim A.K, Scherer T., Ulvik A., McCann A., Spriet E. Thöny B., & Martinez A. (2021) **The Pah-R261Q mouse reveals oxidative stress associated with amyloid-like hepatic aggregation of mutant phenylalanine hydroxylase.** *Nature Communications.* **12**(1):2073. doi: 10.1038/s41467-021-22107-1.†

III Jorge-Finnigan A., Kleppe R., Jung-KC K., Ying M., Marie M., Rios-Mondragon I., Salvatore M.F., Saraste J. & Martinez A. (2017) **Phosphorylation at serine 31 targets tyrosine hydroxylase to vesicles for transport along microtubules.** *Journal of Biological Chemistry.* **292**(34):14092–14107 doi: 10.1074/jbc.M116.762344. †

IV Jung-KC K., Jorge-Finnigan A. & Martinez A. **Phosphorylation at threonine 8 is associated with nuclear localisation of recombinant human tyrosine hydroxylase in SH-SY5Y cells.** *Manuscript in preparation.*

* Paper I reprint allowed as part of doctoral thesis submission according to Wiley article sharing policy.

† This article is licensed under a Creative Commons Attribution 4.0 International License (CC BY 4.0), which permits reproduction in any medium or format.

RELATED PUBLICATIONS NOT INCLUDED IN THE PHD THESIS

V Baumann A, Jorge-Finnigan A., Jung-KC K., Sauter A., Horvath I., Morozova-Roche L.A. & Martinez A. (2016) **Tyrosine Hydroxylase Binding to Phospholipid Membranes Prompts Its Amyloid Aggregation and Compromises Bilayer Integrity.** *Scientific Reports.* **6**:39488 doi: 10.1038/srep39488.

VI Bezem M.T., Johannessen F.G., Jung-KC K., Gundersen E.T., Jorge-Finnigan A., Ying M., Betbeder D., Herfindal L. & Martinez A. (2018) **Stabilization of Human Tyrosine Hydroxylase in Maltodextrin Nanoparticles for Delivery to Neuronal Cells and Tissue.** *Bioconjugate Chemistry* **29**(2):493-502. doi: 10.1021/acs.bioconjchem.7b00807.

1 GENERAL INTRODUCTION

1.1 PROTEIN HOMEOSTASIS

Proteostasis refers to the maintenance of function, amount, interactions, and location (both intracellular and extracellular) of each individual protein [1]. Thus, the state of a balanced proteome is crucial under normal conditions or in the face of an intrinsic or environmental stressor to prevent disease onset. Proteostasis depends on several regulated protein networks that control protein synthesis (transcription and translation), folding (chaperone assisted), trafficking, assembly/disassembly and degradation (ubiquitin-proteasome system and autophagy) [1, 2]. The robustness and adaptability of the integrated proteostasis networks govern the life of the protein from beginning to end, which is essential for the long-term health of the cell. Defects in any of the regulatory protein processing due to ageing, metabolic or environmental stress, or mutations associated with genetic disorders can trigger the breakdown of the entire network, loss of proteostasis, and disease development [3, 4].

1.1.1 PROTEIN FOLDING

Protein folding is described as the self-assembly of a polypeptide, where the primary structure – the amino acid sequence – includes the necessary information to reach a three-dimensional native structure. However, despite Anfinsen's discovery of the spontaneous self-assembly of an unfolded protein into its native conformation over 50 years ago [5] and decades of intense research to understand the molecular mechanisms involved in protein folding, it remains a grand challenge to predict how proteins fold into their native state. The protein-folding problem poses several questions; i) The folding code: how the tertiary/quaternary native structure of a protein is determined by the physicochemical properties encoded in its simple amino-acid sequence?; ii) The folding rate: how can proteins fold so fast, given an almost unfathomable number of

possible conformations?; iii) The protein structure prediction: the long-standing problem of predicting the native structure of a protein from its amino acid sequence [6]. However, the recent breakthrough in protein structure prediction by artificial intelligence, the AlphaFold, holds a promising future in the research [7].

Anfinsen and colleagues' thermodynamic hypothesis of protein folding is a milestone in protein science. They postulated that the native structure of a protein is the thermodynamically stable structure with the lowest free energy (ΔG) [8]. Hydrophobicity and steric constraints are the primary determinants in folding complemented by many different small interactions, such as hydrogen bonds, van der Waals forces and salt bridges, giving rise to a stable and dynamic architecture [9, 10].

The folding rate conundrum made Cyrus Levinthal raise the question in the meeting Société de Chimie Physique, referred to as the “Levinthal’s paradox” [11]: “How does a protein quickly fold into its native state in microseconds out of near-infinite possible ways to fold?” This question led to the development of a powerful array of new experimental methods and advances in protein science [12]. As a consequence the kinetics of protein folding developed to emphasize a funnel-shaped energy landscape [13], which has been further supported by several studies [14]. The landscape has many high-energy states on the top and a few low-energy states at the bottom. The nascent polypeptides travel down the funnel, followed by a quick hydrophobic collapse and stochastic conformations to reach the most stable native conformation resulting in a decreased free energy, associated to a larger decrease in enthalpy than the decrease in entropy upon folding [6].

Over the years, the notion of a funnel-shaped free energy landscape has evolved to include the revised concept of the native state; rather than indicating the unique structure with the lowest energy, it represents the ensemble of soluble functional and fluctuating conformers, which fits with the increasing realisation of proteins as dynamic structures [15, 16]. The conformational fluctuations of proteins on the complex landscape are driven by their intrinsic thermodynamic properties [16], and the

inclusion of water interactions further exacerbates the complexity. The energy landscape becomes even more complicated when the system deviates into a misfolding and aggregation pathway. Similar to protein folding, even aggregation follows a hydration change (Figure 1.1) [17].

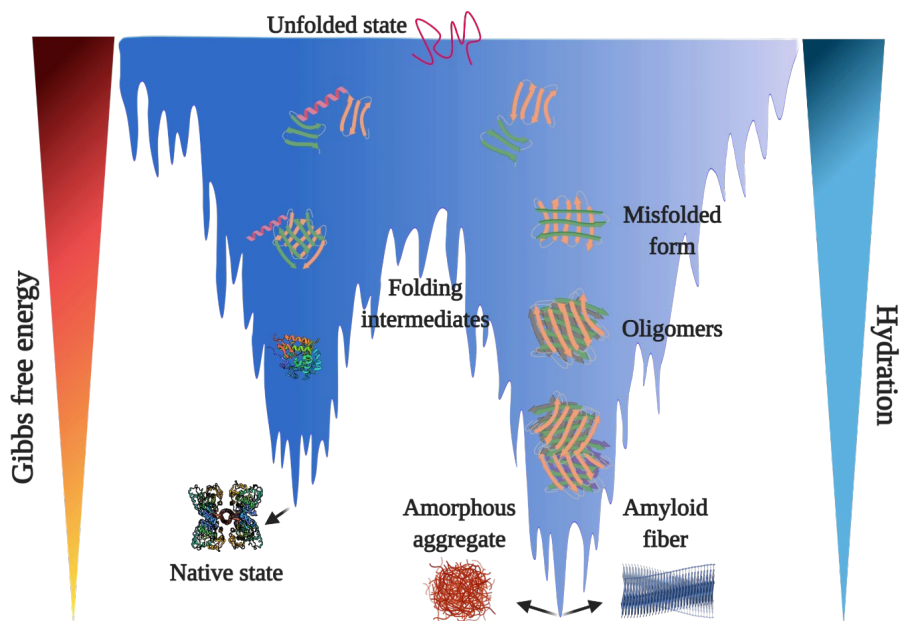


Figure 1.1: Free energy and hydration landscape of the protein-folding process. Unfolded proteins are highly hydrated and have high conformational entropy. The proteins form more ordered intermediates that are less hydrated as they evolve downwards in the funnel. In some cases, these intermediates face a change in the landscape, which gives rise to metastable conformations, leading to less hydrated aggregated species (ordered or amyloid). Illustration adapted from [17] and created using Biorender.

The other factors that can steer biologically active protein to aggregation depend on the intermediates formed during the folding process and their energy state, the energy barrier, and the exposed hydrophobic surface to an aqueous milieu [17].

Contrary to the protein folding *in vitro*, the cell interior is densely populated with different macromolecules and metabolites in a controlled redox environment; therefore, the protein folding *in vivo* employs a different mechanism to avoid

aggregation. Proteins are synthesized at the ribosomes as linear chains that must fold into the functional native structure, as defined above, in a crowded environment [18]. The crowded milieu puts an unfolded protein at risk of aberrant misfolding and aggregation, a hallmark of many neurodegenerative diseases [19]; therefore, cells have devised a complex network of molecular chaperones that prevent aggregation and promote folding [20]. Although several factors involved in protein folding *in vivo* have been identified, it remains challenging to determine the folding landscape in the cellular environment. Nevertheless, several experimental and theoretical studies have put forward the folding mechanism in a crowded environment in the cell. Proteins can start folding cotranslationally inside the ribosome exit tunnel as small modules and coalesce upon emergence from the exit tunnel [21]. Several ribosome-binding chaperones interact with nascent polypeptides, followed by chaperones, such as HSP70, with no affinity to the ribosome [21]. Furthermore, the molecular crowding increases the stability of compact states [22, 23], enhances folding rates [24] and induces conformational changes necessary for protein function [25].

1.1.2 CHAPERONE SYSTEM

Molecular chaperones are proteins that interact, stabilize and assist another protein in the folding process and the maintenance of their native state [26]. Chaperones are categorized based on their sequence homology, and many are known as stress proteins or heat-shock proteins (HSPs), as their synthesis is induced under the condition of stress, such as heat shock or oxidative stress. Chaperones were initially named according to their molecular weight (HSP40, HSP60, HSP70, HSP90, HSP100 and the small HSPs). The chaperones that are involved in *de novo* protein folding and refolding, such as the HSP70s, HSP90s and the chaperonins (HSP60s), are ATP regulated and recognise exposed hydrophobic amino acid side chains of a non-native state; folding is then promoted during binding and release cycles driven by ATP and co-chaperones [27]. The small HSPs act as first-line defenders, buffering unfolded proteins against aggregation in an ATP-independent manner [28]. Moreover, molecular chaperones are

involved in diverse protein quality control roles, including oligomeric assembly, subcellular trafficking, and proteolytic degradation [20, 29].

1.1.2.1 The HSP70 cycle

The HSP70s are one of the most ubiquitous classes of chaperones and are involved in all the typical chaperone functions mentioned above [30]. HSP70s almost always require HSP40s (also known as DNAJ proteins; discussed in section 1.4.2) and nucleotide exchange factors (NEF) as cofactors to function (Figure 1.2). These cofactors regulate the binding of client proteins to HSP70s by affecting the interaction between nucleotides and HSP70s [31]. The amino-terminal ATP-binding domain regulates the carboxy-terminal peptide-binding domain's conformation. The latter constitutes a β -sandwich subdomain that recognizes hydrophobic amino acids and an α -helical lid segment. Together both domains regulate the binding affinity of client proteins in an ATP-dependent manner. The lid's ATP-bound open conformation state allows a high "on" and "off" rate for the folding polypeptides. Through ATP hydrolysis, which HSP40 accelerates, client interaction with HSP70 is stabilised due to closure of the lid [20]. DNAJ proteins can directly interact with unfolded client proteins and recruit HSP70 to the client protein [31]. NEF then catalyses ADP-ATP exchange resulting in lid opening and substrate release. The cycle begins again if the native state of the client protein is not achieved upon release to avoid aggregation.

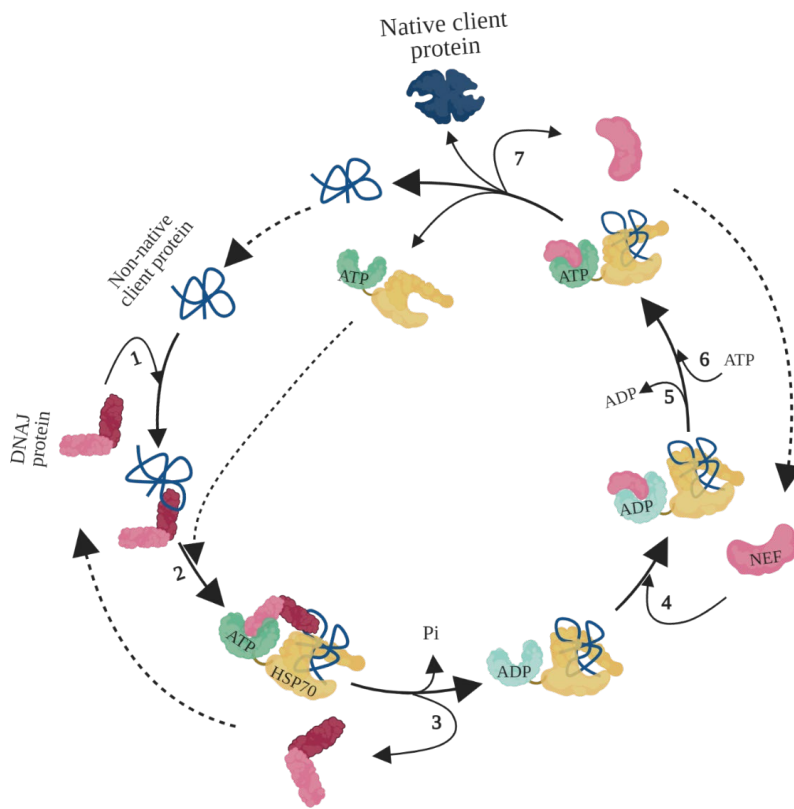


Figure 1.2: The HSP70 cycle. Illustration adapted from [31] and created using Biorender. (1) The DNAJ-protein binds to the client protein and (2) interacts with Hsp70-ATP via its J-domain, which facilitates the transient interaction of the client protein with the “open” peptide binding site of Hsp70. The J-domain and the client induce (3) ATP hydrolysis, causing a conformational change in Hsp70, closing the helical lid over the cleft, stabilizing client interaction and departure of J-protein from the complex. (4) Nucleotide exchange factor (NEF) then binds HSP70-ADP with high affinity; (5) a distortion of the ATP binding domain dissociates ADP, after which (6) ATP binds to Hsp70. Low-affinity interaction of the client protein with Hsp70-ATP causes its release from the complex. In the case that the native state is not attained upon release, the J-protein rebinds to exposed hydrophobic regions of the client protein, and the cycle begins again. Illustration adapted from [31] and created using Biorender.

The (re)binding of HSP70 most likely results in conformational remodelling to remove kinetic traps in the folding process [32]. Moreover, increased expression of the molecular chaperone HSP70 could be critical in mitigating toxicity induced by protein

aggregation in disease models [33]. Several studies have suggested that chaperones, particularly HSP70, may have an essential role in the degradation of proteins through the ubiquitin-dependent proteasome system and the autophagic pathway by collaborating with other chaperones and co-chaperones [34, 35].

1.1.3 UBIQUITIN-PROTEASOME SYSTEM

Cellular proteins are dynamically moving between states with varying turnover rates. In the midst of it, the ubiquitin-proteasome system (UPS) plays a crucial role in the degradation of most cellular proteins, including short-lived, misfolded and damaged proteins. Therefore, the UPS is critical in maintaining cellular function and represents the main pathway involved in the clearance of proteins, consisting of two consecutive steps: ubiquitination and proteolytic degradation [36]. However, when UPS is impaired due to increased accumulation of misfolded proteins, evidence suggests cooperative crosstalk between UPS and autophagy (Section 1.1.4) to maintain proteostasis [37].

The ubiquitination pathway involves a three-step enzymatic cascade mechanism of ubiquitin activation, conjugation and ligation. This leads to the covalent attachment of ubiquitin, a highly conserved 76-amino acid residue protein, to a substrate protein to target it for proteolytic degradation (Figure 1.3). The ATP-dependent activation of ubiquitin by ubiquitin-activating enzyme E1 occurs by forming a thioester bond between the C-terminal glycine residue of ubiquitin and the sulfhydryl side group of a cysteine residue in the E1 protein. The activated ubiquitin is then transferred to the cysteine residue of a ubiquitin-conjugating enzyme E2. The ubiquitin ligase E3 catalyses the final step of covalent attachment of ubiquitin to an ϵ -amino group of a lysine residue in the substrate protein [36, 38, 39]. The linkage of a ubiquitin molecule to a substrate is usually followed by the synthesis of polyubiquitin chain formation, in which the C-terminus of each ubiquitin is linked to the lysine residue (usually Lys⁴⁸) of the previous ubiquitin. Proteins marked by mono-ubiquitin or polyubiquitin chains are typically degraded by the 26S proteasome complex [40, 41].

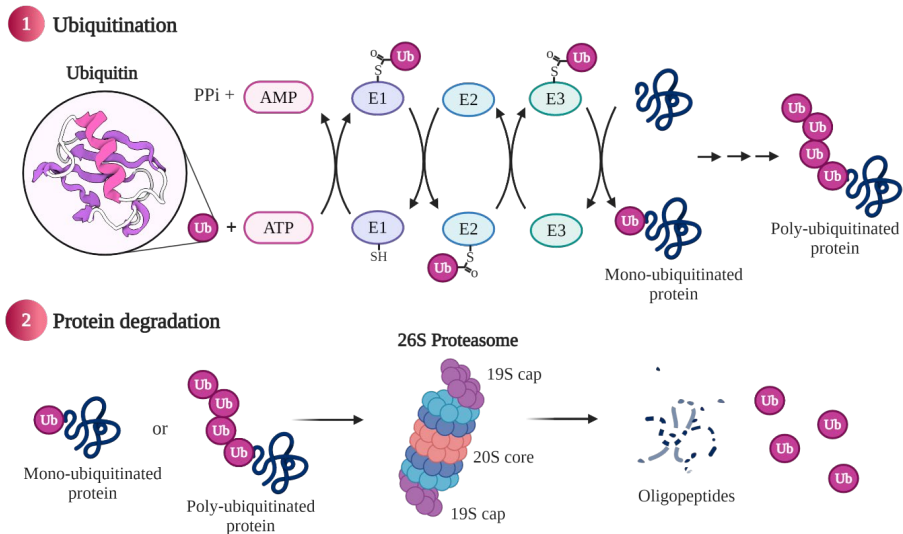


Figure 1.3: The ubiquitin-proteasome system. Illustration created using Biorender. Overview of the ubiquitin-proteasome pathway. (1) In the first step, ubiquitin is activated by the E1 enzyme through adenylation and high-energy thioester bond formation. Second, the ubiquitin molecule is conjugated with the E2 enzyme via a high-energy thioester linkage. Finally, the E3 enzyme receives the ubiquitin molecule, recognises a protein substrate and catalyses the covalent attachment of ubiquitin to the substrate protein (mono-ubiquitination). (2) The mono- or poly-ubiquitinated protein substrate is then shuttled to the 26S proteasome for degradation. Illustration created using Biorender.

The ATP-dependent assembly of two 19S cap-like regulatory particles on each end of a 20S cylindrical core particle forms the 26S proteasome complex [36]. The regulatory 19S particles impart specificity and control, and the active site of the 20S core particle exhibits chymotrypsin-like, trypsin-like, and caspase-like proteolytic activities [42, 43]. The proteasome unfolds, cleaves, and releases the substrates into short peptides which are then rapidly processed by aminopeptidases into amino acids and then recycled [44, 45].

1.1.4 AUTOPHAGY

Autophagy, which means self-eating, is a cellular process essential for balancing energy sources in response to nutrient stress and maintaining cellular homeostasis by

degrading cellular components. Although there are theme-specific variations, three forms of autophagy have been described: macroautophagy, microautophagy and chaperone-mediated autophagy, all of which lead to the same proteolytic degradation of cellular components in the lysosome [46].

Macro and microautophagy can be either selective or non-selective (bulk), triggered by different signals. Selective autophagy involves selective degradation of, e.g., misfolded/aggregated proteins (aggrephagy), organelles (mitophagy, pexophagy, ribophagy, nucleophagy, reticulophagy), macromolecular complexes (lipophagy) and foreign bodies (bacterial and viral xenophagy) [47]. Both selective and non-selective autophagy engage the same core machinery. However, in selective autophagy, several receptor proteins (such as p62/SQSTM1 (sequestosome1), NBR1 and optineurin) facilitate the cargo selectivity that links labelled cargo to the growing phagophore by interacting with other adaptor proteins [48]. In macroautophagy, the cargo is sequestered into a double membrane-bound vesicle (autophagosomes) and delivered to the lysosome by vesicular fusion, forming the autolysosomes [49]. In the case of microautophagy, the cargo protein interacts with the surface protein of the lysosome and is internalized by the invagination of the lysosomal membrane creating small vesicles that detach into the lumen for degradation [50, 51]. Chaperone-mediated autophagy is selective. The only substrates processed by this mechanism are proteins containing a specific KFERQ motif in their amino acid sequence [52]. Heat shock cognate 70 (HSC70) is the only chaperone identified to directly bind to this motif [53].

Briefly, the core autophagosomal machinery consists of more than 30 autophagy-related (Atg) proteins that have been identified and characterized. Initially identified in yeast, homologues are now known for all eukaryotes [54-57]. Atg machinery assembles upon autophagy induction at one or several phagophore assembly sites [58]. The phagophore formation is initiated by activation of unc-51-like kinase 1 (ULK1; human homologue of Atg protein) complex, regulated by mammalian target of rapamycin complex 1 (mTORC1) and adenosine monophosphate-activated protein kinase [59].

The ULK1 targets class III phosphatidylinositol-3 kinases, notably Vps34 (vesicular protein sorting 34) and its binding partner beclin-1, promoting the production of PIP3 (phosphatidylinositol 3-phosphate), which is essential for phagophore elongation and maturation [60]. Although ULK1 plays a crucial role in autophagy, the cascade can also be triggered by ULK1-independent pathways [61]. Other critical proteins involved in the autophagosome biogenesis and maturation are categorized into three subfamilies: LC3 (microtubule-associated protein light chain 3), GABARAP (γ -aminobutyric acid receptor-associated protein) and GATE-16 (Golgi-associated ATPase enhancer of 16 kDa) [62]. Membrane trafficking factors such as the coat complexes COPI and COPII (coat protein complexes I and II), the vesicle- and organelle-identifying RAB (Ras-related protein) GTPases, HOPS (homotypic vacuole fusion and protein sorting), and SNARE (soluble N-ethylmaleimide sensitive fusion protein receptor) mediate autophagosome fusion with lysosome [49, 63].

1.2 AROMATIC AMINO ACID HYDROXYLASES

1.2.1 BACKGROUND

The enzyme family of the (6R)-L-erythro-5,6,7,8-tetrahydrobiopterin (BH₄)- and non-heme iron-dependent aromatic amino acid hydroxylases (AAAHs) includes the enzymes phenylalanine hydroxylase (PAH), tyrosine hydroxylase (TH) and the tryptophan hydroxylases (TPH1 and TPH2). Phylogenetic studies propose a common ancestry for AAAHs, and studies in lower eukaryotes indicate that PAH most likely is the ancestor of metazoan AAAHs [64-66]. The three mammalian enzymes are very similar in structure and domain organisation. TH and TPHs are homotetramers, containing four identical subunits, whereas PAH presents an equilibrium of dimeric and tetrameric forms [67, 68] (The representative tetrameric form of human PAH (hPAH) is shown in Figure 1.4). Each subunit of the mammalian enzymes is organized in three domains: An N-terminal regulatory domain including an ACT-domain fold (yellow), a catalytic domain (pink), containing an active-site with coordinated non-

heme iron where the respective amino acid substrate is hydroxylated, and a C-terminal oligomerisation domain (green). PAH is also present in bacteria, both as dimeric [69] or monomeric [70, 71] forms, which only include the catalytic domain.

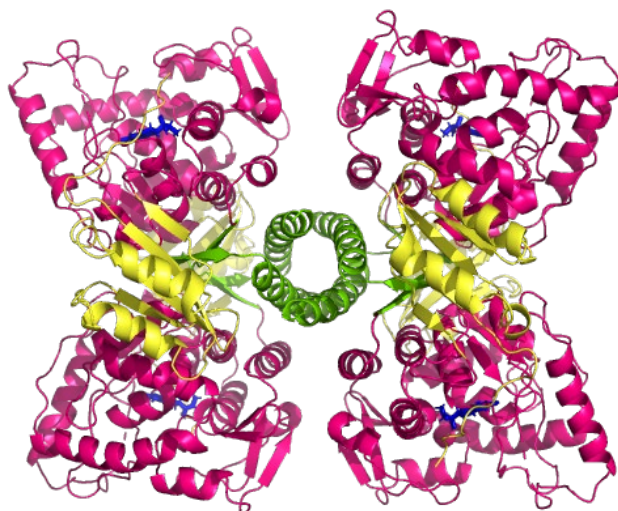


Figure 1.4 Crystal structure of full-length human PAH with bound BH4. The figure was created in PyMol version 2.4.1 using PDB id 6HYC. Ribbon representation of tetrameric hPAH with BH4 drawn as sticks (blue) in all the active sites. Each subunit has three domains represented in different colours; N-terminal domain (yellow), the catalytic domain (pink) and the oligomerisation domain (green). The tetrameric PAH is a dimer of dimers.

Each of the AAAs enzymes uses dioxygen (O₂) and the cofactor BH₄ to catalyse the incorporation of a hydroxyl group on the aromatic ring of the amino acid substrate. The AAAs catalyze crucial neurometabolic reactions. PAH catalyses the hydroxylation of phenylalanine (L-Phe) into tyrosine (L-Tyr), which is further converted into fumarate, which converges on the citric acid cycle (Figure 1.5). The PAH-catalysed reaction is the rate-limiting step in the catabolic degradation of L-Phe and is mainly carried out in the liver. L-Tyr is also the precursor of the biosynthesis of catecholamine

(CA) neurotransmitters and hormones; dopamine (DA), norepinephrine and epinephrine. CAs are produced in the brain and the periphery, mainly in the adrenal medulla and sympathetic nervous system. TH catalyzes the first and rate-limiting step, which is the hydroxylation of L-Tyr in the meta position to convert it to 3,4-dihydroxyphenylalanine (L-DOPA) (Figure 1.5). There are four isoforms of human TH (hTH, i.e. hTH1-4), resulting from alternative splicing of the *TH* gene.

Deficiency of PAH activity, mainly due to mutations in the *PAH* gene, results in phenylketonuria (PKU), characterised by dramatically elevated levels of Phe in the blood, which is toxic for the brain and may result in irreversible neurological impairment if untreated [72]. Catecholamines are essential neuromodulators and are involved in proper motor function, cognition, memory, learning, reward, maintaining normal blood pressure and blood sugar, and dysfunctional TH leads to neuropsychiatric disorders [73, 74]. The disorders associated with deficiencies of the AAHs are presented in Section 1.3.

TPH1 is localised in the periphery, mainly the pineal gland and enterochromaffin cells of the digestive system, whereas TPH2 is found in the central nervous system (CNS). TPH catalyses the first and rate-limiting step in the biosynthesis of serotonin, which is a precursor of the hormone melatonin. Serotonin is vital for regulating the sleep-wake cycle, thermoregulation, cardiovascular regulation, aggression, appetite, sexual behaviour, and learning [75], whereas melatonin is associated with regulation of the circadian rhythms such as consolidation of sleep and regulation of core body temperature, and sexual development [73, 75, 76]. Decreased levels of serotonin have also been linked to major depression, attention deficit hyperactivity disorder, generalised anxiety disorder and posttraumatic stress disorder [77-80].

This thesis is mainly focused on mammalian PAH and TH.

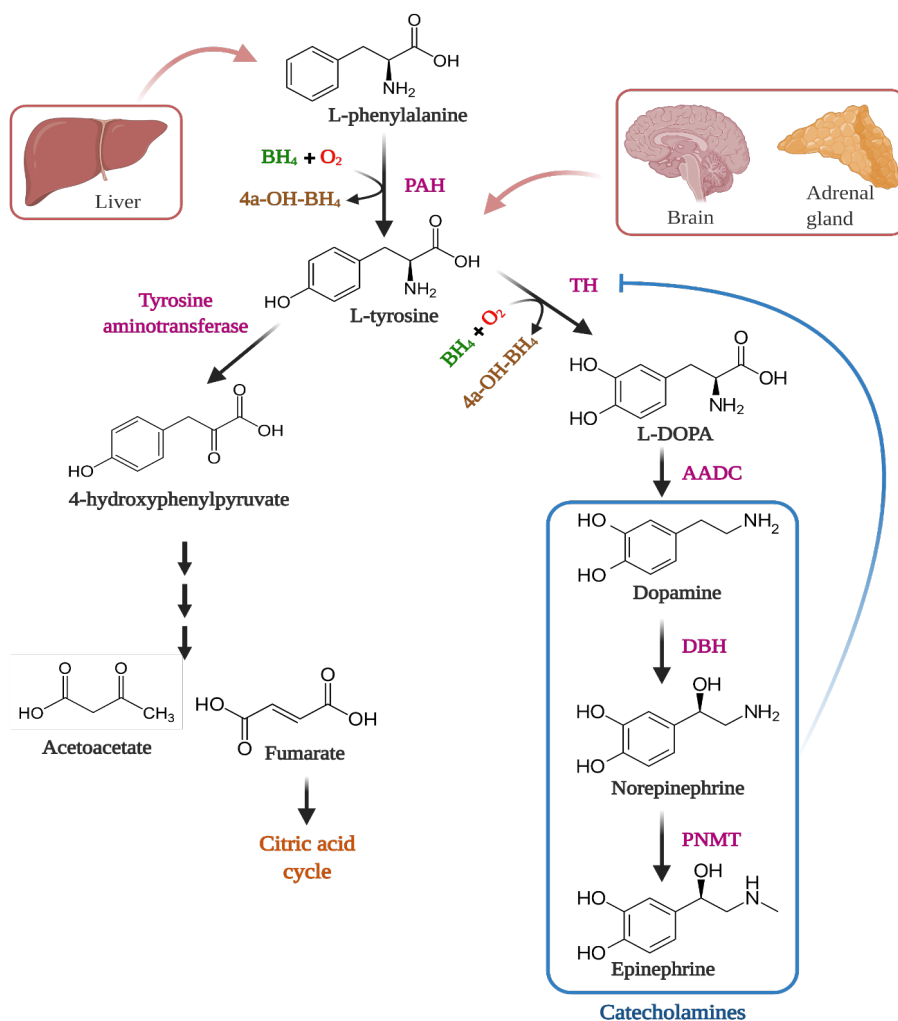


Figure 1.5: The L-Phe metabolism and catecholamine biosynthesis. L-Phe is converted into L-Tyr in the liver by phenylalanine hydroxylase (PAH), which is further catabolised to fumarate, that feeds into the citric acid cycle, and acetoacetate. Catecholamine (dopamine, norepinephrine and epinephrine) biosynthesis occurs in the brain and adrenal gland, where L-Tyr is hydroxylated to L-DOPA by tyrosine hydroxylase (TH). L-DOPA is then converted into dopamine by the enzyme aromatic L-amino acid dopa decarboxylase (AADC). Dopamine is the precursor in the synthesis of neurotransmitters norepinephrine and epinephrine by dopamine beta-hydroxylase (DBH) and phenylethanolamine N-methyltransferase (PNMT), respectively. Catecholamines regulate TH by feedback inhibition. The illustration was created using Biorender.

1.2.2 AAAH₅ STRUCTURE

As mentioned above, the AAAHs are homotetramers with identical subunits that are composed of divergent N-terminal regulatory domains (residues 22-110 in PAH), a central catalytic- (residues 111-410) and C-terminal oligomerisation (residues 411-452) domains (see Figure 1.4 for the organization in PAH). The N-terminal regulatory domain varies in size and sequence identity (<15%), which is consistent with the different regulatory mechanisms for the different AAAHs, e.g. by phosphorylation/dephosphorylation, allosteric activation by L-Phe (PAH) or feedback inhibition by catecholamines (TH) and/or interaction with different protein partners [67, 81, 82]. The non-heme iron, substrate and cofactor bind in the catalytic domain, which shows the highest sequence identity among AAAH mammalian sequences (80%) [81], as well as high structural homology, as evidenced by accumulated partial and full-length AAAHs structures [83-87]. The C-terminal tetramerisation domain includes a long alpha-helix (residues 428-452 in PAH; 473-497 in hTH1; 415-438 in TPH1), which contains conserved hydrophobic heptad repeats that are critical for tetramer formation via coiled-coil interactions, although slightly different orientations of this domain are observed in the hydroxylase family [68].

The regulatory domain exhibits a typical α - β sandwich ($\beta\alpha\beta\beta\alpha\beta$) motif, characteristic of archetypical ACT domain fold. ACT is an abbreviation of three proteins that contain this fold- Aspartate kinase-Chorismate mutase-TyrA [88]. Architecturally, four-stranded antiparallel β -sheets are flanked, on one side, by two short α -helices and, on the other side, by the catalytic domain. In addition to the ACT domain, the regulatory region includes an N-terminal extension of different lengths among AAAHs.

In the unactivated state of PAH, the ACTs are in physical contact with the core structure arranged as monomers, whereas in TH, the ACT regulatory domains dimerise and are located away from the central part of the core structure [85, 86, 89, 90]. The full-length structures of hPAH with BH₄ [85] and hTH [86] have been solved by X-ray crystallography and cryo-electron microscopy (CryoEM), respectively, finally

superseding the composite models of AAAHs [67]. Moreover, evidence has been put forward that activation of PAH by its substrate L-Phe leads to dimerisation of ACTs similarly to TH [84, 91, 92].

The catalytic domain is predominantly made of α -helices (13 α -helices and 6 β -strands) and has a basket-like arrangement, with the iron in the active-site located 10 Å below the protein surface and coordinated by two histidine and one glutamic acid residues (Figure 1.6), forming a 2-His-1-carboxylate facial triad (H285, H290, and E330 in hPAH and H331, H336 and E376 in hTH1) along with 2-3 three coordinated water molecules [82, 83].

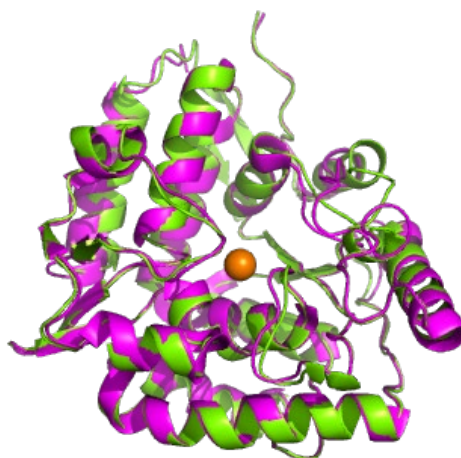


Figure 1.6 **Overlay of the catalytic domain of hPAH and hTH.** The figure was created by PyMol using the PDB id 1PAH for hPAH (green) and 2XSN for hTH (magenta). The figure represents similarity in the structure of their catalytic domains. The orange sphere represents the catalytic iron.

The tetramerisation domain comprises two antiparallel β -strands and a single 40 Å long C-terminal α -helix that forms the coiled-coil core of the tetramer, which is a dimer of dimers [83]. As mentioned above, PAH presents as an equilibrium of dimers, and tetramers, and the tetramer dissociates into functional dimers in a pH-dependent manner [84, 93]. Unlike TH and TPHs, PAH lacks a proper leucine zipper and has

abundant polar residues in the oligomerisation helices, which may explain the presence of dimeric PAH species [84].

1.2.3 MECHANISM OF AROMATIC AMINO ACID HYDROXYLATION AND BH₄ SYNTHESIS

The reaction of the AAAs is the BH₄- and non-heme iron-dependent hydroxylation of the aromatic ring of their respective substrates. Although a complete comparison of the enzymes relative substrate specificity is lacking, several studies have demonstrated that the AAAs show partially overlapping substrate specificity [82, 94]. Both PAH and TPH can hydroxylate each other substrate in addition to their own but not L-Tyr. PAH hydroxylates L-Trp at a much slower rate than TPH hydroxylates L-Phe. TH can hydroxylate all three aromatic amino acids, with the highest affinity for L-Tyr, and it hydroxylates L-Phe at a much higher rate than L-Trp [95]. Also, L-DOPA has been shown to be a substrate for TH suggesting a DOPA oxidase activity that could contribute to neuromelanin formation [96].

In any case, the catalytic mechanism is rather similar for all the AAAs and require BH₄, molecular oxygen and ferrous iron. The proposed hydroxylation mechanism is divided into two steps: (1) iron-mediated oxidation of the pterin cofactor to form the oxygen-containing reactive hydroxylating intermediate, followed by (2) incorporation of oxygen into the aromatic amino acid substrate [97]. As a result, both BH₄ and substrate get hydroxylated in the reaction [98]. The hydroxylated BH₄ (4a-OH-BH₄) is regenerated back to the reduced form. First, the 4a-hydroxytetrahydrobiopterin dehydratase converts 4a-OH-BH₄ to quinoid dihydrobiopterin (qBH₂), which is then converted to BH₄ by NADH-dependent dihydropteridine reductase. In the absence of dihydropteridine reductase, qBH₂ is converted non-enzymatically to 7,8-dihydropterin (BH₂), which is further converted to BH₄ by NADPH-dependent dihydrofolate reductase. In addition, BH₄ is constantly supplied by the *de novo* pathway from guanosine triphosphate (GTP). The enzymes involved in the BH₄ biosynthesis are GTP

cyclohydrolase I, 6-pyruvoyltetrahydropterin synthase and sepiapterin reductase (Figure 1.7) [99].

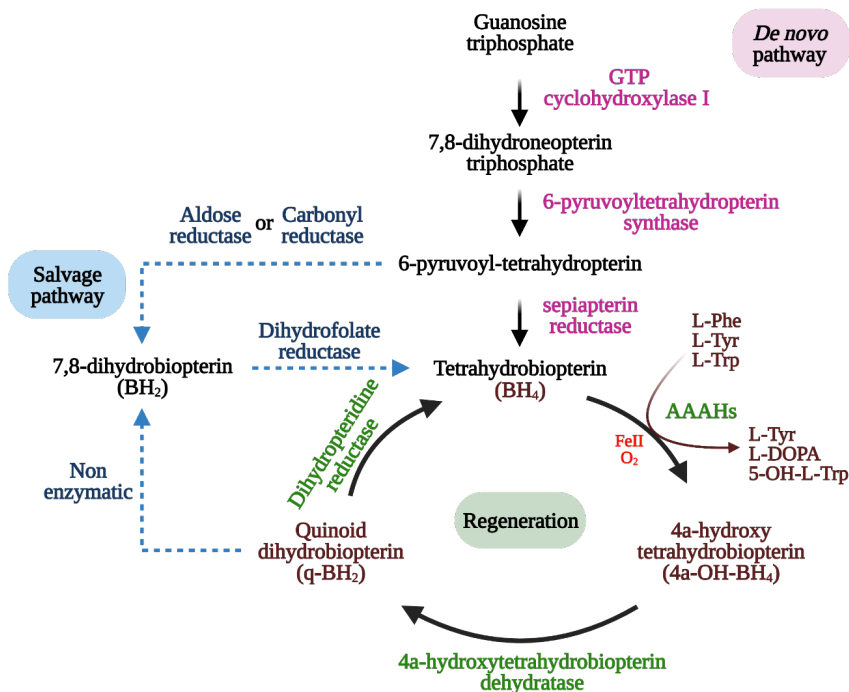


Figure 1.7 The synthesis and regeneration of BH₄. In the *de novo* pathway, guanosine triphosphate is converted to BH₄ by three enzymes. GTP cyclohydrolase I, 6-pyruvoyltetrahydropterin synthase and sepiapterin reductase. Two enzymes are involved in the regeneration of oxidised BH₄ (4a-OH-BH₄), 4a-hydroxytetrahydrobiopterin dehydratase and dihydropteridine reductase. The alternative salvage pathway includes non-enzymatic conversion of quinoid dihydrobiopterin (qBH₂) to BH₂ or 6-pyruvoyl-tetrahydropterin conversion to BH₂ by a combination of aldose and carbonyl reductase, which is then converted to BH₄ by dihydrofolate reductase. The illustration was created using Biorender.

Malfunctioning of the final enzyme sepiapterin reductase can be bypassed by alternative salvage pathways by aldose and carbonyl reductase in the liver to synthesize BH₄ (Figure 1.7).

1.2.4 REGULATION OF PHENYLALANINE HYDROXYLASE

Full-length hPAH is abundant in the liver, but it is also expressed in the kidney and gall bladder [100]. L-Phe acts as a positive allosteric regulator of PAH *in vitro* and *in vivo* by inducing an activating conformational change [101, 102]. However, since the 1970s, it has been debated whether the conformational change is initiated by L-Phe binding to an allosteric binding site in the regulatory domain [101, 103-108] or at the active site [109-111]. Isolated regulatory domains certainly dimerise in the presence of L-Phe, which binds at the dimerisation interface, as revealed by X-ray crystallography [112], suggesting that the final activating conformational change includes dimerisation of these domains. Small-angle X-ray scattering analyses also indicated that dimerisation happens in the full-length enzyme [84, 113, 114]. However, the 3D-structure of L-Phe activated PAH has not been solved yet, and the mechanism by which L-Phe elicits the conformational change, including the initial binding site, has not been established.

PAH shows positive cooperativity in response to increasing concentrations of L-Phe to avoid its neurotoxic accumulation [106, 115]. At low substrate concentration, the enzyme activity is reduced to maintain sufficient levels of phenylalanine for protein synthesis [106, 115]. Preincubation with L-Phe increases the enzyme activity and this effect is higher in rat PAH (10- to 30-fold increase), compared to humans (3- to 6-fold) due to a higher level of basal activity before activation [116, 117]. The enzyme activity shows an initial lag, which is increased by decreasing temperature and pH and can be eliminated by preincubating the enzyme with L-Phe [101, 118]. Several other amino acids can activate PAH, albeit at a much higher concentration than L-Phe [119, 120].

In contrast, the cofactor BH₄ is a negative allosteric regulator of PAH in the absence of any other ligands. In hepatocytes, BH₄ and PAH subunits are in equimolar concentration [121]. At low concentrations of L-Phe, PAH is believed to be mostly in complex with BH₄ as an inactive and stable binary complex that is not easily activated by L-Phe [121]. The recently solved crystal structure of full-length hPAH in complex

with BH₄ alone shows that the cofactor binds to the active site but in a position not suitable for catalysis [85]. Upon L-Phe binding at the active site, BH₄ moves closer to the iron in a favourable catalytic position, appropriate for the formation of the ferryl hydroxylating intermediate.

PAH activity is also regulated by phosphorylation. Several kinases can phosphorylate PAH at Ser16 *in vitro*, including PKA [106]. Phosphorylation decreases the concentration of L-Phe required to activate the enzyme, most probably by causing a subtle conformational change at the N-terminal tail that increases the accessibility of the substrate to the active site [122, 123].

1.2.5 REGULATION OF TYROSINE HYDROXYLASE AND CATECHOLAMINE SYNTHESIS

The catecholamines are physiologically important neurotransmitters/hormones and a variety of regulatory mechanisms modulate the rate-limiting TH activity through both long-term (transcription, alternative RNA splicing, mRNA stability, and protein translation) and short-term regulation (substrate availability, allosterism, feedback inhibition by catecholamines, phosphorylation/dephosphorylation, protein-protein interactions (PPIs)) [124].

The *TH* gene encodes a single form of TH protein in most mammals but 4 different isoforms of TH in humans due to alternative splicing of TH mRNA [125, 126]. The isoform 1 of human TH (hTH1) is very similar to the isoform in most other species, and since it is also the most abundant in the brain, hTH1 is the most studied. The four isoforms of hTH differ by the number of residues inserted after the N-terminal of Ser31 in hTH1. While isoform 2 (hTH2) and 3 (hTH3) have an additional 4 and 27 amino acid inserted, respectively; isoform 4 (hTH4) has both the 4 and 27 amino acid inserts. Although all isoforms are expressed in the brain and periphery, hTH1 and hTH2 are the most abundant in the brain [127]. The steady-state kinetic parameters of each

isoform are similar [128], which is expected given that the protein is identical in all isoforms except for the N-terminus region.

TH activity is short-term and reversibly activated by heparin [129, 130], phospholipids [131], and other polyanions [132] by decreasing the K_m of the enzyme for its cofactor BH_4 [133]. These polyanions bind to the N-terminal region of TH via electrostatic interactions and induce a conformational change that activates the enzyme [134-136]. It has been reported that nucleic acid (total RNA from liver and yeast, transfer and ribosomal RNA, and salmon sperm DNA) could also activate TH in a non-specific manner, most likely due to their polyanionic character [130].

1.2.5.1 Catecholamine synthesis and feedback inhibition

As mentioned above, TH catalyses the rate-limiting step in CA synthesis, i.e. it converts L-tyrosine to L-DOPA. L-DOPA is actively converted into DA by the enzyme aromatic amino acid decarboxylase (Figure 1.5). In the brain, dopamine is efficiently loaded into vesicles by vesicular monoamine transporter 2 (VMAT2) and transported from the soma toward the terminals, in addition to the local synthesis of CA in the terminal [137]. Calcium influx causes DA release from the vesicles into the synaptic cleft, where it acts as a neurotransmitter and binds to postsynaptic dopamine receptors. Also, dopamine D_2 autoreceptor activation on the presynaptic terminal regulates TH activity via adenylyl cyclase inhibition, reducing cAMP-dependent protein kinase (PKA) phosphorylation of TH [138]. Thus, the dopamine autoreceptors provide a mechanism whereby the extracellular DA concentration provides feedback inhibition of TH. Some of the DA is reuptaken by the presynaptic dopamine transporter (DAT) and stored in synaptic vesicles for the next release. In the adrenal medulla and brain, DA is further converted into norepinephrine (locus coeruleus) and epinephrine (medulla oblongata) by DBH and PNMT, respectively (Figure 1.5).

Several studies have demonstrated that catecholamines DA, norepinephrine, and epinephrine form a bidentate $CA-Fe^{3+}$ complex with ferric iron resulting in feedback

inhibition on TH activity, which gives the enzyme its peculiar “blue-green” colour [139, 140]. The half-maximal concentration (IC₅₀) of catecholamines that inhibits TH, obtained with both isolated enzyme [140] and in rat striatal synaptosomes [141]), is in the low μM concentration and in agreement with the free cytoplasmic concentration of DA in neurons ($\sim 2 \mu\text{M}$) [142]. A range of catechols can inhibit TH activity, but catecholamines have the highest affinity [140, 143]. The binding of CA in the catalytic site is competitive towards BH₄ binding and inhibits catalysis; however, increasing concentration of reduced pterin decreases inhibition of TH by CAs [133]. The binding of CA not only blocks the activity but stabilises the enzyme as well [144]. Recently, the first-ever CryoEM structure of DA bound hTH revealed several the specific interactions of DA with the catalytic and regulatory domains of TH and the steric clash with BH₄ in the active site, proving the decades-long observations of of DA/BH₄ competitive binding with TH [86, 133, 145]. Bueno-Carrasco *et al.* also offered the structural explanation of the feedback inhibition by DA and activation by Ser40 phosphorylation of TH [140, 146]. Overall, it has been proposed that catecholamines exhibit two types of feedback inhibition on TH. Firstly, as a sensor of catecholamines' local concentration, a classical kinetic-mediated short-term, reversible inhibition. Secondly, a long-term, almost irreversible inhibition leading to a less active but more stable form of the enzyme [133].

1.2.5.2 Regulation of tyrosine hydroxylase by phosphorylation/dephosphorylation

Phosphorylation is an important regulatory mechanism of TH and CA synthesis and has been reviewed extensively [82, 137, 145, 147]. TH1 is phosphorylated at N-terminal Ser/Thr residues 8, 19, 31, and 40 by several protein kinases (Figure 1.8), *in vitro*, *in situ*, and *in vivo* [137, 147]. Ser40 was the first phosphorylation site of TH to be identified [148-150], and eight different protein kinases have been reported to phosphorylate this site *in vitro* (Figure 1.8). The cAMP-dependent protein kinase, protein kinase C (PKC) and cGMP-dependent protein kinase (PKG) have been shown

to phosphorylate Ser40 of TH *in situ* [147]. Upon phosphorylation at Ser40, TH is released from the feedback-inhibited state by CA, increasing its activity several-fold with a concomitant decrease in K_m for BH₄ [151]. DA is stabilised by hydrophobic interactions with L41, P326 and Y370, hydrogen bonds with the iron-coordinating residues H330, H335 and E375, and electrostatic interaction between the amine group and D44 [86]. Phosphorylation at Ser40 would create steric hindrance in this interaction freeing the regulatory domain from the active site resulting in the release of DA and activation of the enzyme.



Figure 1.8 Schematic diagram of tyrosine hydroxylase (TH) phosphorylation sites. The kinases capable of modulating TH at phosphosites Thr8, Ser19, 31 and 40 are shown in their representative colours. PKA, protein kinase A; PKG, protein kinase G; PKC, protein kinase C; CaMKII, calcium- and calmodulin-stimulated protein kinase II; ERK, extracellular signal-regulated protein kinase; MAPKAPK, MAPK-activated protein kinase; MSK, mitogen- and stress-activated protein kinase; CDK1, Cyclin-dependent kinase1; PRAK, p38-regulated/activated kinase. The illustration was adapted from [147] and created by using Biorender.

All isoforms of human TH (except hTH2) are phosphorylated at Ser31 or equivalent by an extracellular signal-regulated kinase (ERK) 1/2 and cyclin-dependent kinase (CDK) 5 [152-154], which leads to increased TH activity and stability *in vitro* and *in situ* [155-157]. Phosphorylation of Ser31 increases the phosphorylation rate of Ser40 by 9-fold and TH activity more than 2-fold *in vitro*. Several stimulants can increase TH phosphorylation at Ser31; e. g., phorbol esters and nerve growth factor (NGF) increase the phosphorylation at Ser31 (THpSer31), but not at Ser40 (THpSer40) in the rat

pheochromocytoma (PC12) cells, which increases TH activity [158, 159]. Glial cell-derived neurotrophic factor also increases THpSer31 both in substantia nigra and striatum of rat [160]. However, more recent studies have reported that ERK activation leads to increased Ser31 phosphorylation without increasing TH activity [161, 162]. THpSer31 is abundant in the terminals of dopaminergic neurons [137, 163].

TH is phosphorylated at Ser19 by calcium/calmodulin-dependent protein kinase II (CaMKII), MAPK-activated protein kinase, and p38-regulated/activated kinase *in vitro* [150, 155, 164]. There is indirect evidence that CaMKII might be the kinase responsible for phosphorylating TH at Ser19 *in vivo* [165]. THpSer19 results in increased TH activity and stability through high-affinity binding to 14-3-3 proteins and by increasing the rate of phosphorylation at Ser40 in a hierarchical manner [164, 166-168]. Recently, Ghorbani *et al.* reported that only in the absence of 14-3-3 proteins THpSer19 stimulates phosphorylation of Ser31 [169]. Furthermore, THpSer19 has also been reported to be mainly distributed in the nucleus of PC12D cells and to be a critical trigger for the degradation of TH by the ubiquitin-proteasome system [170, 171].

Although phosphorylation of TH at the Ser/Thr8 site has been investigated the least, some studies report that this site is phosphorylated by a proline-directed protein kinase, i.e., CDK1 *in vitro* and in cultured cells [150, 172, 173]. It has been reported that Ser8 can be phosphorylated by ERK2 *in vitro* but at a slower rate than Ser31 [174]. In any case, the physiological role of Ser/Thr8 phosphorylation has not been established yet.

Dephosphorylation plays a crucial role in modulating enzyme activity; among others, THpSer40 can be dephosphorylated by several protein phosphatases (PPs) *in vitro*. Both PP2A and PP2C can dephosphorylate TH at pSer40 and pSer19 in the bovine adrenal medulla, rabbit corpus striatum, rat brain, and dopaminergic cells [175-179]. In PC12 cells, treatment with the specific inhibitor of protein phosphatases okadaic acid increased Ser31 phosphorylation, suggesting the involvement of PP1 or PP2A in its dephosphorylation [177, 180]. In bovine adrenal chromaffin cells, PP2A but not PP1 could dephosphorylate TH at pSer31 [177]. In bovine adrenal chromaffin cells, PP2A

but not PP1 could dephosphorylate TH at pSer31 [179]. The dephosphorylation rate of pSer31 is decreased in the presence of pSer19. The binding of 14-3-3 proteins to THpSer19 inhibits dephosphorylation of both pSer40 and pSer31 *in vitro* [169]. There are conflicting reports on the dephosphorylation of pSer8 [177, 179]. One study suggests that PP2A is responsible for dephosphorylating pSer8, whereas another study contradicts that finding. Overall, several studies have indicated that PP2A is the dominating phosphatase that predominantly acts on phosphorylated TH.

1.3 DISEASES ASSOCIATED WITH DYSFUNCTIONAL AAAHS

Dysfunctional enzymatic activity of AAAHS due to mutations has been associated with severe neurometabolic diseases leading to mental retardation and neuropsychiatric disorders. In this section, we will introduce diseases associated with dysfunctional PAH and TH.

1.3.1 PHENYLKETONURIA

Once described as an epitome of molecular genetics pathology, phenylketonuria is an inborn error of amino acid metabolism. Phenylketonuria (PKU; Online Mendelian Inheritance in Man (OMIM) #261600) is an autosomal recessive genetic disease caused by mutations in *PAH*, which can lead to intellectual disability if untreated [72]. The normal blood Phe concentration range is 50-110 μM and, depending on the severity of the L-phenylalanine accumulation, PKU is classified as mild hyperphenylalaninaemia (HPA) (120-600 μM), mild PKU (600-1200 μM) and classic PKU (>1200 μM) [72].

The discovery of PKU was made by the Norwegian doctor Asbjørn Følling, who called the condition “phenylpyruvic oligophrenia” [181], shortly after it was renamed to “phenylketonuria” by Penrose and Quastel [182]. In the mid-90s, a low-phenylalanine diet to treat phenylketonuria was introduced, and a diagnostic test suitable for mass screening for HPA in the newborns was developed [183, 184]. The prevalence of PKU

is rare and varies worldwide, but PKU is the most recurrent among the inborn errors of metabolism group of disorders. In Europe, the prevalence is approximately 1:10,000 live births, 1:15,000 in the USA; and in Latin America, it varies from one case per 50,000 to one per 25,000 births. Asia and Africa have the lowest prevalence [72, 185].

The gene coding for PAH in humans is located in chromosome 12, region 12q23.2. Chromosome 12 is rich in disease-associated loci, with 487 loci accounting for 5.2% of known “disease genes” [186]. The *PAH* genomic sequence spans about 170 kilobase pairs (kb) including its flanking regions with 13 exons (2.5 kb) and corresponding introns (85 kb). The *PAH* gene codes for a mature mRNA of approximately 2.4 kb, hence conforming to one of the lowest ratios for coding to non-coding among eukaryotic genes [187]. To date, more than 1188 human *PAH* mutations have been registered (<http://www.biopku.org/home/pah.asp>); these variations comprise missense mutations (65%), deletions (15%), splice variants (12%), insertions, duplications and indels (4%) and synonymous mutants (4%) indicating the existence of heterogeneity in PKU. The type of mutation and its position in the protein impose the effect on PAH stability and catalytic activity, which can lead to a spectrum of *in vitro* phenotypic outcomes [188, 189]. Very little or no residual enzyme activity results in the classic PKU phenotype, whereas partial inhibition of the enzymatic activity gives rise to mild HPA or mild PKU. The genotype-phenotype correlations reported in the past have varied widely. The majority of PKU patients are compound heterozygotes, as they carry two different *PAH* mutations leading to a phenomenon known as interallelic complementation, which can result in either a milder (positive complementation) or a more severe phenotype (negative complementation) than expected from the single allele [190]. Besides, even homozygous patients display differences in the phenotype, showing that genotype-phenotype correlations can be complicated even for monogenic diseases such as PAH deficiency [191, 192]. Thus, other factors may influence the phenotype, such as epigenetics, environmental factors, and gene products involved in proteostasis regulation, transport and metabolism of Phe, making PKU a complex trait disorder [192].

Nevertheless, the large number of studies in cells have helped identifying genotype-phenotype relationships and to classify the pathogenic loss-of-function for each mutation [193]. Overall, destabilising PAH mutations have emerged as the major pathomechanistic cause of PKU [188, 189]. Table I presents a selection of missense mutations, which are mostly located in the catalytic domain and/or induces instability, and are ordered by their frequency of occurrence from high to low.

Table I. PAH missense mutants with differing allele frequency, residual enzyme activity, protein stability and associated patient phenotype.

PAH protein mutants	Allele frequency (%) ^a	PAH activity (%) ^b	PAH domain/protein stability	Phenotypic group
p.R408W	19.2	≤10	Catalytic/destabilising	Severe PKU
p.R261Q	5.5	≤50	Catalytic/destabilising	Mild PKU
p.A403V	2.4	≤50	Catalytic/destabilising	Mild HPA
p.A300S	1.5	≥50	Catalytic/destabilising	Mild HPA
p.R297H	0.14	≤50	Catalytic/destabilising	Mild PKU
p.V190A	0.13	≤50	Catalytic/destabilising	Mild HPA
p.G218V	0.11	≤50	Catalytic/destabilising	Severe PKU
p.R68G	0.05	≤50	Destabilising	Mild PKU
p.E76G	0.04	≤50	Destabilising	Mild PKU
p.A47V	0.03	≥50	Destabilising	Mild HPA
p.A313T	0.01	≤50	Catalytic/destabilising/affects splicing	Mild HPA

^a Allele frequency according to the BIOPKU database (<http://www.biopku.org>).

^b Residual *in vitro* PAH activity relative to Wt-PAH (100%) in expression studies in COS cells [193].

There is irrefutable evidence that Phe accumulation in the brain causes the symptomatology observed in PKU patients. Amino acid entry into the brain is mediated by L-amino acid transporter1 at the blood-brain barrier [194]. A high concentration of Phe inhibits this transporter hence blocking the influx of other neutral amino acids, including Tyr and Trp, increasing the probability of neurotransmitter dysfunction. In fact, a reduced level of protein synthesis and neurotransmitters (serotonin and DA) has been reported in the brain of PKU patients [195, 196]. In addition, high Phe would also compete with Tyr and Trp, lowering TH and TPH activity, respectively.

Genetically modified mice are powerful research models that are commonly used for studying human diseases. The first generation PKU mouse models were created by phenotype driven N-ethyl-N-nitrosourea (ENU) germline mutagenesis and named Enu1, Enu2 and Enu3. The Enu1 (*enu1* allele) with the p.V106A-PAH mutation located in the PAH regulatory domain affects PAH stability resulting in reduced steady-state levels of PAH protein and enzymatic activity (approx. 5% of wildtype (Wt)), leading to mild HPA [197, 198]. The Enu2 (*enu2* allele) presents the p.F263S-PAH mutation in the catalytic domain [197], and the Enu3 (*enu3* allele) shows a splice site mutation generating frameshifted amino acids and premature termination codon affecting total PAH activity [198]. Both Enu2 and Enu3 mice exhibit high blood L-Phe levels (>1200 μ M), and are suitable models for severe, classic PKU.

Overall, Phe accumulation appears to have multifactorial effects, and the clinical manifestation of untreated PKU is broad; such as morphological abnormalities of the brain (reduced size, hypomyelination, limited dendritic branching and synaptic density), motor dysfunction (tremor, dystonia), psychiatric symptoms (anxiety, psychosocial difficulties and depressed mood), cognitive dysfunction (mental retardation, repetitive behaviour, speech delay, autism), seizures and hypopigmentation [72, 199-202]. Several animal studies have also indicated oxidative stress in PKU, which has been associated with a high level of Phe or the diet [203-205]. Oxidative stress is associated with the generation of reactive radical species, reduced antioxidant

defences, protein and DNA damage, lipid peroxidation, and changes in the lipid profile, adding to the pathological phenotypes of PKU [206].

1.3.1.1 PKU management

As the pathophysiology of PKU is associated with high levels of Phe, the low-Phe diet is the cornerstone to manage PKU/HPA and prevent the most severe consequences of the disease. However, the diet should also contain sufficient caloric content to maintain biological needs and avoid the breakdown of body tissue which can lead to an elevated level of Phe in the plasma [207]. Phe tolerance must be scrutinised for each patient to avoid such a consequence. Undoubtedly dietary treatment is very successful; nevertheless, several studies have shown that early-treated PKU patients present several clinical psychiatric features as adults, notably depression and anxiety-related disorders [202], with an elevated risk of comorbidities [208]. In recent years, many alternative therapies for PKU have been approved or are in development [209]. The synthetic form of BH₄ (Sapropterin, Kuvan®) combined with a low-Phe diet could be used as an adjunct to the patients that are responsive to BH₄ [210]. Another alternative (enzyme substitution therapy) that has recently been approved by the Food and Drug Administration (FDA) is based on the enzyme phenylalanine ammonia lyase (PAL) that is present in yeast, higher plants and some prokaryotes. PAL catalyses the non-oxidative deamination of phenylalanine into trans-cinnamic acid and ammonia, which are non-toxic [211, 212]. Since the enzyme is non-human, it induces an immune response; hence, a PEGylated derivative of PAL (polyethylene glycol attached to PAL) was created to protect and stabilise the enzyme. In the United States, it is sold under the brand name Palynziq™ (pegcaliase-pqp3); and it has been approved in Europe for patients aged 16 and older to treat the underlying cause of PKU [212]. Although the therapy has proven to be useful for treating PKU, one cannot disregard its limitations, such as injection-site reaction, joint pain, rash, fatigue, headache, gastrointestinal symptoms, inguinal or axillary lymphadenopathy, dizziness and anaphylaxis [213]. Also, enzyme substitution therapy does not address the toxicity and oxidative stress

caused by misfolding of the mutant PAH, potentially leading to gain-of-function contribution to the HPA/PKU pathology.

Pharmacological chaperones (PC) are small molecular compounds that are being used in clinical practice for some rare diseases caused by protein instability and could be a potential therapeutic approach to treat PKU, given the ability of PCs to bind a protein specifically and stabilise it [214]. BH₄, the PAH cofactor, indeed shows a chaperone-like effect on PAH [215], but not all patients respond to this treatment [216, 217]. Thus, a small molecule specific to PAH protein that can stabilise and rescue the mutant is optimal as a therapeutic PC to revert a disease phenotype caused by an unstable mutant protein. Compounds with PC potential for PKU treatment have previously been identified by screening diversity libraries monitoring PAH thermal stabilization [218, 219].

1.3.2 TYROSINE HYDROXYLASE DEFICIENCY

Tyrosine hydroxylase deficiency (THD; OMIM #605407) is a rare autosomal recessive disorder caused by mutations in the *TH* gene, which lead to catecholamine deficiency [220]. The gene coding for TH in humans is located in the short (p) arm of chromosome 11 at position 15.5. In the past, THD was known as Segawa syndrome or dopa-responsive dystonia (DRD). Among other genes involved in regulating DA synthesis, mutations in GTP cyclohydrolase I, an enzyme that catalyses the first step in the synthesis of BH₄ (Figure 1.7), cause autosomal dominant DRD [221, 222]. So far, fewer than 100 patients with THD have been reported in the scientific literature, with a total of 40 different disease-related missense mutations, five nonsense mutations, and three mutations in the promoter region of the *TH* gene [223, 224].

THD has a broad phenotypic spectrum and has been categorised into various types. Furukawa and Kish described three groups based on the severity of the symptoms and responsiveness to levodopa: mild form (TH-deficient DRD), severe form (TH-deficient infantile parkinsonism), and very severe form (TH-deficient progressive infantile

encephalopathy) [225]. Willemsen *et al.* categorised THD in two phenotypes: an infantile-onset, progressive, hypokinetic-rigid syndrome with dystonia (type A), and a complex neonatal parkinsonism with severe encephalopathy (type B) [222].

Symptom onset in mild type TH-deficient DRD and TH-deficient infantile parkinsonism is in the early years of life with normal development up to this point. Initial symptoms include lower limb dystonia, difficulty walking with diurnal fluctuation of the symptoms to truncal hypotonia, and parkinsonian symptoms such as hypokinesia, the rigidity of extremities, and tremor. Like type A described by Willemsen *et al.*, the patients show a positive response to L-DOPA treatment without adverse motor side effects [222, 225]. The more severe phenotype (type B) has an onset of symptoms within a year of birth with a broader range of movement disorder to cognitive impairment and does not show a robust response to L-DOPA, usually hypersensitive to it, developing motor fluctuations and dyskinesia on low doses [222, 225-227]. In any case, an accurate diagnosis of THD requires both clinical and laboratory findings, including genetic tests.

Cerebrospinal fluid (CSF) analysis of catecholamine metabolites can support the clinical diagnosis of THD. DA is converted into homovanillic acid (HVA), norepinephrine and epinephrine into 3-methoxy-4-hydroxyphenylethylene (MHPG). Low HVA and MHPG reflect catecholamine deficiency in THD due to decreased TH activity. However, serotonin biosynthesis is not affected, hence the expected normal level of 5-hydroxyindolacetic acid (5-HIAA). Therefore, a low HVA:5-HIAA ratio in CSF suggests THD [222, 225, 228]. Also, mutational analysis of genes involved in DA biosynthesis and regulation is considered in the diagnosis [221, 229].

As mentioned above, a broad range of movement disorders as well as reduced TH activity and DA levels are associated with THD [228]. Although neurodegeneration is not observed in THD, it shares several traits with Parkinson's disease (PD), in which motor abnormalities reflect striatal DA loss due to neurodegeneration in the brain [230].

Several animal studies aiming to mimic THD by inactivating the *TH* gene (*TH* knock-out) provided valuable insights into the catecholamines importance in perinatal development [231, 232]. A *TH* knock-in mouse model with the p.R203H mutation, equivalent to the human hTH1-p.R202H, has been generated and displays salient clinical features of human type B THD phenotype, including biochemical markers, making it an ideal model for the investigation of disease mechanisms and novel therapeutic approaches [227].

1.4 PROTEIN-PROTEIN INTERACTION IN AAAH_S

Several proteins have been identified that interact with aromatic amino acid hydroxylases. Still, the one that has been investigated the most in terms of PPIs, are 14-3-3 proteins, α -synuclein, VMAT2, DNAJC12, aromatic amino acid decarboxylase, protein phosphatase 2, guanosine tri-phosphate cyclohydrolase, DJ-1 have been detected as physical interactors and contribute in its overall regulation [137, 233-235]. A few of the protein interactants were selected due to their involvement in the regulation of the AAAHs, contributing to overall proteostasis. The PPI partners of TH that are studied in this thesis are discussed in the following paragraphs.

1.4.1 THE 14-3-3 PROTEINS

The 14-3-3 proteins are ubiquitously expressed in all eukaryotic cells and consist of several isoforms. They are very conserved and display high sequence and structural identity, both within and across species. The number of isoforms differs among species ranging from 2 in the unicellular organisms *Saccharomyces cerevisiae* and *Schizosaccharomyces pombe* [236] to 12 in the plant *Arabidopsis thaliana* [237]. In mammals, the 14-3-3 protein family consists of seven known isoforms, named beta, gamma, epsilon, sigma, zeta, eta, and tau (β , γ , ϵ , σ , ζ , η and τ). Moore *et al.* in 1968 first discovered and named the 14-3-3 protein family based on its elution and migration pattern on the two-dimensional diethylaminoethyl cellulose chromatography and starch gel electrophoresis (as compiled by [238]).

The 14-3-3s are ~30 kDa acidic proteins that can function as both homo- and heterodimers, except for 14-3-3 σ which is a homodimer [239, 240]. Crystallographic studies of ligand-free 14-3-3 showed a cup-shaped dimer with nine antiparallel helices where the N-terminal helices of the two subunits form the dimer interface, and the C-terminal form its walls [241]. The inner phosphopeptide-binding pocket is the most highly conserved region; however, the residues on the outer surface of the proteins exhibit variability among isoforms and may also play a role in isoform-substrate specificity [242]. Muslin *et al.* demonstrated that a phosphoserine motif is essential to interact with the 14-3-3s [243]. The binding of 14-3-3 can induce at least three effects in the target protein: (A) conformational change, (B) masking of a specific region (active site, a ligand-binding region, or PPI site), or (C) scaffolding of the two proteins [240].

The 14-3-3 proteins are adaptor proteins involved in a plethora of biological processes such as cell signalling, cell cycle progression, transcription, intracellular trafficking, apoptosis, regulation of enzyme activity, and protection against proteolysis [238, 244]. The family of proteins are also involved in a wide range of neurodegenerative disorders such as Creutzfeldt–Jakob disease, Alzheimer’s disease, PD and polyglutamine repeat diseases [238]. 14-3-3 proteins regulate several signalling pathways involved in cancer [245].

The first proteins identified to interact with 14-3-3 proteins were TH and TPH, which are activated upon binding [246, 247]. *In vitro* studies have revealed that phosphorylated TH (either THpSer19, THpSer19pSer40 or THpSer19pSer31) binds to 14-3-3, but the affinity is increased if TH is phosphorylated at both sites [164, 169, 248]. The extent of activation of phosphorylated TH by 14-3-3 proteins differs based on isoform, shown by some cellular studies [249, 250]. Ghorbani *et al.* have shown that all 14-3-3 homodimers and heterodimers bound with similar affinity but moderate differences in their activation of TH between the 14-3-3 isotypes, the total activation was highest for THpSer19pSer40 in the presence of 14-3-3 γ [169, 251]. The 14-3-3

proteins assist in regulating access to both Ser31 and Ser40 and modulate their phosphorylation state dynamics [169].

1.4.2 DNAJC12

DNAJC12 is a co-chaperone that belongs to the class III (subfamily C) of the DNAJ/HSP40 protein family [235]. The J-proteins or HSP40s that function as co-chaperones of HSP70s represent a large protein family with at least 50 members in human [31, 252]. The *DNAJC12* gene is 1.2 kb-long encompassing 5 exons which mapped *in silico* to chromosome 10q21.1 [253, 254]. The gene is expressed in most tissues, but at high levels in the adrenal gland, brain, liver, kidney, and pituitary gland [100].

DNAJC12 is a 24 kDa cytosolic protein comprised of 198 amino acids, and so far, only the structure of the first 100 amino acids, which corresponds to the J-domain, has been solved by NMR (PDB ID 2CTQ). The highly conserved J-domains include four α -helices, with the central ones (helix II and III) forming an anti-parallel helical coiled-coil motif around a hydrophobic core [255]. The most highly conserved short motif in the family, the histidine-proline-aspartate (HPD), is located in the loop between helix II and helix III. This motif is crucial for ATPase stimulation and *in vivo* function [256]. Still, little is known about the mechanism by which it exerts its function. DNAJC12, together with HSP70, is involved in folding newly synthesized and partially folded proteins in several compartments of eukaryotic cells as well as in promoting the degradation of its client protein [257]. Several studies have indicated that stress and physiological stimuli can regulate the expression of DNAJC12 [254, 258, 259].

Recently, mutations in the *DNAJC12* gene have been reported to cause HPA, dystonia, early-onset parkinsonism, and intellectual disability without mutations in the *AAAHs* gene or any other gene involved in BH₄ metabolism [235, 260, 261]. Affinity capture-mass spectrometry data from human interactome and human cells have shown direct interactions of DNAJC12 with PAH, TH, and TPHs, indicating that DNAJC12 is a

specific co-chaperone of AAAHs and maintains intracellular stability of its clients [235, 262].

However, DNAJC12 functions extend beyond the AAAHs as several studies have suggested that they can be used as a potential biomarker of tumour progression. For example, the transcripts of DNAJC12 were upregulated in triple-negative breast cancer and aggressive phenotype of gastric cancer [263, 264]. A significant correlation to inadequate response to neoadjuvant concurrent chemoradiotherapy, characterized by lower tumour regression grade, was observed in rectal cancer with high expression of DNAJC12 [265]. Lastly, the co-chaperone may act as a potential therapeutic target as knocking down the expression of DNAJC12 significantly reduced the proliferation and invasiveness of gastric cancer cells [263, 264].

1.4.3 ALPHA-SYNUCLEIN

In 1912 Friederich Lewy made the first observations of the inclusions that are indicative of PD - the so-called 'Lewy bodies' [266]. Decades later, electron microscopy revealed that the true nature of Lewy bodies is abnormal filaments [267]; however, it was still unclear the role of inclusions in the aetiology of neurodegeneration. Two studies brought α -synuclein (α -syn) into the frontline, as they reported that missense mutations (p.A53T) in the *SNCA* gene coding for α -syn caused a rare, familial form of PD [268], and the presence of α -syn in the Lewy body of sporadic PD [269].

Synucleins are abundant neuronal protein, and the family consists of three members - α -synuclein, β -synuclein and γ -synuclein, which are similar in length and domain organization and share 55-62% sequence identity [270]. The first synuclein sequence was obtained from the Pacific electric ray (*Torpedo californica*), and it was named synuclein, because of its apparent localisation in presynaptic nerve terminals and the nuclear envelope [271].

The α -syn is 140 amino acids in length and has an amphipathic lysine-rich, highly helical amino terminus, critical in membrane interactions, and a disordered, acidic

carboxy-terminal tail that has been implicated in interactions with proteins, metals and small molecules [272, 273]. The central region of α -syn (residues 65–90) is highly hydrophobic and it is known as the non-amyloid- β component of AD amyloid plaques, which is crucial for α -syn oligomerization [274, 275]. Conformational flexibility grants multifunction properties to α -syn and allows it to interact with membranes, proteins and protein complexes [276]; however, little is known about its conformational state. Native α -syn may exist in equilibrium between different conformational and/or oligomeric states, which can be influenced by several factors such as post-translational modification, fatty acid concentration, phospholipids, and metal ions, oxidative stress, etc. [277-282]. A complex and dynamic interplay between these modifications may affect α -syn aggregation, which may provide potential targets for future therapeutics.

The α -syn protein is ubiquitously expressed throughout the brain, mainly at the presynaptic terminal and its exact function is still unclear. There is evidence that α -syn negatively regulates dopamine synthesis by inhibiting TH activity [178, 283]. α -syn also negatively regulates DA neurotransmission, as mice lacking α -syn show increased DA release upon electrical stimulation and significant reduction of vesicles at the distal pool of the presynaptic terminals [284]. *In vitro* studies have demonstrated that dopamine can modulate the aggregation of α -syn (both Wt and A53T); under physiological conditions, α -syn can self-assemble into small oligomers and protofibrils, which could further elongate into a mature amyloid fibril [285, 286]. Thus, incubating DA with pre-formed amyloid fibrils can disengage them into non-fibrillar soluble oligomers [287]. On the other hand, prolonged incubation with DA can promote α -syn aggregation into fibrils via off-pathway, soluble SDS-resistant and Thioflavin T negative oligomers intermediates [288]. Recently Mor *et al.* demonstrated *in vivo* aggregation of α -syn by DA, resulting in oligomeric species that reflect neurotoxic oligomers induced by DA *in vitro* [289]. Moreover, they showed that increased production of DA in A53T transgenic mice caused severe loss of dopaminergic nerve terminals before cell bodies, offering a new model of disease progression in PD [289, 290].

1.4.4 VMAT2

The vesicular monoamine transporter 2 (VMAT2), also known as solute carrier family 18 member 2 (SLC18A2) protein, is expressed in monoaminergic neurons of the central and peripheral sympathetic nervous systems and is encoded by the *SLC18A2* gene [291, 292]. Its 3D structure is not resolved yet; however, sequence analyses of related proteins suggest that VMAT2 includes 12 transmembrane domains with both C- and N-terminals located in the cytosolic side of the vesicle [291]. Putative glycosylation sites (three or four) are located in a loop between transmembrane domains I and II facing the vesicular matrix [291], which serves as part of a trafficking signal [293].

VMAT2 is a transmembrane protein that transports monoamines (DA, norepinephrine, epinephrine, serotonin and histamine) into synaptic vesicles for its subsequent Ca^{2+} -stimulated release from the neuron [294]. The first evidence about monoamine uptake into bovine chromaffin granules through reserpine-sensitive VMAT was initially demonstrated by Kirshner [295]. Several studies have confirmed monoamine transport into the storage vesicles against a large concentration gradient ($>10^5$), which is driven by the electrochemical gradient generated by a transmembrane proton vesicular H^+ -ATPase [291]. The proton-monoamine exchange occurs at a ratio of two translocated protons per one translocated amine; the first proton's efflux from the granule matrix generates a conformational change with high-affinity amine binding in the cytosolic phase of a transporter. The second proton's efflux induces large conformational change facilitating the movement of the amine from the cytosolic phase to the matrix phase with the consequent reduction of the amine binding affinity [296]. Structure-function studies have established the critical role of VMAT2 not only in sorting, storing and releasing of monoamines but also protecting them from autooxidation [291].

VMAT2 is the only vesicular monoamine transporter expressed in CNS. Interference with its function could lead to impaired catecholamine homeostasis, DA-related cellular toxicity and neurodegeneration in the nigrostriatal DA system. Also, deletion of the VMAT2 gene leads to neonatal death in mice due to severely impaired

monoamine storage and vesicular release [297-300]. Although the function of VMAT2 is demonstrated, other regulatory mechanisms such as its post-translational modification and PPIs are not well understood. Nevertheless, there are reports of VMAT2 interacting with TH and other enzymes in the DA biosynthesis pathway [233]. Moreover, HSC70 and α -synuclein have been reported to inhibit VMAT2 activity in synaptic vesicles and SH-SY5Y cells [301, 302].

2 AIMS

The main goal of this thesis is to study the regulation of the aromatic amino acid hydroxylases PAH and TH in normal and pathological states. We focus on two major regulatory mechanisms, PPIs and phosphorylation, investigating how they contribute to the function and proteostasis of aromatic amino acid hydroxylases in health and disease. The overarching goal is addressed through the following specific aims:

- Investigate the role of DNAJC12 in the proteostasis of normal and PAH mutants in cellular and *in vivo* models. Specifically, using COS cells and the *Enu1* mouse model of HPA, compare the interaction of Wt DNAJC12 with either Wt or PAH mutants associated with HPA/PKU.
- Characterise the behavioural and metabolic phenotype of a novel knock-in PKU mouse bearing the *Pah-R261Q*, as well as investigate the effects of the *R261Q* mutation on PAH proteostasis *in vivo*, as *in vitro* studies have shown that it results in unstable and misfolded PAH.
- Investigate the functional role of THpSer31, going beyond its customary association with an increased TH activity, and rather focusing on the subcellular localisation of TH and its PPIs using cellular models and immuno-based imaging.
- Study the biological significance of the THpSer8 state, focusing on its role in the subcellular localisation of TH, notably nuclear localisation. This investigation is motivated because Thr8 phosphorylation in TH has been largely unexplored. We addressed this question using a range of complementary molecular and cellular biology approaches in a cellular model.

3 SUMMARY OF THE PAPERS

Paper I

Phenylalanine hydroxylase variants interact with the co-chaperone DNAJC12.

Kunwar Jung-KC, Nastassja Himmelreich, Karina S. Prestegård, Tie-Jun Sten Shi, Tanja Scherer, Ming Ying, Ana Jorge-Finnigan, Beat Thöny, Nenad Blau, and Aurora Martinez

Hum Mutat. 2019 Jan 22; 40(4): 483-494. doi: 10.1002/humu.23712

Paper II

The Pah-R261Q mouse reveals oxidative stress associated with amyloid-like hepatic aggregation of mutant phenylalanine hydroxylase.

Oscar Aubi, Karina S. Prestegård, Kunwar Jung-KC, Tie-Jun Sten Shi, Ming Ying, Ann Kari Grindheim, Tanja Scherer, Arve Ulvik, Adrian McCann, Endy Spriet, Beat Thöny, Aurora Martinez

Nat Commun. 2021 Apr 6;12(1):2073. doi: 10.1038/s41467-021-22107-1

Paper III

Phosphorylation at serine 31 targets tyrosine hydroxylase to vesicles for transport along microtubules.

Ana Jorge-Finnigan, Rune Kleppe, Kunwar Jung-KC, Ming Ying, Michael Marie, Ivan Rios-Mondragon, Michael F. Salvatore, Jaakko Saraste, and Aurora Martinez

J Biol Chem. 2017 Aug 25; 292(34): 14092–14107 doi: 10.1074/jbc.M116.762344

Paper IV

Phosphorylation at threonine 8 is associated with nuclear localisation of recombinant human tyrosine hydroxylase in SH-SY5Y cells.

Kunwar Jung-KC, Ana Jorge-Finnigan and Aurora Martinez

Manuscript in preparation.

3.1 PAPER I

In paper I, we aimed to investigate the role of DNAJC12 in PAH – Wt and mutants – on folding and degradation. We first investigated the endogenous expression of DNAJC12 in COS-7 cells by transiently expressing PAH mutants associated with HPA/PKU of different severity. We observed a positive correlation between the levels of immunoquantified PAH and endogenous DNAJC12. The immunodetected levels of endogenous DNAJC12 were reduced for the most unstable PAH mutants, e.g., p.R408W, which gives rise to a highly unstable and misfolded PAH enzyme, resulting in rapid degradation and low immunodetection levels.

We next sought to investigate the relation of DNAJC12 with mutant PAH *in vivo*, for which we used a mouse model (*Enu1*) that expresses the unstable and misfolded PAH mutant p.V106A-PAH. Western blot of liver lysates showed a reduction of mutant PAH levels in the *Enu1*, which mostly appeared to be mono-ubiquitinated compared to Wt mice that presented a significant fraction of full-length non-ubiquitinated-PAH. DNAJC12, however, was only immunodetected in the liver lysate of Wt mice and not in the mutant. To investigate if the reduction of DNAJC12 is due to accumulation in a specific compartment, we prepared nuclear and cytosolic fractions of liver lysates of Wt, heterozygote (*Enu1^{wt}*) and homozygote (*Enu1^{1/1}*) mice. The level of DNAJC12 was strongly reduced in heterozygous mice compared to *Wt* and almost absent in both fractions in the homozygote.

Considering transcriptional down-regulation of the co-chaperone as a reason for the reduced immunodetection in *Enu1^{1/1}* liver lysate, we performed mRNA quantification of *Dnajc12* and *Pah*, as well as other selected genes based on their possible interactions with DNAJC12. However, no significant differences in mRNA expression were measured for any of the genes when comparing *Wt* and *Enu1^{1/1}* mice liver samples. We then hypothesised if an intracellular co-aggregation of PAH and DNAJC12 could be the cause of the reduced immunodetection. To test this hypothesis, we prepared liver lysate using a buffer with lower ionic strength to diminish hydrophobic interaction. We

improved solubilisation by treating with Triton X-100 (1%) before subjecting the samples to SDS-PAGE. The optimised lysate preparation improved the immunodetection of DNAJC12 in the liver of homozygous mice. Immunohistochemistry data was very similar to western blot data, i.e., reduced PAH and DNAJC12 detection in *Enu^{1/1}* compared to *Wt*. Lastly, we performed immunoprecipitation assays to study possible complex formation between PAH and DNAJC12 in *Wt* and *Enu^{1/1}* mice. PAH was immunoprecipitated mainly as non-ubiquitinated in *Wt*, whereas in *Enu^{1/1}*, it was mostly mono-ubiquitinated. DNAJC12 and HSC70/HSP70 were co-immunoprecipitated in both samples.

Our results reveal a role of DNAJC12 in the processing of misfolded ubiquitinated PAH and support that this HSP40 co-factor is an important player both for proper folding and degradation of PAH.

3.2 PAPER II

This study set out to characterise a new custom-made *Pah-R261Q* knock-in mouse model generated by introducing the mutation c.782G>A in the *Pah* gene by CRISPR/Cas9 technology. The mouse was subjected to heteroduplex mobility assay to screen for possible off-target mutation by guide RNA, and the colony was backcrossed frequently to avoid genomic drift. L-Phe levels, measured in dried blood spots, in 3-month-old mice, showed a significant increase in *Pah-R261Q* ($108.0 \pm 36.6 \mu\text{M}$, $n = 23$ mice) compared to both *Wt* ($59.9 \pm 7.7 \mu\text{M}$, $n = 9$; $p < 0.0001$) and heterozygous *Pah^{R261Q/Wt}* ($71.22 \pm 21.86 \mu\text{M}$; $n = 6$; $p = 0.0201$), corresponding to mild HPA. Although *Pah-R261Q* mice were similar to their heterozygote and *Wt* counterparts in length, pigmentation, and behaviour, three-month-old male *Pah-R261Q* mice were heavier than *Wt* (27.8 ± 0.4 vs 25.1 ± 0.3 g, respectively). Analysis of various physiological parameters revealed reduced O₂ consumption, CO₂ production and respiratory exchange ratio when normalized to body mass for *Pah-R261Q* compared with *Wt* (0.988 ± 0.087 vs 1.014 ± 0.093).

Metabolic profiling, by chromatographic separation and mass spectrometry detection, revealed lipid metabolism alterations and oxidative stress in the *Pah-R261Q* mice. However, no significant alterations of the levels of BH₄, aromatic amino acids and monoamine neurotransmitters in the brain were detected, and the neuromuscular function was similar as confirmed by rotarod performance. However, the concentration of BH₄ in the liver was reduced by 50% in *Pah-R261Q* (28.0±1.7 pmol BH₄/mg protein) compared with *Wt* mice (56.2±3.2 pmol/mg). We then tested the sensitivity toward the L-Phe challenge by administering 200 µg L-Phe/g body weight. Forty minutes post i.p. injection, *Pah-R261Q* showed a massive increase in L-Phe concentrations (990±220 µM) compared to *Wt* and *heterozygous* mice before returning to the basal level after 300 minutes. *Pah-R261Q* responded to BH₄ treatment resulting in a 28% decrease in L-Phe content.

The stability study on PAH protein was carried by Western blot and immunohistochemistry using liver samples. The results showed a reduction of total p.R261Q-PAH protein levels and increased ubiquitination in *Pah-R261Q* compared to *Wt* mice, indicative of instability or misfolding of this PAH mutant. To compare the mutation-specific aggregation pattern of PAH protein, a mouse model with mild HPA (*Enu1*) expressing the unstable p.V106A-PAH mutant, which is associated with PAH instability, was included in this study. The PAH aggregates' size was larger in *Pah-R261Q* than in *Enu1* mice as quantified from 3,3'-Diaminobenzidine (DAB) staining (the averaged area of DAB-stained particles was 0.18±0.06 and 0.11±0.03 µm² for *Pah-R261Q* and *Enu1*, respectively). The distribution of PAH aggregates in the hepatocytes of both mice was different; PAH aggregates in *Enu1* were distributed both in the cytoplasm and nucleus, whereas in *Pah-R261Q*, they were distributed at the cytoplasmic side of the nuclear membrane.

The difference in size and distribution pattern of PAH aggregates in both mice suggested a distinct mechanism involved in misfolding and aggregation of these mutants. Interestingly, *in silico* evaluation by the program TANGO predicted a high

propensity (>50%) to form intermolecular cross- β (amyloid-like) aggregates in region 254-263 (FLGGLAFQVF) only in the p.R261Q-PAH mutant, which was complemented by Amytracker™ 680 fluorescence assay and transmission electron microscopy (TEM), which showed a formation of amyloid-like amorphous aggregates for purified p.R261Q-PAH compared to p.Wt-PAH.

We next investigated the mechanism involved in the clearance of mutant PAH. As the autophagy pathway removes larger aggregates [303], we performed immunohistochemical analysis on liver tissue of *Wt*, *Pah-R261Q* and *Enu1* mice using the autophagic marker Ser403-phosphorylated p62 protein (p62/SQSTM1) and LC3. Both phosphorylated p62 and LC3 levels were elevated and colocalised with mutant PAH in *Pah-R261Q* compared to *Wt* and *Enu1*. These results suggest that the larger PAH aggregates in *Pah-R261Q* engage the autophagic system but not the smaller aggregates in *Enu1*. Also, TEM analysis showed a higher number of lysosomes and autophagic structures, i.e. double-membrane autophagosomes and autolysosomes in the *Pah-R261Q* mice.

Finally, *PAH* and some genes related to BH₄-synthesis, protein quality control, and oxidative stress pathways were selected and subjected to quantitative PCR analysis using *Wt* and *Pah-R261Q* mice's liver extracts. The data analysis indicated no significant change in *PAH* expression in both mice. The *GCH1-feedback regulatory* (*Gchfr*) and *DNAJC12* gene were upregulated in the mutant mice, whereas the transcription factor *Hsf1* and the molecular chaperone *Hsp70* were downregulated. The expression levels of genes connected to protein degradation, e.g. *Stub1*, *p62/SQSTM1* and the oxidative stress-responsive transcription factor *Ap-1*, were not altered.

In conclusion, the *Pah-R261Q* mouse exhibited lipid profile alterations and increased oxidative stress due to the accumulation of mutant PAH aggregates. The selective autophagy-lysosome pathway mediated by Ser403-phosphorylated p62 protein appears to be involved in the degradation of p.R261Q-PAH aggregates.

3.3 PAPER III

This study aimed to investigate the functional role of Ser31 phosphorylation and its relationship with interacting partners in the regulation of TH. Different cell lines, such as PC12 cells, SH-SY5Y, HEK293 and iCell DopaNeurons, were used to carry out this study.

We studied the cellular distribution of THpSer31 using specific antibodies towards this phosphorylated form. THpSer31 signal resembled Golgi complex (GC) pattern in PC12 cells and was co-detected with the GC marker GM130 in PC12Adh, iCell DopaNeurons, and PC12 cells. Treatment with brefeldin A, a drug that causes a reversible disruption of the Golgi, abolished the THpSer31 signal. Co-detection of THpSer31 and synaptic-like vesicle marker synaptotagmin I in iCell DopaNeurons, and PC12 cells, in addition to colocalisation of fluorescence signals of immunolabeled VMAT2 and THpSer31 in iCell DopaNeurons indicated that THpSer31 associates with synaptic vesicles. Moreover, chemical inhibition of the kinases (Cdk5 and ERK1/2) that are responsible for the phosphorylation of TH at Ser31 led to a strong reduction of both total-TH and THpSer31 in the microsomal fraction of PC12 cells. SH-SY5Y cells transiently expressing a phospho-null mutant of Ser31 (V5-TH-S31A) was also reduced in the microsomal fraction compared to cell transiently expressing the phospho-mimicking mutants (V5-TH-S31E).

Surface plasmon resonance studies using purified recombinant humanTH1 showed a certain degree of interaction with trypsinised chromaffin-vesicle membranes. However, there was no difference in the interaction between TH (non-phosphorylated/THpSer31) and the membrane, indicating that TH does not interact directly with the vesicles. VMAT2, a vesicular membrane protein that facilitates THpSer31 interaction with vesicles and α -syn was disclosed by *in situ* proximity ligation assay in SH-SY5Y cells and confirmed by immunoprecipitation, which was performed using mouse brain lysates. We next sought to investigate if this interaction leads to localisation of TH toward the terminals by disrupting the microtubule network

with nocodazole. In SH-SY5Y cells, the treatment led to reduced V5-TH-S31E signal in the neurite, whereas V5-TH-S31A signal was mostly accumulated in soma with or without treatment. In iCell DopaNeuron cells, inhibition of phosphorylation and disrupted microtubule system lead to decreased THpSer31 signal both in soma and neurites. However, drug washout led to the recovering of the lost signal both in soma and neurites, indicating that the axonal transport of TH depends on microtubule integrity. The anterograde transport of TH was also affected by mutant α -syn when co-expressed with V5-TH-S31E in SH-SY5Y cells.

Finally, we studied whether phosphorylation at Ser31 can modulate phosphorylation at Ser19 and Ser40. Our results in neuroblastoma cells showed less Ser19 and Ser40 phosphorylation for the V5-TH-S31E mutant compared to V5-TH-S31A, suggesting that conformational constraints and its interaction with partners, such as α -syn or VMAT2, may affect its availability for phosphorylation in cellular models.

To conclude, Ser31 phosphorylation appears to enable the association of TH with synaptic vesicles by interacting with VMAT2 and α -syn. This PPI facilitates the subcellular localisation of TH toward axon terminals via the microtubule system.

3.4 PAPER IV

This study aimed to investigate the physiological role of Thr8 phosphorylation in the regulation of TH. We relied on the use of overexpression of phospho-mimicking, and phospho-null TH mutants and detection of their V5-epitope tag due to the lack of useful commercially available phospho-Thr8 (pThr8) antibody and failure to custom create pThr8 antibody. We first examined the distribution of endogenous total-TH, which was both cytosolic and nuclear, whereas THpSer19 was mostly nuclear in SH-SY5Y cells. THpSer19 detection in the cytosol was improved upon treatment with guanidinium chloride (GuHCl), which breaks the protein-protein interaction. To investigate the role of Ser19 phosphorylation in TH nuclear localisation, we created the V5-TH-S19A (phospho-null) and V5-TH-S19E (phospho-mimicking) mutants by site-directed

mutagenesis. Immunofluorescence assay could not explain the difference in the nuclear distribution of Wt and mutant mutants when expressed in SH-SY5Y cells. Subcellular fractionation, followed by Western blot analysis, revealed that V5-TH-S19A was significantly higher in the nuclear fraction than V5-TH-Wt, eliminating the possibility that Ser19 phosphorylation has a role in the nuclear localisation of TH.

We then hypothesised that Thr8 phosphorylation might have specific involvement in the nuclear localisation of TH since there are two nuclear localisation signals predicted by cNLS mapper (a web-based tool) adjacent to it [304]. We created V5-TH-T8A (phospho-null) and V5-TH-T8E (phospho-mimicking) mutants and expressed them in SH-SY5Y cells. Western blot analysis of nuclear and cytosolic fractions expressing phospho-null and phospho-mimicking mutants of Thr8 showed a significant reduction of V5-TH-T8A by 34% \pm 6 (p-value=0.0009; n=3) in the nuclear fraction compared to Wt, revealing the role of Thr8 phosphorylation in the regulation of nuclear localisation of recombinant TH. Surprisingly, V5-TH-T8E was also reduced in the nuclear fraction compared to Wt, but its level was however higher than for V5-TH-T8A.

We further investigated whether nuclear localisation is regulated by hierarchical phosphorylation; we analysed phospho-null and phospho-mimicking mutants of Ser31 and Ser40 in the nuclear and cytosolic fractions by Western blot, which did not show any difference in the detection of mutant mutants compared to Wt, further supporting the importance of Thr8 phosphorylation in the nuclear localisation of TH. Finally, we studied the mechanism involved in the nuclear import of TH by treating SH-SY5Y cells with importazole, an inhibitor of importin- β . Wb analysis showed a significant reduction of V5-TH-Wt by 39% \pm 22 (p-value= 0.04; n=3) in the nuclear fraction when compared to untreated samples. Overall, our data suggest that Thr8 phosphorylation regulates the nuclear localisation of TH via the importin- β /RanGTP pathway.

4 DISCUSSION

The reactions catalysed by AAAHs are of physiological and clinical importance and are tightly regulated, both short-term and long-term. Disturbances in the function of AAAHs can lead to severe neurometabolic and neuropsychiatric disorders, caused by mutations in the hydroxylases themselves or on the regulatory proteins, as clearly exemplified in DNAJC12 deficiency [235]. Dysfunctional PAH can elevate phenylalanine in the blood to a toxic level, causing a detrimental effect on the brain development and function [72]. Reduced TH activity leads to decreased DA levels and a broad range of movement disorders [228]. Therefore, it is crucial to study mechanisms, such as post-translational modifications and protein-protein interactions, which regulate these enzymes to better understand the associated disorders and contribute to the development of optimised therapies.

In this work, we have studied regulatory PPIs involved in the function and proteostasis of PAH and TH using cellular and animal models. Importantly, we characterised a novel *Pah-R261Q* knock-in mouse line with the nucleotide change c.782G>A in *Pah* exon 7, coding for p.R261Q-PAH, one of the most common PKU mutations in humans.

4.1 CO-CHAPERONE DNAJC12: A DOUBLE EDGED SWORD?

Recently, DNAJC12, a member of the HSP40 family, was reported as a specific co-chaperone of AAAHs. Moreover, DNAJC12 deficiency has been associated with the clinical and metabolic spectrum of HPA, as well as dystonia and intellectual disability [235], without evidence of PAH, TH, TPHs or BH₄ deficiency. The typical role of DNAJ/HSP40 co-chaperones is to assist the HSC70/HSP70 family of molecular chaperones in properly folding its client proteins in an ATP-dependent binding/release cycle. As further DNAJ proteins are characterised, several proteostatic control aspects have been revealed. In addition to protein folding, they protect misfolded clients from

aggregation and/or facilitate ubiquitination and active delivery of terminally misfolded proteins to degradative pathways (UPS or autophagy) [31, 305, 306].

Anikster *et al.* demonstrated the role of DNAJC12 in the proper folding of PAH [235]. Our work (**paper I**) provides new insights into the role of DNAJC12 on the degradation of its clients. We observed a positive correlation between the amount of soluble DNAJC12 and PAH (wildtype and mutants) in COS-7 cells and the *Enu1* hyperphenylalaninemic mouse expressing the unstable and misfolded p.V106A-PAH [307]. Surprisingly, DNAJC12 in the liver of mutant mice was not immunodetected in tissue homogenates, however solubilisation with Triton led to its immunodetection, but in reduced amounts. Quantitative analysis of mRNA transcripts dismissed the possibility that PAH mutation could affect gene expression of *Dnajc12*. Interestingly, in **paper II**, a mouse with p.R261Q-PAH mutation showed upregulation of *Dnajc12* expression, most likely due to oxidative stress [254, 308]. Furthermore, co-aggregation of DNAJC12 mutants with Wt PAH, TH and TPH2 have been reported in a cellular system [261].

We detected DNAJC12 as co-immunoprecipitant with both Wt and mono-ubiquitinated mutant PAH, suggesting a role of DNAJC12 in the degradation of the client. In addition, it has been shown that overexpression of DNAJC12 in the presence of different PAH mutants leads to either an increase or decrease in PAH amount and activity, indicating a mutation-specific selective function in the folding and/or degradation of mutant PAH [261]. DNAJC12 may also have a role in the degradation of Wt PAH when the protein reaches the end of its life cycle, since comparable amounts of mono-ubiquitinated Wt and mutant PAH was observed (**paper I**). There are reports of HSP40 promoting ubiquitination of its client protein, preventing deubiquitination and subsequent sorting to the proteasome [309, 310].

Mutations in DNAJC12 have also been reported to cause early-onset, dopa-responsive non-progressive parkinsonism [260]. Additionally, the deficiency of monoamines and their metabolites, including DA, serotonin, homovanillic acid, and 5-

hydroxyindoleacetic acid, in the cerebrospinal fluid of the affected individuals indicate the importance of DNAJC12 in the proper function of the enzymes involved in the biosynthesis of monoamines [311]. Although direct interaction of DNAJC12 with TH has been shown [235], we still lack substantial knowledge on how this interaction with either Wt or mutant TH affects their regulation at a cellular and molecular level.

Based on our results and the knowledge available in the scientific community on the effects on PKU-associated PAH mutations [261], DNAJC12 could contribute to alleviate or even aggravate disease progression. Whereas the former effect may be associated with an effective folding of certain mutant clients prone to degradation and/or aggregation, the latter may appear related to a too effective degradation of mutants with catalytic activity. Understanding the mechanisms involved is, therefore, crucial to identify therapeutic strategies for the associated disorders.

4.2 PROTEOSTASIS REGULATION OF WT AND MUTANT PAH AND TH; DEGRADATION SYSTEMS

Both PAH and TH are subjected to various short-term regulatory mechanisms, contributing to their activity, stability and localisation. On the other hand, mutations can affect either their enzymatic activity directly or their regulation, but in any case, they often result in reduced stability and intracellular half-life, thus also resulting in reduced total activity [223, 227, 312]. To date, >1000 human *PAH* mutants have been registered in the locus-specific BIOPKU database (<http://www.biopku.org/home/pah.asp>). Actually, enzyme stability algorithms (FoldX) and enzyme activity are powerful predictors of phenotype and BH₄ response using data from BIOPKU [188]. The large number of registered and characterized patients has resulted in reliable genotype-phenotype correlations. However, PKU patients homozygous for the frequent p.R261Q-PAH mutation exhibit highly variable phenotypes, from mild to severe PKU, with different BH₄ responsiveness [189, 313-315], indicating strong modifier traits and revealing this mutation as a very exciting

focus of study. The knock-in mouse encoding the p.R261Q-PAH mutation (**paper II**) exhibited lipid profile alterations and increased oxidative stress, which was likely due to the accumulation of p.R261Q-PAH aggregates, introducing a toxic gain-of-function concept for specific PKU-associated mutations.

Mouse and human PAH share high sequence homology (92.5 % identity), structure, regulatory mechanisms and specific activity, with Arg261 being in the evolutionarily conserved catalytic domain. The residue R261 has a structural role, stabilising the active site secondary structure and dimer/tetramer formation [216]. The Arg261 substitution to Gln would disrupt intra- and inter-subunit interactions, giving rise to an unstable protein [216, 312] (Figure S1; Paper II). More often than not, instability leads to accelerated degradation, but instability can also be followed by misfolding and aggregation. In fact, *in silico* prediction (TANGO [316]) showed a high propensity to form intermolecular cross- β (amyloid-like) aggregates for both human and mouse PAH in region 254-263 in the mutant (FLGGLAFQVF) but not in Wt (**paper II**). Using purified recombinant p.R261Q-PAH, we confirmed the prediction by performing a fluorescence assay utilising luminescent conjugated oligothiophene dyes, a tracer molecule for visualising amyloid-like protein aggregates. Immunohistochemistry and TEM analysis further corroborated the hypothesis that the R261Q mutation leads to large amorphous aggregates but not fibrils.

The present knowledge for many PKU-associated PAH mutants is the destabilisation of mutant proteins and degradation carried out preferentially by the UPS [317]. Our study on *Pah-R261Q* mice showed that selective autophagy might be involved in the degradation of the mutant PAH. The co-detection of p.R261Q-PAH with Ser403-phosphorylated p62 and LC3 indicated the engagement of the autophagic system. The affinity of p62 for ubiquitinated protein increases when phosphorylated at Ser403; thus, Ser403-phosphorylated p62 enhances the autophagic degradation of ubiquitinated proteins in case of toxic accumulation of mutant aggregates [318]. The ubiquitinated-protein bound to Ser403-phosphorylated p62 is efficiently sequestered in the

sequestosome, a membrane-free body of aggregates [319], followed by engulfment in the autophagosome through p62 interaction with lipidated LC3 and subsequent fusion with the lysosome, where the actual degradation process takes place [48]. The ubiquitinated-PAH mutants' selectivity for the degradation pathways appears dependent on the nature of the aggregates, as moderately aggregating *Enu1* mutant p.V106A-PAH (not predicted to form amyloid-like aggregates by TANGO, **paper II**), is also highly ubiquitinated but displays no co-detection with the autophagic markers.

Døskeland and Flatmark initially showed recombinant hTH1 to be ubiquitinated and degraded in the reticulocyte lysate system [320]. Since then, several reports have emerged indicating phosphorylation of TH at the N-terminal to be a critical trigger for its proteasomal degradation [170, 171, 304, 321-323]. Furthermore, inhibition of proteasome increases ubiquitinated-THpSer40 to form insoluble aggregates in NGF-stimulated PC12D cells [321]. Given the long half-life of TH (approximately 17 h, 30 h and 29 in PC12 cells, in a subclone of PC12 cells and in chromaffin cells, respectively [324-326]), it is logical to expect that TH is subjected to both short-term and long-term regulation by degradative pathways. In fact, it has been reported to be short-term regulated in a phosphorylation-dependent manner by UPS and long-term by the lysosome [323].

4.3 REGULATORY SER/THR PHOSPHORYLATION OF TH AND CONSEQUENT PPI FORMATION

PAH has one phosphosite and exhibits relatively simple phosphorylation mediated regulation compared to TH, which has four phosphosites with distinct roles. PAH is phosphorylated at Ser16, which facilitates its activation by L-Phe by inducing a subtle N-terminal conformational change and providing higher stability toward limited tryptic proteolysis [123]. Phosphorylation of TH not only increases enzyme activity *in situ* but also facilitates protein-protein interactions, promotes subcellular localisation, and

maintains protein availability which in turn maintains optimal catecholamine levels in cells [133, 137, 147, 327, 328] (**paper III** and **paper IV**).

In **paper III**, we investigated a novel functional role of Ser31 phosphorylation. Our results showed that TH associates with the Golgi complex and synaptic-like vesicles in a phosphorylation-dependent manner. The perinuclear distribution of THpSer31 resembled a GC pattern in several cellular models (PC12 cells, iCell DopaNeurons), indicating a possible early TH interaction with vesicles. This hypothesis was further corroborated when we observed THpSer31 co-distribution with vesicle marker synaptotagmin I and VMAT2. Additionally, the data obtained from transient overexpression of V5-TH-S31A (phospho-null) and V5-TH-S31E (phospho-mimicking) mutants were consistent with our observation. Ser31 phosphorylation of TH is important for its interaction with VMAT2 and α -syn since the phospho-null mutant exhibited reduced co-distribution (**paper III**).

A growing body of evidence suggests that synaptic and non-synaptic proteins are transported together as constituents of common cargoes, perhaps as a multiprotein complex; e.g., α -syn, synapsin-I and glyceraldehyde-3-phosphate dehydrogenase have been shown to co-transport in the axons of cultured hippocampal neurons [329, 330]. Both TH and α -syn have been shown to be rapidly transported by the fast components of the axonal transport, which mainly carry vesicular cargoes [331, 332]. Thus, TH and α -syn might tether to VMAT2 and co-transport as part of a multivesicular complex. The results from mice brain lysates and cellular models confirmed the interaction of THpSer31 with VMAT2 and α -syn. Moreover, it is known that α -syn interacts with TH inhibiting its activity [178]. Our results indicate that TH, together with VMAT2 and α -syn, is transported toward the axon terminal, most likely in an inhibited state. Furthermore, additional regulatory or stabilising proteins, such as Hsc70 and DOPA decarboxylase, are known to interact with VMAT2 and TH [301, 333], which might co-transport with the same cargo [301, 333]. This kind of efficient “packaging” of multiple proteins may allow them to perform their complementary roles [334].

TH and THpSer31 levels are higher in the terminals than soma, and the modulation of TH activity is maintained locally in each compartment [163]. Moreover, hTH2, which cannot be phosphorylated at the equivalent Ser31 site of hTH1 (due to the 4-amino acid insert of hTH2), shows abundance in the substantia nigra and is reduced at the terminals, indicating the importance of Ser31 phosphorylation in the subcellular localisation of TH [127, 335]. Still, hTH2, which is expressed in similar amounts in cells as hTH1, is present at the terminals [127]. This may be facilitated by the formation of heterotetramers with the more transport competent hTH1. However, this has to be confirmed experimentally.

Stabilisation of TH seems to be important for the transport to the terminals, and binding of DA to TH is one of the strongest stabilising mechanisms [86]. A mouse model with dopamine transporter knockout exhibits reduced DA tissue content, TH expression and phosphorylation only in the terminals [336]. In line with this hypothesis, the knock-in mouse with the mutation p.R203H, equivalent to hTH1-p.R202H, shows reduced stabilisation by DA and exhibits a deficit in the striatal distribution of TH [227]. The altered nigrostriatal distribution of TH and lack of DA in synapse also affect DA reuptake by DAT, which is regulated by the D2 autoreceptor [337]. DA deficiency also leads to an increase in Ser40 phosphorylation and subsequent degradation of TH by the UPS in PC12D cells [322].

Prior studies have emphasised TH to be a cytosolic enzyme; however, its physiological interaction with membranes has been reported [338], and along with our study (**paper III**), the subcellular distribution of TH in different compartments has been established [137]. For the first time, Nakashima *et al.* reported the nuclear distribution of Ser19 phosphorylated TH in PC12D cells and associated the phosphorylation site with the proteasomal degradation of TH in the nucleus [170, 304]. However, the relationship between phosphorylation and nuclear localisation still remains unclear. Consistent with the previous report [170], we observed in SH-SY5Y cells that Ser19 phosphorylated TH presented a nuclear distribution (**paper IV**). Yet, it was intriguing to see a lack of

THpSer19 in the cytosol, as initially expected due to TH abundance in the cytosol. It is well known that THpSer19 interacts with 14-3-3 proteins [247, 339]. We hypothesised that this PPI might protect the epitope, hence the reduced detection of THpSer19 in the cytosol. Surprisingly, when V5-TH-S19A (phospho-null) and V5-TH-S19E (phospho-mimicking) mutants were transiently expressed in SH-SY5Y cells, the amount of phospho-null mutant in the nuclear fraction was significantly higher than Wt and phospho-mimicking mutants, contradicting our initial hypothesis. Cellular distribution analysis of THpSer31 and THpSer40 did not suggest a role for these sites in TH nuclear localisation. We then tested if Thr8 phosphorylation is involved in the nuclear distribution of TH. The V5-TH-T8A mutant showed a significant reduction in the nuclear fraction of SH-SY5Y cells compared to V5-TH-Wt. Our data was not incompatible with other phosphosites being detected in the nuclear fraction, as these might reflect “passenger phosphosites”, whereas THpThr8 could actively be involved in the interaction with proteins related to nuclear import.

It is known that several nuclear transport factors or carrier proteins, collectively called β -karyopherins, facilitate the translocation of large cargoes either into or out of the nucleus. β -karyopherins are divided into importins and exportins for their import and export roles, respectively. It is a prerequisite for cargoes to possess a Nuclear Localisation Signal (NLS) that can be recognised by an importin directly or by an adaptor protein [340]. TH has been predicted to contain two NLS downstream of Thr8 phosphosite; Pro9-Arg38 and Lys12-Ile42 [304]. Furthermore, evidence of phosphorylation-mediated upregulation of nuclear import is emerging [341]. Phosphorylation within or upstream of NLS can promote nuclear localisation of cargoes either by increasing their affinity for a specific import factor that recognises the phosphate moiety or by modulating the recognition of NLS [342, 343].

Since nuclear import requires protein-protein interaction, inhibiting the proteins involved in the pathway should affect the transport process. Treatment with importazole, a small molecule inhibitor of importin- β [344], decreased the nuclear

content of recombinant TH in SH-SY5Y cells, indicating an involvement of the importin- β /RanGTP pathway. The energy-dependent importin- β /RanGTP pathway relies on the Ran (RAS-related Nuclear protein) nucleotide state, which cycles between GDP- and GTP-bound states that regulate interactions between cargoes and carriers. Thus, by indicating its involvement of Thr8 phosphorylation in nuclear uptake, our results support a previously unavailable specific role for this phosphosite. Although the kinase responsible for phosphorylating Thr8 is still ambiguous, it has been reported that CDK1 is involved in the phosphorylation of Thr8 in cultured cells [150, 173]. However, among all the phospho-sites in TH, Thr8 has the lowest stoichiometry *in situ* and *in vivo* [147]. Ser8 phosphorylation of rat TH is high in PC12 cells and low in the corpus striatum, perfused rat adrenal medulla and bovine chromaffin cells [177], which correlates with the expression level of CDK1, low in non-mitotic tissues and high in PC12 cells [345].

So far, the nuclear localisation of TH has only been associated with proteasomal degradation. Phosphorylation mediated nuclear degradation has been shown for proteins, such as the transcription factor MYC oncoprotein [346]. Besides, we have observed the nuclear distribution of PAH aggregates in the hepatocytes of *Enul* mice (**paper II**), where the nuclear UPS may degrade them [347]. However, further research is necessary to investigate if TH has an additional role in the nucleus since it has been long known to interact with polyanions [130, 132] yet the functional relevance of this interaction has not been clarified.

5 CONCLUSIONS AND FUTURE PERSPECTIVES

In this thesis, we have studied the proteostatic regulation of two aromatic amino acid hydroxylases, PAH and TH, to elucidate the protein-protein interactions involved in their availability, distribution and subcellular localisation.

In particular, we demonstrated a PAH mutation-specific interaction of the specific HSP40 co-chaperone of the AAAHs, DNAJC12, with non-ubiquitinated PKU-associated mutants in COS cells. Furthermore, we showed a tight interaction of DNAJC12 with ubiquitinated mutant PAH *in vivo*, revealing a role in the degradation of PAH. These findings underscore the complex quality control system involved in the intracellular stability of PAH, and especially of disease-associated mutants. However, further investigations are necessary to unravel the mechanisms and interactions between DNAJC12 and AAAHs clients at the molecular level.

We presented the metabolic and biochemical characterization of the novel *Pah-R261Q* knock-in mouse, and our findings imply a paradigm shift in the understanding of PKU pathology from a loss-of-function disorder to include a gain-of-function contribution from toxic protein misfolding and aggregation. We showed a strong connection between intracellular toxic aggregation of the p.R261Q-PAH mutant and increased oxidative stress with lipid profile alteration in the knock-in mice *Pah-R261Q*. Our results indicate that in this mouse model, the large PAH aggregates may be degraded by the p62/sequestosome-LC3 mediated autophagic pathway. The *Pah-R261Q* mouse model thus represents a valuable research tool to further investigate the proteostasis regulation of mutant PAH, and evaluate and discover additional biomarkers in PKU related to mutation-specific comorbidities. Moreover, this mouse model could help investigate pharmacological chaperone-based therapies targeting unstable and misfolded PAH mutants.

We also revealed a novel role for TH phosphorylated at Ser31 phosphorylation, elucidated in cellular models. Our data shows the co-distribution of TH with synaptic vesicles through association with VMAT2 and α -syn in a THpSer31 phosphorylation-dependent manner. Furthermore, this phosphorylation-mediated PPI interaction facilitates the transportation of TH from the cell soma to the terminals. Moreover, our study directs toward a prospect for a therapeutic strategy to revert neuronal mislocalisation in disorders associated with THD by targeting and stabilising the PPI involved in the transport of TH.

We investigated the nuclear distribution Ser19 and elucidated the role of the long under-researched Thr8 phosphorylation of TH in SH-SY5Y cells. We identified that Thr8 phosphorylation regulates the nuclear localisation of TH via the importin- β /RanGTP pathway. Besides, hierarchical phosphorylation did not affect nuclear localisation. The nuclear distribution of TH has been associated with its proteasomal degradation. However, it is important to investigate if TH can enter the nucleus to perform an additional function or other reasons than to be degraded, such as modulation of gene expression by establishing PPIs. Furthermore, the role of Thr8 phosphorylation in an animal model needs to be investigated.

REFERENCES

1. Balch, W.E., et al., *Adapting Proteostasis for Disease Intervention*. Science, 2008. **319**(5865): p. 916-919.
2. Morimoto, R.I. and A.M. Cuervo, *Proteostasis and the Aging Proteome in Health and Disease*. The Journals of Gerontology Series A: Biological Sciences and Medical Sciences, 2014. **69**(Suppl 1): p. S33-S38.
3. Goh, K.I., et al., *The human disease network*. Proceedings of the National Academy of Sciences, 2007. **104**(21): p. 8685-8690.
4. Ideker, T. and R. Sharan, *Protein networks in disease*. Genome Research, 2008. **18**(4): p. 644-652.
5. Anfinsen, C.B., et al., *THE KINETICS OF FORMATION OF NATIVE RIBONUCLEASE DURING OXIDATION OF THE REDUCED POLYPEPTIDE CHAIN*. Proceedings of the National Academy of Sciences, 1961. **47**(9): p. 1309-1314.
6. Dill, K.A. and J.L. MacCallum, *The Protein-Folding Problem, 50 Years On*. Science, 2012. **338**(6110): p. 1042-1046.
7. Service, R.F., *'The game has changed.'* *AI triumphs at protein folding*. Science, 2020. **370**(6521): p. 1144-1145.
8. Anfinsen, C., *Principles that Govern the Folding of Protein Chains*. Science, 1973. **181**(4096): p. 223-30.
9. Anfinsen, C.B. and H.A. Scheraga, *Experimental and Theoretical Aspects of Protein Folding*. Hoppe-Seylers Zeitschrift Fur Physiologische Chemie, 1979. **360**(8): p. 1015-1016.
10. Dill, K.A., *Dominant Forces in Protein Folding*. Biochemistry, 1990. **29**(31): p. 7133-7155.
11. Levinthal, C., *Are There Pathways for Protein Folding*. Journal De Chimie Physique Et De Physico-Chimie Biologique, 1968. **65**(1): p. 44-+.
12. Dill, K.A., et al., *The protein folding problem*. Annual Review of Biophysics, 2008. **37**: p. 289-316.
13. Dill, K.A. and H.S. Chan, *From Levinthal to pathways to funnels*. Nature Structural & Molecular Biology, 1997. **4**(1): p. 10-19.
14. Dill, K.A., *Polymer principles and protein folding*. Protein Science, 1999. **8**(6): p. 1166-1180.
15. Halskau, O., et al., *Large-scale modulation of thermodynamic protein folding barriers linked to electrostatics*. Proceedings of the National Academy of Sciences, 2008. **105**(25): p. 8625-8630.
16. Wei, G., et al., *Protein Ensembles: How Does Nature Harness Thermodynamic Fluctuations for Life? The Diverse Functional Roles of Conformational Ensembles in the Cell*. Chemical Reviews, 2016. **116**(11): p. 6516-6551.

17. Foguel, D. and J.L. Silva, *New Insights into the Mechanisms of Protein Misfolding and Aggregation in Amyloidogenic Diseases Derived from Pressure Studies*†. *Biochemistry*, 2004. **43**(36): p. 11361-11370.
18. Ellis, R.J., *Macromolecular crowding: obvious but underappreciated*. *Trends in Biochemical Sciences*, 2001. **26**(10): p. 597-604.
19. Iadanza, M.G., et al., *A new era for understanding amyloid structures and disease*. *Nature Reviews Molecular Cell Biology*, 2018. **19**(12): p. 755-773.
20. Hartl, F.U., A. Bracher, and M. Hayer-Hartl, *Molecular chaperones in protein folding and proteostasis*. *Nature*, 2011. **475**(7356): p. 324-332.
21. Balchin, D., M. Hayer-Hartl, and F.U. Hartl, *In vivo aspects of protein folding and quality control*. *Science*, 2016. **353**(6294): p. aac4354.
22. Charlton, L.M., et al., *Residue-Level Interrogation of Macromolecular Crowding Effects on Protein Stability*. *Journal of the American Chemical Society*, 2008. **130**(21): p. 6826-6830.
23. Engel, R., et al., *Macromolecular Crowding Compacts Unfolded Apoflavodoxin and Causes Severe Aggregation of the Off-pathway Intermediate during Apoflavodoxin Folding*. 2008. **283**(41): p. 27383-27394.
24. Mittal, J. and R.B. Best, *Thermodynamics and kinetics of protein folding under confinement*. *Proceedings of the National Academy of Sciences of the United States of America*, 2008. **105**(51): p. 20233-20238.
25. Homouz, D., et al., *Crowded, cell-like environment induces shape changes in aspherical protein*. *Proceedings of the National Academy of Sciences*, 2008. **105**(33): p. 11754-11759.
26. Kim, Y.E., et al., *Molecular Chaperone Functions in Protein Folding and Proteostasis*. *Annual Review of Biochemistry*, 2013. **82**(1): p. 323-355.
27. Fernández-Fernández, M.R. and J.M. Valpuesta, *Hsp70 chaperone: a master player in protein homeostasis*. *F1000Research*, 2018. **7**: p. 1497.
28. Iburg, M., et al., *The non-canonical small heat shock protein HSP-17 from *C. elegans* is a selective protein aggregase*. *Journal of Biological Chemistry*, 2020: p. jbc.RA119.01118.
29. Hartl, F.U., *Molecular chaperones in cellular protein folding*. *Nature*, 1996. **381**(6583): p. 571-580.
30. Bukau, B., J. Weissman, and A. Horwich, *Molecular Chaperones and Protein Quality Control*. *Cell*, 2006. **125**(3): p. 443-451.
31. Kampinga, H.H. and E.A. Craig, *The HSP70 chaperone machinery: J proteins as drivers of functional specificity (vol 11, pg 579, 2010)*. *Nature Reviews Molecular Cell Biology*, 2010. **11**(10).
32. Sharma, S.K., et al., *The kinetic parameters and energy cost of the Hsp70 chaperone as a polypeptide unfoldase*. *Nature Chemical Biology*, 2010. **6**(12): p. 914-920.
33. Auluck, P.K., *Chaperone Suppression of alpha -Synuclein Toxicity in a *Drosophila* Model for Parkinson's Disease*. *Science*, 2002. **295**(5556): p. 865-868.

34. Arndt, V., et al., *Chaperone-Assisted Selective Autophagy Is Essential for Muscle Maintenance*. Current Biology, 2010. **20**(2): p. 143-148.
35. Fernández-Fernández, M.R., et al., *Hsp70 – a master regulator in protein degradation*. FEBS Letters, 2017. **591**(17): p. 2648-2660.
36. Hershko, A. and A. Ciechanover, *THE UBIQUITIN SYSTEM*. Annual Review of Biochemistry, 1998. **67**(1): p. 425-479.
37. Lamark, T. and T. Johansen, *Autophagy: links with the proteasome*. Current Opinion in Cell Biology, 2010. **22**(2): p. 192-198.
38. Ciechanover, A., *The ubiquitin-proteasome proteolytic pathway*. Cell, 1994. **79**(1): p. 13-21.
39. Hershko, A. and A. Ciechanover, *The Ubiquitin System for Protein Degradation*. Annual Review of Biochemistry, 1992. **61**(1): p. 761-807.
40. Coux, O., K. Tanaka, and A.L. Goldberg, *Structure and functions of the 20S and 26S proteasomes*. Annual Review of Biochemistry, 1996. **65**: p. 801-847.
41. Braten, O., et al., *Numerous proteins with unique characteristics are degraded by the 26S proteasome following monoubiquitination*. Proceedings of the National Academy of Sciences, 2016. **113**(32): p. E4639-E4647.
42. Schwartz, A.L. and A. Ciechanover, *Targeting Proteins for Destruction by the Ubiquitin System: Implications for Human Pathobiology*. Annual Review of Pharmacology and Toxicology, 2009. **49**(1): p. 73-96.
43. Bedford, L., et al., *Assembly, structure, and function of the 26S proteasome*. Trends in Cell Biology, 2010. **20**(7): p. 391-401.
44. Bhattacharyya, S., et al., *Regulated protein turnover: snapshots of the proteasome in action*. Nature Reviews Molecular Cell Biology, 2014. **15**(2): p. 122-133.
45. Reits, E., et al., *Peptide Diffusion, Protection, and Degradation in Nuclear and Cytoplasmic Compartments before Antigen Presentation by MHC Class I*. Immunity, 2003. **18**(1): p. 97-108.
46. Glick, D., S. Barth, and K.F. Macleod, *Autophagy: cellular and molecular mechanisms*. The Journal of pathology, 2010. **221**(1): p. 3-12.
47. Galluzzi, L., et al., *Molecular definitions of autophagy and related processes*. The EMBO Journal, 2017. **36**(13): p. 1811-1836.
48. Lamark, T., S. Svenning, and T. Johansen, *Regulation of selective autophagy: the p62/SQSTM1 paradigm*. Essays in Biochemistry, 2017. **61**(6): p. 609-624.
49. Hurley, J.H. and L.N. Young, *Mechanisms of Autophagy Initiation*. Annual Review of Biochemistry, 2017. **86**(1): p. 225-244.
50. Marzella, L., J. Ahlberg, and H. Glaumann, *Autophagy, heterophagy, microautophagy and crinophagy as the means for intracellular degradation*. Virchows Archiv B Cell Pathology Including Molecular Pathology, 1981. **36**(1): p. 219-234.
51. Sakai, Y., et al., *Peroxisome Degradation by Microautophagy in Pichia pastoris: Identification of Specific Steps and Morphological Intermediates*. Journal of Cell Biology, 1998. **141**(3): p. 625-636.

-
52. Fred Dice, J., *Peptide sequences that target cytosolic proteins for lysosomal proteolysis*. Trends in Biochemical Sciences, 1990. **15**(8): p. 305-309.
 53. Kaushik, S. and A.M. Cuervo, *The coming of age of chaperone-mediated autophagy*. Nature Reviews Molecular Cell Biology, 2018. **19**(6): p. 365-381.
 54. Thumm, M., et al., *Isolation of autophagocytosis mutants of Saccharomyces cerevisiae*. FEBS Letters, 1994. **349**(2): p. 275-280.
 55. Tsukada, M. and Y. Ohsumi, *Isolation and characterization of autophagy-defective mutants of Saccharomyces cerevisiae*. FEBS Letters, 1993. **333**(1-2): p. 169-174.
 56. Meijer, W.H., et al., *ATG Genes Involved in Non-Selective Autophagy are Conserved from Yeast to Man, but the Selective Cvt and Pexophagy Pathways also Require Organism-Specific Genes*. Autophagy, 2007. **3**(2): p. 106-116.
 57. Mizushima, N., T. Yoshimori, and Y. Ohsumi, *The Role of Atg Proteins in Autophagosome Formation*. Annual Review of Cell and Developmental Biology, 2011. **27**(1): p. 107-132.
 58. Suzuki, K., et al., *The pre-autophagosomal structure organized by concerted functions of APG genes is essential for autophagosome formation*. Embo Journal, 2001. **20**(21): p. 5971-5981.
 59. Stolz, A., A. Ernst, and I. Dikic, *Cargo recognition and trafficking in selective autophagy*. Nature Cell Biology, 2014. **16**(6): p. 495-501.
 60. Russell, R.C., et al., *ULK1 induces autophagy by phosphorylating Beclin-1 and activating VPS34 lipid kinase*. Nature Cell Biology, 2013. **15**(7): p. 741-750.
 61. Alers, S., et al., *Atg13 and FIP200 act independently of Ulk1 and Ulk2 in autophagy induction*. Autophagy, 2011. **7**(12): p. 1424-1433.
 62. Slobodkin, M.R. and Z. Elazar, *The Atg8 family: multifunctional ubiquitin-like key regulators of autophagy*. Autophagy: Molecules and Mechanisms, 2013. **55**: p. 51-64.
 63. Reggiori, F. and C. Ungermann, *Autophagosome Maturation and Fusion*. Journal of Molecular Biology, 2017. **429**(4): p. 486-496.
 64. Cao, J., et al., *Phylogenetic analysis and evolution of aromatic amino acid hydroxylase*. Febs Letters, 2010. **584**(23): p. 4775-4782.
 65. Siltberg-Liberles, J., et al., *The phylogeny of the aromatic amino acid hydroxylases revisited by characterizing phenylalanine hydroxylase from Dictyostelium discoideum*. Gene, 2008. **427**(1-2): p. 86-92.
 66. Lye, L.F., et al., *Phenylalanine hydroxylase (PAH) from the lower eukaryote Leishmania major*. Molecular and Biochemical Parasitology, 2011. **175**(1): p. 58-67.
 67. Skjærven, L., Teigen, K. and Martinez, A., *Structure–Function Relationships in the Aromatic Amino Acid Hydroxylases Enzyme Family: Evolutionary Insights*, in *eLS*. 2014.
 68. Fitzpatrick, P.F., *Structural insights into the regulation of aromatic amino acid hydroxylation*. Current Opinion in Structural Biology, 2015. **35**: p. 1-6.

69. Leiros, H.K.S., M.I. Flydal, and A. Martinez, *Structural and thermodynamic insight into phenylalanine hydroxylase from the human pathogen Legionella pneumophila*. *Febs Open Bio*, 2013. **3**: p. 370-378.
70. Leiros, H.-K.S., et al., *Structure of Phenylalanine Hydroxylase from Colwellia psychrerythraea 34H, a Monomeric Cold Active Enzyme with Local Flexibility around the Active Site and High Overall Stability*. *Journal of Biological Chemistry*, 2007. **282**(30): p. 21973-21986.
71. Erlandsen, H., et al., *Structural Comparison of Bacterial and Human Iron-dependent Phenylalanine Hydroxylases: Similar Fold, Different Stability and Reaction Rates*. *Journal of Molecular Biology*, 2002. **320**(3): p. 645-661.
72. Blau, N., F.J. van Spronsen, and H.L. Levy, *Phenylketonuria*. *Lancet*, 2010. **376**(9750): p. 1417-1427.
73. Ng, J., et al., *Monoamine neurotransmitter disorders-clinical advances and future perspectives*. *Nature Reviews Neurology*, 2015. **11**(10): p. 567-584.
74. Eisenhofer, G., I.J. Kopin, and D.S. Goldstein, *Catecholamine metabolism: A contemporary view with implications for physiology and medicine*. *Pharmacological Reviews*, 2004. **56**(3): p. 331-349.
75. Amireault, P., D. Sibon, and F. Cote, *Life without Peripheral Serotonin: Insights from Tryptophan Hydroxylase 1 Knockout Mice Reveal the Existence of Paracrine/Autocrine Serotonergic Networks*. *Acs Chemical Neuroscience*, 2013. **4**(1): p. 64-71.
76. Turek, F.W. and M.U. Gillette, *Melatonin, sleep, and circadian rhythms: rationale for development of specific melatonin agonists*. *Sleep Medicine*, 2004. **5**(6): p. 523-532.
77. Belmaker, R.H. and G. Agam, *Mechanisms of disease: Major depressive disorder*. *New England Journal of Medicine*, 2008. **358**(1): p. 55-68.
78. Banerjee, E. and K. Nandagopal, *Does serotonin deficit mediate susceptibility to ADHD?* *Neurochemistry International*, 2015. **82**: p. 52-68.
79. Baldwin, D.S. and C. Polkinghorn, *Evidence-based pharmacotherapy of generalized anxiety disorder*. *International Journal of Neuropsychopharmacology*, 2005. **8**(2): p. 293-302.
80. Southwick, S.M., et al., *Neurotransmitter alterations in PTSD: catecholamines and serotonin*. *Semin Clin Neuropsychiatry*, 1999. **4**(4): p. 242-8.
81. Kappock, T.J. and J.P. Caradonna, *Pterin-dependent amino acid hydroxylases*. *Chemical Reviews*, 1996. **96**(7): p. 2659-2756.
82. Fitzpatrick, P.F., *The Aromatic Amino Acid Hydroxylases*, in *Advances in Enzymology and Related Areas of Molecular Biology*. 2000. p. 235-294.
83. Flatmark, T. and R.C. Stevens, *Structural insight into the aromatic amino acid hydroxylases and their disease-related mutant forms*. *Chemical Reviews*, 1999. **99**(8): p. 2137-2160.
84. Arturo, E.C., et al., *First structure of full-length mammalian phenylalanine hydroxylase reveals the architecture of an autoinhibited tetramer*. *Proceedings of the National Academy of Sciences of the United States of America*, 2016. **113**(9): p. 2394-2399.

-
85. Flydal, M.I., et al., *Structure of full-length human phenylalanine hydroxylase in complex with tetrahydrobiopterin*. Proceedings of the National Academy of Sciences of the United States of America, 2019. **116**(23): p. 11229-11234.
 86. Bueno-Carrasco, T., et al., *The Structure of Human Tyrosine Hydroxylase Reveals the Mechanism for Feedback Inhibition by Dopamine*. 2020, Research Square: Preprint.
 87. Wang, L., et al., *Three-dimensional structure of human tryptophan hydroxylase and its implications for the biosynthesis of the neurotransmitters serotonin and melatonin*. Biochemistry, 2002. **41**(42): p. 12569-12574.
 88. Aravind, L. and E.V. Koonin, *Gleaning non-trivial structural, functional and evolutionary information about proteins by iterative database searches*. Journal of Molecular Biology, 1999. **287**(5): p. 1023-1040.
 89. Zhang, S.N., et al., *The Solution Structure of the Regulatory Domain of Tyrosine Hydroxylase*. Journal of Molecular Biology, 2014. **426**(7): p. 1483-1497.
 90. Bezem, M.T., et al., *Stable preparations of tyrosine hydroxylase provide the solution structure of the full-length enzyme*. Scientific Reports, 2016. **6**.
 91. Meisburger, S.P., et al., *Domain Movements upon Activation of Phenylalanine Hydroxylase Characterized by Crystallography and Chromatography-Coupled Small-Angle X-ray Scattering*. Journal of the American Chemical Society, 2016. **138**(20): p. 6506-6516.
 92. Arturo, E.C., et al., *Biophysical characterization of full-length human phenylalanine hydroxylase provides a deeper understanding of its quaternary structure equilibrium*. Journal of Biological Chemistry, 2019. **294**(26): p. 10131-10145.
 93. Kappock, T.J., et al., *Spectroscopic and Kinetic Properties of Unphosphorylated Rat Hepatic Phenylalanine Hydroxylase Expressed in Escherichia coli*. Journal of Biological Chemistry, 1995. **270**(51): p. 30532-30544.
 94. McKinney, J., P.M. Knappskog, and J. Haavik, *Different properties of the central and peripheral forms of human tryptophan hydroxylase*. Journal of Neurochemistry, 2005. **92**(2): p. 311-320.
 95. Teigen, K., et al., *Selectivity and affinity determinants for ligand binding to the aromatic amino acid hydroxylases*. Current Medicinal Chemistry, 2007. **14**(4): p. 455-467.
 96. Haavik, J., *l-DOPA Is a Substrate for Tyrosine Hydroxylase*. Journal of Neurochemistry, 1997. **69**(4): p. 1720-1728.
 97. Eser, B.E., et al., *Direct spectroscopic evidence for a high-spin Fe(IV) intermediate in tyrosine hydroxylase*. Journal of the American Chemical Society, 2007. **129**(37): p. 11334-+.
 98. Fitzpatrick, P.F., *Mechanism of Aromatic Amino Acid Hydroxylation†*. Biochemistry, 2003. **42**(48): p. 14083-14091.
 99. Werner, Ernst R., N. Blau, and B. Thöny, *Tetrahydrobiopterin: biochemistry and pathophysiology*. Biochemical Journal, 2011. **438**(3): p. 397-414.

100. Uhlén, M., et al., *Tissue-based map of the human proteome*. Science, 2015. **347**(6220): p. 1260419.
101. Shiman, R. and D.W. Gray, *Substrate Activation of Phenylalanine-Hydroxylase - a Kinetic Characterization*. Journal of Biological Chemistry, 1980. **255**(10): p. 4793-4800.
102. Shiman, R., et al., *Regulation of phenylalanine hydroxylase activity by phenylalanine in vivo, in vitro, and in perfused rat liver*. J Biol Chem, 1982. **257**(19): p. 11213-6.
103. Tourian, A., *Activation of phenylalanine hydroxylase by phenylalanine*. Biochimica et Biophysica Acta (BBA) - Enzymology, 1971. **242**(2): p. 345-354.
104. Xia, T., D.W. Gray, and R. Shiman, *Regulation of rat liver phenylalanine hydroxylase. III. Control of catalysis by (6R)-tetrahydrobiopterin and phenylalanine*. Journal of Biological Chemistry, 1994. **269**(40): p. 24657-24665.
105. Li, J., L.J. Dangott, and P.F. Fitzpatrick, *Regulation of Phenylalanine Hydroxylase: Conformational Changes Upon Phenylalanine Binding Detected by Hydrogen/Deuterium Exchange and Mass Spectrometry*. Biochemistry, 2010. **49**(15): p. 3327-3335.
106. Flydal, M.I. and A. Martinez, *Phenylalanine hydroxylase: function, structure, and regulation*. IUBMB Life, 2013. **65**(4): p. 341-9.
107. Fitzpatrick, P.F., *Allosteric regulation of phenylalanine hydroxylase*. Archives of Biochemistry and Biophysics, 2012. **519**(2): p. 194-201.
108. Kobe, B., et al., *Structural basis of autoregulation of phenylalanine hydroxylase*. Nature Structural Biology, 1999. **6**(5): p. 442-448.
109. Martinez, A., J. Haavik, and T. Flatmark, *Cooperative homotropic interaction of l-noradrenaline with the catalytic site of phenylalanine 4-monooxygenase*. European Journal of Biochemistry, 1990. **193**(1): p. 211-219.
110. Martinez, A., S. Olafsdottir, and T. Flatmark, *The cooperative binding of phenylalanine to phenylalanine 4-monooxygenase studied by 1H-NMR paramagnetic relaxation. Changes in water accessibility to the iron at the active site upon substrate binding*. European Journal of Biochemistry, 1993. **211**(1-2): p. 259-266.
111. Thóroúlfsson, M., et al., *l-Phenylalanine Binding and Domain Organization in Human Phenylalanine Hydroxylase: A Differential Scanning Calorimetry Study*. Biochemistry, 2002. **41**(24): p. 7573-7585.
112. Patel, D., et al., *Structural basis for ligand-dependent dimerization of phenylalanine hydroxylase regulatory domain*. Scientific Reports, 2016. **6**(1): p. 23748.
113. Jaffe, E.K., *New protein structures provide an updated understanding of phenylketonuria*. Mol Genet Metab, 2017. **121**(4): p. 289-296.
114. Meisburger, S.P., et al., *Domain Movements upon Activation of Phenylalanine Hydroxylase Characterized by Crystallography and Chromatography-Coupled Small-Angle X-ray Scattering*. J Am Chem Soc, 2016. **138**(20): p. 6506-16.

-
115. Kaufman, S., *The Phenylalanine Hydroxylating System*. Advances in Enzymology and Related Areas of Molecular Biology, Vol 67, 1993. **67**: p. 77-264.
 116. Kowlessur, D., B.A. Citron, and S. Kaufman, *Recombinant Human Phenylalanine Hydroxylase: Novel Regulatory and Structural Properties*. Archives of Biochemistry and Biophysics, 1996. **333**(1): p. 85-95.
 117. Thórólfsson, M., K. Teigen, and A. Martínez, *Activation of Phenylalanine Hydroxylase: Effect of Substitutions at Arg68 and Cys237†*. Biochemistry, 2003. **42**(12): p. 3419-3428.
 118. Nielsen, K.H., *Rat Liver Phenylalanine Hydroxylase. A Method for the Measurement of Activity, with Particular Reference to the Distinctive Features of the Enzyme and the Pteridine Cofactor*. European Journal of Biochemistry, 1969. **7**(3): p. 360-369.
 119. Kaufman, S. and K. Mason, *Specificity of Amino-Acids as Activators and Substrates for Phenylalanine-Hydroxylase*. Journal of Biological Chemistry, 1982. **257**(24): p. 4667-4678.
 120. Phillips, R.S., M.A. Parniak, and S. Kaufman, *The Interaction of Aromatic-Amino-Acids with Rat-Liver Phenylalanine-Hydroxylase*. Journal of Biological Chemistry, 1984. **259**(1): p. 271-277.
 121. Mitnaul, L.J. and R. Shiman, *Coordinate regulation of tetrahydrobiopterin turnover and phenylalanine hydroxylase activity in rat liver cells*. Proceedings of the National Academy of Sciences, 1995. **92**(3): p. 885-889.
 122. Døskeland, A.P., et al., *Phosphorylation of recombinant human phenylalanine hydroxylase: effect on catalytic activity, substrate activation and protection against non-specific cleavage of the fusion protein by restriction protease*. Biochemical Journal, 1996. **313**(2): p. 409-414.
 123. Miranda, F.F., et al., *Phosphorylation and Mutations of Ser16in Human Phenylalanine Hydroxylase*. Journal of Biological Chemistry, 2002. **277**(43): p. 40937-40943.
 124. Tekin, I., et al., *Complex molecular regulation of tyrosine hydroxylase*. Journal of Neural Transmission, 2014. **121**(12): p. 1451-1481.
 125. Grima, B., et al., *A single human gene encoding multiple tyrosine hydroxylases with different predicted functional characteristics*. Nature, 1987. **326**(6114): p. 707-11.
 126. Lebourdelles, B., et al., *Analysis of the 5' Region of the Human Tyrosine-Hydroxylase Gene - Combinatorial Patterns of Exon Splicing Generate Multiple Regulated Tyrosine-Hydroxylase Isoforms*. Journal of Neurochemistry, 1988. **50**(3): p. 988-991.
 127. Shehadeh, J., et al., *Expression of tyrosine hydroxylase isoforms and phosphorylation at serine 40 in the human nigrostriatal system in Parkinson's disease*. Neurobiology of Disease, 2019. **130**.
 128. Sura, G.R., S.C. Daubner, and P.F. Fitzpatrick, *Effects of phosphorylation by protein kinase A on binding of catecholamines to the human tyrosine*

- hydroxylase isoforms (vol 90, pg 970, 2004)*. Journal of Neurochemistry, 2004. **90**(5): p. 1280-1280.
129. Kuczynski, R.T. and A.J. Mandell, *Allosteric Activation of Hypothalamic Tyrosine-Hydroxylase by Ions and Sulfated Mucopolysaccharides*. Journal of Neurochemistry, 1972. **19**(1): p. 131-+.
 130. Gahn, L.G. and R. Roskoski, *Tyrosine-Hydroxylase Activity and Extrinsic Fluorescence Changes Produced by Polyanions*. Biochemical Journal, 1993. **295**: p. 189-194.
 131. Lloyd, T. and S. Kaufman, *The stimulation of partially purified bovine caudate tyrosine hydroxylase by phosphatidyl-L-serine*. Biochem Biophys Res Commun, 1974. **59**(4): p. 1262-70.
 132. Katz, I.R., T. Yamauchi, and S. Kaufman, *Activation of Tyrosine-Hydroxylase by Polyanions and Salts - Electrostatic Effect*. Biochimica Et Biophysica Acta, 1976. **429**(1): p. 84-95.
 133. Kumer, S.C. and K.E. Vrana, *Intricate regulation of tyrosine hydroxylase activity and gene expression*. J Neurochem, 1996. **67**(2): p. 443-62.
 134. Weiner, N., et al., *The activation of tyrosine hydroxylase in noradrenergic neurons during acute nerve stimulation*. Life Sci, 1978. **22**(13-15): p. 1197-215.
 135. Daubner, S.C., D.L. Lohse, and P.F. Fitzpatrick, *Expression and characterization of catalytic and regulatory domains of rat tyrosine hydroxylase*. Protein Sci, 1993. **2**(9): p. 1452-60.
 136. Daubner, S.C. and M.M. Piper, *Deletion mutants of tyrosine hydroxylase identify a region critical for heparin binding*. Protein Science, 2008. **4**(3): p. 538-541.
 137. Dunkley, P.R. and P.W. Dickson, *Tyrosine hydroxylase phosphorylation in vivo*. Journal of Neurochemistry, 2019. **149**(6): p. 706-728.
 138. Lindgren, N., et al., *Dopamine D2receptors regulate tyrosine hydroxylase activity and phosphorylation at Ser40 in rat striatum*. European Journal of Neuroscience, 2001. **13**(4): p. 773-780.
 139. Andersson, K.K., et al., *Resonance Raman Studies on the Blue-Green-Colored Bovine Adrenal Tyrosine 3-Monooxygenase (Tyrosine-Hydroxylase) - Evidence That the Feedback Inhibitors Adrenaline and Noradrenaline Are Coordinated to Iron*. Journal of Biological Chemistry, 1988. **263**(35): p. 18621-18626.
 140. Almas, B., et al., *Regulation of Recombinant Human Tyrosine-Hydroxylase Isozymes by Catecholamine Binding and Phosphorylation - Structure Activity Studies and Mechanistic Implications*. European Journal of Biochemistry, 1992. **209**(1): p. 249-255.
 141. Compton, D.R. and K.M. Johnson, *Striatal synaptosomal dopamine synthesis: Evidence against direct regulation by an autoreceptor mechanism*. European Journal of Pharmacology, 1985. **110**(2): p. 157-162.

-
142. Olefirowicz, T.M. and A.G. Ewing, *Dopamine concentration in the cytoplasmic compartment of single neurons determined by capillary electrophoresis*. Journal of Neuroscience Methods, 1990. **34**(1-3): p. 11-15.
 143. Ramsey, A.J. and P.F. Fitzpatrick, *Effects of phosphorylation on binding of catecholamines to tyrosine hydroxylase: Specificity and thermodynamics*. Biochemistry, 2000. **39**(4): p. 773-778.
 144. Okuno, S. and H. Fujisawa, *Conversion of Tyrosine-Hydroxylase to Stable and Inactive Form by the End-Products*. Journal of Neurochemistry, 1991. **57**(1): p. 53-60.
 145. Kaufman, S., *Tyrosine Hydroxylase*, in *Advances in Enzymology and Related Areas of Molecular Biology*. 1995. p. 103-220.
 146. Haavik, J., A. Martinez, and T. Fiatmark, *pH-dependent release of catecholamines from tyrosine hydroxylase and the effect of phosphorylation of Ser-40*. FEBS Letters, 1990. **262**(2): p. 363-365.
 147. Dunkley, P.R., et al., *Tyrosine hydroxylase phosphorylation: regulation and consequences*. Journal of Neurochemistry, 2004. **91**(5): p. 1025-1043.
 148. Morgenroth, V.H., 3rd, et al., *Evidence for involvement of protein kinase in the activation by adenosine 3':5'-monophosphate of brain tyrosine 3-monooxygenase*. J Biol Chem, 1975. **250**(5): p. 1946-8.
 149. Lovenberg, W., E.A. Bruckwick, and I. Hanbauer, *ATP, cyclic AMP, and magnesium increase the affinity of rat striatal tyrosine hydroxylase for its cofactor*. Proc Natl Acad Sci U S A, 1975. **72**(8): p. 2955-8.
 150. Campbell, D.G., D.G. Hardie, and P.R. Vulliet, *Identification of four phosphorylation sites in the N-terminal region of tyrosine hydroxylase*. J Biol Chem, 1986. **261**(23): p. 10489-92.
 151. Kumer, S.C. and K.E. Vrana, *Intricate Regulation of Tyrosine Hydroxylase Activity and Gene Expression*. Journal of Neurochemistry, 2002. **67**(2): p. 443-462.
 152. Haycock, J.W., et al., *ERK1 and ERK2, two microtubule-associated protein 2 kinases, mediate the phosphorylation of tyrosine hydroxylase at serine-31 in situ*. Proc Natl Acad Sci U S A, 1992. **89**(6): p. 2365-9.
 153. Gordon, S.L., et al., *Differential regulation of human tyrosine hydroxylase isoforms 1 and 2 in situ: Isoform 2 is not phosphorylated at Ser35*. Biochim Biophys Acta, 2009. **1793**(12): p. 1860-7.
 154. Kansy, J.W., et al., *Identification of tyrosine hydroxylase as a physiological substrate for Cdk5*. Journal of Neurochemistry, 2004. **91**(2): p. 374-384.
 155. Sutherland, C., et al., *Phosphorylation and Activation of Human Tyrosine-Hydroxylase in-Vitro by Mitogen-Activated Protein (Map) Kinase and Map-Kinase-Activated Kinase-1 and Kinase-2*. European Journal of Biochemistry, 1993. **217**(2): p. 715-722.
 156. Salvatore, M.F., J.C. Waymire, and J.W. Haycock, *Depolarization-stimulated catecholamine biosynthesis: involvement of protein kinases and tyrosine hydroxylase phosphorylation sites in situ*. Journal of Neurochemistry, 2001. **79**(2): p. 349-360.

157. Moy, L.Y. and L.H. Tsai, *Cyclin-dependent kinase 5 phosphorylates serine 31 of tyrosine hydroxylase and regulates its stability*. Journal of Biological Chemistry, 2004. **279**(52): p. 54487-54493.
158. Tachikawa, E., et al., *Tyrosine-Hydroxylase Is Activated and Phosphorylated on Different Sites in Rat Pheochromocytoma Pc12 Cells Treated with Phorbol Ester and Forskolin*. Journal of Neurochemistry, 1987. **48**(5): p. 1366-1376.
159. Mitchell, J.P., D.G. Hardie, and P.R. Vulliet, *Site-Specific Phosphorylation of Tyrosine-Hydroxylase after Kcl Depolarization and Nerve Growth-Factor Treatment of Pc12 Cells*. Journal of Biological Chemistry, 1990. **265**(36): p. 22358-22364.
160. Salvatore, M.F., et al., *Striatal GDNF administration increases tyrosine hydroxylase phosphorylation in the rat striatum and substantia nigra*. Journal of Neurochemistry, 2004. **90**(1): p. 245-254.
161. Luke, T.M. and T.D. Hexum, *Tyrosine hydroxylase phosphorylation increases in response to ATP and neuropeptide Y co-stimulation of ERK2 phosphorylation*. Pharmacological Research, 2008. **58**(1): p. 52-57.
162. Aita, Y., et al., *Effect of Urotensin II on PC12 Rat Pheochromocytoma Cells*. Journal of Neuroendocrinology, 2010. **22**(2): p. 83-91.
163. Salvatore, M.F. and B.S. Prueett, *Dichotomy of Tyrosine Hydroxylase and Dopamine Regulation between Somatodendritic and Terminal Field Areas of Nigrostriatal and Mesoaccumbens Pathways*. Plos One, 2012. **7**(1).
164. Toska, K., et al., *Regulation of tyrosine hydroxylase by stress-activated protein kinases*. Journal of Neurochemistry, 2002. **83**(4): p. 775-783.
165. Salvatore, M.F., et al., *Transient striatal GLT-1 blockade increases EAAC1 expression, glutamate reuptake, and decreases tyrosine hydroxylase phosphorylation at ser19*. Experimental Neurology, 2012. **234**(2): p. 428-436.
166. Itagaki, C., et al., *Stimulus-coupled interaction of tyrosine hydroxylase with 14-3-3 proteins*. Biochemistry, 1999. **38**(47): p. 15673-15680.
167. Haycock, J.W., et al., *Role of serine-19 phosphorylation in regulating tyrosine hydroxylase studied with site- and phosphospecific antibodies and site-directed mutagenesis*. Journal of Neurochemistry, 1998. **71**(4): p. 1670-1675.
168. Bevilaqua, L.R.M., et al., *Phosphorylation of Ser(19) alters the conformation of tyrosine hydroxylase to increase the rate of phosphorylation of Ser(40)*. Journal of Biological Chemistry, 2001. **276**(44): p. 40411-40416.
169. Ghorbani, S., et al., *Serine 19 phosphorylation and 14 - 3 - 3 binding regulate phosphorylation and dephosphorylation of tyrosine hydroxylase on serine 31 and serine 40*. Journal of Neurochemistry, 2020. **152**(1): p. 29-47.
170. Nakashima, A., et al., *Phosphorylation of the N-terminal portion of tyrosine hydroxylase triggers proteasomal digestion of the enzyme*. Biochem Biophys Res Commun, 2011. **407**(2): p. 343-7.
171. Nakashima, A., et al., *Inhibition of deubiquitinating activity of USP14 decreases tyrosine hydroxylase phosphorylated at Ser19 in PC12D cells*. Biochemical and Biophysical Research Communications, 2016. **472**(4): p. 598-602.

-
172. Vulliet, P.R., et al., *Identification of a Novel Proline-Directed Serine Threonine Protein-Kinase in Rat Pheochromocytoma*. Journal of Biological Chemistry, 1989. **264**(27): p. 16292-16298.
 173. Hall, F.L., et al., *Characterization of the Cytoplasmic Proline-Directed Protein-Kinase in Proliferative Cells and Tissues as a Heterodimer Comprised of P34cdc2 and P58cyclin A*. Journal of Biological Chemistry, 1991. **266**(26): p. 17430-17440.
 174. Royo, M., S.C. Daubner, and P.F. Fitzpatrick, *Specificity of the MAP kinase ERK2 for phosphorylation of tyrosine hydroxylase*. Archives of Biochemistry and Biophysics, 2004. **423**(2): p. 247-252.
 175. Haavik, J., et al., *Identification of Protein Phosphatase-2a as the Major Tyrosine-Hydroxylase Phosphatase in Adrenal-Medulla and Corpus Striatum - Evidence from the Effects of Okadaic Acid*. Febs Letters, 1989. **251**(1-2): p. 36-42.
 176. Berresheim, U. and D.M. Kuhn, *Dephosphorylation of Tyrosine-Hydroxylase by Brain Protein Phosphatases - a Predominant Role for Type 2a*. Brain Research, 1994. **637**(1-2): p. 273-276.
 177. Haycock, J.W., *Phosphorylation of tyrosine hydroxylase in situ at serine 8, 19, 31, and 40*. J Biol Chem, 1990. **265**(20): p. 11682-91.
 178. Peng, X.M.M., et al., *alpha-Synuclein activation of protein phosphatase 2A reduces tyrosine hydroxylase phosphorylation in dopaminergic cells*. Journal of Cell Science, 2005. **118**(15): p. 3523-3530.
 179. Leal, R.B., et al., *Tyrosine hydroxylase dephosphorylation by protein phosphatase 2A in bovine adrenal chromaffin cells*. Neurochemical Research, 2002. **27**(3): p. 207-213.
 180. Takai, A., et al., *Inhibitory Effect of Okadaic Acid-Derivatives on Protein Phosphatases - a Study on Structure Affinity Relationship*. Biochemical Journal, 1992. **284**: p. 539-544.
 181. Fölling, A., *Über Ausscheidung von Phenylbrenztraubensäure in den Harn als Stoffwechselanomalie in Verbindung mit Imbezillität*. Biological Chemistry, 1934. **227**(1-4): p. 169.
 182. Penrose, L. and J.H. Quastel, *Metabolic studies in phenylketonuria*. Biochemical Journal, 1937. **31**(2): p. 266-274.
 183. Bickel, H., J. Gerrard, and E. Hickmans, *Preliminary Communication*. The Lancet, 1953. **262**(6790): p. 812-813.
 184. Guthrie, R. and A. Susi, *A Simple Phenylalanine Method for Detecting Phenylketonuria in Large Populations of Newborn Infants*. Pediatrics, 1963. **32**(3): p. 338-&.
 185. Hillert, A., et al., *The Genetic Landscape and Epidemiology of Phenylketonuria*. The American Journal of Human Genetics, 2020. **107**(2): p. 234-250.
 186. Scriver, C.R., *The PAH gene, phenylketonuria, and a paradigm shift*. Human Mutation, 2007. **28**(9): p. 831-845.

-
187. Dilella, A.G., et al., *Molecular structure and polymorphic map of the human phenylalanine hydroxylase gene*. *Biochemistry*, 1986. **25**(4): p. 743-749.
 188. Pey, A.L., et al., *Predicted Effects of Missense Mutations on Native-State Stability Account for Phenotypic Outcome in Phenylketonuria, a Paradigm of Misfolding Diseases*. *The American Journal of Human Genetics*, 2007. **81**(5): p. 1006-1024.
 189. Wettstein, S., et al., *Linking genotypes database with locus-specific database and genotype-phenotype correlation in phenylketonuria*. *European Journal of Human Genetics*, 2015. **23**(3): p. 302-309.
 190. Shen, N., et al., *Co-expression of phenylalanine hydroxylase variants and effects of interallelic complementation on in vitro enzyme activity and genotype-phenotype correlation*. *Molecular Genetics and Metabolism*, 2016. **117**(3): p. 328-335.
 191. Garbade, S.F., et al., *Allelic phenotype values: a model for genotype-based phenotype prediction in phenylketonuria*. *Genetics in Medicine*, 2019. **21**(3): p. 580-590.
 192. Scriver, C.R. and P.J. Waters, *Monogenic traits are not simple: lessons from phenylketonuria*. *Trends in Genetics*, 1999. **15**(7): p. 267-272.
 193. Himmelreich, N., et al., *Relationship between genotype, phenylalanine hydroxylase expression and in vitro activity and metabolic phenotype in phenylketonuria*. *Molecular Genetics and Metabolism*, 2018. **125**(1): p. 86-95.
 194. Hawkins, R.A., et al., *Structure of the blood-brain barrier and its role in the transport of amino acids*. *Journal of Nutrition*, 2006. **136**(1): p. 218s-226s.
 195. Hoeksma, M., et al., *Phenylketonuria: High plasma phenylalanine decreases cerebral protein synthesis*. *Molecular Genetics and Metabolism*, 2009. **96**(4): p. 177-182.
 196. McKean, C.M., *The effects of high phenylalanine concentrations on serotonin and catecholamine metabolism in the human brain*. *Brain Res*, 1972. **47**(2): p. 469-76.
 197. McDonald, J.D. and C.K. Charlton, *Characterization of Mutations at the Mouse Phenylalanine Hydroxylase Locus*. *Genomics*, 1997. **39**(3): p. 402-405.
 198. Sarkissian, C.N., et al., *A heteroallelic mutant mouse model: A new orthologue for human hyperphenylalaninemia*. *Molecular Genetics and Metabolism*, 2000. **69**(3): p. 188-194.
 199. Anderson, P.J. and V. Leuzzi, *White matter pathology in phenylketonuria*. *Molecular Genetics and Metabolism*, 2010. **99**: p. S3-S9.
 200. Hörster, F., et al., *Phenylalanine Reduces Synaptic Density in Mixed Cortical Cultures from Mice*. *Pediatric Research*, 2006. **59**(4 Part 1): p. 544-548.
 201. Yalaz, K., et al., *Phenylketonuria in Pediatric Neurology Practice: A Series of 146 Cases*. *Journal of Child Neurology*, 2006. **21**(11): p. 987-990.
 202. Bone, A., A.K. Kuehl, and A.F. Angelino, *A Neuropsychiatric Perspective of Phenylketonuria I: Overview of Phenylketonuria and Its Neuropsychiatric Sequelae*. *Psychosomatics*, 2012. **53**(6): p. 517-523.

-
203. Kienzle Hagen, M.E., et al., *Experimental hyperphenylalaninemia provokes oxidative stress in rat brain*. *Biochimica et Biophysica Acta (BBA) - Molecular Basis of Disease*, 2002. **1586**(3): p. 344-352.
 204. Ercal, N., et al., *Oxidative stress in a phenylketonuria animal model*. *Free Radical Biology and Medicine*, 2002. **32**(9): p. 906-911.
 205. Martinez-Cruz, F., et al., *Oxidative stress induced by phenylketonuria in the rat: Prevention by melatonin, vitamin E, and vitamin C*. *Journal of Neuroscience Research*, 2002. **69**(4): p. 550-558.
 206. Ribas, G.S., et al., *Oxidative Stress in Phenylketonuria: What is the Evidence?* 2011. **31**(5): p. 653-662.
 207. Macdonald, A., et al., *Nutrition in phenylketonuria*. *Molecular Genetics and Metabolism*, 2011. **104**: p. S10-S18.
 208. Burton, B.K., et al., *Prevalence of comorbid conditions among adult patients diagnosed with phenylketonuria*. *Molecular Genetics and Metabolism*, 2018. **125**(3): p. 228-234.
 209. Blau, N. and N. Longo, *Alternative therapies to address the unmet medical needs of patients with phenylketonuria*. *Expert Opinion on Pharmacotherapy*, 2015. **16**(6): p. 791-800.
 210. Levy, H.L., et al., *Efficacy of sapropterin dihydrochloride (tetrahydrobiopterin, 6R-BH4) for reduction of phenylalanine concentration in patients with phenylketonuria: a phase III randomised placebo-controlled study*. *Lancet*, 2007. **370**(9586): p. 504-510.
 211. MacDonald, M.J. and G.B. D'Cunha, *A modern view of phenylalanine ammonia lyase*. *Biochemistry and Cell Biology*, 2007. **85**(3): p. 273-282.
 212. Levy, H.L., C.N. Sarkissian, and C.R. Scriver, *Phenylalanine ammonia lyase (PAL): From discovery to enzyme substitution therapy for phenylketonuria*. *Molecular Genetics and Metabolism*, 2018. **124**(4): p. 223-229.
 213. Sacharow, S., et al., *First 1.5 years of pegvaliase clinic: Experiences and outcomes*. *Molecular Genetics and Metabolism Reports*, 2020. **24**: p. 100603.
 214. Liguori, L., et al., *Pharmacological Chaperones: A Therapeutic Approach for Diseases Caused by Destabilizing Missense Mutations*. *International Journal of Molecular Sciences*, 2020. **21**(2): p. 489.
 215. Martinez, A., et al., *Rescuing Proteins of Low Kinetic Stability by Chaperones and Natural Ligands: Phenylketonuria, a Case Study*. *Molecular Biology of Protein Folding, Pt A*, 2008. **83**: p. 89-+.
 216. Erlandsen, H., et al., *From The Cover: Correction of kinetic and stability defects by tetrahydrobiopterin in phenylketonuria patients with certain phenylalanine hydroxylase mutations*. *Proceedings of the National Academy of Sciences*, 2004. **101**(48): p. 16903-16908.
 217. Blau, N., et al., *Diagnosis, classification, and genetics of phenylketonuria and tetrahydrobiopterin (BH4) deficiencies*. *Molecular Genetics and Metabolism*, 2011. **104**: p. S2-S9.

-
218. Pey, A.L., et al., *Identification of pharmacological chaperones as potential therapeutic agents to treat phenylketonuria*. Journal of Clinical Investigation, 2008. **118**(8): p. 2858-2867.
 219. Hole, M., et al., *Pharmacological Chaperones that Protect Tetrahydrobiopterin Dependent Aromatic Amino Acid Hydroxylases Through Different Mechanisms*. Current Drug Targets, 2016. **17**(13): p. 1515-1526.
 220. Zafeiriou, D.I., et al., *Tyrosine hydroxylase deficiency with severe clinical course*. Molecular Genetics and Metabolism, 2009. **97**(1): p. 18-20.
 221. Clot, F., et al., *Exhaustive analysis of BH4 and dopamine biosynthesis genes in patients with Dopa-responsive dystonia*. Brain, 2009. **132**(7): p. 1753-1763.
 222. Willemsen, M.A., et al., *Tyrosine hydroxylase deficiency: a treatable disorder of brain catecholamine biosynthesis*. Brain, 2010. **133**: p. 1810-1822.
 223. Fossbakk, A., et al., *Functional Studies of Tyrosine Hydroxylase Missense Variants Reveal Distinct Patterns of Molecular Defects in Dopa-Responsive Dystonia*. Human Mutation, 2014. **35**(7): p. 880-890.
 224. Nagatsu, T., et al., *Human tyrosine hydroxylase in Parkinson's disease and in related disorders*. Journal of Neural Transmission, 2019. **126**(4): p. 397-409.
 225. Furukawa, Y. and S. Kish, *Tyrosine Hydroxylase Deficiency*, in *GeneReviews((R))*, M.P. Adam, et al., Editors. 1993: Seattle (WA).
 226. Yeung, W.-L., et al., *Expanding Phenotype and Clinical Analysis of Tyrosine Hydroxylase Deficiency*. Journal of Child Neurology, 2011. **26**(2): p. 179-187.
 227. Korner, G., et al., *Brain catecholamine depletion and motor impairment in aThkknock-in mouse with type B tyrosine hydroxylase deficiency*. Brain, 2015. **138**(10): p. 2948-2963.
 228. Kurian, M.A., et al., *The monoamine neurotransmitter disorders: an expanding range of neurological syndromes*. The Lancet Neurology, 2011. **10**(8): p. 721-733.
 229. Haavik, J., N. Blau, and B. Thony, *Mutations in human monoamine-related neurotransmitter pathway genes*. Human Mutation, 2008. **29**(7): p. 891-902.
 230. Obeso, J.A., et al., *Missing pieces in the Parkinson's disease puzzle*. Nature Medicine, 2010. **16**(6): p. 653-661.
 231. Kobayashi, K., et al., *Targeted Disruption of the Tyrosine Hydroxylase Locus Results in Severe Catecholamine Depletion and Perinatal Lethality in Mice*. Journal of Biological Chemistry, 1995. **270**(45): p. 27235-27243.
 232. Zhou, Q.-Y., C.J. Quaipe, and R.D. Palmiter, *Targeted disruption of the tyrosine hydroxylase gene reveals that catecholamines are required for mouse fetal development*. 1995. **374**(6523): p. 640-643.
 233. Cartier, E.A., et al., *A Biochemical and Functional Protein Complex Involving Dopamine Synthesis and Transport into Synaptic Vesicles*. Journal of Biological Chemistry, 2010. **285**(3): p. 1957-1966.
 234. Bowling, K.M., et al., *Direct binding of GTP cyclohydrolase and tyrosine hydroxylase: regulatory interactions between key enzymes in dopamine biosynthesis*. The Journal of biological chemistry, 2008. **283**(46): p. 31449-31459.

-
235. Anikster, Y., et al., *Biallelic Mutations in DNAJC12 Cause Hyperphenylalaninemia, Dystonia, and Intellectual Disability*. American Journal of Human Genetics, 2017. **100**(2): p. 257-266.
 236. Van Heusden, G.P.H. and H. Yde Steensma, *Yeast 14-3-3 proteins*. Yeast, 2006. **23**(3): p. 159-171.
 237. Rosenquist, M., et al., *Evolution of the 14-3-3 protein family: Does the large number of isoforms in multicellular organisms reflect functional specificity?* Journal of Molecular Evolution, 2000. **51**(5): p. 446-458.
 238. Aitken, A., *14-3-3 proteins: A historic overview*. Seminars in Cancer Biology, 2006. **16**(3): p. 162-172.
 239. Benzinger, A., et al., *The crystal structure of the non-liganded 14-3-3 σ protein: insights into determinants of isoform specific ligand binding and dimerization*. Cell Research, 2005. **15**(4): p. 219-227.
 240. Bridges, D. and G.B.G. Moorhead, *14-3-3 Proteins: A Number of Functions for a Numbered Protein*. Science's STKE, 2005. **2005**(296): p. re10-re10.
 241. Liu, D., et al., *Crystal structure of the zeta isoform of the 14-3-3 protein*. Nature, 1995. **376**(6536): p. 191-194.
 242. Gardino, A.K., S.J. Smerdon, and M.B. Yaffe, *Structural determinants of 14-3-3 binding specificities and regulation of subcellular localization of 14-3-3-ligand complexes: A comparison of the X-ray crystal structures of all human 14-3-3 isoforms*. Seminars in Cancer Biology, 2006. **16**(3): p. 173-182.
 243. Muslin, A.J., et al., *Interaction of 14-3-3 with Signaling Proteins Is Mediated by the Recognition of Phosphoserine*. Cell, 1996. **84**(6): p. 889-897.
 244. Hermeking, H. and A. Benzinger, *14-3-3 proteins in cell cycle regulation*. Seminars in Cancer Biology, 2006. **16**(3): p. 183-192.
 245. Hermeking, H., *The 14-3-3 cancer connection*. Nature Reviews Cancer, 2003. **3**(12): p. 931-943.
 246. Yamauchi, T., H. Nakata, and H. Fujisawa, *A new activator protein that activates tryptophan 5-monoxygenase and tyrosine 3-monoxygenase in the presence of Ca²⁺, calmodulin-dependent protein kinase*. Purification and characterization. Journal of Biological Chemistry, 1981. **256**(11): p. 5404-5409.
 247. Ichimura, T., et al., *Brain 14-3-3 protein is an activator protein that activates tryptophan 5-monoxygenase and tyrosine 3-monoxygenase in the presence of Ca²⁺, calmodulin-dependent protein kinase II*. FEBS Lett, 1987. **219**(1): p. 79-82.
 248. Kleppe, R., K. Toska, and J. Haavik, *Interaction of phosphorylated tyrosine hydroxylase with 14-3-3 proteins: evidence for a phosphoserine 40-dependent association*. Journal of Neurochemistry, 2001. **77**(4): p. 1097-1107.
 249. Wang, J., et al., *14-3-3 ζ Contributes to Tyrosine Hydroxylase Activity in MN9D Cells: LOCALIZATION OF DOPAMINE REGULATORY PROTEINS TO MITOCHONDRIA*. Journal of Biological Chemistry, 2009. **284**(21): p. 14011-14019.

-
250. Nakashima, A., et al., *RNAi of 14-3-3 η protein increases intracellular stability of tyrosine hydroxylase*. Biochemical and Biophysical Research Communications, 2007. **363**(3): p. 817-821.
 251. Ghorbani, S., et al., *Regulation of tyrosine hydroxylase is preserved across different homo- and heterodimeric 14-3-3 proteins*. Amino Acids, 2016. **48**(5): p. 1221-1229.
 252. Kampinga, H.H., et al., *Guidelines for the nomenclature of the human heat shock proteins*. Cell Stress and Chaperones, 2009. **14**(1): p. 105-111.
 253. Lee, J., et al., *Characterization of JDP genes, an evolutionarily conserved J domain-only protein family, from human and moths* *11The nucleotide sequence data have been submitted to GenBank database under accession numbers AF176012–AF176015, AF192462, and AF192463*. Biochimica et Biophysica Acta (BBA) - Gene Structure and Expression, 2000. **1491**(1): p. 355-363.
 254. Choi, J., et al., *The co-chaperone DNAJC12 binds to Hsc70 and is upregulated by endoplasmic reticulum stress*. Cell Stress Chaperones, 2014. **19**(3): p. 439-46.
 255. Pellicchia, M., et al., *NMR structure of the J-domain and the Gly/Phe-rich region of the Escherichia coli DnaJ chaperone*. J Mol Biol, 1996. **260**(2): p. 236-50.
 256. Horne, B.E., et al., *The Hsp40 J-domain Stimulates Hsp70 When Tethered by the Client to the ATPase Domain*. Journal of Biological Chemistry, 2010. **285**(28): p. 21679-21688.
 257. Craig, E.A., et al., *The diverse roles of J-proteins, the obligate Hsp70 co-chaperone*. Reviews of Physiology Biochemistry and Pharmacology, Vol 156, 2006. **156**: p. 1-21.
 258. De Bessa, S.A., et al., *JDPI (DNAJC12/Hsp40) expression in breast cancer and its association with estrogen receptor status*. Int J Mol Med, 2006. **17**(2): p. 363-367.
 259. Aicha, S.B., et al., *Transcriptional profiling of genes that are regulated by the endoplasmic reticulum-bound transcription factor AlbZIP/CREB3L4 in prostate cells*. Physiological Genomics, 2007. **31**(2): p. 295-305.
 260. Straniero, L., et al., *DNAJC12 and dopa-responsive nonprogressive parkinsonism*. Annals of Neurology, 2017. **82**(4): p. 640-646.
 261. Gallego, D., et al., *Pathogenic variants of DNAJC12 and evaluation of the encoded cochaperone as a genetic modifier of hyperphenylalaninemia*. Human Mutation, 2020. **41**(7): p. 1329-1338.
 262. Huttlin, E.L., et al., *The BioPlex Network: A Systematic Exploration of the Human Interactome*. Cell, 2015. **162**(2): p. 425-440.
 263. Filho, P.R.d.A., et al., *Gene expression profiling of triple-negative breast tumors with different expression of secreted protein acidic and cysteine rich (SPARC)*. Breast Cancer Management, 2018. **7**(2): p. BMT09.
 264. Uno, Y., et al., *Increased Expression of DNAJC12 is Associated with Aggressive Phenotype of Gastric Cancer*. Annals of Surgical Oncology, 2019. **26**(3): p. 836-844.

-
265. He, H.-L., et al., *Overexpression of DNAJC12 predicts poor response to neoadjuvant concurrent chemoradiotherapy in patients with rectal cancer*. *Experimental and Molecular Pathology*, 2015. **98**(3): p. 338-345.
266. Goedert, M., *Alpha-synuclein and neurodegenerative diseases*. *Nature Reviews Neuroscience*, 2001. **2**(7): p. 492-501.
267. Duffy, P.E. and V.M. Tennyson, *Phase and Electron Microscopic Observations of Lewy Bodies and Melanin Granules in the Substantia Nigra and Locus Caeruleus in Parkinson's Disease**. *Journal of Neuropathology & Experimental Neurology*, 1965. **24**(3): p. 398-414.
268. Polymeropoulos, M.H., et al., *Mutation in the α -Synuclein Gene Identified in Families with Parkinson's Disease*. *Science*, 1997. **276**(5321): p. 2045-2047.
269. Spillantini, M.G., et al., *α -Synuclein in Lewy bodies*. *Nature*, 1997. **388**(6645): p. 839-840.
270. Lavedan, C., *The Synuclein Family*. *Genome Research*, 1998. **8**(9): p. 871-880.
271. Maroteaux, L., J. Campanelli, and R. Scheller, *Synuclein: a neuron-specific protein localized to the nucleus and presynaptic nerve terminal*. *The Journal of Neuroscience*, 1988. **8**(8): p. 2804-2815.
272. Ulmer, T.S., et al., *Structure and Dynamics of Micelle-bound Human α -Synuclein*. *Journal of Biological Chemistry*, 2005. **280**(10): p. 9595-9603.
273. Lashuel, H.A., et al., *The many faces of α -synuclein: from structure and toxicity to therapeutic target*. *Nature Reviews Neuroscience*, 2013. **14**(1): p. 38-48.
274. Ueda, K., et al., *Molecular cloning of cDNA encoding an unrecognized component of amyloid in Alzheimer disease*. *Proc Natl Acad Sci U S A*, 1993. **90**(23): p. 11282-6.
275. Giasson, B.I., et al., *A Hydrophobic Stretch of 12 Amino Acid Residues in the Middle of α -Synuclein Is Essential for Filament Assembly*. *Journal of Biological Chemistry*, 2001. **276**(4): p. 2380-2386.
276. Ullman, O., C.K. Fisher, and C.M. Stultz, *Explaining the structural plasticity of α -synuclein*. *Journal of the American Chemical Society*, 2011. **133**(48): p. 19536-19546.
277. Zhang, J., X. Li, and J.-D. Li, *The Roles of Post-translational Modifications on α -Synuclein in the Pathogenesis of Parkinson's Diseases*. *Frontiers in neuroscience*, 2019. **13**: p. 381-381.
278. Oueslati, A., M. Fournier, and H.A. Lashuel, *Chapter 7 - Role of post-translational modifications in modulating the structure, function and toxicity of α -synuclein: Implications for Parkinson's disease pathogenesis and therapies*, in *Progress in Brain Research*, A. Björklund and M.A. Cenci, Editors. 2010, Elsevier. p. 115-145.
279. Sharon, R., et al., *The Formation of Highly Soluble Oligomers of α -Synuclein Is Regulated by Fatty Acids and Enhanced in Parkinson's Disease*. *Neuron*, 2003. **37**(4): p. 583-595.

-
280. Haque, F., et al., *Adsorption of α -Synuclein on Lipid Bilayers: Modulating the Structure and Stability of Protein Assemblies*. The Journal of Physical Chemistry B, 2010. **114**(11): p. 4070-4081.
281. Bisaglia, M., et al., *Interaction Between α -Synuclein and Metal Ions, Still Looking for a Role in the Pathogenesis of Parkinson's Disease*. NeuroMolecular Medicine, 2009. **11**(4): p. 239-251.
282. Hashimoto, M., et al., *Oxidative stress induces amyloid-like aggregate formation of NACP/ α -synuclein in vitro*. NeuroReport, 1999. **10**(4).
283. Perez, R.G., et al., *A Role for α -Synuclein in the Regulation of Dopamine Biosynthesis*. The Journal of Neuroscience, 2002. **22**(8): p. 3090-3099.
284. Abeliovich, A., et al., *Mice Lacking α -Synuclein Display Functional Deficits in the Nigrostriatal Dopamine System*. Neuron, 2000. **25**(1): p. 239-252.
285. Conway, K.A., J.D. Harper, and P.T. Lansbury, *Accelerated in vitro fibril formation by a mutant α -synuclein linked to early-onset Parkinson disease*. Nature Medicine, 1998. **4**(11): p. 1318-1320.
286. Wood, S.J., et al., *α -Synuclein Fibrillogenesis Is Nucleation-dependent*. Journal of Biological Chemistry, 1999. **274**(28): p. 19509-19512.
287. Li, J., et al., *Dopamine and L - dopa disaggregate amyloid fibrils: implications for Parkinson's and Alzheimer's disease*. The FASEB Journal, 2004. **18**(9): p. 962-964.
288. Leong, S.L., et al., *Modulation of α -Synuclein Aggregation by Dopamine: A Review*. 2009. **34**(10): p. 1838-1846.
289. Mor, D.E., et al., *Dopamine induces soluble α -synuclein oligomers and nigrostriatal degeneration*. Nature Neuroscience, 2017. **20**(11): p. 1560-1568.
290. Mor, D.E., M.J. Daniels, and H. Ischiropoulos, *The usual suspects, dopamine and alpha - synuclein, conspire to cause neurodegeneration*. Movement Disorders, 2019. **34**(2): p. 167-179.
291. Wimalasena, K., *Vesicular Monoamine Transporters: Structure-Function, Pharmacology, and Medicinal Chemistry*. Medicinal Research Reviews, 2011. **31**(4): p. 483-519.
292. Eiden, L.E. and E. Weihe, *VMAT2: a dynamic regulator of brain monoaminergic neuronal function interacting with drugs of abuse*. Annals of the New York Academy of Sciences, 2011. **1216**(1): p. 86-98.
293. Yao, J. and L.B. Hersh, *The vesicular monoamine transporter 2 contains trafficking signals in both its N-glycosylation and C-terminal domains*. Journal of Neurochemistry, 2007. **100**(5): p. 1387-1396.
294. Eiden, L.E., et al., *The vesicular amine transporter family (SLC18): amine/proton antiporters required for vesicular accumulation and regulated exocytotic secretion of monoamines and acetylcholine*. Pflügers Archiv, 2004. **447**(5): p. 636-640.
295. Kirshner, N., *Uptake of Catecholamines by a Particulate Fraction of the Adrenal Medulla*. Journal of Biological Chemistry, 1962. **237**(7): p. 2311-2317.

-
296. Parsons, S.M., *Transport mechanisms in acetylcholine and monoamine storage*. The FASEB Journal, 2000. **14**(15): p. 2423-2434.
 297. Caudle, W.M., et al., *Reduced vesicular storage of dopamine causes progressive nigrostriatal neurodegeneration*. Journal of Neuroscience, 2007. **27**(30): p. 8138-8148.
 298. Fon, E.A., et al., *Vesicular Transport Regulates Monoamine Storage and Release but Is Not Essential for Amphetamine Action*. Neuron, 1997. **19**(6): p. 1271-1283.
 299. Takahashi, N., et al., *VMAT2 knockout mice: Heterozygotes display reduced amphetamine-conditioned reward, enhanced amphetamine locomotion, and enhanced MPTP toxicity*. Proceedings of the National Academy of Sciences, 1997. **94**(18): p. 9938-9943.
 300. Wang, Y.-M., et al., *Knockout of the Vesicular Monoamine Transporter 2 Gene Results in Neonatal Death and Supersensitivity to Cocaine and Amphetamine*. Neuron, 1997. **19**(6): p. 1285-1296.
 301. Requena, D.F., et al., *The molecular chaperone Hsc70 interacts with the vesicular monoamine transporter-2*. Journal of Neurochemistry, 2009. **110**(2): p. 581-594.
 302. Guo, J.T., et al., *Inhibition of Vesicular Monoamine Transporter-2 Activity in α -Synuclein Stably Transfected SH-SY5Y Cells*. Cellular and Molecular Neurobiology, 2008. **28**(1): p. 35-47.
 303. Levine, B. and G. Kroemer, *Autophagy in the pathogenesis of disease*. Cell, 2008. **132**(1): p. 27-42.
 304. Nakashima, A., et al., *Proteasome-mediated degradation of tyrosine hydroxylase triggered by its phosphorylation: a new question as to the intracellular location at which the degradation occurs*. J Neural Transm (Vienna), 2018. **125**(1): p. 9-15.
 305. Shiber, A. and T. Ravid, *Chaperoning Proteins for Destruction: Diverse Roles of Hsp70 Chaperones and their Co-Chaperones in Targeting Misfolded Proteins to the Proteasome*. Biomolecules, 2014. **4**(3): p. 704-724.
 306. Zarouchlioti, C., et al., *DNAJ Proteins in neurodegeneration: essential and protective factors*. Philosophical Transactions of the Royal Society B: Biological Sciences, 2018. **373**(1738): p. 20160534.
 307. Gersting, S.W., et al., *Pah enul is a mouse model for tetrahydrobiopterin-responsive phenylalanine hydroxylase deficiency and promotes analysis of the pharmacological chaperone mechanism in vivo*. Human Molecular Genetics, 2010. **19**(10): p. 2039-2049.
 308. Jagannathan, L., S. Cuddapah, and M. Costa, *Oxidative Stress Under Ambient and Physiological Oxygen Tension in Tissue Culture*. Current Pharmacology Reports, 2016. **2**(2): p. 64-72.
 309. Westhoff, B., et al., *HSJ1 Is a Neuronal Shuttling Factor for the Sorting of Chaperone Clients to the Proteasome*. Current Biology, 2005. **15**(11): p. 1058-1064.

-
310. Fan, G.-H., et al., *Heat shock proteins reduce α -synuclein aggregation induced by MPP+ in SK-N-SH cells*. FEBS Letters, 2006. **580**(13): p. 3091-3098.
 311. Van Spronsen, F.J., et al., *Heterogeneous clinical spectrum of DNAJC12-deficient hyperphenylalaninemia: from attention deficit to severe dystonia and intellectual disability*. Journal of Medical Genetics, 2018. **55**(4): p. 249-253.
 312. Pey, A.L., et al., *Mechanisms underlying responsiveness to tetrahydrobiopterin in mild phenylketonuria mutations*. Human Mutation, 2004. **24**(5): p. 388-399.
 313. Danecka, M.K., et al., *Mapping the functional landscape of frequent phenylalanine hydroxylase (PAH) genotypes promotes personalised medicine in phenylketonuria*. Journal of Medical Genetics, 2015. **52**(3): p. 175-185.
 314. Zurflüh, M.R., et al., *Molecular genetics of tetrahydrobiopterin-responsive phenylalanine hydroxylase deficiency*. Human Mutation, 2008. **29**(1): p. 167-175.
 315. Muntau, A.C., et al., *Tetrahydrobiopterin as an Alternative Treatment for Mild Phenylketonuria*. New England Journal of Medicine, 2002. **347**(26): p. 2122-2132.
 316. Fernandez-Escamilla, A.-M., et al., *Prediction of sequence-dependent and mutational effects on the aggregation of peptides and proteins*. Nature Biotechnology, 2004. **22**(10): p. 1302-1306.
 317. Scheller, R., et al., *Toward mechanistic models for genotype-phenotype correlations in phenylketonuria using protein stability calculations*. Human Mutation, 2019. **40**(4): p. 444-457.
 318. Matsumoto, G., et al., *Serine 403 Phosphorylation of p62/SQSTM1 Regulates Selective Autophagic Clearance of Ubiquitinated Proteins*. Molecular Cell, 2011. **44**(2): p. 279-289.
 319. Bjørkøy, G., et al., *p62/SQSTM1 forms protein aggregates degraded by autophagy and has a protective effect on huntingtin-induced cell death*. Journal of Cell Biology, 2005. **171**(4): p. 603-614.
 320. Døskeland, A.P. and T. Flatmark, *Ubiquitination of soluble and membrane-bound tyrosine hydroxylase and degradation of the soluble form*. European Journal of Biochemistry, 2002. **269**(5): p. 1561-1569.
 321. Kawahata, I., et al., *Accumulation of phosphorylated tyrosine hydroxylase into insoluble protein aggregates by inhibition of an ubiquitin-proteasome system in PC12D cells*. Journal of Neural Transmission, 2009. **116**(12): p. 1571-1578.
 322. Kawahata, I., et al., *Dopamine or biopterin deficiency potentiates phosphorylation at 40 Ser and ubiquitination of tyrosine hydroxylase to be degraded by the ubiquitin proteasome system*. Biochemical and Biophysical Research Communications, 2015. **465**(1): p. 53-58.
 323. Carbajosa, N.A.L., et al., *Tyrosine Hydroxylase Is Short-Term Regulated by the Ubiquitin-Proteasome System in PC12 Cells and Hypothalamic and Brainstem Neurons from Spontaneously Hypertensive Rats: Possible Implications in Hypertension (vol 10, e0116597, 2015)*. Plos One, 2015. **10**(6).

-
324. Wu, D.K. and C.L. Cepko, *The Stability of Endogenous Tyrosine Hydroxylase Protein in PC-12 Cells Differs from That Expressed in Mouse Fibroblasts by Gene Transfer*. Journal of Neurochemistry, 1994. **62**(3): p. 863-872.
325. Tank, A.W., L. Ham, and P. Curella, *Induction of tyrosine hydroxylase by cyclic AMP and glucocorticoids in a rat pheochromocytoma cell line: effect of the inducing agents alone or in combination on the enzyme levels and rate of synthesis of tyrosine hydroxylase*. Molecular Pharmacology, 1986. **30**(5): p. 486-496.
326. Fernández, E. and G.L. Craviso, *Protein Synthesis Blockade Differentially Affects the Degradation of Constitutive and Nicotinic Receptor-Induced Tyrosine Hydroxylase Protein Level in Isolated Bovine Chromaffin Cells*. Journal of Neurochemistry, 2002. **73**(1): p. 169-178.
327. Fujisawa, H. and S. Okuno, *Regulatory mechanism of tyrosine hydroxylase activity*. Biochemical and Biophysical Research Communications, 2005. **338**(1): p. 271-276.
328. Daubner, S.C., T. Le, and S. Wang, *Tyrosine hydroxylase and regulation of dopamine synthesis*. Arch Biochem Biophys, 2011. **508**(1): p. 1-12.
329. Roy, S., et al., *Rapid and Intermittent Cotransport of Slow Component-b Proteins*. Journal of Neuroscience, 2007. **27**(12): p. 3131-3138.
330. Scott, D.A., et al., *Mechanistic logic underlying the axonal transport of cytosolic proteins*. Neuron, 2011. **70**(3): p. 441-454.
331. Brimijoin, S. and M.J. Wiermaa, *Rapid axonal transport of tyrosine hydroxylase in rabbit sciatic nerves*. Brain Research, 1977. **121**(1): p. 77-96.
332. Jensen, P.H., et al., *Axonal transport of synucleins is mediated by all rate components*. European Journal of Neuroscience, 1999. **11**(10): p. 3369-3376.
333. Parra, L.A., et al., *The Molecular Chaperone Hsc70 Interacts with Tyrosine Hydroxylase to Regulate Enzyme Activity and Synaptic Vesicle Localization**. Journal of Biological Chemistry, 2016. **291**(34): p. 17510-17522.
334. Sytnyk, V., *Trans-Golgi network delivery of synaptic proteins in synaptogenesis*. Journal of Cell Science, 2003. **117**(3): p. 381-388.
335. Lehmann, I.T., et al., *Differential regulation of the human tyrosine hydroxylase isoforms via hierarchical phosphorylation*. Journal of Biological Chemistry, 2006. **281**(26): p. 17644-17651.
336. Salvatore, M.F., E.S. Calipari, and S.R. Jones, *Regulation of Tyrosine Hydroxylase Expression and Phosphorylation in Dopamine Transporter-Deficient Mice*. ACS Chemical Neuroscience, 2016. **7**(7): p. 941-951.
337. Benoit-Marand, M., et al., *Inhibition of dopamine uptake by D2 antagonists: an in vivo study*. Journal of Neurochemistry, 2011. **116**(3): p. 449-458.
338. Kuczenski, R.T. and A.J. Mandell, *Regulatory Properties of Soluble and Particulate Rat Brain Tyrosine Hydroxylase*. Journal of Biological Chemistry, 1972. **247**(10): p. 3114-3122.
339. Yamauchi, T., H. Nakata, and H. Fujisawa, *A New Activator Protein That Activates Tryptophan 5-Monooxygenase and Tyrosine 3-Monooxygenase in the Presence of Ca-(2+)-Dependent, Calmodulin-Dependent Protein-Kinase -*

-
- Purification and Characterization*. Journal of Biological Chemistry, 1981. **256**(11): p. 5404-5409.
340. Stewart, M., *Molecular mechanism of the nuclear protein import cycle*. Nature Reviews Molecular Cell Biology, 2007. **8**(3): p. 195-208.
341. Nardoizzi, J.D., K. Lott, and G. Cingolani, *Phosphorylation meets nuclear import: a review*. Cell Commun Signal, 2010. **8**: p. 32.
342. Fontes, M.R., et al., *Role of flanking sequences and phosphorylation in the recognition of the simian-virus-40 large T-antigen nuclear localization sequences by importin-alpha*. Biochem J, 2003. **375**(Pt 2): p. 339-49.
343. Kitamura, R., et al., *Nuclear import of Epstein-Barr virus nuclear antigen 1 mediated by NPI-1 (Importin alpha5) is up- and down-regulated by phosphorylation of the nuclear localization signal for which Lys379 and Arg380 are essential*. J Virol, 2006. **80**(4): p. 1979-91.
344. Soderholm, J.F., et al., *Importazole, a small molecule inhibitor of the transport receptor importin-beta*. ACS Chem Biol, 2011. **6**(7): p. 700-8.
345. Negis, Y., et al., *Cell cycle markers have different expression and localization patterns in neuron-like PC12 cells and primary hippocampal neurons*. Neuroscience Letters, 2011. **496**(2): p. 135-140.
346. Farrell, A.S. and R.C. Sears, *MYC Degradation*. Cold Spring Harbor Perspectives in Medicine, 2014. **4**(3): p. a014365-a014365.
347. Prasad, R., C. Xu, and D.T.W. Ng, *Hsp40/70/110 chaperones adapt nuclear protein quality control to serve cytosolic clients*. Journal of Cell Biology, 2018. **217**(6): p. 2019-2032.

PAPER I

Phenylalanine hydroxylase variants interact with the co-chaperone DNAJC12.

Kunwar Jung-KC, Nastassja Himmelreich, Karina S. Prestegård, Tie-Jun Sten Shi, Tanja Scherer, Ming Ying, Ana Jorge-Finnigan, Beat Thöny, Nenad Blau, and Aurora Martinez



Hum Mutat. 40(4): 483-494. doi: 10.1002/humu.23712 (2019)

Abstract

DNAJC12, a type III member of the HSP40/DNAJ family, has been identified as the specific co-chaperone of phenylalanine hydroxylase (PAH) and the other aromatic amino acid hydroxylases. DNAJ proteins work together with molecular chaperones of the HSP70 family to assist in proper folding and maintenance of intracellular stability of their clients. Autosomal recessive mutations in DNAJC12 were found to reduce PAH levels, leading to hyperphenylalaninemia (HPA) in patients without mutations in PAH. In this work, we investigated the interaction of normal wild-type DNAJC12 with mutant PAH in cells expressing several PAH variants associated with HPA in humans, as well as in the *Enu1/1* mouse model, homozygous for the V106A-Pah variant, which leads to severe protein instability, accelerated PAH degradation and mild HPA. We found that mutant PAH exhibits increased ubiquitination, instability, and aggregation compared with normal PAH. In mouse liver lysates, we showed that DNAJC12 interacts with monoubiquitin-tagged PAH. This form represented a major fraction of PAH in the *Enu1/1* but was also present in liver of wild-type PAH mice. Our results support a role of DNAJC12 in the processing of misfolded ubiquitinated PAH by the ubiquitin-dependent proteasome/autophagy systems and add to the evidence that the DNAJ proteins are important players both for proper folding and degradation of their clients.

RESEARCH ARTICLE

Phenylalanine hydroxylase variants interact with the co-chaperone DNAJC12

Kunwar Jung-KC¹ | Nastassja Himmelreich² | Karina S. Prestegård¹ |
Tie-Jun Sten Shi¹ | Tanja Scherer³ | Ming Ying¹ | Ana Jorge-Finnigan¹ |
Beat Thöny³ | Nenad Blau^{2,3}  | Aurora Martinez¹ 

¹Department of Biomedicine, University of Bergen, Bergen, Norway

²Dietmar-Hopp-Metabolic Center, University Children's Hospital, Heidelberg, Germany

³Division of Metabolism, University Children's Hospital Zürich, Zürich, Switzerland

Correspondence

Aurora Martinez, Department of Biomedicine, University of Bergen, Bergen, Norway.

Email: aurora.martinez@uib.no

Nenad Blau, Dietmar-Hopp-Metabolic Center, University Children's Hospital, Heidelberg, Germany.

Email: Nenad.Blau@med.uni-heidelberg.de

Funding information

This work was supported by Research Council of Norway grants FRIMEDBIO 261826/F20 and FORNY 248889/O30, the K.G. Jebsen Centre for Neuropsychiatric Disorders, and the Western Norway Regional Health Authorities (Helse-Vest project 912246) (to A.M.), and by the European Commission FP7-HEALTH-2012-INNOVATION-1 EU Grant No. 305444 (to N.B.).

Communicated by David S. Rosenblatt

Kunwar Jung-KC and Nastassja Himmelreich have contributed equally to this work.

Abstract

DNAJC12, a type III member of the HSP40/DNAJ family, has been identified as the specific co-chaperone of phenylalanine hydroxylase (PAH) and the other aromatic amino acid hydroxylases. DNAJ proteins work together with molecular chaperones of the HSP70 family to assist in proper folding and maintenance of intracellular stability of their clients. Autosomal recessive mutations in *DNAJC12* were found to reduce PAH levels, leading to hyperphenylalaninemia (HPA) in patients without mutations in *PAH*. In this work, we investigated the interaction of normal wild-type DNAJC12 with mutant PAH in cells expressing several PAH variants associated with HPA in humans, as well as in the *Enu*^{1/1} mouse model, homozygous for the *V106A-Pah* variant, which leads to severe protein instability, accelerated PAH degradation and mild HPA. We found that mutant PAH exhibits increased ubiquitination, instability, and aggregation compared with normal PAH. In mouse liver lysates, we showed that DNAJC12 interacts with monoubiquitin-tagged PAH. This form represented a major fraction of PAH in the *Enu*^{1/1} but was also present in liver of wild-type PAH mice. Our results support a role of DNAJC12 in the processing of misfolded ubiquitinated PAH by the ubiquitin-dependent proteasome/autophagy systems and add to the evidence that the DNAJ proteins are important players both for proper folding and degradation of their clients.

KEYWORDS

HSP40 co-chaperones, hyperphenylalanine, molecular chaperones, protein aggregation, protein misfolding

1 | INTRODUCTION

The aromatic amino acid hydroxylases (AAAHs) are a family of non-heme iron- and tetrahydrobiopterin (BH₄)-dependent enzymes that catalyze the hydroxylation of their respective aromatic amino acid substrates using O₂ as an additional substrate (Fitzpatrick, 2015; Skjærven, Teigen, & Martinez, 2014). In vertebrates, four genes code for the AAAHs: phenylalanine hydroxylase (*PAH*), tyrosine hydroxylase (*TH*), and tryptophan hydroxylases 1 and 2 (*TPH1* and *TPH2*). The AAAHs catalyze physiologically and clinically important reactions, as the hydroxylation of L-Phe to L-Tyr, which is the first step in the catabolic degradation of L-Phe (by *PAH*), the hydroxylation of L-Tyr to L-DOPA, the rate-limiting step in the biosynthesis of catecholamines

(by *TH*), and the hydroxylation of L-Trp to 5-hydroxytryptophan, the rate-limiting reaction in the synthesis of serotonin (by the *TPHs*). Dysfunction of the AAAHs is associated with serious neurometabolic disorders, such as phenylketonuria (PKU), which is caused by the hyperphenylalaninemia (HPA) that results from variants in *PAH*, and neurological and neuropsychiatric disorders caused by malfunction and dysregulation of *TH* or the *TPHs* (Waløen, Kleppe, Martinez, & Haavik, 2017).

Recent work has shown that mutations in *DNAJC12*—a co-chaperone of the HSP40/DNAJ family, type III—lead to HPA, dystonia, and intellectual disability (Anikster et al., 2017; Blau, Martinez, Hoffmann, & Thony, 2018; Bouchereau et al., 2018; Straniero et al., 2017; van Spronsen et al., 2017; Veenma, Cordeiro,

Sondheimer, & Mercimek-Andrews, 2018). Moreover, affinity capture-mass spectrometry analysis in human cells has shown direct interactions of DNAJC12 with PAH, TH, and the TPHs (Anikster et al., 2017; Huttlin et al., 2015), which indicates that DNAJC12 is a specific co-chaperone for the AAAHs that contributes to the maintenance of their intracellular stability. The function of the DNAJ proteins in the quality control machinery is believed to be the transfer of its specific protein clients to the molecular chaperone HSC70/HSP70-HSP90 network for proper folding (Kampinga & Craig, 2010), and PAH protein level and activity are indeed reduced in cells that express mutant DNAJC12 (Anikster et al., 2017). Nevertheless, the complex molecular chaperone machinery is essential to maintain proteostasis in eukaryotic cells not only by assisting in the folding of client proteins but also in the intertwined triage decisions that affect the disposition of misfolded proteins, which are degraded to avoid toxic aggregation and cellular damage (Dekker, Kampinga, & Bergink, 2015; Pratt, Morishima, Peng, & Osawa, 2010). In this context, the DNAJ-co-chaperones appear essential for ubiquitin (Ub)-tagging and further degradation of the clients by the Ub-dependent proteasome (Kampinga & Craig, 2010). Furthermore, DNAJ and HSC70/HSP70 also participate in the degradation of aggregated proteins by autophagy (Kaushik & Cuervo, 2012). Proteins such as PAH, which do not include a specific sequence motif for chaperone-mediated autophagy allowing direct translocation across the lysosome membrane, usually follow a mechanism known as selective autophagy (Kaushik & Cuervo, 2012). This selective autophagosomal-lysosomal system also requires Ub-tagging of the clients and collaborates with the Ub-proteasome in the degradation of misfolded and aggregated proteins, where HSP70s and DNAJs play an important role in the crosstalk between both systems (Fernandez-Fernandez, Gragera, Ochoa-Ibarrola, Quintana-Gallardo, & Valpuesta, 2017; Kraft, Peter, & Hofmann, 2010).

PAH mutants often form amorphous aggregates when expressed in *Escherichia coli* (Björge, Knappskog, Martínez, Stevens, & Flatmark, 1998), and fibril formation has also been observed in vitro (Leandro, Simonsen, Saraste, Leandro, & Flatmark, 2011). However, in vivo amyloid or other fibrillary deposits, which are the pathological manifestation of other protein folding defects via gain-of-function toxicity (Gregersen, 2006), have not been reported for PKU-associated variants. The misfolded PAH mutants are considered to be effectively degraded by the cellular quality control system when they are expressed in eukaryote cells (Himmelreich et al., 2018; Pey, Desviat, Gamez, Ugarte, & Perez, 2003; Waters, Parniak, Akerman, & Sriver, 2000) or as observed in mammalian liver of mouse models of HPA (Gersting et al., 2010; Sarkissian, Boulais, McDonald, & Sriver, 2000; Sarkissian, Ying, Scherer, Thony, & Martinez, 2012). PKU is therefore considered a paradigm of misfolding disorders in which the metabolic phenotype is mainly related to the conformational destabilization caused by the mutation in the PAH structure, which in turn is associated to the remaining PAH protein expression and activity (Pey, Stricher, Serrano, & Martinez, 2007; Wettstein et al., 2015). Recently, the aggregation of the unstable PAH variant p.V106A, which is expressed by the *Enu*^{1/1} mouse model of mild HPA (Sarkissian et al., 2000), has also been observed when the mutant protein is expressed in primary hepatocytes and COS-7 cells (Eichinger et al.,

2018). Furthermore, studies with both, the *Enu*^{1/1} and the *Enu*^{1/2} heteroallelic mouse models, which carry both the unstable V106A-PAH (*enu1* allele) and/or the catalytically deficient but stable F263S-PAH (*enu2* allele) variants, have shown that mutant forms of PAH, notably p.V106A, are highly ubiquitinated and very unstable in vivo, indicating that they are targets for proteasome-mediated degradation and selective autophagy (Sarkissian et al., 2012).

To further investigate the involvement of DNAJC12 in the degradation of mutant PAH, we studied the interactions of the wild-type (wt) co-chaperone with normal and mutant PAH forms expressed in COS cells and in mouse liver. To study the interactions in vivo, we selected the homozygote *Enu*^{1/1} mouse model. Despite the fact that the *PAH* variant carried by these mice is extremely rare in human subjects (0.2% of alleles in Japan) (Okano, Kudo, Nishi, Sakaguchi, & Aso, 2011), the *Enu*^{1/1} is a model for pathological states associated with human PAH instability and accelerated degradation (Gersting et al., 2010; Sarkissian et al., 2000). We demonstrated that in the livers of these mice, mutant p.V106A-PAH is found largely in a mono-ubiquitinated state and forms a complex with DNAJC12, which supports the functional association of the co-chaperone with PAH degradation.

2 | MATERIALS AND METHODS

2.1 | Generation of plasmids for cellular expression of PAH and DNAJC12

Generation of plasmids for recombinant expression of the PAH variants was performed as described (Himmelreich et al., 2018; Shen et al., 2016) (Supporting Information Table S1). To generate an expression plasmid for DNAJ12 (based on pCiNeo-Myc), total RNA was extracted from 1×10^6 cells (control fibroblasts) using the MasterPure RNA purification kit (Epicentre Biotechnologies). Using random hexamer primers (Invitrogen) and RevertAid reverse transcriptase (Thermo Scientific), 1 μ g of total RNA was reverse transcribed into cDNA, using manufacturer's protocol (5 min at 25°C, 60 min at 42°C, and 5 min at 70°C). Nested-PCR for human DNAJC12 (NM_021800.2; CDS: 169–765) was performed with the following parameters: Step 1: 98°C, 1 min; Step 2: 98°C, 15 s; Step 3: 55°C, 30 s; Step 4: 72°C, 40 s; Step 5: 72°C, 5 min; Step 6: 4°C, indefinitely. Steps 2–4 were repeated 35 times. The amplification primers for DNAJC12 were F1_hDNAJC12: 5'-₄GTCTAGGATGACATCTGGTGTATTG₂₉-3' together with R1_hDNAJC12: 5'-₈₈₄GTACTCAGCAATTCACAGACATGAC₈₅₉-3' and F2_hDNAJC12: 5'-₁₁₁TTCGAAGCTCACTGTGCCCTCTTG₁₃₃-3' together with R2_hDNAJC12: 5'-₈₁₃GCATAGGGGACAGCTCTTGCT₇₉₁-3'. After gel extraction (Bioline) and Sanger sequencing of the DNAJC12-PCR fragment, a third PCR was performed to attach flanking *NotI* endonuclease restriction sites for ligation with T4-DNA-ligase (Fermentas) into vector pCiNeo-Myc (Promega) (F3_hDNAJC12_NOT_ATG: 5'-ACGCGGCCG CATGGATGCAATACT together with R4_hDNAJC12_Not_STOP: 5'-TACGCGCCGCTATTTTCATAGTTTCT-3'). The *NotI* restriction fragment was ligated into vector pCiNeo-Myc overnight at room temperature before transformation into *E. coli DH5a* cells. The constructs were rechecked after plasmid miniprep (Bioline) and

thereafter stably transfected into the COS-7 cell line upon selection with Neomycin in the cell culture medium (225 $\mu\text{g}\cdot\text{ml}^{-1}$ G418, Life Technologies).

2.2 | Cell culture, transient transfection of PAH-expressing plasmids, PAH and DNAJC12 expression, and cell lysate preparation

COS-7 cells were used for transient transfection of human PAH-expressing plasmids. Cells were cultured in Dulbecco's Modified Eagle Medium, enriched with a 10% fetal calf serum plus 1% Pen/Strep under standard conditions (37°C with 5% CO₂) in a sterile environment. One day before transfection, 10⁶ COS-7 cells were seeded in 10 cm culture dishes (Sarstedt). For the transfection with Fugene HD reagent (Promega), the cells had a density of 50–70% confluence, and the experiments were carried out according to the manufacturer's manual. Plasmids pCMV-Flag-PAH (10 μg) expressing either the wt or a PAH-variant were co-transfected with 2 μg of pSV- β -Galactosidase control vector (Promega) using 30 μl of liposomal transfection reagent in antibiotic-free media. After culturing the transfected cells for 72 hr, the cells were harvested with trypsin, washed with 1 \times PBS, pH 6.8, and shock-frozen in liquid N₂ for storage at –80°C. COS-7 cells stably expressing DNAJC12 were used in three different variants, that is, as “un-transfected” controls, and transfected with either wt or one of the mutant PAH. Cell lysates were prepared by macerating the cells in 1 M Sucrose, 1 \times PBS buffer, pH 6.8, containing protease inhibitor cocktail (Roche Applied Science) (except DNAJC12 overexpressing cells, which were lysed in water) 20 times through a 20 G needle followed by 3 \times 20 s sonification and centrifugation for 30 min at 13,000 rpm at 4°C. The cell extracts were desalted and further purified using Zebra Desalt Spin columns (Pierce Biotechnology). The Myc-Tagged DNAJC12 was also used as a marker for immunodetection of the antigen, and to validate the antibody, which was selected based on its highest selectivity for DNAJC12 toward other DNAJ-proteins.

2.3 | Mice husbandry and genotyping

Heterozygous C57BL/6-*enu1* mice (*Enu1*^{1/wt}) were kindly donated by Dr. Soren W. Gersting from the Ludwig-Maximilians-University in Munich to the University of Zurich (Beat Thöny) for colony forming, and thereafter transferred to the laboratory animal facility at the University of Bergen. The here presented animal studies received approval from the National committee for the use of animals in research (Norwegian Food Safety Authority) and were conducted in accordance with the International and National regulations on the use of animals in research. Homozygote mutant mice *enu1/enu1* (*Enu1*^{1/1}) were generated by cross-breeding heterozygous females with homozygous males. C57BL/6 mice were used as wt controls. Animals used for experiments were between 18 and 21 weeks of age with a body weight of 25–35 g. Animals were housed in a controlled temperature room maintained under alternating 12 hr light and dark cycles and, in between experiments, had free access to food (standard chow) and water. Ear biopsies were collected for genotyping following a method as described (McDonald & Charlton, 1997).

2.4 | Preparation of mouse liver lysates

Immediately after the sacrifice with CO₂, the entire liver was resected, frozen in liquid nitrogen, and stored at –80°C. The liver tissue was manually ground into fine powder and stored in aliquots at –80°C until analysis. Liver lysate preparation was performed at 4°C. For standard initial immunodetection experiments, liver powder aliquots were homogenized with a Tissue Lyser II (Qiagen) in PBS buffer, pH 7.4, containing a protease inhibitor cocktail (Roche). The lysates were clarified by centrifugation at 13,000 \times g for 20 min, and the supernatants were collected and stored in liquid nitrogen prior to use. To improve the solubilization of aggregates, the liver powder aliquots were homogenized with a Tissue Lyser II in 4 \times volumes of 20 mM Hepes, pH 7.4, 125 mM NaCl, 1 mM EDTA, 2 mM PMSF supplemented with protease inhibitor cocktail (Roche Applied). The lysates were clarified by centrifugation at 16,000 \times g for 20 min. The supernatants were collected and treated with 1% Triton X-100 for 1 hr with rotation, and centrifuged at 20,000 \times g for 15 min. The protein concentrations were measured using a Direct Detect® Infrared Spectrometer (Merck Life Science). These conditions were also used for the preparation of lysates for co-immunoprecipitation. Subcellular fractionation of nuclear and cytoplasmic fraction of liver extracts was performed using a nuclear extraction kit (Merck Life Science) on the liver powder.

2.5 | mRNA quantification

Quantification of selected mouse mRNAs by RT-qPCR was performed as described (Scherer et al., 2018), using the ABI assay number Mm00500918_m1 (NCBI nucleotide sequence number NM_008777.3) for *Pah*-mRNA, Mm01731394_gH (NM_031165.4) for *Hspa8*-mRNA, Mm00517691_m1 (NM_001163434.1) for *Hspa5(BIP)*-mRNA, Mm01322973_m1 (NM_008102.3) for *Gch1*-mRNA, Mm00433149_m1 for *Esr1*-mRNA, Mm01201402_m1 (NM_008296.2) for *Hsf1*-mRNA, Mm00490634_m1 (NM_019719.3) for *Stub1*-mRNA, Mm00622819_m1 (NM_177157.4) for *Gchfr*-mRNA, Mm00497038_m1 (NM_001253685.1) for *Dnajc12*-mRNA, Mm01729741_g1 (NM_001285429.1) for *Eef1d*-mRNA, Mm00517691_m1 (NM_010478.2) for *Hspa1b(Hsp70)*-mRNA, Mm02620446_s1 (NM_029771.3) for *Gper1*-mRNA, and Mm00599821_m1 (NM_010157.3) for *Esr2*-mRNA. The murine *Gapdh* gene was used as a control (ABI assay ID Mm9999915_g1; NCBI nucleotide sequence number NM_008084.3).

2.6 | Expression and immunoblotting of PAH and DNAJC12

Western blotting of the cell lysates was performed as described (Himmelreich et al., 2018); 20 μg of the total protein from the supernatant was resolved in a 12 % SDS-PAGE, blotting for 50 min to a nitrocellulose membrane (GE Healthcare) using a semidry transfer method and blocking for 1 hr at room temperature in 5% milk powder either in TBST with 0.1% (v/v) Tween (for DNAJC12 or M2-Flag) or PBST 0.1 with 0.1% (v/v) Tween (for PAH, HSP70, and β -actin). Primary antibodies against DNAJC12 (1:500 dilution, Abcam ab167425),

PAH (1:1,000 dilution, Millipore MAB5278), M2-Flag (1:1,000 dilution, Sigma F1804), HSP70 (1:1,000 dilution, ab2787), and β -actin (1:10,000, Sigma A5441) were incubated overnight at 4°C under constant movement. The secondary antibodies against rabbit (Dianova) and against mouse (Santa Cruz) were labeled with a horseradish peroxidase tag, and detection with an ECL reagent (Pierce) was performed according to manufacturer's recommendations. Western blots of the liver lysates were performed using SDS-PAGE 10% TGX™ gels (Bio-Rad) with 15 μ g total protein in sample buffer consisting of 1% SDS and 100 mM DTT (final concentration) in each lane. The samples were transferred onto PVDF membranes using a Transblot Turbo system (Bio-Rad) and immunostained using as primary antibodies: anti-PAH (clone PH8) (1:5,000, mouse; Merck Life Science), anti-DNAJC12 (1:300, rabbit; Abcam), anti-ubiquitin (1:1,000, mouse; Thermo Fisher Scientific), anti- β -actin (1:1,000, mouse; Merck Life Science), anti-HSC70/HSP70 (1:5,000, mouse; Enzo; this antibody recognizes both HSC70 and HSP70), anti-GAPDH (1:1,000, rabbit; Abcam). Secondary antibodies for both goat anti-rabbit IgG (H+L) horseradish peroxidase conjugate and goat anti-mouse IgG (H+L) horseradish peroxidase conjugate were from Bio-Rad. The membranes were developed by enhanced chemiluminescence and visualized using a ChemiDoc instrument (Bio-Rad). The band intensities were quantified using Image Lab software v 5.1 (Bio-Rad).

2.7 | Immunohistochemistry

Enu^{1/1} and wt mice (male, 6-month-old) were deeply anesthetized with sodium pentobarbital (Mebumal; 20 mg·kg⁻¹, ip), and then transcardially perfused with 20 ml of warm saline solution (0.9%; 37°C), followed by 20 ml of a warm mixture of paraformaldehyde (4%; 37°C) with 0.4% picric acid in 0.16 M phosphate buffer, pH 7.2, and finally with 50 ml of the same, but ice-cold, fixative. After perfusion, the livers were dissected and post-fixed in the same fixative for 90 min at 4°C and subsequently stored in 20% sucrose in PBS, pH 7.4, containing 0.01% sodium azide (Merck Life Science) and 0.02% bacitracin (Merck Life Science) at 4°C for 4 days. The tissues were then embedded in OCT compound (Tissue Tek, Miles Laboratories), frozen, cut into 20- μ m-thick sections in a cryostat (Microm) and mounted on Superfrost Plus microscope slides (Thermo Fisher Scientific). The sections were dried at room temperature (RT) for 30 min and rinsed with PBS for 10 min. The sections were pretreated with 0.5 or 1% Triton X-100 (as indicated) in PBS for 1 hr at RT, and then incubated for 24 hr at 4°C in a humid chamber with rabbit anti-PAH (1:200; Abcam) or rabbit anti-DNAJC12 (1:400; Abcam) antisera diluted in PBS containing 5% (w/v) normal goat serum. After incubation, the slides were rinsed with PBS for 15 min at RT followed by a 2 hr incubation with donkey anti-rabbit IgG-H&L (Alexa Fluor® 488; 1:100; Abcam) diluted in 5% normal goat serum in PBS, then washed in PBS for 15 min. Finally, the sections were mounted with glycerol/PBS (9:1) containing 2.5% DABCO (Merck Life Science). The specimens were analyzed using a Leica TCS SP5 microscope (Leica Microsystems) equipped with X10 (0.5 numerical aperture, NA) and X20 water (0.75 NA) objectives, and images were acquired with the LasAF software from Leica.

2.8 | Co-immunoprecipitation

The supernatants from the liver lysates treated with 1% Triton X-100 (see above) were incubated with an antibody against PAH (clone PH8) (mouse; Merck Life Science), control IgGs (Merck Life Science), or no antibody (only beads) with overnight rotation. Protein A/G PLUS-agarose beads (Santa Cruz Biotechnology, Inc.) were incubated with gentle rotation for 1 hr with the samples. The immunoprecipitates were then pelleted, washed, and incubated at 95°C for 10 min in 50 μ l of sample buffer. The samples were analyzed using SDS-PAGE and immunoblotting with anti-PAH (1:1,000, mouse, Merck Life Science), anti-DNAJC12 (1:300, rabbit; Abcam), anti-ubiquitin (1:1,000, mouse; Thermo Fisher Scientific), and anti-HSC70/HSP70 (1:5,000, mouse; Enzo) antibodies as primary antibodies; anti-mouse kappa light chain (HRP) (Abcam) and anti-rabbit IgG heavy chain (HRP) (Abcam) antibodies were used as secondary antibodies for the detection of primary antibodies to prevent unspecific recognition of accumulated heavy and light chain from the immunoprecipitation. Also, for PAH immunodetection, both in input and immunoprecipitation, samples from wt mice were diluted 10 times compared to *Enu*^{1/1} samples to prevent obscuring of the weak PAH signal in the latter due to dynamic range.

2.9 | Statistical analysis

Using Student's *t*-test, two-way comparison was performed for statistical analysis, considering *p*-value <0.05 statistically significant. The sample size *n* was in all cases ≥ 3 .

3 | RESULTS

3.1 | Immunodetection of DNAJC12 in lysates of COS cells expressing different PAH variants

To investigate the relative expression of PAH variants and endogenous DNAJC12, we chose COS-7 cells as they have recently been used to express PKU-associated PAH variants (Himmelreich et al., 2018). COS-7 cells expressed low amounts of endogenous DNAJC12 (Figure 1a, first lane) until they were subjected to transient transfection of PAH (wt and variants) (Figure 1a), and we also observed that the endogenous DNAJC12 also increased in stably transfected COS-7 cells expressing DNAJC12 with a Myc-Tag (Supporting Information Figure S1, last lane). Normal COS-7 cells are thus a useful system to overexpress human PAH-wt and PKU associated variants, as COS-7 cells with stable expression of DNAJC12 appeared to result in the overexpression of the endogenous form of the co-chaperone that may cause alteration of mechanisms and interaction with partners, such as PAH. We selected 11 PAH variants characterized by different relative residual PAH activity for inclusion in the present study according to PAHvdb: Phenylalanine Hydroxylase Gene Locus-Specific Database (www.biopku.org), that is, p.A47V, p.V190A, p.A300S, p.A313T and p.A403V associated with mild HPA; p.R68G, p.E76 and p.R297H with mild PKU; and p.G218V and p.R408W, associated with severe, classic PKU (Figure 1a). Cell lysates were analyzed by Western blotting for immunodetection of overexpressed PAH variants, both

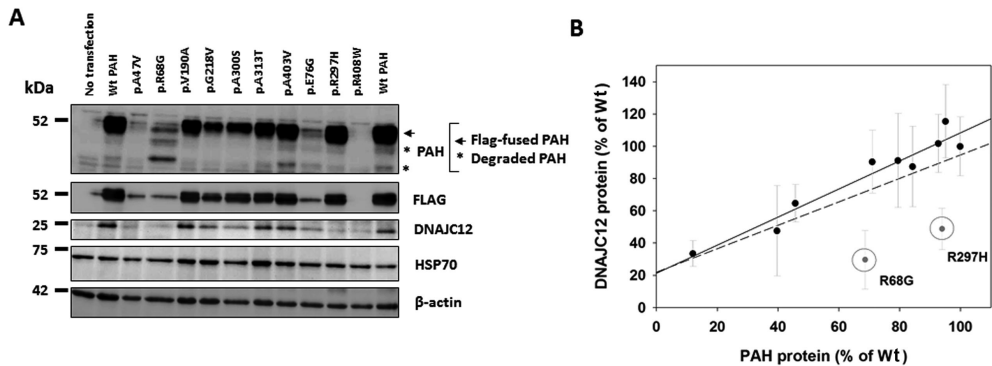


FIGURE 1 Expression analyses of the transient transfection of a subset of PAH-variants in COS-7 cells and endogenous DNAJC12 and HSP70. (a) Western blots of PAH wt and variants (Himmelreich et al., 2018), the Flag-tag, DNAJC12, and HSP70 ($n \geq 3$). (b) Correlations between immunoquantified DNAJC12 and PAH for each PAH variant expressed in the COS-7 cells, relative to immunoquantified DNAJC12 and PAH in the wt-PAH sample normalized against β -actin, respectively. A moderate positive correlation was measured between the levels of immunoquantified PAH with the PAH antibody (on the ~ 52 -kDa Flag-fused PAH) and endogenous DNAJC12 (~ 24 kDa) ($R^2 = 0.5$; dashed line). A stronger relationship was measured for a subset of variants, excluding p.R68G and p.R297H ($R^2 = 0.93$; solid line)

with antibodies against PAH itself and Flag-tagged PAH, and for endogenous DNAJC12 and HSP70 (Figure 1a). For PAH-wt, the immunodetection pattern showed a strong 52-kDa full-length band, corresponding to PAH with a fused Flag-tag, some minor degradation bands of lower molecular weight, as well as bands of higher molecular weight associated in previous studies with post-translationally modified PAH (Doskeland & Flatmark, 1996; Sarkissian et al., 2012) (see also Supporting Information Figure S1, showing results from a different experiment; $n = 7$ performed). Moreover, a similar band pattern was found for several of the PAH variants, with most revealing decreased levels of the full-length PAH, whereas other variants, such as p.R68G, presented stronger degradation bands (Figure 1a and Supporting Information Figure S1). The immunoquantification of the PAH variants relative to PAH-wt provided very similar values by using either PAH or Flag antibodies. The immunodetected levels of DNAJC12 were reduced for the most unstable PAH variants. In particular, the expression of p.R408W, which produces a strongly misfolded PAH enzyme, results in degraded PAH and provided very low levels of immunodetected PAH protein and of endogenous DNAJC12 (Figure 1a). As depicted in Figure 1b, we observed a moderate positive correlation between the levels of immunoquantified PAH with the PAH antibody (on the ~ 52 -kDa Flag-tagged PAH) and endogenous DNAJC12 (~ 24 kDa) ($R^2 = 0.51$). Similar positive correlations were obtained between the immunoquantified Flag epitope and endogenous DNAJC12 (data not shown). The relationship was actually very strong for a subset of variants excluding p.R68G and p.R297H ($R^2 = 0.93$). On the other hand, the immunodetected endogenous HSP70 was not affected by the PAH variant expressed, and the levels of this molecular chaperone appeared rather constant (Figure 1a).

The correlation between PAH and DNAJC12 levels supports an association between both proteins, and indicates a specific interaction of the co-chaperone with the most severely misfolded PAH mutants.

We aimed to investigate the underlying molecular mechanisms for the interaction, but in order to avoid any differences in expression of endogenous DNAJC12 due to transcriptional and translational interference from the transient expression of PAH, we selected the *Enu*^{1/1} HPA mouse model for analysis of endogenous expression of DNAJC12 and variant PAH.

3.2 | Immunodetection of PAH, DNAJC12 and HSC70/HSP70, and ubiquitination state of PAH in liver lysates of wild-type and *Enu*^{1/1} mice prepared under standard conditions

We investigated the interactions between DNAJC12 and PAH in liver of *Enu*^{1/1} mice as they express the highly unstable PAH variant p.V106A-PAH. Western blot analyses of liver lysates showed the expected reduction of PAH levels in the *Enu*^{1/1} compared with wt mice (Gersting et al., 2010; Sarkissian et al., 2000) (Figure 2). We also performed Western blot analysis of ubiquitin in livers, where wt mice showed a major fraction of full-length non-ubiquitinated-PAH (~ 50 kDa) and a smaller fraction of monoubiquitinated-PAH, whereas a large proportion of mutant PAH appeared to be monoubiquitinated (55 kDa) in *Enu*^{1/1} livers (Figure 2a). These bands have previously been identified based on immunodetection in *Enu*^{1/1} and *Enu*^{1/2} and immunoprecipitation in *Enu*^{1/2} liver lysates (Sarkissian et al., 2000; Sarkissian et al., 2012). Weak polyubiquitinated bands were observed for both wt and *Enu*^{1/1} mice. As observed in the lysates of COS-7 cells expressing wt and the most unstable PAH mutants (Figure 1a), DNAJC12 was immunodetected in the liver lysates from wt mice but not in lysates from *Enu*^{1/1} (Figure 2a). On the other hand, the expression levels of HSC70/HSP70 were not affected by the PAH genotype and these molecular chaperones presented very similar levels in wild-type and *Enu*^{1/1} mice samples (Figure 2a).

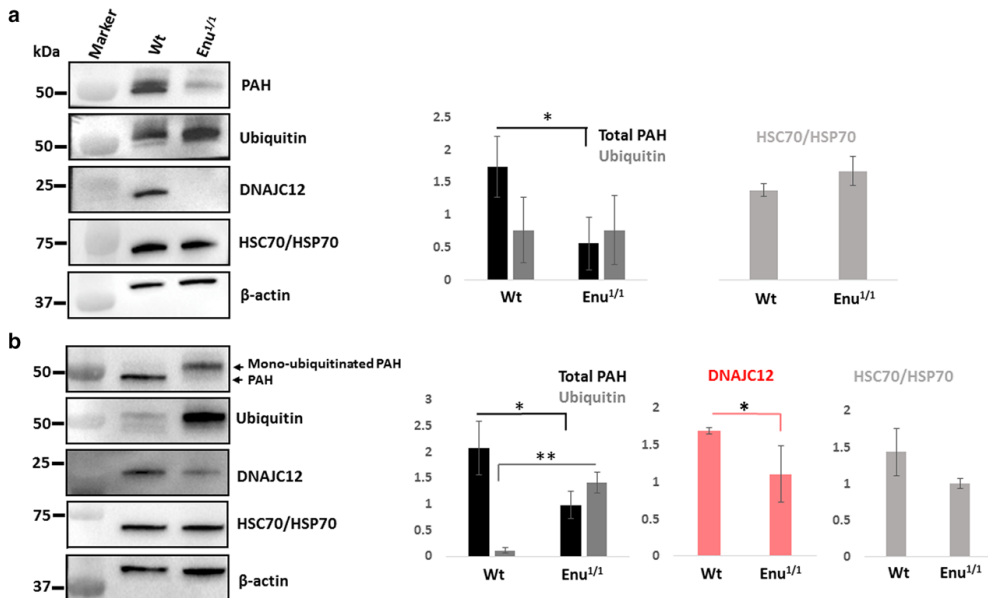


FIGURE 2 Immunodetection of PAH, ubiquitinated protein, DNAJC12, and HSC70/HSP70 from liver lysates of wt and *Enu*^{1/1} mice prepared in PBS buffer (a) and solubilizing buffer (b). β -actin was used as a loading control in both cases ($n = 3$). The histograms in both panels represent immunoquantified protein levels by densitometric analysis; * $p < 0.05$; ** $p < 0.0005$

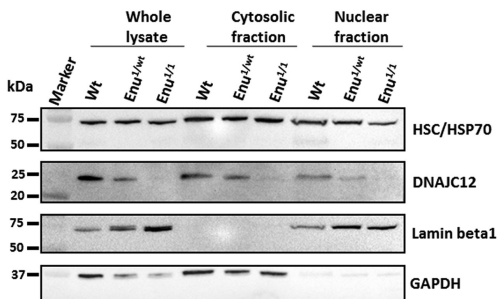


FIGURE 3 Cellular distribution of DNAJC12 and HSC70/HSP70 in wt, *Enu*^{1/wt}, and *Enu*^{1/1} mice. DNAJC12 and HSC70/HSP70 were detected in the whole lysate, nuclear, and cytosolic fractions. The purity of the fractions was tested with lamin beta1 (nuclear fraction marker) and GAPDH (cytosolic fraction marker)

DNAJC12 is mainly a cytoplasmic protein with a minor nuclear localization (Choi, Djebbar, Fournier, & Labrie, 2014), and since nuclear proteins are often poorly detected in whole tissue lysates, we investigated whether a different cytoplasmic/nuclear distribution of DNAJC12 in the normal and HPA mice could explain the different immunodetected levels. The liver lysates of wt, heterozygous *Enu*^{1/wt}, and *Enu*^{1/1} were fractionated into cytosolic and nuclear fractions prior to the SDS-PAGE and immunodetection. Lamin beta 1 and GAPDH were used as the nuclear and cytoplasmic markers, respectively, to validate the purity of the fractions obtained (Figure 3). PAH is mainly

distributed in the cytoplasmic fraction (data not shown), but DNAJC12 was detected in both the cytoplasmic and nuclear fractions, preferentially in the former. The levels of DNAJC12 were in any case strongly reduced in heterozygous mice compared with wt, and almost absent in both fractions in the homozygote *Enu*^{1/1} (Figure 3), which indicated that a change in the subcellular distribution is probably not the main reason for the lack of immunodetected DNAJC12 in *Enu*^{1/1} mice.

We then considered two possibilities for the observed reduction of immunodetected DNAJC12 in the liver lysates of *Enu*^{1/1} mice (Figure 2a): (i) a possible transcriptional down-regulation of the co-chaperone, or (ii) aggregation of the mutant p.V106A-PAH, leading to concomitant aggregation of DNAJC12 in this case complexed with PAH. We proceeded first with analysis of the *Dnajc12*-mRNA level and a few associated genes.

3.3 | Quantification of gene expression of *Pah*, *Dnajc12*, and associated players in liver of wild-type and *Enu*^{1/1} mice

Possible differences in the transcriptional regulation between wt and *Enu*^{1/1} mice were determined by mRNA quantification (RT-qPCR). We measured the mRNA levels of *Dnajc12* and *Pah*, as well as those for other selected genes based on their possible interactions with DNAJC12, including (i) the molecular chaperones Hsp70 (*Hspa1b*), Hsc70 (*Hspa8*), HSF1 (*Hsf1*), and BIP (*Hspa5*), the latter being an endoplasmic reticulum chaperone that is associated with DNAJC12 in situations of cellular stress (Choi et al., 2014), and the

TABLE 1 Relative mRNA quantification for *Dnajc12*-mRNA, *Pah*-mRNA, and other selected genes in liver of wt and *Enu*^{1/1} mice

Gene	<i>Pah</i> genotype	Relative to <i>Dnajc12</i> in wt mice defined as 1	p-Value
<i>Pah</i>	wt/wt	111.99 (86.84 ± 144.42)	0.45
(n = 5)	<i>Enu</i> ^{1/1}	98.14 (74.59 ± 129.13)	
<i>Hspa8 (Hsc70)</i>	wt/wt	415.85 (298.88 ± 578.60)	0.57
(n = 5)	<i>Enu</i> ^{1/1}	374.13 (295.79 ± 473.22)	
<i>Hspa5 (Bip)</i>	wt/wt	237.25 (153.15 ± 367.54)	0.89
(n = 5)	<i>Enu</i> ^{1/1}	250.38 (117.99 ± 531.33)	
<i>Gch1</i>	wt/wt	39.48 (28.74 ± 54.23)	0.83
(n = 11)	<i>Enu</i> ^{1/1}	38.24 (26.03 ± 56.18)	
<i>Esr1</i>	wt/wt	19.77 (10.70 ± 36.53)	0.86
(n = 5)	<i>Enu</i> ^{1/1}	21.25 (10.56 ± 42.79)	
<i>Hsf1</i>	wt/wt	7.35 (5.90 ± 9.15)	0.21
(n = 6)	<i>Enu</i> ^{1/1}	5.90 (4.21 ± 8.27)	
<i>Stub1</i>	wt/wt	4.48 (3.54 ± 5.66)	0.49
(n = 6)	<i>Enu</i> ^{1/1}	3.98 (2.85 ± 5.56)	
<i>Gchfr</i>	wt/wt	3.47 (2.49 ± 4.83)	0.58
(n = 11)	<i>Enu</i> ^{1/1}	3.76 (2.68 ± 5.27)	
<i>Dnajc12</i>	wt/wt	1.00 (0.45 ± 2.23)	0.78
(n = 11)	<i>Enu</i> ^{1/1}	0.82 (0.29 ± 2.29)	
<i>Eef1d</i>	wt/wt	1.11 (1.01 ± 1.23)	0.76
(n = 5)	<i>Enu</i> ^{1/1}	1.07 (0.81 ± 1.41)	
<i>Hspa1b (Hsp70)</i>	wt/wt	0.13 (0.07 ± 0.26)	0.73
(n = 5)	<i>Enu</i> ^{1/1}	0.11 (0.05 ± 0.26)	
<i>Gper1</i>	wt/wt	0.03 (0.02 ± 0.05)	0.61
(n = 11)	<i>Enu</i> ^{1/1}	0.04 (0.02 ± 0.07)	
<i>Esr2</i>	wt/wt	0.02 (0.01 ± 0.02)	0.91
(n = 5)	<i>Enu</i> ^{1/1}	0.02 (0.01 ± 0.02)	

co-chaperone/E3 ubiquitin-protein ligase CHIP (*Stub1*); (ii) the eukaryotic translation elongation factor 1 delta EEF1D (*Eef1d*), which has been found to interact with DNAJC12 in a transcription factor interaction network (Miyamoto-Sato et al., 2010); (iii) the estrogen receptors 1 and 2 ESR1 and 2 (*Esr1*, *Esr2*), and the G protein-coupled estrogen receptor 1 (*Gper1*), which were analyzed because DNAJC12 expression has been associated with estrogen receptor status in breast cancers (De Bessa et al., 2006); and (iv) GTP cyclohydrolase 1 (*Gch1*) and GTP cyclohydrolase 1 feedback regulatory protein (*Gchfr*), which are involved in the synthesis of the PAH-cofactor tetrahydrobiopterin (BH₄). The results are presented in Table 1. *Esr2* was not expressed, *Gper1* was faintly expressed, and *Hsp70* also showed low expression. Both *Dnajc12* and *Pah*, notably the latter, were abundantly expressed in mouse livers, with ~112-fold higher expression of *Pah* with respect to *Dnajc12*, and no difference in the mRNA levels for these two genes between wt and *Enu*^{1/1} samples. Overall, no significant differences on mRNA expression were measured for any of the studied genes upon *Pah* mutation.

3.4 | Immunodetection of PAH, DNAJC12, and HSC70/HSP70, and ubiquitination state of PAH in liver lysates of wild-type and *Enu*^{1/1} mice prepared using improved solubilization conditions

We then investigated whether an intracellular co-aggregation of PAH and DNAJC12 might lead to decreased immunodetection. Aggregated proteins and complexes are often poorly solubilized by 1% SDS and are therefore prone to low detection in SDS-PAGE and Western blotting due to precipitation upon sample preparation, notably under the heat pretreatment (Juenemann, Wiemhoefer, & Reits, 2015). We thus optimized the lysis of liver tissue and sample preparation steps by reducing the ionic strength of the buffers to diminish hydrophobic interactions and favor the extraction and immunodetection of proteins that may form intracellular aggregates. We also included treatment with the non-ionic detergent Triton X-100 (1%) before subjecting the samples to SDS-PAGE (see Section 3.2 for details). Following immunoblotting, it was indeed observed that these conditions lead to the detection of DNAJC12 in the *Enu*^{1/1} liver lysates, at almost similar levels as for the wt mice (Figure 2b). The use of the improved solubilization lysis conditions also resulted in an increased level of immunodetected PAH in the *Enu*^{1/1} mice relative to the wt (Figure 2a,b), but densitometric analysis still revealed the expected reduction of total PAH and the increased proportion of ubiquitinated-PAH in *Enu*^{1/1} when compared to wt mice. Immunoquantification of HSC70/HSP70 showed similar levels of this molecular chaperone in both mice.

3.5 | Expression and distribution of PAH and DNAJC12 analyzed by immunohistochemistry in livers of wild-type and *Enu*^{1/1} mice

Further analyses of the DNAJC12 protein were performed using immunohistochemistry in livers of the wt and *Enu*^{1/1} mice, which also supported a preferential cytoplasmic localization of both PAH and DNAJC12-like immunoreactivities (Figure 4). With the standard protocol in which 0.5% Triton X-100 was included, the PAH signal was largely decreased in the *Enu*^{1/1} livers compared to the wt (Figure 4, a,a1-a3,e,f), whereas DNAJC12, although strongly reduced in the *Enu*^{1/1} mice, was clearly detected (Figure 4, b,b1-b3). Furthermore, despite the fact that higher concentrations of Triton X-100 may alter the organelle integrity and protein distribution, the ability of the detergent to solubilize possible complexes that include DNAJC12 and to facilitate its interaction with the anti-DNAJC12 antibody was investigated. As seen in Figure 4c,c1-c3 and d,d1-d3, treatment with a higher concentration (1%) of Triton X-100 did not alter the relative proportions of PAH-like immunoreactivity, but reduced the difference between levels of DNAJC12-like immunoreactivity in the livers of the wt and *Enu*^{1/1} mice.

3.6 | PAH ubiquitination state and co-immunoprecipitation of DNAJC12

We next performed immunoprecipitation assays to study a possible complex formation between PAH and DNAJC12 in mice liver. PAH was

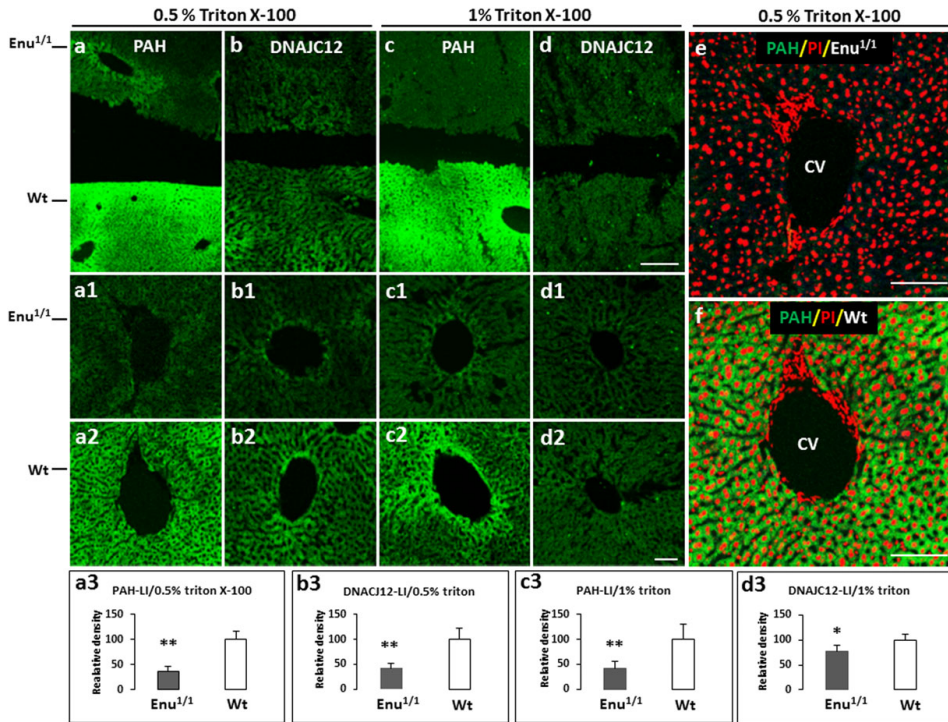


FIGURE 4 Expression of PAH and DNAJC12-like immunoreactivities (LIs) in the liver tissues of *Enu^{1/1}* and *wt* mice. Low-magnification (a–d), high-magnification (a1–d1, a2–d2) and high magnification merged images (e, f). PAH-LI (green; a, a1, a2 and c, c1, c2, e, f) and DNAJC12-LI (green; b, b1, b2 and d, d1, d2) are mainly expressed in the cytoplasm of the liver cells. In the samples processed with 0.5% Triton X-100, significant reduction of PAH and DNAJC12-LIs was observed in *Enu^{1/1}* compared to *wt* (a3, b3). With a higher concentration of Triton X-100 (1%), the relative levels of PAH-LI were not affected (a3, c3) and the level of DNAJC12 was increased in *Enu^{1/1}* and reduced in *wt*, though the difference between both samples was still significant (b3, d3). Hepatocyte nuclei were counterstained with propidium iodide (PI; red; e, f). Lumen like sub-structures are central vein (CV; a1–d1, a2–d2, e, f). Scale bars 250 μ m (a–d) and 75 μ m (a1–d1, a2–d2, e, f)

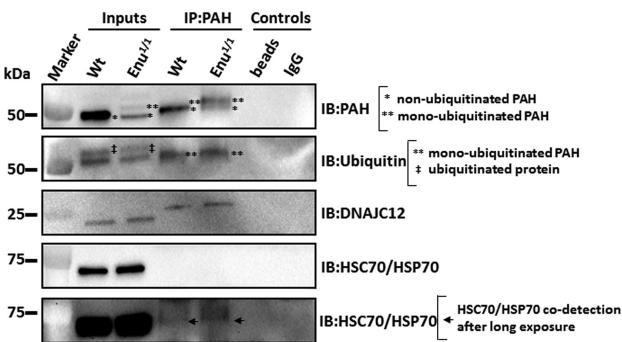


FIGURE 5 Immunoprecipitation (IP) of PAH and co-IP of ubiquitinated proteins, DNAJC12, and HSC70/HSP70 in the livers of the *wt* and *Enu^{1/1}* mice. PAH-IP was performed in liver lysates of *wt* and *Enu^{1/1}* mice prepared at the improved solubilizing conditions (see main text). Ubiquitinated proteins and DNAJC12 were co-detected by immunoblotting (IB) with the indicated antibodies. HSC70/HSP70 was faintly detected as a co-immunoprecipitant and required longer exposure of the blot for the detection. Lysates incubated with only beads and IgGs were used as controls

immunoprecipitated (IP) from liver lysates of *wt* and *Enu^{1/1}* prepared at the improved solubilizing conditions and the samples were examined for PAH, ubiquitination, DNAJC12, and HSC70/HSP70 by Western blot (Figure 5). The IP-PAH in *wt* liver is mainly non-ubiquitinated, but a monoubiquitinated fraction is also present, whereas in the *Enu^{1/1}* mice a similar monoubiquitinated fraction was obtained, which for these mice corresponds with the major IP-PAH form (Figure 5). Fur-

thermore, co-IP DNAJC12 was obtained in the IP-PAH samples from both mice livers. It should be noted that the shift in the band pattern of DNAJC12 in the co-IP sample compared with the migration of the endogenous protein in the input (tissue lysate) (Figure 5) is due to the often observed higher apparent molecular weight for the more purified proteins, as is the case in IP samples. On the other hand, HSC70/HSP70 was faintly immunodetected in the IP-PAH samples (Figure 5), which

suggested that HSC70 and/or HSP70, most probably have transient interactions in complexes with both wt and mutant PAH. Furthermore, all attempts to perform IP of DNAJC12 and detect co-IP PAH were unsuccessful due to the inadequacy of the available DNAJC12 antibodies for this procedure (data not shown).

4 | DISCUSSION

The function of the HSP70 family of molecular chaperones requires the binding both of DNAJ/HSP40 co-chaperones that stimulate the ATPase activity and facilitate client capture and of nucleotide exchange factors that promote the dissociation of the ADP and the release of the client protein (Dekker et al., 2015; Kampinga & Craig, 2010). The binding of DNAJ to the HSP70s involves the conserved His-Pro-Asp motif in the J-domain, and this interaction is a requirement for the function of the molecular chaperones. Stimulation of ATP hydrolysis by HSP70s as well as the coordination of client binding for proper folding, refolding, and release, are considered to be the main functions of the DNAJ/HSP40 proteins. However, as more DNAJ proteins are characterized, their varied involvement in many aspects of proteostatic control, in addition to folding, is being revealed, including protection of misfolded clients from aggregation and contribution to the ubiquitination and delivery of terminally misfolded proteins to the ubiquitin-proteasome or autophagy systems for degradation (Kampinga & Craig, 2010; Kraft et al., 2010; Shiber & Ravid, 2014; Zarouchlioti, Parfitt, Li, Gittings, & Cheetham, 2018).

Except for the common J-domain (Hageman & Kampinga, 2009; Kampinga et al., 2009), the large number of DNAJ proteins (50 annotated DNAJ/HSP40 proteins compared with the 11 HSC70/HSP70s as of October 2018) present a highly variable sequence that contributes to the additional role of these proteins. In particular, type III (class C) DNAJ-proteins present very little sequence similarity or domain sharing, which seems to be associated to a high selectivity in client binding. DNAJC12 was earlier classified as a DNAJ protein with client-independent function (Kampinga & Craig, 2010), but its interaction with the AAAHs and its important role in proper folding of PAH has recently been demonstrated (Anikster et al., 2017). Our present results provide additional insights into the DNAJC12 role on PAH folding. By analyzing a number of PAH variants associated with HPA/PKU of different severity, we observed a moderate positive correlation between the immunodetected contents of soluble PAH and DNAJC12. Subsequent immunodetection of PAH and DNAJC12 levels in both wt and *Enu*^{1/1} mice, the latter expressing the unstable and misfolded p.V106A-PAH variant (Gersting et al., 2010), contributed to reveal the mechanisms behind the correlation. Thus, the immunodetected content of both proteins increased in the mutant mice upon application of solubilizing conditions to prepare the liver lysates, strongly indicating a co-aggregation of DNAJC12 both in lysates of COS-7 cells expressing unstable PAH variants and in liver lysates of *Enu*^{1/1} mice. Furthermore, the IP and co-IP experiments with *Enu*^{1/1} mice liver lysates showed an interaction of DNAJC12 with the monoubiquitinated PAH variant, pointing to a major role of the co-chaperone in targeting the degradation of misfolded PAH.

It has been suggested that the proteostatic pathways in disease states differ from those in the normal cellular cycles (Klaips, Jayaraj, & Hartl, 2018). Our results, on the other hand, suggest that— notwithstanding an increased aggregation and accelerated degradation for the PAH mutants (Figures 1 and 2)—the pathways may be similar for both normal and variant PAH, since lysates from wt mice, in addition to their specific major non-ubiquitinated PAH form, also present monoubiquitinated PAH at comparable levels as for the *Enu*^{1/1} mice. Quantification of *Dnajc12*- and *Pah*-mRNA levels (Table 1) supports a much lower expression of DNAJC12 compared with PAH, as also indicated by the relation of protein levels (Figure 4). This lower expression of DNAJC12 may be associated to a regulatory role of the co-chaperone in the folding/degradation of PAH. Together with ubiquitination, DNAJC12 binding may determine the upper value for the degradation-competent fraction of PAH, contributing to regulate the steady-state levels of this enzyme, as also described for DNAJB members interacting with wild-type and mutants of parkin (Kakkar, Kuiper, Pandey, Braakman, & Kampinga, 2016). One can expect a challenged proteostatic regulation in *Enu*^{1/1} liver, biased toward the degradation of ubiquitinated misfolded mutant PAH, which recruits most of the available DNAJC12.

The fact that DNAJC12 was co-immunoprecipitated with monoubiquitinated IP-PAH from the *Enu*^{1/1} liver also provides information on the possible mechanism for the degradation of PAH. The general mechanism for the DNAJ- and HSC70/HSP70-assisted degradation of misfolded client proteins with a tendency to aggregate is believed to be the recognition of the non-ubiquitinated misfolded client by the DNAJ followed by the recruitment of the HSP70 machinery (Dekker et al., 2015; Houck, Singh, & Cyr, 2012). This phase is actually similar to the complex formation for folding or refolding of the clients. However, in the case of misfolding, CHIP or other specific E3-ubiquitin ligases can be recruited to the complex for polyubiquitination and targeting to the proteasome or, if the aggregation is severe, to the autophagy system (Dekker et al., 2015; Houck et al., 2012; Kampinga & Craig, 2010; Shiber & Ravid, 2014). Nevertheless, there is also evidence that DNAJ proteins can recognize and bind clients that are already mono- or polyubiquitinated, or that may be ubiquitinated while bound to the co-chaperone, previous to complex formation with the HSP70 machinery for further polyubiquitination (Dekker et al., 2015; Kampinga & Craig, 2010; Shiber, Breuer, Brandeis, & Ravid, 2013). In particular, if the client tends to aggregate, it is expected that the DNAJ:ubiquitinated-client complexes are more stable. On the other hand, the dynamic complexes that engage HSP70 present a quick dissociation of the HSPs and release the client toward degradation as fast as the ATP is hydrolyzed (Misselwitz, Staeck, Matlack, & Rapoport, 1999). Thus, these complexes including DNAJ:client:HSP70 are very transient, unstable, and difficult to isolate and characterize (Alderson, Kim, & Markley, 2016; Malinverni, Jost Lopez, De Los Rios, Hummer, & Barducci, 2017), probably explaining that in our IP experiments we mainly isolated the stable DNAJC12:monoubiquitinated PAH complexes, whereas HSP70 is only present in a minor proportion in the immunoprecipitated sample (Figure 5).

The direct interaction of DNAJ proteins with ubiquitinated clients has been studied for DNAJB2 (alternatively known as HSJ1),

which has an important role determining the fate of the clients prior to the interaction with HSP70 and sorting to the proteasome (Kampinga & Craig, 2010; Westhoff, Chapple, van der Spuy, Hohfeld, & Cheetham, 2005). The selectivity of DNAJB2 toward mono- and polyubiquitinated clients is provided by its ubiquitin interacting motifs (UIMs). DNAJC12 does not have a canonical UIM, and it is therefore not possible to speculate if it has an inherent higher affinity for ubiquitinated-PAH than for non-ubiquitinated-PAH. DNAJC12 is actually one of the shortest DNAJ proteins and does not contain identifiable domains other than the J-domain (Kampinga & Craig, 2010). Further structural and biophysical studies on the interaction between DNAJC12 and PAH and the other AAAHs are required to increase our understanding on the selectivity and the mechanisms for folding and degradation of these clients, both in health and in AAAH-associated diseases (Blau et al., 2018; Bouchereau et al., 2018; Straniero et al., 2017).

Knowledge on the proteostatic pathways and the chaperone networks that regulate the intracellular stability of PAH appears to be essential to understand how the system is affected by PKU-associated mutations and other factors. Because PKU is known to be a complex trait disease (Scriver & Waters, 1999), it is expected that mutations and polymorphisms in genes that control the intracellular stability of PAH, such as DNAJC12, may contribute to understanding the deviations from the general genotype-phenotype correlations in PKU. Not much is yet known about the interactions of DNAJC12 with the proteasome and autophagy systems, and such knowledge may promote the research on novel therapies for disorders associated to the AAAHs. Nevertheless, previous attempts to regulate HSP40 and HSP70 levels pharmacologically have not been very successful and have shown the complexity of the proteostatic regulation in health and disease, as well as particular differences for each disease (Labbadia & Morimoto, 2015). Specifically, whereas DNAJC12 has been shown to be upregulated by endoplasmic reticulum stress (Choi et al., 2014), which is known to induce protein misfolding and aggregation, this upregulation has not been observed for cellular stress in general (Vleminckx et al., 2002). In this work, we did not observe upregulation of either *Dnajc12* or *Hspa1b* expression (Table 1), which may indicate a mild stress effect caused by the *enu1* allele.

In conclusion, the present work showed the tight interaction of DNAJC12 with ubiquitinated, mutant PAH, which indicated the involvement of DNAJC12 in the degradation of PAH. Based on the myriad of different mechanisms by which the DNAJ-proteins can regulate the ubiquitination and degradation of proteins by the proteasome and/or autophagy, further studies are necessary to demonstrate the detailed mechanisms and interactions between DNAJC12 and the AAAHs clients at the molecular level. The work also reveals the complex quality control system implicated in the intracellular stability of PAH and contributes to the understanding of this disease as a complex trait disease.

ACKNOWLEDGMENTS

This work was supported by Research Council of Norway grants FRIMEDBIO 261826/F20 and FORNY 248889/O30, the K.G. Jeb-

sen Centre for Neuropsychiatric Disorders, and the Western Norway Regional Health Authorities (Helse-Vest project 912246) (to A.M.), and by the FP7-HEALTH-2012-INNOVATION-1 EU Grant No. 305444 (to N.B.).

CONFLICTS OF INTEREST

The authors have no conflict of interest to declare.

ORCID

Nenad Blau  <https://orcid.org/0000-0003-4347-3230>

Aurora Martinez  <https://orcid.org/0000-0003-1643-6506>

REFERENCES

- Alderson, T. R., Kim, J. H., & Markley, J. L. (2016). Dynamical structures of Hsp70 and Hsp70-Hsp40 complexes. *Structure (London, England)*, 24(7), 1014–1030.
- Anikster, Y., Haack, T. B., Vilboux, T., Pode-Shakked, B., Thony, B., Shen, N., ... Schiff, M. (2017). Biallelic mutations in DNAJC12 cause hyperphenylalaninemia, dystonia, and intellectual disability. *American Journal of Human Genetics*, 100(2), 257–266.
- Björge, E., Knappskog, P. M., Martínez, A., Stevens, R. C., & Flatmark, T. (1998). Partial characterization and three-dimensional-structural localization of eight mutations in exon 7 of the human phenylalanine hydroxylase gene associated with phenylketonuria. *European Journal of Biochemistry*, 257(1), 1–10.
- Blau, N., Martínez, A., Hoffmann, G. F., & Thony, B. (2018). DNAJC12 deficiency: A new strategy in the diagnosis of hyperphenylalaninemia. *Molecular Genetics and Metabolism*, 123(1), 1–5.
- Bouchereau, J., Huttlin, E. L., Guarani, V., Pichard, S., Anikster, Y., & Schiff, M. (2018). DNAJC12: A molecular chaperone involved in proteostasis, PKU, biogenic amines metabolism and beyond? *Molecular Genetics and Metabolism*, 123(3), 285–286.
- Choi, J., Djebbar, S., Fournier, A., & Labrie, C. (2014). The co-chaperone DNAJC12 binds to Hsc70 and is upregulated by endoplasmic reticulum stress. *Cell Stress & Chaperones*, 19(3), 439–446.
- De Bessa, S. A., Salaorni, S., Patrao, D. F., Neto, M. M., Brentani, M. M., & Nagai, M. A. (2006). JDP1 (DNAJC12/Hsp40) expression in breast cancer and its association with estrogen receptor status. *International Journal of Molecular Medicine*, 17(2), 363–367.
- Dekker, S. L., Kampinga, H. H., & Bergink, S. (2015). DNAJs: More than substrate delivery to HSPA. *Frontiers in Molecular Biosciences*, 2, 35.
- Doskeland, A. P., & Flatmark, T. (1996). Recombinant human phenylalanine hydroxylase is a substrate for the ubiquitin-conjugating enzyme system. *Biochemical Journal*, 319(Pt 3), 941–945.
- Eichinger, A., Danecka, M. K., Moglich, T., Borsch, J., Woidy, M., Buttner, L., ... Gersting, S. W. (2018). Secondary BH4 deficiency links protein homeostasis to regulation of phenylalanine metabolism. *Human Molecular Genetics*, 27(10), 1732–1742.
- Fernandez-Fernandez, M. R., Gragera, M., Ochoa-Ibarrola, L., Quintana-Gallardo, L., & Valpuesta, J. M. (2017). Hsp70: A master regulator in protein degradation. *FEBS Letters*, 591(17), 2648–2660.
- Fitzpatrick, P. F. (2015). Structural insights into the regulation of aromatic amino acid hydroxylation. *Current Opinion in Structural Biology*, 35, 1–6.
- Gersting, S. W., Lagler, F. B., Eichinger, A., Kemter, K. F., Danecka, M. K., Messing, D. D., ... Muntau, A. C. (2010). Pahenu1 is a mouse model for tetrahydrobiopterin-responsive phenylalanine hydroxylase deficiency

- and promotes analysis of the pharmacological chaperone mechanism in vivo. *Human Molecular Genetics*, 19(10), 2039–2049.
- Gregersen, N. (2006). Protein misfolding disorders: Pathogenesis and intervention. *Journal of Inherited Metabolic Disease*, 29(2–3), 456–470.
- Hageman, J., & Kampinga, H. H. (2009). Computational analysis of the human HSPH/HSPA/DNAJ family and cloning of a human HSPH/HSPA/DNAJ expression library. *Cell Stress & Chaperones*, 14(1), 1–21.
- Himmelreich, N., Shen, N., Okun, J. G., Thiel, C., Hoffmann, G. F., & Blau, N. (2018). Relationship between genotype, phenylalanine hydroxylase expression and in vitro activity and metabolic phenotype in phenylketonuria. *Molecular Genetics and Metabolism*, 125(1–2), 86–95. <https://doi.org/10.1016/j.jmgme.2018.06.011>
- Houck, S. A., Singh, S., & Cyr, D. M. (2012). Cellular responses to misfolded proteins and protein aggregates. *Methods in Molecular Biology*, 832, 455–461.
- Huttlin, E. L., Ting, L., Bruckner, R. J., Gebreab, F., Gygi, M. P., Szpyt, J., ... Gygi, S. P. (2015). The BioPlex network: A systematic exploration of the human interactome. *Cell*, 162(2), 425–440.
- Juenemann, K., Wiemhoefer, A., & Reits, E. A. (2015). Detection of ubiquitinated huntingtin species in intracellular aggregates. *Frontiers in Molecular Neuroscience*, 8, 1.
- Kakkar, V., Kuiper, E. F. E., Pandey, A., Braakman, I., & Kampinga, H. H. (2016). Versatile members of the DNAJ family show Hsp70 dependent anti-aggregation activity on RING1 mutant parkin C289G. *Scientific Reports*, 6, 34830.
- Kampinga, H. H., & Craig, E. A. (2010). The HSP70 chaperone machinery: J proteins as drivers of functional specificity. *Nature Reviews Molecular Cell Biology*, 11(8), 579–592.
- Kampinga, H. H., Hageman, J., Vos, M. J., Kubota, H., Tanguay, R. M., Bruford, E. A., ... Hightower, L. E. (2009). Guidelines for the nomenclature of the human heat shock proteins. *Cell Stress & Chaperones*, 14(1), 105–111.
- Kaushik, S., & Cuervo, A. M. (2012). Chaperones in autophagy. *Pharmacological Research*, 66(6), 484–493.
- Klaips, C. L., Jayaraj, G. G., & Hartl, F. U. (2018). Pathways of cellular proteostasis in aging and disease. *Journal of Cell Biology*, 217(1), 51–63.
- Kraft, C., Peter, M., & Hofmann, K. (2010). Selective autophagy: Ubiquitin-mediated recognition and beyond. *Nature Cell Biology*, 12(9), 836–841.
- Labbadia, J., & Morimoto, R. I. (2015). The biology of proteostasis in aging and disease. *Annual Review of Biochemistry*, 84, 435–464.
- Leandro, J., Simonsen, N., Saraste, J., Leandro, P., & Flatmark, T. (2011). Phenylketonuria as a protein misfolding disease: The mutation pG465 in phenylalanine hydroxylase promotes self-association and fibril formation. *Biochimica Et Biophysica Acta*, 1812(1), 106–120.
- Malinverni, D., Jost Lopez, A., De Los Rios, P., Hummer, G., & Barducci, A. (2017). Modeling Hsp70/Hsp40 interaction by multi-scale molecular simulations and coevolutionary sequence analysis. *Elife*, 6, pii: e23471; <https://doi.org/10.7554/eLife.23471>
- McDonald, J. D., & Charlton, C. K. (1997). Characterization of mutations at the mouse phenylalanine hydroxylase locus. *Genomics*, 39(3), 402–405.
- Misselwitz, B., Staack, O., Matlack, K. E., & Rapoport, T. A. (1999). Interaction of BiP with the J-domain of the Sec63p component of the endoplasmic reticulum protein translocation complex. *Journal of Biological Chemistry*, 274(29), 20110–20115.
- Miyamoto-Sato, E., Fujimori, S., Ishizaka, M., Hirai, N., Masuoka, K., Saito, R., ... Yanagawa, H. (2010). A comprehensive resource of interacting protein regions for refining human transcription factor networks. *Plos One*, 5(2), e9289.
- Okano, Y., Kudo, S., Nishi, Y., Sakaguchi, T., & Aso, K. (2011). Molecular characterization of phenylketonuria and tetrahydrobiopterin-responsive phenylalanine hydroxylase deficiency in Japan. *Journal of Human Genetics*, 56(4), 306–312.
- Pey, A. L., Desviat, L. R., Gamez, A., Ugarte, M., & Perez, B. (2003). Phenylketonuria: Genotype-phenotype correlations based on expression analysis of structural and functional mutations in PAH. *Human Mutation*, 21(4), 370–378.
- Pey, A. L., Stricher, F., Serrano, L., & Martinez, A. (2007). Predicted effects of missense mutations on native-state stability account for phenotypic outcome in phenylketonuria, a paradigm of misfolding diseases. *American Journal of Human Genetics*, 81(5), 1006–1024.
- Pratt, W. B., Morishima, Y., Peng, H. M., & Osawa, Y. (2010). Proposal for a role of the Hsp90/Hsp70-based chaperone machinery in making triage decisions when proteins undergo oxidative and toxic damage. *Experimental Biology and Medicine (Maywood, NJ)*, 235(3), 278–289.
- Sarkissian, C. N., Boulais, D. M., McDonald, J. D., & Scriver, C. R. (2000). A heteroallelic mutant mouse model: A new orthologue for human hyperphenylalaninemia. *Molecular Genetics and Metabolism*, 69(3), 188–194.
- Sarkissian, C. N., Ying, M., Scherer, T., Thony, B., & Martinez, A. (2012). The mechanism of BH4-responsive hyperphenylalaninemia—as it occurs in the ENU1/2 genetic mouse model. *Human Mutation*, 33(10), 1464–1473.
- Scherer, T., Allegri, G., Sarkissian, C. N., Ying, M., Grisch-Chan, H. M., Rassi, A., ... Thony, B. (2018). Tetrahydrobiopterin treatment reduces brain L-Phe but only partially improves serotonin in hyperphenylalaninemic ENU1/2 mice. *Journal of Inherited Metabolic Disease*, 41(4), 709–718.
- Scriver, C. R., & Waters, P. J. (1999). Monogenic traits are not simple: Lessons from phenylketonuria. *Trends in Genetics*, 15(7), 267–272.
- Shen, N., Heintz, C., Thiel, C., Okun, J. G., Hoffmann, G. F., & Blau, N. (2016). Co-expression of phenylalanine hydroxylase variants and effects of interallelic complementation on in vitro enzyme activity and genotype-phenotype correlation. *Molecular Genetics and Metabolism*, 117(3), 328–335.
- Shiber, A., Breuer, W., Brandeis, M., & Ravid, T. (2013). Ubiquitin conjugation triggers misfolded protein sequestration into quality control foci when Hsp70 chaperone levels are limiting. *Molecular Biology of the Cell*, 24(13), 2076–2087.
- Shiber, A., & Ravid, T. (2014). Chaperoning proteins for destruction: Diverse roles of Hsp70 chaperones and their co-chaperones in targeting misfolded proteins to the proteasome. *Biomolecules*, 4(3), 704–724.
- Skjærven, L., Teigen, K., & Martinez, A. (2014). *Structure-function relationships in the aromatic amino acid hydroxylases enzyme family: Evolutionary insights*. eLS. Chichester, United Kingdom: John Wiley & Sons.
- Straniero, L., Guella, I., Cilia, R., Parkkinen, L., Rimoldi, V., Young, A., ... Duga, S. (2017). DNAJC12 and dopa-responsive nonprogressive parkinsonism. *Annals of Neurology*, 82(4), 640–646.
- van Spronsen, F. J., Himmelreich, N., Rufenacht, V., Shen, N., Vliet, D. V., Al-Owain, M., ... Thöny, B. (2017). Heterogeneous clinical spectrum of DNAJC12-deficient hyperphenylalaninemia: From attention deficit to severe dystonia and intellectual disability. *Journal of Medical Genetics*, pii: jmedgenet-2017-104875; <https://doi.org/10.1136/jmedgenet-2017-104875>
- Veenna, D., Cordeiro, D., Sondheimer, N., & Mercimek-Andrews, S. (2018). DNAJC12-associated developmental delay, movement disorder, and mild hyperphenylalaninemia identified by whole-exome sequencing re-analysis. *European Journal of Human Genetics*, 26, 1867–1870.
- Vlemminckx, V., Van Damme, P., Goffin, K., Delye, H., Van Den Bosch, L., & Robberecht, W. (2002). Upregulation of HSP27 in a transgenic model of ALS. *Journal of Neuro pathology and Experimental Neurology*, 61(11), 968–974.

- Waløen, K., Kleppe, R., Martinez, A., & Haavik, J. (2017). Tyrosine and tryptophan hydroxylases as therapeutic targets in human disease. *Expert Opinion on Therapeutic Targets*, 21(2), 167–180.
- Waters, P. J., Parniak, M. A., Akerman, B. R., & Scriver, C. R. (2000). Characterization of phenylketonuria missense substitutions, distant from the phenylalanine hydroxylase active site, illustrates a paradigm for mechanism and potential modulation of phenotype. *Molecular Genetics and Metabolism*, 69(2), 101–110.
- Westhoff, B., Chapple, J. P., van der Spuy, J., Hohfeld, J., & Cheetham, M. E. (2005). HSF1 is a neuronal shuttling factor for the sorting of chaperone clients to the proteasome. *Current Biology*, 15(11), 1058–1064.
- Wettstein, S., Underhaug, J., Perez, B., Marsden, B. D., Yue, W. W., Martinez, A., & Blau, N. (2015). Linking genotypes database with locus-specific database and genotype-phenotype correlation in phenylketonuria. *European Journal of Human Genetics*, 23(3), 302–309.
- Zarouchlioti, C., Parfitt, D. A., Li, W., Gittings, L. M., & Cheetham, M. E. (2018). DNAJ proteins in neurodegeneration: Essential and protective factors. *Philosophical Transactions of the Royal Society of London. Series B: Biological Sciences*, 373(1738).

SUPPORTING INFORMATION

Additional supporting information may be found online in the Supporting Information section at the end of the article.

How to cite this article: Jung-KC K, Himmelreich N, Prestegård KS, et al. Phenylalanine hydroxylase variants interact with the co-chaperone DNAJC12. *Human Mutation*. 2019;40: 483–494. <https://doi.org/10.1002/humu.23712>

PAPER II

The Pah-R261Q mouse reveals oxidative stress associated with amyloid-like hepatic aggregation of mutant phenylalanine hydroxylase.






Oscar Aubi, Karina S. Prestegård, Kunwar Jung-KC, Tie-Jun Sten Shi, Ming Ying, Ann Kari Grindheim, Tanja Scherer, Arve Ulvik, Adrian McCann, Endy Spriet, Beat Thöny, Aurora Martinez

Nat Commun. 12(1):2073. doi: 10.1038/s41467-021-22107-1 (2021)

Abstract

Phenylketonuria (PKU) is caused by autosomal recessive variants in phenylalanine hydroxylase (PAH), leading to systemic accumulation of L-phenylalanine (L-Phe) that may reach neurotoxic levels. A homozygous Pah-R261Q mouse, with a highly prevalent misfolding variant in humans, reveals the expected hepatic PAH activity decrease, systemic L-Phe increase, L-tyrosine and L-tryptophan decrease, and tetrahydrobiopterin-responsive hyperphenylalaninemia. Pah-R261Q mice also present unexpected traits, including altered lipid metabolism, reduction of liver tetrahydrobiopterin content, and a metabolic profile indicative of oxidative stress. Pah-R261Q hepatic tissue exhibits large ubiquitin-positive, amyloid-like oligomeric aggregates of mutant PAH that colocalize with selective autophagy markers. Together, these findings reveal that PKU, customarily considered a loss-of-function disorder, can also have toxic gain-of-function contribution from protein misfolding and aggregation. The proteostasis defect and concomitant oxidative stress may explain the prevalence of comorbid conditions in adult PKU patients, placing this mouse model in an advantageous position for the discovery of mutation-specific biomarkers and therapies.

The *Pah-R261Q* mouse reveals oxidative stress associated with amyloid-like hepatic aggregation of mutant phenylalanine hydroxylase

Oscar Aubi ^{1,4}, Karina S. Prestegård ^{1,4}, Kunwar Jung-KC ¹, Tie-Jun Sten Shi¹, Ming Ying¹, Ann Kari Grindheim¹, Tanja Scherer², Arve Ulvik³, Adrian McCann³, Endy Spriet¹, Beat Thöny ² & Aurora Martinez ¹✉

Phenylketonuria (PKU) is caused by autosomal recessive variants in phenylalanine hydroxylase (*PAH*), leading to systemic accumulation of L-phenylalanine (L-Phe) that may reach neurotoxic levels. A homozygous *Pah-R261Q* mouse, with a highly prevalent misfolding variant in humans, reveals the expected hepatic *PAH* activity decrease, systemic L-Phe increase, L-tyrosine and L-tryptophan decrease, and tetrahydrobiopterin-responsive hyperphenylalaninemia. *Pah-R261Q* mice also present unexpected traits, including altered lipid metabolism, reduction of liver tetrahydrobiopterin content, and a metabolic profile indicative of oxidative stress. *Pah-R261Q* hepatic tissue exhibits large ubiquitin-positive, amyloid-like oligomeric aggregates of mutant *PAH* that colocalize with selective autophagy markers. Together, these findings reveal that PKU, customarily considered a loss-of-function disorder, can also have toxic gain-of-function contribution from protein misfolding and aggregation. The proteostasis defect and concomitant oxidative stress may explain the prevalence of comorbid conditions in adult PKU patients, placing this mouse model in an advantageous position for the discovery of mutation-specific biomarkers and therapies.

¹Department of Biomedicine, University of Bergen, Bergen, Norway. ²Division of Metabolism, University Children's Hospital Zürich and Children's Research Centre, Zürich, Switzerland. ³Bevital AS, Laboratoriebygget, Bergen, Norway. ⁴These authors contributed equally: Oscar Aubi, Karina S. Prestegård ✉email: aurora.martinez@uib.no

Phenylketonuria (PKU; MIM261600) is an autosomal recessive inborn error of metabolism characterized by the inability to break down the amino acid L-phenylalanine (L-Phe). PKU is primarily caused by mutations in the human *PAH* gene (NM_000277.2) encoding phenylalanine hydroxylase (PAH; EC 1.14.16.1). PAH is a tetrameric, non-heme iron aromatic amino acid hydroxylase that catalyzes the hydroxylation of L-Phe to L-tyrosine (L-Tyr) using molecular oxygen as additional substrate and the cofactor (6R)-5,6,7,8-tetrahydrobiopterin (BH₄)^{1,2}. This is the rate-limiting step in the catabolic degradation of L-Phe, which occurs predominantly in the cytoplasm of hepatic cells. A consequence of deficient PAH catalysis is the accumulation of L-Phe in the blood and ultimately in the brain of untreated patients, causing growth retardation, intellectual disability, and behavioral and neuropsychiatric disorders³. PKU has a prevalence of approximately 1:10,000 livebirths worldwide and can be classified, based on the off-diet blood L-Phe concentrations, as mild hyperphenylalaninemia (HPA) (120–600 μmol/L), mild PKU (600–1200 μmol/L), and classic PKU (>1200 μmol/L)³. The low-Phe diet is the cornerstone of PKU/HPA management and prevents the most severe consequences of the disease. However, controlled studies have shown that early treated PKU patients present several psychiatric disturbances as adults, notably depression and anxiety-related disorders⁴. Moreover, recent investigations have revealed an elevated risk of comorbidities with unexplained etiology in both early- and late-treated adult PKU patients, with a high prevalence of cardiovascular and renal diseases and overweight^{5,6}. In the last years, many new treatments for PKU have been approved or are in clinical development⁷. A fraction of patients typically with mild and moderate *PAH* mutations are responsive to synthetic formulations of BH₄ (Sapropterin, Kuvan®), which is often used in combination with a less restrictive diet⁸. Notwithstanding the considerable amount of accumulated knowledge on PKU, there is a need for a more profound mechanistic and pathophysiological understanding of the disease, as well as novel therapies. These required studies would greatly benefit from the availability of useful model organisms.

Mouse (*Mus musculus*) models are a powerful research tool owing to the small size, high reproductive rate, and relative ease of genetic manipulation, compared to other mammals, and are therefore most commonly selected to study human disease⁹. There are evident differences between mice and humans, primarily related to evolutionary divergences, for instance in size, metabolic rate, life expectancy, and immune system, but overall, the genetic and physiological similarities are high⁹. The first generation of mouse models of PKU were created by phenotype-driven N-ethyl-N-nitrosourea (*ENU*) germline mutagenesis. In this manner, three HPA/PKU mouse models have previously been established; namely, (i) *Enu1* (*enu*¹ allele), with the p.V106A-PAH mutation, located in the PAH regulatory domain¹⁰; (ii) *Enu2* (*enu*² allele), with the p.F263S-PAH mutation, located in the catalytic domain¹⁰; and (iii) *Enu3* (*enu*³ allele), with a splice site mutation generating frameshifted amino acids and premature termination codon¹¹. *Enu2* and *Enu3* mice exhibit high blood L-Phe concentrations (>1200 μmol/L) and appear as suitable models for severe, classic PKU, with a total absence of PAH activity albeit normal protein stability (*Enu2*), or total absence of expressed PAH protein and activity (*Enu3*)¹¹. In contrast, *Enu1* mice present reduced PAH stability and thus decreased steady-state levels of PAH protein and enzymatic activity (approximately 5% of normal controls), leading to mild HPA¹². The available mouse models have undoubtedly contributed to a better understanding of PKU at a biochemical and behavioral level and have allowed testing of novel therapies such as enzyme substitution¹³ or genome base editing¹⁴. An increasing body of evidence

indicates that PKU is a prototypic genetic conformational disorder wherein the principal pathogenic determinant is the degree of PAH protein instability caused by the specific mutations¹⁵. The available strains do not adequately represent this primary pathogenic mechanism (*Enu2* and *Enu3*) or include murine mutations that are non-existent or low recurrent in the human *PAH* gene (*Enu1*), prompting us to generate a PKU mouse model with a common *PAH* mutant associated with protein misfolding.

There are over 1100 registered human PAH variants (<http://www.biopku.org/>), among which the nucleotide aberration c.782 G > A in *Pah* exon 7 coding for p.Arg261Gln (p.R261Q) mutation seems to be an optimal candidate to generate a knock-in mouse model. The *R261Q* mutation is one of the most abundant among PKU patients, with an average allele frequency of approx. 6% (9–14% in Mediterranean countries and the Middle East) and ~2% of patients homozygous for this mutation (up to 12% in Mediterranean countries and the Middle East)^{15,16} (<http://www.biopku.org/>). The associated phenotype when in homozygosity, exhibits an unusual and unexplained variability from mild PKU to classic PKU, with approximately 78% of the patients being responsive to BH₄^{15–17} (<http://www.biopku.org/>). The *R261Q* mutation has been predicted¹⁵ and indeed proven to result in unstable and misfolded PAH^{18,19}.

Hence, in the reported custom-made mouse model, the mutation c.782G > A was introduced in the *Pah* gene by CRISPR/Cas9 technology based on the use of programmable nucleases as a tool for targeted gene-editing, which is an efficacious and precise genome engineering method²⁰. In this work, we present the generation and metabolic, biochemical and biological characterization of this *Pah-R261Q* knock-in mouse line. The results obtained highlight (i) the robustness of this mouse model as a general archetype for mild HPA associated with PAH instability and misfolding, and (ii) the observation of large amyloid-like aggregates of mutant (p.R261Q-PAH) *in vivo*, which appears associated to the observed proteostasis dysregulation, oxidative stress and additional comorbidities. Overall, the *Pah-R261Q* mouse model paves the way for new exploratory avenues of research and treatment.

Results

Generation, genotyping, and breeding of *Pah-R261Q* mice.

There is a high PAH sequence homology (92.5% identity) between mouse and human PAHs, with Arg261 being in an evolutionarily conserved region (Supplementary Fig. 1a). Structurally, the residue Arg261 establishes several intra- and inter-subunit H-bonding and electrostatic contacts in the dimers that are crucial to maintaining the stability of the protein as well as proper oligomeric configuration^{21,22} (detailed in Supplementary Fig. 1b, c). The mutation p.R261Q is thus expected to trigger disruption of this interaction network and, as seen in expression analyses in different systems, elicit an unstable protein^{18,19,23} without substantially affecting the catalytic efficiency of the folded tetramer¹⁹.

The custom-made mouse model with the p.R261Q-PAH mutation was generated by CRISPR/Cas9 genome editing technology, as schematically represented in Supplementary Fig. 2a, and proven to have the correct genotype (Supplementary Fig. 2b, c). The designed primers for genotyping amplified a 537 bp polymerase chain reaction (PCR) product, which, after restriction fragment analysis with endonuclease BsmI, made it possible to discriminate electrophoretically between *Pah*^{WT/WT} (2 fragments: 294 and 243 bp), homozygous *Pah*^{R261Q/R261Q} (3 fragments: 243, 171, and 123 bp), and heterozygous *Pah*^{R261Q/WT} (4 fragments: 294, 243, 171, and 123 bp) mice (Supplementary Fig. 2c). There is evidence that BLAST hits with three or more total nucleotide mismatches have a low probability of off-target effects, specifically if two of these mismatches are situated in the

seed region²⁴. In any case, we evaluated all 16 candidate loci susceptible to being secondarily affected by the guide RNA sequence (Supplementary Table 1). These genes were subjected to heteroduplex analysis, all showing wild-type sequence, with no detection of off-target interactions.

A retrospective examination of the maternal genotype effect in the breeding revealed no abnormalities between homozygous *Pah^{R261Q/R261Q}* mice (referred to as *Pah-R261Q*) and *Pah^{WT/WT}* (*WT*) mice with respect to litters per mated female (3.7 ± 0.6 vs. 4.0) and progeny per litter (7.1 ± 0.4 vs. 7.0)²⁵. Furthermore, the compilation of historical data confirmed the expected offspring genotypic distribution as predicted by Mendelian laws.

***Pah-R261Q* mice exhibit mild HPA, higher body weight in the case of males, and reduced respiratory exchange ratio.** *Pah-R261Q* mice presented a small but significant increase in basal blood L-Phe levels, measured in dried blood spots in 3-month old mice ($108.0 \pm 36.6 \mu\text{M}$, $n = 23$ mice) compared to both *WT* ($59.9 \pm 7.7 \mu\text{M}$, $n = 9$; $p < 0.0001$) and heterozygous *Pah^{R261Q/WT}* ($71.22 \pm 21.86 \mu\text{M}$; $n = 6$; $p = 0.0201$), analyzed by Brown–Forsythe and Welch ANOVA test followed by Dunnett’s multiple comparisons tests. Source data are provided as a Source Data file. The blood L-Phe level in *Pah-R261Q* corresponds to very mild HPA in human subjects. In contrast to the *Enu2* PKU mouse model, which presents weight and length reduction, hypopigmentation, behavioral, and neurological problems²⁶, *Pah-R261Q* were no different from their heterozygote and *WT* counterparts in length, pigmentation, and behavior. Three-month-old male *Pah-R261Q* mice, however, were heavier than their *WT* counterparts (27.8 ± 0.4 vs. 25.1 ± 0.3 g, respectively) (Fig. 1a). *Pah-R261Q* females were as expected lighter than males and were not different in weight than their *WT* counterparts (22.1 ± 1.6 vs. 21.1 ± 1.4 g, respectively). Apart from the higher body weight in mutant males, we did not find gender-associated variations for any other parameter or metabolite measured in this work; thus, the mice groups for each experiment included evenly distributed males and females.

Various physiological murine parameters were controlled for the 48 h metabolic cage examinations for *WT* and *Pah-R261Q* (12 h acclimatization and 36 h of measured observations). The amount of food intake was equal (Fig. 1b), and no significant changes in activity and movement patterns were identified (Fig. 1c). However, the rates of O_2 consumption and CO_2 production normalized to body mass (VO_2 and VCO_2 , respectively) were both decreased for *Pah-R261Q* compared with *WT* (Fig. 1d and Supplementary Fig. 3a, b), and the calculated respiratory exchange ratio ($\text{RER} = \text{VCO}_2/\text{VO}_2$) was also slightly lower for *Pah-R261Q* than for *WT* (0.988 ± 0.087 vs. 1.014 ± 0.093 ; the average for the total 36 h experimentation) (Fig. 1e, inset). *RER* values are approximately 1.0, 0.8, and 0.7 for carbohydrates, proteins, and fat, respectively, as sole metabolic fuel²⁷. Nevertheless, in heavy activity periods *RER* increases and reaches values >1.28 , and *RER* values reflect metabolic fuel utilization more accurately during periods of rest or mild exercise²⁹. During the 12 h resting period, *RER* was closer to 0.8 for *Pah-R261Q* and 1 for *WT* mice (Fig. 1e), indicating a higher utilization of fat and protein as a fuel source during this period among the mutant mice³⁰. The decreased *RER* at rest also contributed to lower energy expenditure in the same period compared with *WT* mice, even for non-weight-normalized values (Fig. 1f), although this difference did not translate into significantly lower energy expenditure for the mutant mice per day.

Metabolic characterization of *Pah-R261Q* mice show lipid metabolism alterations and oxidative stress. Detailed metabolic profiling of *Pah-R261Q* compared with *WT* mice was performed

by measuring 72 relevant metabolic biomarkers in extracted blood serum samples from the results obtained are presented in Supplementary Table 2. Table 1 summarizes the individual values for the 17 metabolites displaying differences at $p < 0.1$ level, with either higher or lower blood serum concentrations for *Pah-R261Q* compared to *WT*. This p value was selected to avoid type II error due to the limited sample size.

A blood serum L-Phe concentration in the mutant mice corresponding to very mild HPA ($113 \pm 22 \mu\text{M}$ vs. $71.9 \pm 10.3 \mu\text{M}$ for *WT*) was obtained in this study, similar to the values obtained from dried blood spots (see above). As seen in Table 1, the increased serum L-Phe was accompanied by decreased levels of L-Trp and L-Tyr, markers of the HPA phenotype, as well as decreased quinolinic acid and a trend for reduced kynurenine, both downstream metabolites of L-Trp. Interestingly, serum trimethyllysine, leucine, and isoleucine, which have been shown to increase in adiposity and altered lipid metabolism in humans³¹, were elevated in *Pah-R261Q* (Table 1). Moreover, increased β -hydroxybutyrate is also an established biomarker associated with impaired glucose homeostasis, diabetes, and defense against oxidative stress^{32,33}. Also, other serum metabolites observed in lower concentrations in *Pah-R261Q* have previously been linked to oxidative stress and immune function, such as α -ketoglutaric acid, glutamic acid, and quinolinic acid^{34–37}. These biomarkers are tightly associated metabolically to creatine and methylmalonic acid, and to the amino acids aspartic acid, alanine, glutamine, and proline, all with decreased trends (Table 1).

The incorporation of these metabolites to the Krebs cycle—a central hub of metabolism—through anaplerotic reactions is increased in situations of oxidative and cellular stress³⁸. Furthermore, the reduction in anaplerotic metabolites and increase in β -oxidation in *Pah-R261Q* are in agreement with increased utilization of proteins and fats as an energy source, as also inferred by the lower resting-state *RER* in these mice compared to *WT* (Fig. 1e). We acknowledge that the use of a high, explorative p value cutoff ($p < 0.1$) may have generated spurious hits among the metabolite biomarkers. However, we believe that the approach is justified by the overall coherence of the findings that support lipidic metabolic alterations and oxidative stress in the *Pah-R261Q* mice, in addition to the expected mild HPA.

***Pah-R261Q* mice show no apparent neurological alteration but a remarkable decrease of hepatic BH_4 .** The elapsed time for a mouse to maintain its balance on a rotating rod is a good indicator of possible neurological deficits, as shown for the *Enu2* mouse³⁹. As illustrated in Supplementary Fig. 3c, *Pah-R261Q* had comparable performance to *WT* on the rotarod test, supporting that the *PAH* mutation has no impact in neuromuscular function or motor coordination, at least for young mice. We also corroborated no alterations in the levels of aromatic amino acids L-Phe, L-Tyr, and L-Trp (Supplementary Table 3) and monoamine neurotransmitters (Fig. 2a) in the brain. In addition, as seen in Fig. 2, we confirmed no significant difference in the total levels of BH_4 in the brain, where BH_4 acts as a cofactor of the other aromatic amino acid hydroxylases tyrosine hydroxylase (TH) and tryptophan hydroxylase 2 (TPH2) and of neuronal nitric oxide synthase (NOS)². However, the concentration of BH_4 in the liver, where it acts as the essential cofactor for the hydroxylating *PAH* reaction, showed a startling 50% reduction in *Pah-R261Q* (28.0 ± 1.7 pmol BH_4/mg protein) compared with *WT* mice (56.2 ± 3.2 pmol/mg) (Fig. 2b).

***Pah-R261Q* mice are sensitive to L-Phe challenge concomitant with BH_4 responsive hyperphenylalaninemia.** When we administered *Pah-R261Q* mice an L-Phe challenge—equivalent to the

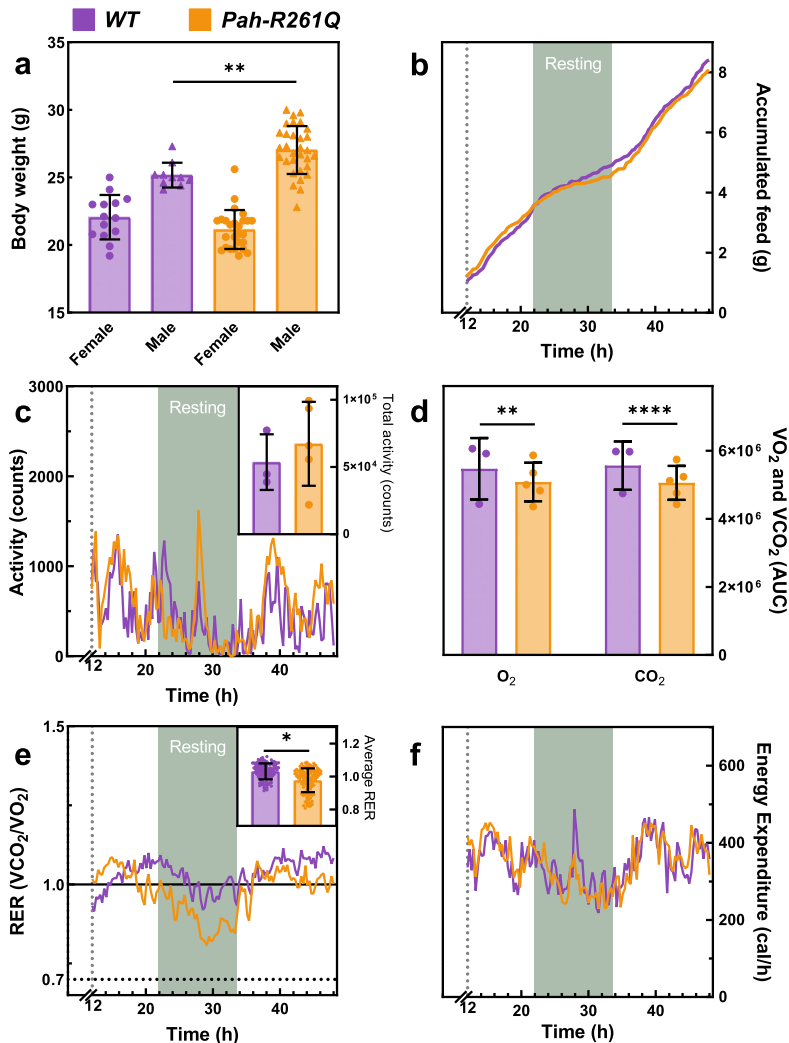


Fig. 1 Physiological and metabolic characterization of *Pah-R261Q* compared with WT mice. **a** Bodyweight distribution by sex and genotype. The weight of WT mice (controls) was in agreement with averaged registered data (<https://www.jax.org/strain/000664>). Data are presented as mean \pm SD, with individual values plotted as circles (females) and triangles (males) ($n = 10$ WT male, 14 WT female, 31 *Pah-R261Q* male, 26 *Pah-R261Q* female mice). Statistical significance for the weight difference for males in the two groups was calculated by two-tailed unpaired t test; $p = 0.0031$ (**). **b–f** Metabolic cage experiments, performed for 48 h, with 12 h of acclimation followed by 36 h of recordings. $n = 3$ WT and 5 *Pah-R261Q* mice in independent experiments, with one mouse per cage and 121 observations/animal. **b** Cumulative feed consumption (g). **c** Mice activity with continuous recording, expressed as mean \pm SD. Inset, total activity for each mouse group presented as mean \pm SD, individual values are plotted as circles. **d** Total Volume of O_2 consumed and volume of CO_2 produced for each mice type, obtained from the integration of the area under the curve (AUC) from data in Supplementary Fig. 3. Data are presented as the mean AUC \pm SD, with individual values plotted as circles. Statistical significance for the difference between both mice groups was calculated by two-tailed unpaired t test; $p = 0.0011$ (***) for O_2 and $p < 0.0001$ (****) for CO_2 . **e** Respiratory exchange ratio (RER) along the recording time. Inset: averaged RER presented as mean \pm SD; the circles represent mean for the group at each time point. Statistical significance for differences between both groups was calculated by two-tailed unpaired t test; $p < 0.0001$ (****). **f** Energy expenditure obtained by indirect calorimetry expressed as mean \pm SD. In all panels, the data for WT are depicted in purple and *Pah-R261Q* in ochre. Source data are provided as a Source Data file.

L-Phe loading test that is applied to HPA/PKU patients for their phenotypic classification⁴⁰—a transient but very prominent elevation of blood L-Phe values was observed. As shown in Supplementary Fig. 4, 40 min after i.p. injection with 200 μ g L-Phe/g body weight, *Pah-R261Q* mice presented a massive increase in

L-Phe concentrations ($990 \pm 220 \mu$ M), before returning to basal levels ca. 300 min later. A similar L-Phe challenge caused much lower increases of L-Phe concentrations in heterozygous and WT mice (Supplementary Fig. 4). The transient L-Phe-increase in *Pah-R261Q* mice allowed us to investigate the response to

Table 1 Blood serum concentrations of the metabolites whose levels were increased/decreased in *Pah-R261Q* mice in respect to the control *WT* group. Concentrations are expressed as arithmetic mean \pm SD; $n = 19$ *WT* and 19 *Pah-R261Q* mice.

Metabolite (name)	WT (μ M)	<i>Pah-R261Q</i> (μ M)	Difference	p Value (MW) ^a
Phenylalanine	71.9 (10.3)	113 (22)	41.1	0.000004
β -Hydroxybutyrate	150 (99)	282 (133)	132	0.029
Trimethyllysine	0.803 (0.165)	0.976 (0.213)	0.173	0.050
Leucine	143 (23)	164 (42)	21	0.075
Isoleucine	87.5 (12.8)	101 (24)	13.5	0.091
α -Ketoglutaric acid	38.6 (15.2)	26.3 (10.8)	-12.3	0.003
Glutamic acid	39.5 (20.7)	29.4 (10.2)	-10.1	0.008
Alanine	444 (71)	362 (80)	-82	0.010
Tryptophan	103 (24)	82.9 (30.9)	-20.1	0.013
Quinolinic acid	0.178 (0.090)	0.130 (0.041)	-0.48	0.023
Creatine	154 (40)	127 (30)	-27	0.026
Aspartic acid	27.4 (14.4)	22.7 (11.0)	-4.7	0.043
Glutamine	687 (76)	622 (112)	-65	0.043
Tyrosine	81.3 (25.3)	77.9 (14.0)	-3.4	0.050
Methylmalonic acid	0.701 (0.095)	0.585 (0.118)	-0.116	0.060
Kynurenine	0.740 (0.234)	0.573 (0.264)	-0.167	0.080
Proline	90.2 (25.4)	73.0 (17.2)	-17.2	0.085

^aTwo-tailed p values for differences between serum concentration in *WT* and *Pah-R261Q* mice were obtained from Mann Whitney (MW) U test. See also Supplementary Table 2.

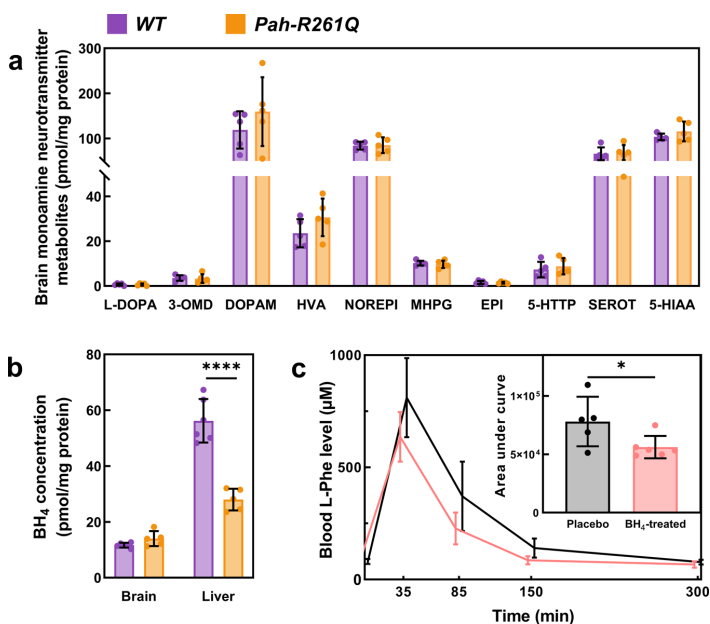


Fig. 2 Neurotransmitter and BH₄ content, and BH₄-responsiveness in the *Pah-R261Q* mouse model. **a** Monoamine neurotransmitter content in brain lysates; data are presented as mean \pm SD, individual values are plotted as circles ($n = 5$ *WT* and 5 *Pah-R261Q* mice). Abbreviations (from left to right): levodopa, 3-ortho-methylidopa, dopamine, homovanillic acid, norepinephrine, 3-methyl-4-hydroxyphenylglycol, epinephrine, 5-hydroxytryptophan, serotonin, and 5-hydroxyindoleacetic acid. **b** BH₄ determination in whole brain and liver lysates, presented as mean \pm SD, individual values are plotted as circles ($n = 6$ *WT* and 5 *Pah-R261Q*). Statistical significance for the difference in brain BH₄ content between both groups was calculated by two-tailed unpaired t test; $p < 0.0001$ (****). **c** Blood L-Phe concentration after L-Phe challenge in placebo-control (black) and BH₄-treated (pink) *Pah-R261Q* mice ($n = 5$ placebo and 6 treated mice). L-Phe (200 μ g L-Phe/g body weight) was administered by i.p. at time 0 and L-Phe concentration was monitored at 0, 35, 90, 150, and 300 min. The BH₄ treated mice received (by i.p.) 20 mg/kg BH₄ in 2% ascorbic acid and 10% DMSO, for 4 days, twice a day, previous to L-Phe administration, and the placebo control received the same solution without BH₄. Data are presented as mean \pm SD. Inset, area under the curve (AUC) for the time dependence of L-Phe concentration between 0 and 300 min for placebo and BH₄-treated groups. Individual values are represented by circles. Statistical significance for the difference between both groups was calculated by two-tailed unpaired t test; $p = 0.0299$ (*). In panels **a** and **b** the data for *WT* are depicted in purple and for *Pah-R261Q* in ochre. Source data are provided as a Source Data file.

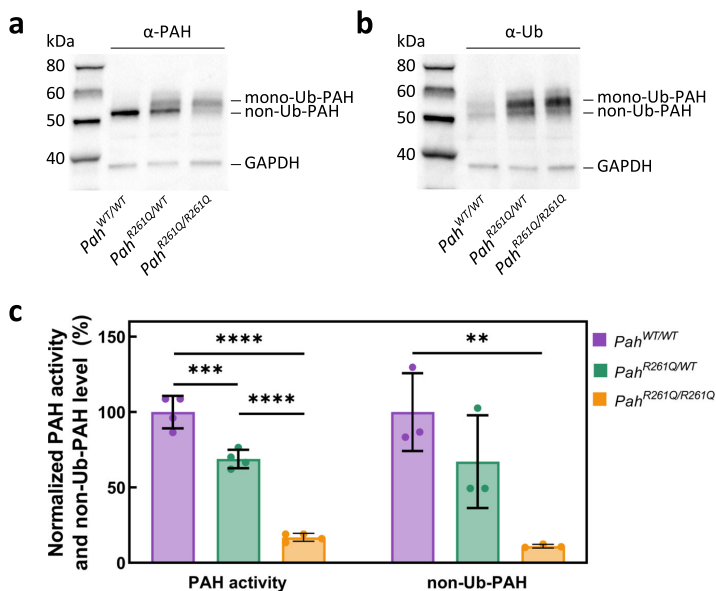


Fig. 3 PAH content in liver lysates of homozygous and heterozygous *Pah-R261Q* mice. **a** Western blots for immunodetection of PAH (α -PAH) (**a**) and ubiquitinated protein (α -Ub) (**b**) showing the decrease in non-ubiquitinated PAH (non-Ub-PAH; -51 kDa band) and increase of mono-ubiquitinated PAH (mono-Ub-PAH; -56 kDa) from genotype *Pah*^{WT/WT} to *Pah*^{R261Q/WT} to *Pah*^{R261Q/R261Q}. The blots are representative from $n = 3$ replicates for each mice group. GAPDH was used as loading control. **c** Overview of relative PAH specific activity normalized to activity in *Pah*^{WT/WT} liver lysates (23.2 ± 2.4 nmol L-Tyr/min/mg protein) ($n = 4$ mice for each genotype) and non-Ub-PAH protein (51 kDa) levels from densitometric analysis normalized to both *Pah*^{WT/WT} liver lysates as well as to GAPDH loading control ($n = 3$ mice for each genotype). Data are presented as mean \pm SD for *Pah*^{WT/WT} (purple), *Pah*^{R261Q/WT} (green), and *Pah*^{R261Q/R261Q} (ochre), individual values are represented as circles. Differences between genotypes were analyzed by one-way ANOVA followed by Tukey test; differences in PAH activity, $p = 0.0005$ (***) for *Pah*^{WT/WT} vs. *Pah*^{R261Q/WT}, $p < 0.0001$ (****) for both *Pah*^{WT/WT} vs. *Pah*^{R261Q/R261Q} and *Pah*^{R261Q/WT} vs. *Pah*^{R261Q/R261Q}; differences in PAH level, $p = 0.0080$ (**) for *Pah*^{WT/WT} vs. *Pah*^{R261Q/R261Q}. Source data are provided as a Source Data file.

BH₄-treatment. As seen in Fig. 2c, significantly lower blood L-Phe level was measured after an L-Phe challenge (200 μ g/kg body weight) was administered following a BH₄ treatment (20 mg/kg body weight for 4 days, twice a day⁴¹), compared with placebo. BH₄ treatment resulted in a 28% decrease in L-Phe content as calculated from the area under the curve (Fig. 2c, inset). Patients with the R261Q mutation in homozygosity present variable HPA phenotype but about 74% are positive responders to BH₄ treatment (<http://www.biopku.org/>), and the results with the mutant mice are consistent with the BH₄-responsive phenotype.

Hepatic p.PAH-R261Q protein presents increased ubiquitination and aggregation.

After the investigation of the metabolic status of *Pah-R261Q* mice, we also studied the effect of the mutation on the function and stability of PAH in the mouse liver. Immunodetection by Western blot of the PAH protein (p.R261-PAH and WT-PAH, for the mutant and WT proteins, respectively) in liver lysates showed the typical 51-kDa PAH band for WT mice, and two PAH bands at 51- and 56-kDa for the heterozygous *Pah*^{R261Q/WT} and homozygous *Pah*^{R261Q/R261Q} (*Pah-R261Q*) mutant mice (Fig. 3a). The 56-kDa PAH band, present in both mice with the mutant allele, was recognized by the anti-ubiquitin antibody (Fig. 3b). This band has been identified as mono-ubiquitinated PAH in previous studies with *Enu1* and *Enu1/2* HPA mouse models^{42,43}. The 51-kDa non-ubiquitinated PAH band was strongly reduced in *Pah-R261Q*, as best observed in the immunodetected PAH levels normalized to WT control

mice (Fig. 3c). We also measured PAH activity in the liver lysates, and for each genotype, the relative specific activity correlated well with the relative levels of non-ubiquitinated PAH protein in liver lysates (Fig. 3c). Nevertheless, the results with *Pah-R261Q* ($11.6 \pm 1.5\%$ non-ubiquitinated protein vs. $16.9 \pm 3.3\%$ specific activity, both relative to WT) support low level of PAH activity for the ubiquitinated enzyme.

The reduction of total p.R261Q-PAH protein levels and increased ubiquitination observed by Western blot in *Pah-R261Q* compared to WT mice, indicative of instability and misfolding of this PAH variant (Fig. 3a, b), was followed-up by immunofluorescence staining of hepatic tissue which confirmed a substantial reduction in PAH protein in *Pah-R261Q* (Fig. 4). The specificity of the PAH antibody was further proven by an antigen pre-adsorption test showing almost complete loss of PAH immunoreactivity in hepatic tissue of WT mice after incubation with PAH antibody preabsorbed with purified recombinant PAH (Supplementary Fig. 5). Moreover, the immunofluorescence images of *Pah-R261Q* revealed scattered PAH-immunoreactivity in discrete bright points, consistent with aggregation, as well as an increase in ubiquitination signal that presented substantial colocalization with mutant PAH (Fig. 4). To investigate the mutation dependent PAH misfolding and aggregation, we also performed immunofluorescence of hepatic tissue of the *Enu1* mouse model of mild HPA, which expresses the unstable p.V106A-PAH variant, also associated with PAH instability, leading to a considerable decrease of functional PAH in the liver (5% of WT)^{42,44,45}. *Enu1* liver also presented largely decreased

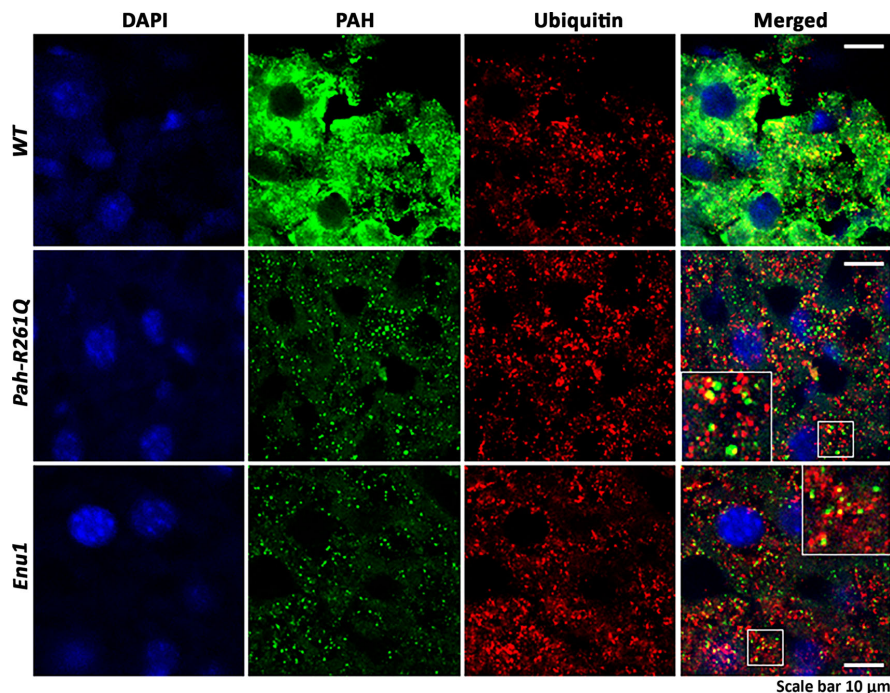


Fig. 4 Distribution of PAH in hepatic tissue of WT and mouse models *Pah-R261Q* and *Enu1*. Immunofluorescence of PAH and ubiquitin (Ub) detection in hepatic tissue of WT, *Pah-R261Q*, and *Enu1* mice, revealing the distribution pattern of PAH (green) and Ub (red). PAH was strongly reduced in both *Enu1* and *Pah-R261Q* when compared to WT, whereas Ub was highly expressed in both mutant mice. The micrographs are representative for $n = 3$ biological replicates in each mice group. The fluorescence intensity (mean \pm SD) calculated in 14 stacks of confocal images, relative to WT (=1), was 0.264 ± 0.105 (*Pah-R261Q*) and 0.154 ± 0.029 (*Enu1*) for PAH, and 1.315 ± 0.035 (*Pah-R261Q*) and 1.405 ± 0.103 (*Enu1*) for Ub. Colocalization of PAH and ubiquitin (yellow) was observed in both mutant mice, as highlighted in the inset. DAPI was used for nuclear staining (blue). Source data are provided as a Source Data file.

and particulate PAH-immunoreactivity and increased ubiquitination. There were, however, differences in the aggregation pattern of mutant PAH between both HPA-mouse models (Fig. 4) as well as in the size of the PAH aggregates, larger in *Pah-R261Q* than in *Enu1*.

We further studied the distribution of PAH aggregates between the nucleus and the cytoplasm in hepatic cells. The use of the nuclear pore marker Nup98 and 3D-rendering of the stacks of confocal images revealed that the smaller aggregates of mutant PAH in *Enu1* appeared more ubiquitously distributed in hepatocytes, where they are also present in the nucleus (Fig. 5a). On the other hand, the PAH aggregates in *Pah-R261Q* did not show nuclear localization and appear distributed at the cytoplasmic side of the nuclear membrane (Fig. 5a). As fluorescence detection may alter the shape and size of macromolecules and complexes, we also performed immunohistochemistry (IHC) with optical detection by DAB staining in order to assess the size of the mutant PAH aggregates in hepatic tissue (Fig. 5b, c). The averaged area of DAB-stained particles was 0.18 ± 0.06 and 0.11 ± 0.03 (SD) μm^2 for *Pah-R261Q* and *Enu1*, respectively (Fig. 5c).

Amyloid-like aggregation of p.PAH-R261Q. The different size and nucleocytoplasmic distribution of the aggregates of p.R261Q and p.V106A PAH variants in *Pah-R261Q* and *Enu1* livers, respectively, suggests different misfolding and aggregation mechanisms for these two mutants. As larger aggregates,

especially those with amyloid aggregation, can be cytotoxic⁴⁶, we investigated if the mutant protein p.R261Q-PAH could aggregate through cross- β -sheet prone motives around the mutation site. Positively, in silico evaluation with the program TANGO⁴⁷ predicted a high (>50%) propensity to form intermolecular cross- β (amyloid-like) aggregates in region 254–263 in the mutant (FLGGLAFQVF), while the same region in the WT sequence (FLGGLAFRVF) was not predicted to be prone to amyloid-like aggregation (Supplementary Fig. 1), for both the human and mouse PAH sequences. We tested the propensity of all PAH missense variants registered at BIOPKU (<http://www.biopku.org>), and also included p.V106A-PAH (*Enu1*), which is very rare in human⁴⁸. The calculations supported a high susceptibility to undergo this type of aggregation for a few variants, i.e., p.E78V, p.N167Y, p.P211L, p.R261G, and p.E390G, all rare, but not for p.V106A (*Enu1*).

To confirm the formation of amyloid-like aggregates by the mutant p.R261Q-PAH we used the Amytracker[®] 680 fluorescence assay with purified recombinant mutant protein. An accelerated formation of amyloid-like aggregates was observed for p.R261Q-PAH compared to WT-PAH (Supplementary Fig. 6a). After 5 h incubation, parallel samples of p.R261Q-PAH without Amytracker were visualized by transmission electron microscopy (TEM). Imaging revealed larger amorphous aggregates of a diameter up to >100 nm, together with small aggregates of about 20 nm diameter, whereas fibrillary structures were not observed (Supplementary Fig. 6b).

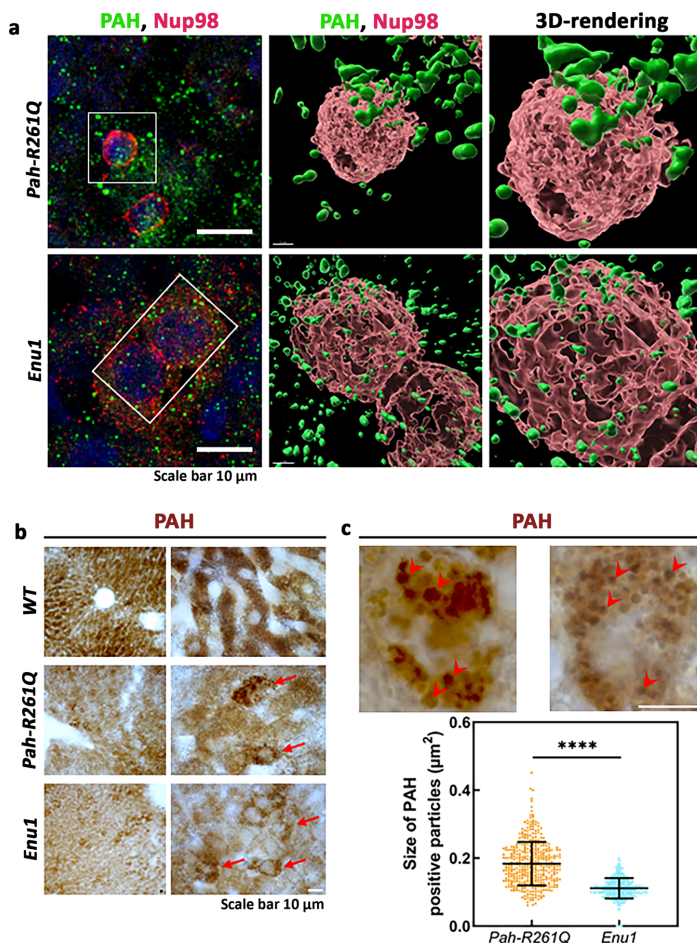


Fig. 5 Nuclear distribution of mutant PAH protein in *Pah-R261Q* and *Enu1* mice liver. a Immunofluorescence of PAH (green) and the nuclear pore marker Nup98 (red) in hepatic tissue of *Enu1* and *Pah-R261Q* mice (left panels), and 3D-rendering of stacks of confocal images using the surface tool in Imaparis software at two different magnifications (middle and right panels). The images reveal the subcellular distribution of PAH in the nucleus and cytoplasm of *Enu1* mice, whereas in *Pah-R261Q* mice PAH is distributed in the cytoplasm. Hoechst was used for nuclear staining (blue). **b** Immunohistochemically DAB-stained hepatocytes from *WT*, *Pah-R261Q* and *Enu1* mice at low (left panels) and high (right panels) magnification. Arrows indicate PAH immunoreactive hepatocytes in *Pah-R261Q* and *Enu1* mice. **a, b** The micrographs are representative of $n = 3$ biological replicates in each mice group. **c** Two representative PAH immunoreactive hepatocytes at higher magnification in *Pah-R261Q* (left) and *Enu1* (right) mice are shown, where arrowheads point to PAH-positive particle-like structures. Measurement of PAH particle size was performed in 30 μm -thick liver sections ($n = 10$) for each mice. At least 400 single PAH-positive particles in randomly selected regions of liver sections from each mice group were analyzed, and the size distribution of PAH-positive particles in *Pah-R261Q* and *Enu1* hepatocytes is shown (lowest panel). Data are presented as mean \pm SD and each dot represents a PAH-positive particle. The difference in size is statistically significant, as calculated by the two-tailed unpaired *t* test; P value < 0.0001 (****). Source data are provided as a Source Data file.

PAH aggregates in *Pah-R261Q* mice colocalize with autophagy markers and are associated with oxidative stress. Larger aggregates are commonly processed by autophagy rather than by the ubiquitin-dependent proteasome system (UPS)⁴⁹. We thus performed immunofluorescence microscopy of liver samples of *WT*, *Pah-R261Q*, and *Enu1* mice with autophagy markers Ser403-phosphorylated p62 protein (p62/SQSTM1 (sequestosome-1)), a selective receptor and marker for autophagic clearance^{50,51}. The level of phosphorylated p62 (P-p62) was indeed much higher in *Pah-R261Q* than in *Enu1* mice, which presented similar immunodetected levels as in *WT* mice (Fig. 6a). Immunofluorescence

staining with the standard marker for autophagosomes LC3 was also increased in *Pah-R261Q*, but not in *Enu1*, compared with *WT* (Fig. 6b). Both autophagy markers P-p62 and LC3 presented colocalization with mutant PAH in *Pah-R261Q* mice (Fig. 6a, b). These results suggest that the larger PAH aggregates in *Pah-R261Q*, but not the smaller aggregates in *Enu1*, engage the autophagic system. Moreover, we also performed TEM imaging of hepatic tissue, which showed hepatocytes with normal cell and organelle morphology in *Pah-R261Q* and no abnormality in nuclei or the nuclear membrane (Supplementary Fig. 7a). We noticed an increased number of lysosomes and of autophagic structures,

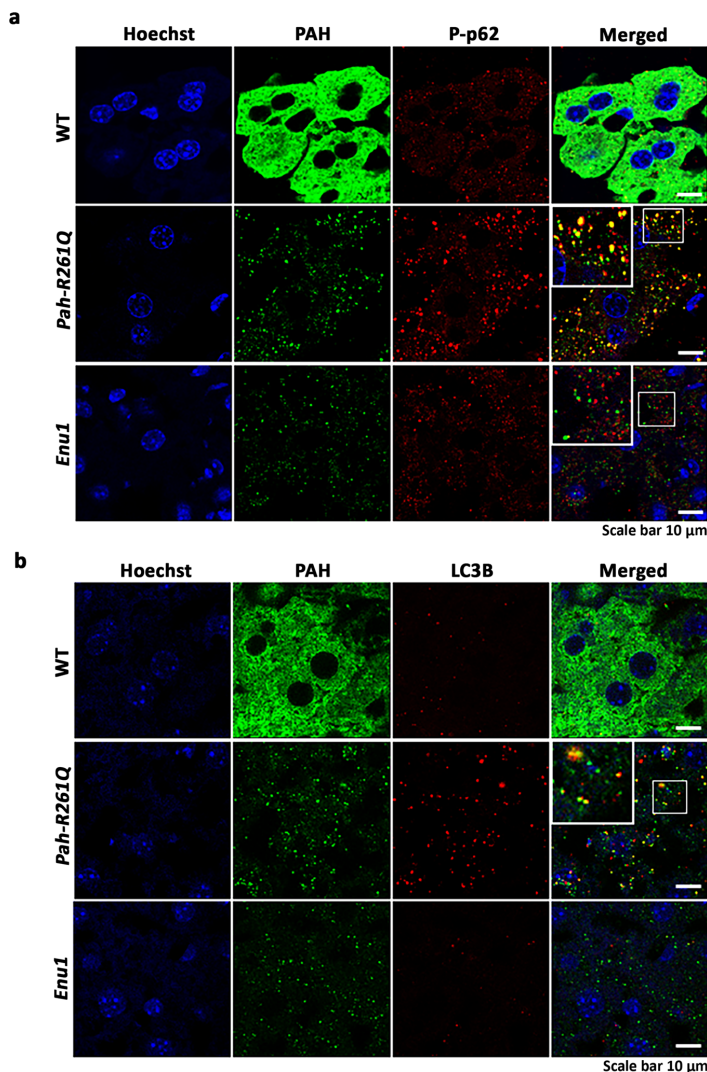


Fig. 6 Colocalization of mutant PAH in *Pah-R261Q* mice with autophagic markers. Immunofluorescence micrographs showing the codistribution of PAH (green) with autophagy markers p62 phosphorylated at Ser403 (P-p62, red) in **(a)** or LC3 (red) in **(b)** in hepatic tissue from WT, *Pah-R261Q* and *Enu1* mice. Both markers were increased in *Pah-R261Q* when compared to both WT and *Enu1*. The fluorescence intensity (mean \pm SD) calculated in 14 stacks of confocal images, relative to WT (=1), was 1.326 ± 0.121 (*Pah-R261Q*) and 0.778 ± 0.158 (*Enu1*) for P-p62 **(a)**, and 2.277 ± 0.174 (*Pah-R261Q*) and 1.535 ± 0.175 (*Enu1*) for LC3 **(b)**. *Pah-R261Q* but not WT or *Enu1* showed clear colocalization (yellow) of PAH with both P-p62 **(a)** and LC3 **(b)**, as highlighted in the insets. Hoechst was used for nuclear staining (blue). All micrographs are representative for $n = 3$ biological replicates in each mice group. Source data are provided as a Source Data file.

i.e., double-membrane autophagosomes and autolysosomes (Supplementary Fig. 7b) and exhaustive counting of these structures confirmed that they were increased in *Pah-R261Q* compared to WT mice whereas no difference in the number of peroxisomes and lipid drops was found (Supplementary Fig. 7c).

The nuclear quality control system customarily collaborates on the degradation of misfolded cytoplasmic proteins and small aggregates⁵². However, larger aggregates may hinder nuclear uptake⁴⁶, leading to toxic accumulation of the aggregates in the cytoplasm, saturation of the autophagy system, and increased oxidative stress^{49,53}. For some aggregation disorders associated

with the formation of amyloid fibrils by Tau, such as polyglutamine diseases, AD and Tau-dementia, invaginations or indentations of the nuclear membrane, filled by fibrillary rods, as well as nuclear pore pathology are observed^{54,55}. These alterations are also observed in ALS/FTD caused by aggregation of TDP-43 in non-fibrillary oligomeric amyloid-like aggregates⁵⁶ and seem related with the interference of the proteins with the nucleocytoplasmic system, e.g., microtubules in the case of Tau⁵⁴ or the nuclear transport machinery in the case of TDP-43⁵⁶, resulting in the invaginations. The lack of nuclear invaginations in *Pah-R261Q* is in accordance with the non-fibrillary nature of the PAH

aggregates and with PAH being a cytoplasmic enzyme with no known functional association with the nucleocytoplasmic system.

Despite a lack of significant disturbances in nuclear morphology in *Pah-R261Q*, it appears that the aggregates of p.R261Q-PAH do not enter the nucleus (Fig. 5a), which can be associated with overload of the cytoplasmic quality control system and oxidative stress. We measured the total equivalent antioxidant capacity (TEAC) in liver lysates of both HPA models (*Enu1* and *Pah-R261Q*) and *WT* mice by the Trolox assay. *Pah-R261Q* but not *Enu1* presented elevated TEAC values compared with *WT* (Supplementary Fig. 8), indicating a specific upregulation of the antioxidant response in *Pah-R261Q* mice in agreement with the metabolic changes associated with oxidative stress (see above and Table 1).

Gene (mRNA) expression assays. Finally, ten genes related to the PAH system, protein quality control, and oxidative stress pathways were selected and subjected to analysis by quantitative TaqMan mRNA expression in liver extracts (RT-qPCR; results overview in Table 2). In absolute terms, *Pah* and *Hsc70* showed the highest levels of gene expression. Comparatively, for *Pah-R261Q* vs. *WT* mice, we found the following: (i) *Pah* expression was not altered; (ii) expression of the *GCH1-feedback regulatory (Gchfr)* gene was upregulated; (iii) the PAH specific Hsp40 co-chaperone *Dnajc12* exhibited increased expression levels while two heat shock family members, namely the transcription factor *Hsf1* and the molecular chaperone *Hsp70* were downregulated, and the expression of the constitutive *Hsc70* was unmodified; (iv) no significant changes in expression levels were identified for targets associated with protein degradation, *Stub1* (coding for the co-chaperone CHIP, with ubiquitin ligase activity) and the autophagy marker *Sqstm1* (coding for p62/SQSTM1), and for the oxidative stress-responsive transcription factor *Ap-1*. The implication of these results together with the other findings in this work are discussed below.

Discussion

Mouse models of genetic diseases do not always entirely recapitulate the main phenotypic characteristics found in patients⁹. The

Pah-R261Q knock-in mouse that carries a frequent mutation in HPA/PKU patients exhibits reduced total hepatic PAH activity and presents phenotypic traits characteristic of homozygous patients with the *R261Q:R261Q* genotype, such as increased L-Phe and decreased L-Trp and L-Tyr in blood compared to *WT*, sensitivity to L-Phe challenge, and responsiveness to BH₄ supplementation (<http://www.biopku.org>)^{8,16}. Moreover, there is similar PAH residual activity (~15% of *WT*) in both *Pah-R261Q* mice and homozygous humans¹⁶, however, we encountered a remarkable difference between absolute blood L-Phe-levels in mice and patients. While patients present metabolic phenotypes from mild PKU to classic PKU (off-diet blood L-Phe values > 600 μmol/L) (247 records in <http://www.biopku.org>; see also refs. ^{16,17}), our mouse model exhibited very mild HPA (~110 μmol L-Phe/L). Thus, for the same PAH genotype with similar remaining activity, the blood L-Phe concentration (metabolic phenotype) is higher in humans, which might be explained by a lower steady-state level of hepatic PAH in humans compared with mice. There is a high similarity in sequence, structure, specific activity and regulatory properties of human and mouse PAH, and thus different PAH amounts between rodents and humans have been associated with differences in the rate of transcription, translation, and/or protein homeostasis⁵⁷. Nevertheless, based on the similar propensity to aggregate through a cross-β-sheet formation for human and mouse PAH around the mutation area (Supplementary Fig. 1), it is very probable that similar amyloid-like soluble aggregates are formed in the liver of patients with the Arg261 → Gln mutation.

The *Pah-R261Q* mouse appears to offer considerable potential for mechanistic and therapeutic investigations as it presents with a tunable blood L-Phe concentration. By applying an L-Phe challenge, we could transiently attain L-Phe concentrations characteristic of PKU, and by adjusting the L-Phe concentration and length of supplementation, it might be possible to modulate the metabolic phenotype and fully develop the capacity of this mouse model as a prototype to study a range of mild to severe forms of HPA. Furthermore, upon L-Phe challenge, the resulting transient HPA in *Pah-R261Q* is responsive to treatment with BH₄ (Kuvan®). Consequently, this mouse model can contribute to evaluate protocols and understand the multifactorial mechanisms

Table 2 Relative mRNA quantification for selected genes in liver of *WT* and *Pah-R261Q* mice.

Gene (name)	<i>Pah</i> genotype	Expression level (relative to <i>WT</i> mice, defined as 1)	Fold change ^a	p Value ^b
<i>Pah</i>	<i>WT</i>	1.0000 (0.7878 ± 1.2693)	1.15	0.2273
	<i>R261Q</i>	1.1524 (1.0967 ± 1.2110)		
<i>Gch1</i>	<i>WT</i>	0.2512 (0.2146 ± 0.2939)	1.08	0.5440
	<i>R261Q</i>	0.2714 (0.2115 ± 0.3483)		
<i>Gchfr</i>	<i>WT</i>	0.0163 (0.0131 ± 0.0203)	1.70	0.0024
	<i>R261Q</i>	0.0277 (0.0228 ± 0.0336)		
<i>Dnajc12</i>	<i>WT</i>	0.0040 (0.0030 ± 0.0053)	1.78	0.0048
	<i>R261Q</i>	0.0071 (0.0057 ± 0.0088)		
<i>Hsp70</i>	<i>WT</i>	0.0010 (0.0007 ± 0.0015)	0.31	0.0012
	<i>R261Q</i>	0.0003 (0.0002 ± 0.0005)		
<i>Hsc70</i>	<i>WT</i>	0.9704 (0.7478 ± 1.2592)	1.34	0.0855
	<i>R261Q</i>	1.2983 (1.0279 ± 1.6399)		
<i>Hsf1</i>	<i>WT</i>	0.0280 (0.0251 ± 0.0313)	0.65	0.0054
	<i>R261Q</i>	0.0183 (0.0140 ± 0.0238)		
<i>Stub1</i>	<i>WT</i>	0.0156 (0.0126 ± 0.0193)	1.22	0.0808
	<i>R261Q</i>	0.0191 (0.0175 ± 0.0208)		
<i>Sqstm1</i>	<i>WT</i>	0.2483 (0.2203 ± 0.2799)	1.04	0.6389
	<i>R261Q</i>	0.2571 (0.2287 ± 0.2892)		
<i>Ap-1</i>	<i>WT</i>	0.0163 (0.0140 ± 0.0189)	1.0	0.9815
	<i>R261Q</i>	0.0163 (0.0149 ± 0.0179)		

^aFold change in *Pah-R261Q* mice relative to *WT* mice.

^bTwo-tailed p values for differences between both mice groups, obtained from the Mann Whitney U test.

Genes upregulated or downregulated in *Pah-R261Q* (*n* = 5 mice) compared to *WT* (*n* = 6 mice) (*p* < 0.05) are highlighted in bold text.

for BH₄ responsiveness in mice, including the increase of total PAH enzyme activity by PAH variant stabilization through protection against oxidative damage and proteolytic degradation, thus prolonging the half-life of PAH as seen in vitro¹⁹.

The large variability and spectrum of metabolic phenotypes presented by homozygous *PAH-R261Q* patients^{15–17} are thus far not observed in the mouse model. *Pah-R261Q* mice, in fact, present low variation in the basal concentration of blood L-Phe and other parameters measured in this work. The proteostasis network that maintains the synthesis, folding, localization, and degradation of proteins, and counteracts the effect of aggregates, involves a large number of protein components that are regulated at the cellular, tissue, and organismal level⁵³. This complex proteostasis network provides additional polymorphic modifier variants that contribute to the broader phenotypic spectrum in patients with unstable PAH variants, but not necessarily in the mouse model where a uniform genetic background has been achieved by careful backcrossing.

In PKU, the neurological defects include monoamine neurotransmitter deficiencies, which are fully manifested in the classical PKU (*Enu2*) mouse that is almost devoid of PAH activity²⁶. The *Enu1/2* mouse, which presents 2.5% of regular PAH activity and blood L-Phe levels just slightly higher (~150 μmol/L) than in *Pah-R261Q*, also shows a decrease in brain serotonin and 5HIAA⁵⁸. However, the remaining 16% PAH activity in *Pah-R261Q* mice appears high enough to result in apparently normal L-Phe catabolism and monoamine neurotransmitter synthesis, as well as in absence of detectable neurological deficiencies. Nevertheless, despite their mild HPA, *Pah-R261Q* mice manifested several biomarkers and indicators of adiposity and altered lipid metabolism, and oxidative stress. These traits have been previously observed in patients and animal models of PKU where they have been related to neurotoxic HPA levels and (micro)nutritional deficiencies of the L-Phe-free diet^{59,60}, factors that are absent in this case. Further evidence suggests that the increased weight in *Pah-R261Q* males is not a direct consequence of elevated L-Phe levels; the classical PKU model *Enu2* is underweight, despite its tenfold higher blood L-Phe levels than in *Pah-R261Q*²⁶. The molecular basis behind the observed mild overweight and oxidative stress in *Pah-R261Q* mice appears to be related to a toxic aggregation of mutant PAH and contributes to the identification of a gain-of-function contribution to the HPA/PKU pathology.

The misfolding defect of the p.R261Q-PAH protein variant is manifested both in biochemical characterizations as a reduced conformational stability and accelerated degradation^{18,19,23} and in computational predictions by FoldX¹⁵. The Arg to Gln residue change is expected to disrupt the interdimer interactions in p.R261Q-PAH (Supplementary Fig. 1), and the area around the mutation would then become available for unspecific intersubunit interactions. Among the few HPA/PKU-associated PAH variants with a high predicted propensity for β-cross amyloid-like aggregation by in silico TANGO calculations⁴⁷, p.R261Q-PAH is the variant with the highest allele frequency among patients.

The *Pah-R261Q* mice presented a reduction in steady-state hepatic PAH levels and PAH-specific activity, as well as increased ubiquitination of the protein in the liver. The current understanding of the loss-of-function of misfolding PAH variants is an accelerated degradation carried out preferentially by the ubiquitination-dependent proteasome system (UPS), as recently proven for a large number of PAH variants in cellular studies⁶¹. Our results with *Pah-R261Q* show that selective autophagy may be involved in the degradation of a PAH variant, as strongly indicated by the colocalization of markers of autophagy Ser403-phosphorylated p62 and LC3 with mutant PAH. In the case of the lightly aggregating *Enu1* variant p.V106A-PAH there is no colocalization of these markers with PAH, and the aggregates

seem to enter the nucleus where they may also be degraded by the nuclear UPS. There is an intricate cross-talk between the UPS and autophagy^{62,63}, and it is thus likely that PAH amyloid-like aggregates in *Pah-R261Q* that are not effectively processed by the UPS can be co-aggregated with phosphorylated p62 for autophagic processing^{51,64}.

Although insoluble deposits may protect from oxidative stress⁶⁵, amyloid-like aggregation-prone conformers—e.g., resulting from mutations—perturb cellular homeostasis and induce oxidative stress, increasing the production of reactive oxygen species (ROS) at the cellular and tissue levels⁵³. Toxic aggregation in the cytoplasm overwhelms the protein quality control system, resulting in increased ROS, further exacerbation of protein aggregation³³, and activation of p62/SQTM1 by phosphorylation⁵¹. Together, our results point to an oxidative and cellular stress condition in *Pah-R261Q* mice associated with a toxic aggregation of the PAH variant. The reduction of BH₄ levels manifested in the liver of *Pah-R261Q* has also been observed in other disorders associated with oxidative stress². In hepatocytes, BH₄ also acts as the cofactor of alkylglycerol monooxygenase², an enzyme involved in the degradation of ether lipids. Alteration of BH₄ synthesis mainly affects the entire cellular lipidome⁶⁶, providing a link between oxidative stress and alterations of lipid metabolism, the two main comorbidities postulated from the metabolic characterization of *Pah-R261Q* mice (Table 1). As part of the physiological and metabolic characterization of *Pah-R261Q*, we noted three related findings: slightly increased body weight of males (26.8 ± 0.4 vs. 25.1 ± 0.3 g (WT)), lower RER in the resting period, and higher serum levels of some metabolites that have been associated with adiposity and altered lipid metabolism, namely trimethyllysine, leucine, and isoleucine³¹. Although no gender-associated changes were found for any parameter or metabolite measured in this work for *Pah-R261Q* compared to WT, including RER and relevant metabolites, a priori indicates a similar propensity for altered metabolism in both genders, only males were heavier than their WT counterparts. A male-specific body weight increase due to altered lipid metabolism and adiposity has been detected in other mice and human studies, which has been associated with a different genetic architecture and potential sex chromosome effects on metabolism (reviewed in ref. 67).

A recent study has also reported the reduction of soluble BH₄ in the liver lysates of *Enu1* and *Enu1/2* mice and the decrease has been linked to the entrapment of the cofactor in aggregates of the p.V106A-PAH variant⁴⁵, resulting in a secondary BH₄-deficiency. Here, we measured total BH₄ in non-centrifuged homogenates, showing a net reduction in *Pah-R261Q* mice, which is also supported by the upregulation of *Gchfr*-mRNA (Table 2). Furthermore, no decrease of hepatic BH₄ was measured by the same method in liver *Enu1/2* mice⁴³, supporting that the BH₄ reduction in *Pah-R261Q* is PAH mutation-specific and associated with the formation of large amyloid-like aggregates and oxidative stress.

Oxidative stress in *Pah-R261Q* mice elicits the activation of the antioxidant response, as seen by increased serum levels of β-hydroxybutyrate³³, as well as an increase in total antioxidant capacity measured by the Trolox assay. Likewise, the reduction of quinolinic acid could also be linked to an increased synthesis of NAD⁺, which polymerizes to poly ADP-ribose for the protection of DNA in case of oxidative stress^{36,37}. Conversely, increased β-oxidation (demonstrated by lower RER and elevated β-hydroxybutyrate) and the concomitant increase in anaplerosis, supported by the observed reduction in α-ketoglutaric acid and other anaplerotic amino acids and metabolites (Table 1) has also been shown to cause an increase in oxidative stress and inflammation³⁸. Another sign of oxidative stress in *Pah-R261Q* is the upregulation of *Dnajc12*, the specific co-chaperone of the aromatic amino acid hydroxylases, which was not altered in

*Enu1*⁴². Interestingly, overexpression of *Dnajc12* has been associated with oxidative stress^{68,69}. On the other hand, the downregulation of both the transcription factor *Hsf1* and the chaperone *Hsp70* appears somehow counterintuitive in this context since *Hsf1* in mammals is the primary regulator of the heat shock response, which is activated by cellular stress and elicits transcriptional upregulation of major HSPs, notably *Hsp70*⁷⁰. In contrast, downregulation of *Hsf1* and consequent reduction in expression of HSF1 target genes is observed in neurodegenerative diseases such as Parkinson's, Alzheimer's, and Huntington's diseases, characterized by toxic amyloid deposits⁷¹, and a similar downregulation of *Hsf1* and *Hsp70* is also observed in this case.

In conclusion, the observation of amyloid-like PAH aggregates in the liver of the *Pah-R261Q* mouse introduces the concept of toxic gain-of-function for specific PKU-associated mutations. Overall, our results suggest that the lipid profile alterations and oxidative stress found in these mice are linked to intracellular toxic aggregation of the p.R261Q-PAH variant rather than to the severity of the HPA and/or the diet. The *Pah-R261Q* mouse model thus represents a unique research tool to support the evaluation and discovery of additional biomarkers in PKU and to investigate mutation-specific comorbidities, of benefit to the large number of PKU patients harboring the *R261Q* mutation. Interestingly, recent studies aiming to assess the prevalence of comorbid associations among large groups of adult PKU patients are starting to reveal several conditions in addition to the known neuropsychiatric disorders, including overweight and renal and cardiovascular dysfunctions^{5,6,72}. A proper patient stratification that takes into account the predisposition of the coded PAH variants to amyloid-like aggregation is expected to result in a better association of the comorbidities and improved patient-tailored treatment, encouraging follow-up investigations of the PAH aggregates. Lastly, this mouse model might contribute to investigations on pharmacological chaperone-based therapies targeting unstable PAH variants.

Methods

Materials. All chemicals in this section were acquired from Sigma-Aldrich unless otherwise indicated. Animals evenly matched for sex were distributed in each group for the different experiments presented. Recombinant human WT-PAH and p.R261Q-PAH proteins were expressed and purified using the pMAL expression vectors^{18,19} coding for the fusion protein maltose-binding protein (MBP)-(pep)xa-PAH), where (pep)xa is the cleavage site for the restriction protease Factor Xa. The fusion proteins were expressed in *Escherichia coli* TBI cells at 28 °C for 16–18 h with 1 mM IPTG and purified by affinity chromatography with amylose resin (New England Biolabs) with elution with 10 mM maltose. The fusion proteins were cleaved for 3 h with Factor Xa (New England Biolabs) at a protease:PAH ratio of 1:300. The tetrameric purified WT-PAH and p.R261Q-PAH proteins were isolated by size exclusion chromatography on a Superdex HiLoad 16/600 200 column (GE Healthcare) in 20 mM Hepes pH 7, 200 mM NaCl.

Generation of *Pah-R261Q* knock-in mouse. The constitutive knock-in mouse model was generated by Taconic Biosciences GmbH (Köln, Germany) via CRISPR/Cas9-mediated gene editing. The guide RNA target sequence + protospacer adjacent motif (PAM) sequence 5'-AGTGGAAAGCTCGGAAGGCC_AGG-3' (non-seed sequence_seed sequence_PAM) was designed and guide RNA was prepared as a hybrid of CRISPR-RNA (crRNA; 6 ng/μl) (Dharmacon, Lafayette, USA) and trans-activating crRNA (tracrRNA; 10.5 ng/μl) (Dharmacon, Lafayette, USA). The guide RNA was co-injected into C57BL/6N zygotes – essentially as described²⁰ – along with Cas9 protein (55 ng/μl; New England Biolabs, Ipswich, USA) and homology-directed repair (HDR) oligonucleotide (5'-GCTTAGATCCATGCCTAA TGACTGTGTGTCAGTGGAAAGACTTGGAAATGCCAGGCCACCCCAAGAAATC TCGAGACAGACATAAGCCAG-3') (100 ng/μl) from Integrated DNA Technologies, Coralville, USA. This HDR oligonucleotide harbored the point mutation c.782 G > A (p.Arg261Gln) to be introduced in exon 7 of the *Pah* gene on murine chromosome 10 (point mutation and exon annotation according to NCBI transcript NM_008777.3) as well as a silent mutation (c.777C > A) to create an additional restriction site (*BsmI*) for analytical purposes (Supplementary Fig. 2). These CRISPR reagents were microinjected (until the pronucleus swells up, typically ~1

pl) into 304 mouse embryos resulting in a total of 51 pups born, and three animals (5.9%) displayed positive detection of the *R261Q* knock-in allele.

Confirmation of the on-target mutation was completed as detailed^{73,74} whereas verification of the absence of undesired potential off-target modifications was achieved by heteroduplex mobility assays conducted on the top 16 hits originated from BLAST analysis of the guide RNA onto *M. musculus* genome assembly (GRCm38/mm10) (Supplementary Table 1).

Animal husbandry and colony expansion. The animal studies were approved by the Norwegian Food Safety Authority and performed at the Laboratory Animal Facility, University of Bergen, according to the guidelines and standards from the Regulation on the use of animals in the research of this institution. Mice were housed in a temperature-controlled (21 °C and 50% air humidity) environment with 12 h light/dark cycles. Food (standard chow pellets) and water were available ad libitum.

The colony was continuously backcrossed to avoid genomic drift. Every 6 months wild-type mice (C57BL/6J, males and females every second time) were bought from an approved vendor (Charles River) and bred with heterozygous *Pah^{R261Q}/WT* mice. Six to eight weeks old heterozygous *Pah^{R261Q}/WT* siblings from this backcrossing and breeding were used to produce homozygous *Pah^{R261Q}/R261Q* mice. The resultant *Pah^{R261Q}/WT* and *Pah^{WT}/WT* mice (siblings) from the breeding were utilized as control counterparts. This method of breeding is recommended to maintain the strain genetic integrity. We make sure to avoid going beyond three generations of inbreeding (F3) before we reset the generation by using new breeding animals from the backcrossing. The strain has been backcrossed eight times (N8) and the latest mice that have been used in the experiments presented in this work are from generation N8F3.

Genotyping. In order to determine the mouse genotype, ear biopsies were collected and DNA was extracted and purified from these tissue samples using the DNeasy Blood and Tissue kit (QIAGEN) following the manufacturer's instructions. After that, DNA was amplified by standard PCR (See primers in Table S4), initial denaturation at 95 °C/5 min followed by 35 cycles of denaturation-annealing-extension, 95 °C/30 s, 60 °C/30 s and 72 °C/1 min, with a final extension at 72 °C for 10 min) using Taq Polymerase (New England Biolabs). The PCR product was then incubated with the endonuclease *BsmI* (New England Biolabs) for 15 min at 65 °C. Finally, the digestion fragments were resolved in 2.5% agarose gel electrophoresis (1x TAE buffer/90 min/90 v) and bands visualized in a ChemiDoc XRS (Bio-Rad Laboratories) imaging system.

Metabolic cage. The physiological parameters: rate of O₂ and CO₂ consumption, food intake and activity of *Pah-R261Q* and control WT mice (4–5-month old; n = 3–5 mice per group, 121 observations/animal) were directly determined using the Oxymax-Comprehensive lab animal system (CLAMS, Columbus Instruments), with data being recorded for 36 h after an acclimatization period of 12 h. Other valuable calorimetric properties such as respiratory exchange rate (RER) and energy expenditure were indirectly calculated using Lusk classical equations provided in the Oxymax processing software.

Rotarod performance test. The assessment of motor function was conducted on a rotarod instrument (Harvard Apparatus) consisting of a 5 cm plastic grooved rod and a platform situated approximately 25 cm below equipped with a lever to trigger the recording for the time of fall. *Pah-R261Q* and control WT mice (3 months old; n = 10–11 mice per group) were, initially, habituated to the setting and trained to stay on the rod for 1 min at a constant speed of 5 rpm. Trained mice were then placed again on the rod with a gradual acceleration from an initial 4 rpm to a final 40 rpm speed over a 5 min testing period. The latency of fall as well as rod revolutions at fall was logged, and trials were repeated three times, separated by a 15 min break.

L-Phe challenge and BH₄-responsiveness. Adult mice (3–4-month-old) were employed in all the animal experiments of this section. For the effect of L-Phe challenge, intraperitoneal injection of an L-Phe solution (200 μg/g body weight) to *Pah^{R261Q}/R261Q*, *Pah^{R261Q}/WT*, and *Pah^{WT}/WT* mice (n = 23, 6 and 4 mice per group, respectively) was followed by whole blood sampling from the saphenous vein at time points: 1 day before injection (baseline level) and 35, 85, 150, and 300 min after injection. For BH₄-responsiveness, a treatment solution of BH₄ (Schircks Laboratories) (12.73 mM BH₄, 2% ascorbic acid, and 10% DMSO; in a dosage of 20 mg BH₄/kg body weight) or placebo solution (2% ascorbic acid and 10% DMSO), were injected into *Pah-R261Q* mice (n = 5–6 mice per group, per experiment) intraperitoneally twice a day⁴¹ for 4 days, before conducting the L-Phe challenge protocol as indicated above. The obtained blood samples were collected onto filter paper cards (PerkinElmer) according to the vendor's guidelines wherein L-Phe was measured by tandem mass spectrometry in, at minimum, 3 h fasted mice.

Metabolic markers analysis. In order to obtain serum specimens, whole blood was collected by cardiac puncture and 1 mL was transferred to a microcentrifuge

tube. Subsequently, blood samples were left for 45 min at room temperature to facilitate coagulation, preceding two consecutive centrifugation steps (2,100 rcf, 10 min, and 4 °C) where the respective supernatants were pipetted out to a clean tube. The isolated serum fractions were stored at -80 °C until examination. The extracted serum samples from *Pah-R261Q* and *WT* mice (4–5 months old; $n = 19$ mice per group) were subjected to an exhaustive analysis to determine the concentration of 72 relevant metabolic biomarkers. Analyses were performed at Bevilat (<http://bevilat.no/>) across four different platforms supporting high-throughput multi-analyte assays. A combination of chromatographic techniques with mass spectrometry detection (GC-MS/MS and LC-MS/MS) was applied (See references for individual experimental protocols in Supplementary Table 2).

Preparation of liver and brain lysates. Mice (age and numbers indicated in the specific studies) were sacrificed in a carbon dioxide euthanize chamber. Immediately after, the brain and liver were surgically excised and snap-frozen in liquid nitrogen, and tissue was manually ground into a fine powder and stored in aliquots at -80 °C. Liver homogenates from the ground aliquots (~200 mg powder) were prepared by adding 800 μ l of a lysis buffer solution containing 1 \times PBS and protease inhibitor cocktail (Roche), a 5 mm diameter stainless steel bead (Qiagen), and a mechanical disruption step in a Tissue Lyser II (Qiagen) instrument (2 \times 1 min 30 s, 20 Hz). Cellular debris was then removed through centrifugation (20,000 rcf, 20 min) to obtain a clear supernatant. The total protein concentration of the liver lysates was determined in a Direct Detect infrared spectrometer (Millipore). For the Trolox equivalent antioxidant capacity assay, 600 μ l of identical lysis buffer, a mechanical homogenization with a pellet pestle sitting on ice, and a modified centrifugation step (18,000 rcf, 10 min) was preferred.

Brain extracts were prepared by powder homogenization in 10 \times volume of 50 mM Tris-HCl, pH 7.5, 100 mM KCl, 1 mM EDTA, 1 mM DTT, 1 μ M leupeptin, 1 μ M pepstatin, and 200 μ M PMSF, at otherwise identical experimental conditions as standard liver extracts (see above).

Neurotransmitters, BH₄, and amino acid determination in tissues. The relative levels of BH₄ in liver and brain and of monoamine neurotransmitter metabolites in the brain of *Pah-R261Q* and *WT* ($n = 5–6$ mice per group) were measured in liver and brain lysates of 3–4-month-old mice as reported⁵⁸. Briefly, tissue lysates were oxidized for 60 min in the dark by 0.5 g/L iodine and 0.1 g/L potassium iodide in 0.1 M HCl. The oxidation was stopped by adding 2 g/L ascorbic acid and adjusting the pH to 8.5 with NaOH before incubation with calf intestine alkaline phosphatase (Roche Applied Science) at 37 °C for 1 h. The lysates were then adjusted to pH 2 with HCl and deproteinized (Ultrafree-MC filters, Millipore) before BH₄ and neurotransmitters were measured by HPLC⁷⁵.

The relative levels of the amino acids L-Phe, L-Tyr, and L-Trp of *Pah-R261Q* and *WT* ($n = 5–6$ mice per group) were measured in liver and brain lysates of 3–4-month-old mice as reported⁷⁶. Samples were prepared according to the Phenomenex EZ:faast kit's manual, with the following modifications: prior to amino acid extraction and derivatization, 20 μ l of each internal standard solution containing 100 μ mol/L Phe-d5 and 20 μ mol/L Tyr-d4 (in 50 mmol/L HCl) were added to 20 μ l of sample lysate. Using the kit's reagents, the amino acids were derivatized with propyl chloroformate resulting in the addition of propyl formate at the amine moiety and a propyl group at the carboxylic end of the amino acids, respectively. The hydroxy group of Tyr was also derivatized by the addition of a propyl formate group, and the amino acids were then measured by LC-ESI-MSMS⁷⁶.

PAH enzymatic activity assay. Liver lysates were first loaded into 0.5 mL Zeba-Spin desalting columns (7,000 Da cutoff; ThermoFisher Scientific), previously equilibrated with 20 mM HEPES, pH 7.0, 200 mM NaCl, and protease inhibitor cocktail solution, and centrifuged (1,700 rcf) for 2 min. PAH activity in the homogenates was measured at 25 °C using 5–20 μ g of total protein in each assay, with 1 mM L-Phe in 20 mM Na-Hepes, 0.2 M NaCl, pH 7.0, containing catalase (0.04 mg/ml). After 4 min preincubation at 25 °C, ferrous ammonium sulfate (100 μ M) was added, and the reaction triggered after 1 min by adding 200 μ M BH₄ and 5 mM DTT (final concentrations in the assay). The reactions were allowed to run for 2 min and stopped with 2% acetic acid in ethanol. Under these conditions, PAH activity was linear to the amount of protein in the extracts. L-Tyr formed was quantified by HPLC with fluorimetric detection.

Immunoblotting. Protein immunodetection was performed by Western blot. Total protein (2.5 μ g/well) was separated using 10% polyacrylamide gel and immunodetected by using primary antibodies, 1:5000 for primary antibody α -PAH (1:5000; Millipore-MAB5278), α -ubiquitin (1:500; Thermo Fisher Scientific-131600); α -glyceraldehyde 3-phosphate dehydrogenase (GAPDH) (1:1000; Abcam-ab9485), and 1:2500 for secondary antibodies goat anti-mouse (GAM) (Bio-Rad Laboratories) and goat anti-rabbit (GAR) (Bio-Rad Laboratories), conjugated to horseradish peroxidase. Quantification of non-ubiquitinated and mono-ubiquitinated PAH and GAPDH proteins was performed by gel band densitometry.

Immunofluorescence and IHC. Mice (4–5-month-old) were anesthetized with pentobarbital (20 mg/kg, IP), and transcardially perfused with 50 ml of warm saline (0.9%, 37 °C), followed by 50 ml of warm paraformaldehyde (4%, 37 °C) in 0.16 M phosphate buffer (PBS; pH 7.2). The hepatic tissue was dissected out and postfixed in the same fixative for 3 h at 4 °C and subsequently stored in 20% sucrose diluted with PBS containing 0.01% sodium azide (Sigma) and 0.02% Bacitracin (Sigma) at 4 °C overnight. Tissues were embedded with Optimal cutting temperature (OCT) compound (Tissue Tek, Miles Laboratories, Elkhart, Ind., USA), frozen and cut in a cryostat (Microm, Heidelberg, Germany) at 20 or 50 μ m thickness, collected and stored free-floating in PBS at 4 °C or mounted onto SuperFrost Plus microscope slides (ThermoFisher Scientific), dried at room temperature for 30 min and stored at -80 °C until use.

For immunofluorescence, Triton-X 100 (0.5%) was used to permeabilize the tissues followed by blocking with 5% FBS in PBS for 1 h prior to the primary antibody incubation. Tissues were then incubated overnight at 4 °C in a humidity chamber with the corresponding primary antibody, α -PAH (1:100; Abcam-ab178430), α -Ubiquitin N-terminal (1:200; ABIN350072), anti-NUP98 (1:100; Abcam-ab50610), α -phospho-p62 (S403) (1:200; MBL-D343-3), and goat anti-LC3B (1:100; Signalway antibody-C48312), in 10% (w/v) NGS, 1 \times PBS, pH 7.4 solution. Then, a 30 min incubation in a humidity chamber at 37 °C was carried out with the corresponding secondary antibody, donkey anti-rabbit IgG H&L (1:200; Alexafluor 488, Invitrogen-A21206), donkey anti-goat IgG H&L (1:400; Alexafluor 555, Abcam-ab150130), donkey anti-goat IgG (1:200; Cy3 conjugate, Millipore-AP180C), goat anti-rat IgG H&L (1:100; TRITC, Jackson immunoresearch-112-025-143), goat anti-rabbit IgG H&L (1:200; Alexafluor 647, Invitrogen-A21245), donkey anti-rat IgG H&L (1:200; Alexafluor 488, ThermoFisher Scientific-A21208), in the same blocking solution. A washing step of 15 min with 1 \times PBS, pH 7.4 was included prior to and after each incubation period. Hoechst or DAPI, as indicated, were used to counterstain the nucleus for 30 min at RT followed by washing in PBS and mounted with DABCO mounting media. Images were acquired by using Leica TCS SP5 confocal microscope (Leica Microsystems GmbH) using a pinhole airy 1 and a 63 \times , 1.4 numeric aperture oil immersion objective. Acquired images were processed using the LAS AF Lite software (Leica Microsystems). For each sample, a stack of images ($n = 14$) with a step-size of either 290 or 170 nm was taken. Fluorescence intensity measurements were performed using Fiji freeware using the stacks of confocal images. Integrated density values of each stack were used to compare the relative fluorescence intensity of the samples. 3D rendering of the confocal images (z-stacks) was performed by using image analysis software Imaris (Bitplane Inc.). The nuclei marked with Nup98 (red) and PAH (green) were reconstructed by using the surface tool.

For immunohistochemistry (IHC), the stored free-floating sections were employed. Sections were first rinsed in 0.3% H₂O₂ in PBS for 10 min at RT for quenching endogenous peroxidase activity, and then incubated with blocking buffer containing Blocking Serum (VECTOR Laboratories), 0.5% Triton X-100 (Sigma), and 5% bovine serum albumin (Sigma-Aldrich) in PBS for 1 h at RT. Sections were incubated for 45 min with primary antibody α -PAH (1:800; Abcam-ab191415) and 30 min with goat anti-rabbit IgG H + L (1:200; HRP, BioRad-1706515) secondary antibody, and followed by a 30-min incubation with prepared VECTASTAIN Elite ABC (VECTOR Laboratories). The sections were immersed in a peroxidase substrate solution (DAB, Sigma) for 7–8 min and washed with water, mounted on Super Frost slides, and coverslipped with glycerol/PBS (9:1) containing 0.1% para-phenylenediamine. Finally, the sections were analyzed and images were captured using a Leica microscope equipped with a Leica camera. The average size and size distribution of PAH-positive “particles” in the cytoplasm of hepatic cells was quantified using ImageJ software. As the PAH staining pattern in the light microscope (objective 100 \times) was evenly distributed in *WT* mouse liver, the quantification was performed on liver sections of *Pah-R261Q* and *Emu1*. Ten liver sections (30 μ m thickness) were randomly selected from each animal. PAH-positive particles were analyzed in randomly selected regions of the sections. Only single PAH-positive particles were analyzed and at least 400 particles from each group, from at least 10–12 hepatic cells, were counted.

Amyloid-like aggregation assay (Amytracker). Amyloid detection was carried out by recording the fluorescence emission of amyloid ligand heptamer formyl thiophene acetic acid (Amytracker™ 680; Ebbia Biotech) at 680 nm in a 96-well plate, black F-bottom (Griener Bio-one), for 24 h at 37 °C in a multimode microplate reader (Tecan spark), with excitation at 540 nm. The time course of the fluorescence intensity for purified WT-PAH and p.R261Q-PAH (20 μ M subunit) with Amytracker™ 680 (1:1000) was acquired in 20 mM HEPES, 150 mM NaCl, pH 6.0. Samples lacking protein were used as controls and normalized. Three measurements were carried out for each protein.

Transmission electron microscopy (TEM). For TEM of hepatic tissue, 5-month-old mice (*WT* and *Pah-R261Q*) were anesthetized with isoflurane and transcardially perfused with 50 ml of warm saline (0.9%, 37 °C), followed by 50 ml of 2.5% glutaraldehyde (diluted in a 0.1 M sodium cacodylate buffer) at RT. The hepatic tissue was dissected out and postfixed in the same fixative for 24 h at 4 °C. The tissues were then transferred to 0.1 M sodium cacodylate buffer and kept at 4 °C. Postfixation was performed for 1 h (on ice) in 1% osmium tetroxide (EMS # 19134)

diluted in 0.1 M sodium cacodylate buffer, followed by two washing steps. The samples were then dehydrated using a graded ethanol series (30%, 50%, 70%, 96%, and 3 × 100%) before transferred to a 1:1 solution of 100% ethanol:propylene oxide (15 min). Samples were then transferred to 100% propylene oxide (15 min) before gradually introducing agar 100 resin (AgarScientific R1031) drop by drop over the next hours. Samples were then transferred to a small drop of 100% resin and excess propylene oxide was allowed to evaporate (1 h). Samples were then transferred to 100% resin and placed in molds and left at RT overnight. The molds were then placed at 60 °C for 48 h to polymerize. Ultrasections of approximately 60 nm were placed on 100 mesh Copper grids (EMS #G100H-Cu) and stained with 2% uranyl acetate (EMS # 22400) and lead citrate (VWR #1.07398). Grids were imaged using a Jeol JEM-1230 transmission electron microscope at 80 kV. Different organelles were counted in images acquired at 20,000× magnification from the cytoplasm in hepatocytes, in liver samples of both WT and *Pah-R261Q* mice (40 TEM micrographs for each mouse).

For protein TEM with negative staining, 5 µl samples of protein solutions (20 µg/ml) in the indicated buffer were allowed to be absorbed (1 min) on a glow discharged, 300 mesh (EMS # G300H-Cu), carbon-coated grid. The grids were then stained for 1 min in 2% uranyl acetate. Grids were allowed to dry for 30 min before imaging. The incorporation of two consecutive washing steps with double distilled water after absorption of the protein improved the background, but we observed loss of aggregates.

Oxidative stress assay (Trolox). The antioxidant capacity of small molecules (such as ascorbate, glutathione, and vitamin E) in *Pah-R261Q* and WT liver homogenates was determined by the Trolox equivalent antioxidant capacity assay using the colorimetric Total Antioxidant Capacity Assay kit (Abcam). Samples were diluted 1:1 with the included reagent Protein Mask to avoid the potential contribution of other biological species. Otherwise, the standard protocol indicated in the product manual was followed. Results were obtained by interpolation to a Trolox (reference antioxidant) standard curve and expressed as Trolox equivalent antioxidant capacity.

Gene (mRNA) expression. Total RNA was extracted from powdered livers of *Pah-R261Q* and WT mice (3-months-old; $n = 5-6$ per group) with the QIAamp RNA Blood Mini Kit (QIAGEN) and translated into cDNA using the Reverse Transcription System (Promega). Quantitative PCR was performed in standard triplicate assays for each mouse sample with 50 ng of cDNA using TaqMan technology, an ABI Prism 7700 sequence detector, and the TaqMan Universal PCR Master Mix from ABI. Detailed information about the specific transcript detection cannot be given, as we used ABI TaqMan Gene Expression Assays, which are under a proprietary license, and the exact primer and probe sequence are not disclosed. The ABI assay numbers for the indicated murine mRNA and NCBI nucleotide sequence numbers are summarized in Supplementary Table 4. Murine *Gapdh*-mRNA was included as a control for normalization and the analyses of the relative gene expression were performed based on the $2^{-\Delta\Delta Ct}$ method⁷⁷.

Software. The computer algorithm TANGO⁴⁷ was used for the prediction of aggregating regions in the relevant mutants and WT PAH sequences. Calculations were performed online (<http://tango.crg.es/>) with default parameters. PAH particles were analyzed and measured using Fiji ImageJ.

Statistics and reproducibility. Quantitative data are presented as mean ± standard deviation (SD). Individual values are plotted as circles in both scatter dot plots and bar graphs, except in the inset of Fig. 1e where the circles represent the mean for the group for each time point. Statistical significant differences were determined by unpaired two-tailed *t* test for pairs of groups, except when indicated, i.e., two-tailed Mann Whitney *U* test were used for the analysis of data in Table 1 and Supplementary Table 2. For comparisons of more than two groups one-way ANOVA followed by post hoc Tukey test was used, except for data in the inset of Supplementary Fig. 4 where due to unequal variance and sample size Brown-Forsythe and Welch ANOVA test was used followed by Dunnett's multiple comparisons test, as indicated. Note that despite the fact that mean ± SD is presented in this figure, the analysis is run on mean AUC ± SEM data, which is also the case for the *t* test applied on the AUC data in the inset of Fig. 1d and inset of Fig. 2c. We considered $p < 0.05$ as statistically significant and *p* values are provided with accurate numbers down to <0.0001. Statistical analyses were performed using GraphPad Prism[™] (version 8.3.0, San Diego) software and the applied analysis in each case is included in the corresponding Table and Figure legend only for the results for which statistical significance was obtained.

For representations of quantitative data, *n* customarily refers to the number of independent biological samples (mice) examined in each analysis, except when explicitly referring to the number of independent enzyme purifications. When required, i.e., Figure 5c and Supplementary Fig. 7, the number of sections and/or particles analyzed is also provided in the corresponding figure legend.

The representative Western blots (Fig. 3a, b) have been repeated at least three times in independent experiments, using different mice in each experiment ($n \geq 3$ for each genotype). Densitometric results obtained with the Western blots are represented in Fig. 3c. The agarose gel in Supplementary Fig. 2c represents the

procedure used for genotyping after breeding and similar results have been obtained at least 20 times in independent experiments including in total $n \geq 40$ mice of each genotype. Representative micrographs showing results from immunofluorescence and IHC (Figs. 4, 5a,b and 6a,b) have been successfully repeated with $n \geq 3$ for each genotype in independent experiments. The results in the representative micrograph from TEM with purified p.R261Q-PAH (Supplementary Fig. 6b) have been observed with $n = 3$ protein preparations. For the TEM of hepatic tissue, representative micrographs with the relevant organelles are shown and have been observed in liver samples from $n = 3$ mice in each genotypic group.

Ethical compliance. We have complied with all relevant ethical regulations for mice breeding, testing and research. The animal experiments in this study have received the appropriate approval from the Norwegian Food Safety Authority (Brumunddal, Norway) (approved application 20168698) and performed at the Laboratory Animal Facility, University of Bergen, according to the guidelines and standards from the Regulation on the use of animals in the research of this institution.

Reporting summary. Further information on research design is available in the Nature Research Reporting Summary linked to this article.

Data availability

Source data underlying Figs. 1–6, Supplementary Figs. 2c and 3–6, Tables 1 and 2 and Supplementary Tables 2 and 3 are provided with this paper as a Source Data file. The rest of the data that support Supplementary Figs. 7 and 8 within this paper, other findings and the mouse and derived materials will be made available upon reasonable request to the correspondence author. Web-links for NCBI nucleotide sequences: *Pah*-mRNA NM_008777.3 https://www.ncbi.nlm.nih.gov/nuccore/NM_008777.3, *Hsc70*-mRNA NM_031165.4 https://www.ncbi.nlm.nih.gov/nuccore/NM_031165.4, *Gch1*-mRNA NM_008102.3 https://www.ncbi.nlm.nih.gov/nuccore/NM_008102.3, *Hsf1*-mRNA NM_008296.2 https://www.ncbi.nlm.nih.gov/nuccore/NM_008296.2, *stb1*-mRNA NM_019719.3 https://www.ncbi.nlm.nih.gov/nuccore/NM_019719.3, *Gchfr* -mRNA NM_177157.4 https://www.ncbi.nlm.nih.gov/nuccore/NM_177157.4, *Dnajc12*-mRNA NM_001253685.1 https://www.ncbi.nlm.nih.gov/nuccore/NM_001253685.1, *p62*-mRNA NM_001290769.1 https://www.ncbi.nlm.nih.gov/nuccore/NM_001290769.1, *Hsp70* -mRNA NM_001163434.1 https://www.ncbi.nlm.nih.gov/nuccore/NM_001163434.1, *Ap-1*-mRNA NM_001243043.1 https://www.ncbi.nlm.nih.gov/nuccore/NM_001243043.1, *Gapdh*-mRNA NM_008084.3 https://www.ncbi.nlm.nih.gov/nuccore/NM_008084.3 Web-link for PAH structure in complex with BH₄ PDB 6HYC (<https://www.rcsb.org/structure/6HYC>) Web-link for data on C57BL/6J mouse strain (<https://www.jax.org/strain/000664>). Source data are provided with this paper.

Received: 15 November 2019; Accepted: 25 February 2021;

Published online: 06 April 2021

References

- Fitzpatrick, P. F. Tetrahydropterin-dependent amino acid hydroxylases. *Annu. Rev. Biochem.* **68**, 355–381 (1999).
- Werner, E. R., Blau, N. & Thony, B. Tetrahydrobiopterin: biochemistry and pathophysiology. *Biochem. J.* **438**, 397–414 (2011).
- Blau, N., van Spronsen, F. J. & Levy, H. L. Phenylketonuria. *Lancet* **376**, 1417–1427 (2010).
- Bone, A., Kuehl, A. K. & Angelino, A. F. A neuropsychiatric perspective of phenylketonuria I: overview of phenylketonuria and its neuropsychiatric sequelae. *Psychosomatics* **53**, 517–523 (2012).
- Burton, B. K. et al. Prevalence of comorbid conditions among adult patients diagnosed with phenylketonuria. *Mol. Genet. Metab.* **125**, 228–234 (2018).
- Trefz, K. F. et al. Clinical burden of illness in patients with phenylketonuria (PKU) and associated comorbidities – a retrospective study of German health insurance claims data. *Orphanet J. Rare Dis.* **14**, 181 (2019).
- Blau, N. & Longo, N. Alternative therapies to address the unmet medical needs of patients with phenylketonuria. *Expert Opin. Pharmacother.* **16**, 791–800 (2015).
- Levy, H. L. et al. Efficacy of saproterin dihydrochloride (tetrahydrobiopterin, 6R-BH₄) for reduction of phenylalanine concentration in patients with phenylketonuria: a phase III randomised placebo-controlled study. *Lancet* **370**, 504–510 (2007).
- Perlman, R. L. Mouse models of human disease: an evolutionary perspective. *Evol. Med. Public Health* **2016**, 170–176 (2016).
- McDonald, J. D. & Charlton, C. K. Characterization of mutations at the mouse phenylalanine hydroxylase locus. *Genomics* **39**, 402–405 (1997).
- Haefele, M. J., White, G. & McDonald, J. D. Characterization of the mouse phenylalanine hydroxylase mutation Pahenu3. *Mol. Genet. Metab.* **72**, 27–30 (2001).

12. Sarkissian, C. N., Boulais, D. M., McDonald, J. D. & Scriver, C. R. A heteroallelic mutant mouse model: a new orthologue for human hyperphenylalaninemia. *Mol. Genet. Metab.* **69**, 188–194 (2000).
13. Sarkissian, C. N. et al. Preclinical evaluation of multiple species of PEGylated recombinant phenylalanine ammonia lyase for the treatment of phenylketonuria. *Proc. Natl Acad. Sci. USA* **105**, 20894–20899 (2008).
14. Villiger, L. et al. Treatment of a metabolic liver disease by in vivo genome base editing in adult mice. *Nat. Med.* **24**, 1519–1525 (2018).
15. Wettstein, S. et al. Linking genotypes database with locus-specific database and genotype-phenotype correlation in phenylketonuria. *Eur. J. Hum. Genet.* **23**, 302–309 (2015).
16. Danecka, M. K. et al. Mapping the functional landscape of frequent phenylalanine hydroxylase (PAH) genotypes promotes personalised medicine in phenylketonuria. *J. Med. Genet.* **52**, 175–185 (2015).
17. Guldberg, P. et al. A European multicenter study of phenylalanine hydroxylase deficiency: classification of 105 mutations and a general system for genotype-based prediction of metabolic phenotype. *Am. J. Hum. Genet.* **63**, 71–79 (1998).
18. Pey, A. L. et al. Mechanisms underlying responsiveness to tetrahydrobiopterin in mild phenylketonuria mutations. *Hum. Mutat.* **24**, 388–399 (2004).
19. Erlandsen, H. et al. Correction of kinetic and stability defects by tetrahydrobiopterin in phenylketonuria patients with certain phenylalanine hydroxylase mutations. *Proc. Natl Acad. Sci. USA* **101**, 16903–16908 (2004).
20. Wang, H. et al. One-step generation of mice carrying mutations in multiple genes by CRISPR/Cas-mediated genome engineering. *Cell* **153**, 910–918 (2013).
21. Arturo, E. C. et al. First structure of full-length mammalian phenylalanine hydroxylase reveals the architecture of an autoinhibited tetramer. *Proc. Natl Acad. Sci. USA* **113**, 2394–2399 (2016).
22. Flydal, M. I. et al. Structure of full-length human phenylalanine hydroxylase in complex with tetrahydrobiopterin. *Proc. Natl Acad. Sci. USA* **116**, 11229–11234 (2019).
23. Gjetting, T., Petersen, M., Guldberg, P. & Guttler, F. In vitro expression of 34 naturally occurring mutant variants of phenylalanine hydroxylase: correlation with metabolic phenotypes and susceptibility toward protein aggregation. *Mol. Genet. Metab.* **72**, 132–143 (2001).
24. Hsu, P. D. et al. DNA targeting specificity of RNA-guided Cas9 nucleases. *Nat. Biotechnol.* **31**, 827–832 (2013).
25. Flurkey K., Curren J. M., Leiter E. H., Wither B. *The Jackson Laboratory Handbook on Genetically Standardized Mice*. (The Jackson Laboratory, 2009).
26. Fiori, E. et al. Early-onset behavioral and neurochemical deficits in the genetic mouse model of phenylketonuria. *PLoS ONE* **12**, e0183430 (2017).
27. Prentice, R. L. et al. An exploratory study of respiratory quotient calibration and association with postmenopausal breast cancer. *Cancer Epidemiol. Biomark. Prev.* **22**, 2374–2383 (2013).
28. Farinatti, P., Castinheiras Neto, A. G. & Amorim, P. R. Oxygen consumption and substrate utilization during and after resistance exercises performed with different muscle mass. *Int. J. Exerc. Sci.* **9**, 77–88 (2016).
29. Speakman, J. R. Measuring energy metabolism in the mouse—theoretical, practical, and analytical considerations. *Front. Physiol.* **4**, 34 (2013).
30. Westbrook, R., Bonkowski, M. S., Strader, A. D. & Bartke, A. Alterations in oxygen consumption, respiratory quotient, and heat production in long-lived GHRKO and Ames dwarf mice, and short-lived bGH transgenic mice. *J. Gerontol. A Biol. Sci. Med. Sci.* **64**, 443–451 (2009).
31. Strand, E. et al. Serum carnitine metabolites and incident type 2 diabetes mellitus in patients with suspected stable angina pectoris. *J. Clin. Endocrinol. Metab.* **103**, 1033–1041 (2018).
32. Mahendran, Y. et al. Association of ketone body levels with hyperglycemia and type 2 diabetes in 3,938 Finnish men. *Diabetes* **62**, 3618–3626 (2013).
33. Puchalska, P. & Crawford, P. A. Multi-dimensional roles of ketone bodies in fuel metabolism, signaling, and therapeutics. *Cell Metab.* **25**, 262–284 (2017).
34. Zdzisinska, B., Zurek, A. & Kandfer-Szerszen, M. Alpha-ketoglutarate as a molecule with pleiotropic activity: well-known and novel possibilities of therapeutic use. *Arch. Immunol. Ther. Exp.* **65**, 21–36 (2017).
35. Liu, S., He, L. & Yao, K. The antioxidative function of alpha-ketoglutarate and its applications. *Biomed. Res. Int.* **2018**, 3408467 (2018).
36. Kubicova, L., Hadacek, F. & Chobot, V. Quinolinic acid: neurotoxin or oxidative stress modulator? *Int. J. Mol. Sci.* **14**, 21328–21338 (2013).
37. Moffett, J. R. & Namboodiri, M. A. Tryptophan and the immune response. *Immunol. Cell Biol.* **81**, 247–265 (2003).
38. Satapati, S. et al. Mitochondrial metabolism mediates oxidative stress and inflammation in fatty liver. *J. Clin. Investig.* **125**, 4447–4462 (2015).
39. Mazzola, P. N. et al. Voluntary exercise prevents oxidative stress in the brain of phenylketonuria mice. *JIMD Rep.* **27**, 69–77 (2016).
40. Blaskovics, M. E., Schaeffler, G. E., & Hack, S. Phenylalaninaemia. Differential diagnosis. *Arch. Dis. Child* **49**, 835–843 (1974).
41. Kor, D., Yilmaz, B. S., Bulut, F. D., Ceylaner, S. & Mungan, N. O. Improved metabolic control in tetrahydrobiopterin (BH4), responsive phenylketonuria with sapropterin administered in two divided doses vs. a single daily dose. *J. Pediatr. Endocrinol. Metab.* **30**, 713–718 (2017).
42. Jung-Kc, K. et al. Phenylalanine hydroxylase variants interact with the co-chaperone DNAJC12. *Hum. Mutat.* **40**, 483–494 (2019).
43. Sarkissian, C. N., Ying, M., Scherer, T., Thony, B. & Martinez, A. The mechanism of BH4-responsive hyperphenylalaninemia—as it occurs in the ENU1/2 genetic mouse model. *Hum. Mutat.* **33**, 1464–1473 (2012).
44. Gersting, S. W. et al. Pahenu1 is a mouse model for tetrahydrobiopterin-responsive phenylalanine hydroxylase deficiency and promotes analysis of the pharmacological chaperone mechanism in vivo. *Hum. Mol. Genet.* **19**, 2039–2049 (2010).
45. Eichinger, A. et al. Secondary BH4 deficiency links protein homeostasis to regulation of phenylalanine metabolism. *Hum. Mol. Genet.* **27**, 1732–1742 (2018).
46. Woerner, A. C. et al. Cytoplasmic protein aggregates interfere with nucleocytoplasmic transport of protein and RNA. *Science* **351**, 173–176 (2016).
47. Fernandez-Escamilla, A. M., Rousseau, F., Schymkowitz, J. & Serrano, L. Prediction of sequence-dependent and mutational effects on the aggregation of peptides and proteins. *Nat. Biotechnol.* **22**, 1302–1306 (2004).
48. Okano, Y., Kudo, S., Nishi, Y., Sakaguchi, T. & Aso, K. Molecular characterization of phenylketonuria and tetrahydrobiopterin-responsive phenylalanine hydroxylase deficiency in Japan. *J. Hum. Genet.* **56**, 306–312 (2011).
49. Levine, B. & Kroemer, G. Autophagy in the pathogenesis of disease. *Cell* **132**, 27–42 (2008).
50. Matsumoto, G., Wada, K., Okuno, M., Kurosawa, M. & Nukina, N. Serine 403 phosphorylation of p62/SQSTM1 regulates selective autophagic clearance of ubiquitinated proteins. *Mol. Cell* **44**, 279–289 (2011).
51. Lamark, T., Svenning, S. & Johansen, T. Regulation of selective autophagy: the p62/SQSTM1 paradigm. *Essays Biochem.* **61**, 609–624 (2017).
52. Prasad, R., Xu, C. & Ng, D. T. W. Hsp40/70/110 chaperones adapt nuclear protein quality control to serve cytosolic clients. *J. Cell Biol.* **217**, 2019–2032 (2018).
53. Sala, A. J., Bott, L. C. & Morimoto, R. I. Shaping proteostasis at the cellular, tissue, and organismal level. *J. Cell Biol.* **216**, 1231–1241 (2017).
54. Paonessa, F. et al. Microtubules deform the nuclear membrane and disrupt nucleocytoplasmic transport in tau-mediated frontotemporal dementia. *Cell Rep.* **26**, 582–593 e585 (2019).
55. Fernández-Nogales, M. et al. Huntington’s disease is a four-repeat tauopathy with tau nuclear rods. *Nat. Med.* **20**, 881–885 (2014).
56. Chou, C.-C. et al. TDP-43 pathology disrupts nuclear pore complexes and nucleocytoplasmic transport in ALS/FTD. *Nat. Neurosci.* **21**, 228–239 (2018).
57. Ledley, F. D., Grenett, H. E., Dunbar, B. S. & Woo, S. L. Mouse phenylalanine hydroxylase. Homology and divergence from human phenylalanine hydroxylase. *Biochem. J.* **267**, 399–405 (1990).
58. Scherer, T. et al. Tetrahydrobiopterin treatment reduces brain L-Phe but only partially improves serotonin in hyperphenylalaninemic ENU1/2 mice. *J. Inher. Metab. Dis.* **41**, 709–718 (2018).
59. Sirtori, L. R. et al. Oxidative stress in patients with phenylketonuria. *Biochim. Biophys. Acta* **1740**, 68–73 (2005).
60. Rocha, J. C. et al. Dietary treatment in phenylketonuria does not lead to increased risk of obesity or metabolic syndrome. *Mol. Genet. Metab.* **107**, 659–663 (2012).
61. Scheller, R. et al. Toward mechanistic models for genotype-phenotype correlations in phenylketonuria using protein stability calculations. *Hum. Mutat.* **40**, 444–457 (2019).
62. Lamark, T. & Johansen, T. Autophagy: links with the proteasome. *Curr. Opin. Cell Biol.* **22**, 192–198 (2010).
63. Kocaturk, N. M. & Gozuacik, D. Crosstalk between mammalian autophagy and the ubiquitin-proteasome system. *Front. Cell Dev. Biol.* **6**, 128 (2018).
64. Bjørkøy, G. et al. p62/SQSTM1 forms protein aggregates degraded by autophagy and has a protective effect on huntingtin-induced cell death. *J. Cell Biol.* **171**, 603–614 (2005).
65. Carjia, A., Navarro, S., de Groot, N. S. & Ventura, S. Protein aggregation into insoluble deposits protects from oxidative stress. *Redox Biol.* **12**, 699–711 (2017).
66. Watschinger, K. et al. Tetrahydrobiopterin and alkylglycerol monoxygenase substantially alter the murine macrophage lipidome. *Proc. Natl Acad. Sci. USA* **112**, 2431–2436 (2015).
67. Zore, T., Palafox, M. & Reue, K. Sex differences in obesity, lipid metabolism, and inflammation—a role for the sex chromosomes? *Mol. Metab.* **15**, 35–44 (2018).
68. Choi, J., Djebbar, S., Fournier, A. & Labrie, C. The co-chaperone DNAJC12 binds to Hsc70 and is upregulated by endoplasmic reticulum stress. *Cell Stress Chaperones* **19**, 439–446 (2014).
69. Jagannathan, L., Cuddapah, S. & Costa, M. Oxidative stress under ambient and physiological oxygen tension in tissue culture. *Curr. Pharm. Rep.* **2**, 64–72 (2016).
70. Morimoto, R. I. Regulation of the heat shock transcriptional response: cross talk between a family of heat shock factors, molecular chaperones, and negative regulators. *Genes Dev.* **12**, 3788–3796 (1998).

71. Gomez-Pastor, R., Burchfiel, E. T. & Thiele, D. J. Regulation of heat shock transcription factors and their roles in physiology and disease. *Nat. Rev. Mol. Cell Biol.* **19**, 4–19 (2018).
72. Rocha, J. C. & MacDonald, A. Dietary intervention in the management of phenylketonuria: current perspectives. *Pediatr. Health Med. Ther.* **7**, 155–163 (2016).
73. Zischewski, J., Fischer, R. & Bortesi, L. Detection of on-target and off-target mutations generated by CRISPR/Cas9 and other sequence-specific nucleases. *Biotechnol. Adv.* **35**, 95–104 (2017).
74. Zhu, X. et al. An efficient genotyping method for genome-modified animals and human cells generated with CRISPR/Cas9 system. *Sci. Rep.* **4**, 6420 (2014).
75. Blau, N. et al. Variant of dihydropteridine reductase deficiency without hyperphenylalaninaemia: effect of oral phenylalanine loading. *J. Inherit. Metab. Dis.* **22**, 216–220 (1999).
76. Heintz, C., Troxler, H., Martinez, A., Thony, B. & Blau, N. Quantification of phenylalanine hydroxylase activity by isotope-dilution liquid chromatography-electrospray ionization tandem mass spectrometry. *Mol. Genet. Metab.* **105**, 559–565 (2012).
77. Livak, K. J. & Schmittgen, T. D. Analysis of relative gene expression data using real-time quantitative PCR and the 2(-Delta Delta C(T)) method. *Methods* **25**, 402–408 (2001).

Acknowledgements

We are very grateful to Altanchimeg Altankhuyag for skilled technical help with genotyping of mice, Trond-André Kråkenes for the TANGO calculations with PAH variants in the BIOPKU database, Dr. Marte Flydal and Dr. Helene Bustad Johannessen for expert help with purification of p.R261Q-PAH and consequent protein electron microscopy. We thank Dr. Øyvind Midttun and Professor Per M. Ueland for useful discussions on analyses and results on metabolic markers. This work was supported by Research Council of Norway grants FRIMEDBIO 261826/F20 and FORNY 248889/O30, the K.G. Jebsen Centre for Neuropsychiatric Disorders, and the Western Norway Regional Health Authorities (project 912246) (to A.M.). We acknowledge the Molecular Imaging Center and the BiSS core facility, both at the Department of Biomedicine, University of Bergen.

Author contributions

O.A., K.S.P., K.J.-K.C., M.Y., T.J.S.S., A.K.G., T.S., A.U., A.McC., and E.S. performed the experiments and analyzed the data. B.T. contributed to analyses and tools. K.S.P. was

responsible for breeding, genotyping and selection of mice, as well as specific mice studies. A.M. conceived and managed the project and analyzed the data. O.A. and A.M. wrote the paper with the contribution from all authors.

Competing interests

The authors declare no competing interests.

Additional information

Supplementary information The online version contains supplementary material available at <https://doi.org/10.1038/s41467-021-22107-1>.

Correspondence and requests for materials should be addressed to A.M.

Peer review information *Nature Communications* thanks Masato Ohtsuka, Eddy Van der Zee and the other, anonymous, reviewer(s) for their contribution to the peer review of this work.

Reprints and permission information is available at <http://www.nature.com/reprints>

Publisher's note Springer Nature remains neutral with regard to jurisdictional claims in published maps and institutional affiliations.



Open Access This article is licensed under a Creative Commons Attribution 4.0 International License, which permits use, sharing, adaptation, distribution and reproduction in any medium or format, as long as you give appropriate credit to the original author(s) and the source, provide a link to the Creative Commons license, and indicate if changes were made. The images or other third party material in this article are included in the article's Creative Commons license, unless indicated otherwise in a credit line to the material. If material is not included in the article's Creative Commons license and your intended use is not permitted by statutory regulation or exceeds the permitted use, you will need to obtain permission directly from the copyright holder. To view a copy of this license, visit <http://creativecommons.org/licenses/by/4.0/>.

© The Author(s) 2021

Supplementary Table 1. Mouse genome off-target analysis. The 16 possible off-target loci selected from BLAST analysis of the guide RNA towards the *Mus musculus* GRCm38/mm10 assembly genome and assayed by heteroduplex mobility. No off-target interactions could be detected.

Chromosome (No.)	DNA sequence ¹ (Non-seed_Seed_PAM)	Mismatches (No.)	Target site (Name)
7	AGgGGAAG_ACTCaGAAGGCC_AGG	2	Overlap exon <i>Shisa7</i> Overlap exon <i>C920025E04Rik</i>
17	AGcGGgAG_ACTCGAAaGCC_AGG	3	Overlap exon <i>Ptk7</i>
15	tGTaGAAG_ACTCGGAAGtCC_CGG	3	Overlap intron <i>Nell2</i>
3	tGTGcAgG_ACTgGGAAGGCC_AAG	4	Overlap exon <i>RP24-275F18.4</i>
5	taTcGAAG_ACTCGGAAGGaC_AGG	4	Overlap exon <i>Pcolce</i>
5	ttTGGAgG_ACTCGGAaggGCC_CGG	4	Overlap exon <i>Cyth3</i>
11	AGgGagAG_ACTgGGAAGGCC_TGG	4	Boundary exon <i>Flt4</i>
10	tGTctAAG_ACTCaGAAGGCC_AGG	4	Overlap intron <i>Stat6</i>
11	tcTaGAAG_cCTCGGAAGGCC_AAG	4	Overlap intron <i>Ntn1</i>
11	AtTccAAG_ACTCGGAAGGct-GAG	4	Overlap intron <i>Fat2</i>
14	cacGGAAG_ACTCGGAAGGct-GAG	4	Overlap intron <i>Arhgap22</i>
16	ccTcGAAG_ACTCGGAAGaCC-TGG	4	Overlap intron <i>Lpp</i>
6	AGTcGgAa_ACTCGGAAGaCC-AGG	4	Overlap intron <i>Plxna4</i>
6	AGTGGgcg_ACTCGGAAGGCa-GAG	4	Overlap intron <i>Raf1</i>
8	gGTGGcAa_ACTCGGAAGtCC-AAG	4	Overlap intron <i>Gm20388</i>

¹The DNA sequence is divided, for clarity purposes, in the non-seed region, seed region, and protospaceradjacent motif (PAM), with lowercases indicating the mismatched nucleotides.

Supplementary Table 2. Complete list of metabolites analyzed in isolated serum samples. The serum levels of 72 metabolites were analyzed by chromatographic separation and mass spectrometry detection.

Metabolite (Name)	<i>Pah-WT</i> (μM)	<i>Pah-R261Q</i> (μM)	<i>p</i> -value ¹	Method
Total Homocysteine	5.23 (2.41)	6.23 (2.37)	0.284	
Methylmalonic acid	0.701 (0.095)	0.585 (0.118)	0.060	
Total cysteine	241 (48)	267 (35)	0.708	
Methionine	61.8 (9.9)	57.8 (11.4)	0.172	
Serine	144 (28)	136 (21)	0.123	
Glycine	318 (55)	293 (45)	0.354	
Cystathionine	1.04 (0.57)	1.10 (0.31)	0.686	
Kynurenine	0.740 (0.234)	0.573 (0.264)	0.080	
Sarcosine	1.29 (0.59)	0.958 (0.414)	0.234	
Histidine	70.0 (10.5)	71.1 (11.5)	0.686	
Tryptophan	103 (24)	82.9 (30.9)	0.013	
Ornithine	61.2 (16.3)	58.9 (12.3)	0.624	
Aspartic acid	27.4 (14.4)	22.7 (11.0)	0.043	
Glutamic acid	39.5 (20.7)	29.4 (10.2)	0.008	
Lysine	306 (46)	279 (45)	0.470	
Alanine	444 (71)	362 (80)	0.010	
Phenylalanine	71.9 (10.3)	113 (22)	0.0000004	
Isoleucine	87.5 (12.8)	101 (24)	0.091	
Leucine	143 (23)	164 (42)	0.075	
Proline	90.2 (25.4)	73.0 (17.2)	0.085	
Valine	220 (28)	233 (38)	0.563	
Asparagine	49.0 (13.0)	47.9 (8.8)	0.103	
Glutamine	687 (76)	622 (112)	0.043	GC-MS/MS ^a
Threonine	145 (29)	140 (30)	0.123	
Tyrosine	81.3 (25.3)	77.9 (14.0)	0.050	
α-Ketoglutaric acid	38.6 (15.2)	26.3 (10.8)	0.003	
3-Hydroxyisobutyrate	22.8 (10.6)	22.1 (10.0)	0.773	
2-Hydroxybutyrate	18.3 (6.4)	14.1 (6.4)	0.529	
β-Hydroxybutyrate	150 (99)	282 (133)	0.029	
Acetoacetate	20.6 (21.7)	28.9 (15.9)	0.579	
Choline	25.7 (9.3)	30.1 (7.4)	0.236	
Betaine	67.3 (39.9)	69.2 (16.8)	0.808	
Dimethylglycine	9.70 (4.32)	10.6 (2.2)	0.715	
Creatinine	8.95 (2.29)	9.24 (2.35)	0.648	
Methionine sulfoxide	2.34 (1.29)	1.92 (1.20)	0.191	
Arginine	115 (17)	112 (19)	0.574	
Asymm.dimethylarginine	0.759 (0.244)	0.872 (0.218)	0.855	
Symm.dimethylarginine	0.296 (0.075)	0.360 (0.087)	0.202	LC-MS/MS ^b
Homoarginine	0.927 (0.207)	0.783 (0.277)	0.403	
Trimethyllysine	0.803 (0.165)	0.976 (0.213)	0.050	
Trimethylamineoxide	3.57 (6.31)	2.86 (6.02)	0.599	
Creatine	154 (40)	127 (30)	0.026	

1-Methylhistidine	2.90 (0.43)	2.70 (0.66)	0.976	
3-Methylhistidine	4.04 (1.50)	5.03 (2.12)	0.354	
5-Methyltetrahydrofolate	131 (23)	119 (33)	0.406	
5-Formyltetrahydrofolate	n.d.	n.d.	----	
Folic acid	1.39 (1.24)	1.32 (0.93)	0.908	
4- α -Hydroxy-5-methyl-THF	6.05 (1.53)	5.53 (2.65)	0.684	LC-MS/MS ^c
<i>p</i> -Aminobenzoylglutamate	35.1 (17.3)	32.5 (16.4)	0.853	
Acetoamidobenzoylglutamate	7.43 (2.96)	6.73 (3.00)	0.853	
Pyridoxal 5'-phosphate	0.232 (0.096)	0.276 (0.050)	0.351	
Pyridoxal	0.223 (0.085)	0.217 (0.102)	0.958	
4-Pyridoxic acid	0.034 (0.09)	0.036 (0.021)	0.681	
Pyridoxine	n.d.	n.d.	----	
Thiamine	0.331 (0.028)	0.273 (0.058)	0.112	
Thiamine monophosphate	0.372 (0.100)	0.425 (0.082)	0.758	
Riboflavin	0.066 (0.007)	0.066 (0.013)	0.918	
Flavin mononucleotide	0.037 (0.004)	0.032 (0.002)	0.252	
Neopterin	0.002 (0.001)	0.002 (0.001)	0.138	
Cotinine	n.d.	n.d.	----	
Trans-3'-hydroxycotinine	n.d.	n.d.	----	
3-Hydroxykynurenine	0.056 (0.019)	0.063 (0.017)	0.408	LC-MS/MS ^d
Kynurenic acid	0.050 (0.021)	0.058 (0.013)	0.351	
Xanthurenic acid	0.030 (0.024)	0.047 (0.019)	0.606	
Anthranilic acid	0.030 (0.005)	0.029 (0.006)	0.837	
3-Hydroxyanthranilic acid	0.012 (0.007)	0.012 (0.004)	0.606	
Picolinic acid	0.108 (0.056)	0.146 (0.058)	0.791	
Quinolinic acid	0.178 (0.090)	0.130 (0.041)	0.023	
Nicotinic acid	n.d.	n.d.	----	
Nicotinamide	4.74 (0.74)	4.29 (1.11)	0.351	
N1-methylnicotinamide	0.314 (0.066)	0.251 (0.140)	0.596	
Trigonelline	2.21 (1.09)	1.49 (1.28)	0.351	

Concentrations are expressed as arithmetic mean \pm SD; $n = 19$ *WT* and 19 *Pah-R261Q* mice. n.d., non-detectable (below detection limit).

¹Two-tailed *p*-values for differences between serum concentration in *Pah-WT* and *Pah-R261Q* from Mann Whitney U test. The highlighted metabolites in bold text show $p \leq 0.5$.

References

- Midttun O, *et al.* Combined Measurement of 6 Fat-Soluble Vitamins and 26 Water-Soluble Functional Vitamin Markers and Amino Acids in 50 μ L of Serum or Plasma by High-Throughput Mass Spectrometry. *Anal Chem* **88**, 10427-10436 (2016).
- Midttun O, Kvalheim G, Ueland PM. High-throughput, low-volume, multianalyte quantification of plasma metabolites related to one-carbon metabolism using HPLC-MS/MS. *Anal Bioanal Chem* **405**, 2009-2017 (2013).
- Hannisdal R, Ueland PM, Svoldal A. Liquid chromatography-tandem mass spectrometry analysis of folate and folate catabolites in human serum. *Clin Chem* **55**, 1147-1154 (2009).
- Midttun O, Hustad S, Ueland PM. Quantitative profiling of biomarkers related to B-vitamin status, tryptophan metabolism and inflammation in human plasma by liquid chromatography/tandem mass spectrometry. *Rapid Commun Mass Spectrom* **23**, 1371-1379 (2009).

Supplementary Table 3. Aromatic amino acid levels in brain

Amino acid	<i>Pah-</i>	<i>n</i> ¹	Brain (nmol/mg protein)
L-Phe	<i>WT</i>	6	0.38 ± 0.04
	<i>R261Q</i>	5	0.42 ± 0.12
L-Tyr	<i>WT</i>	6	0.29 ± 0.10
	<i>R261Q</i>	5	0.31 ± 0.09
L-Trp	<i>WT</i>	6	0.13 ± 0.02
	<i>R261Q</i>	5	0.13 ± 0.02

¹*n*, number of mice analysed in each group (3-month-old).

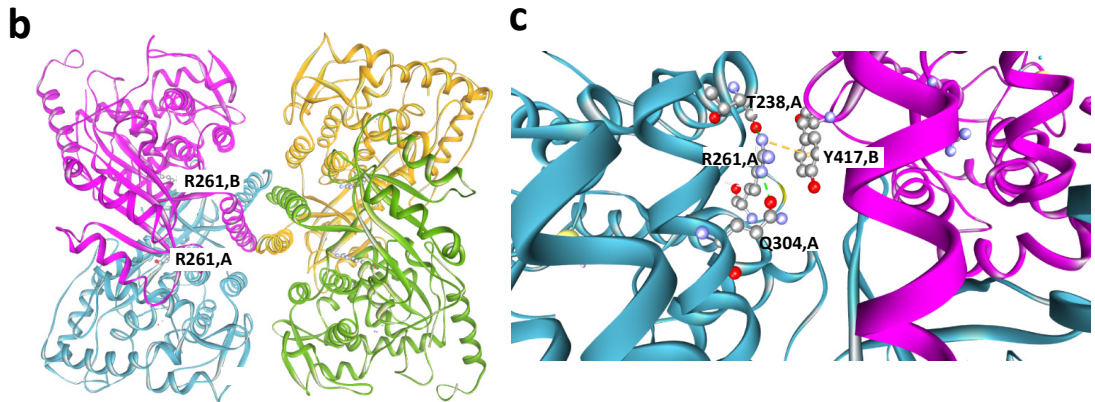
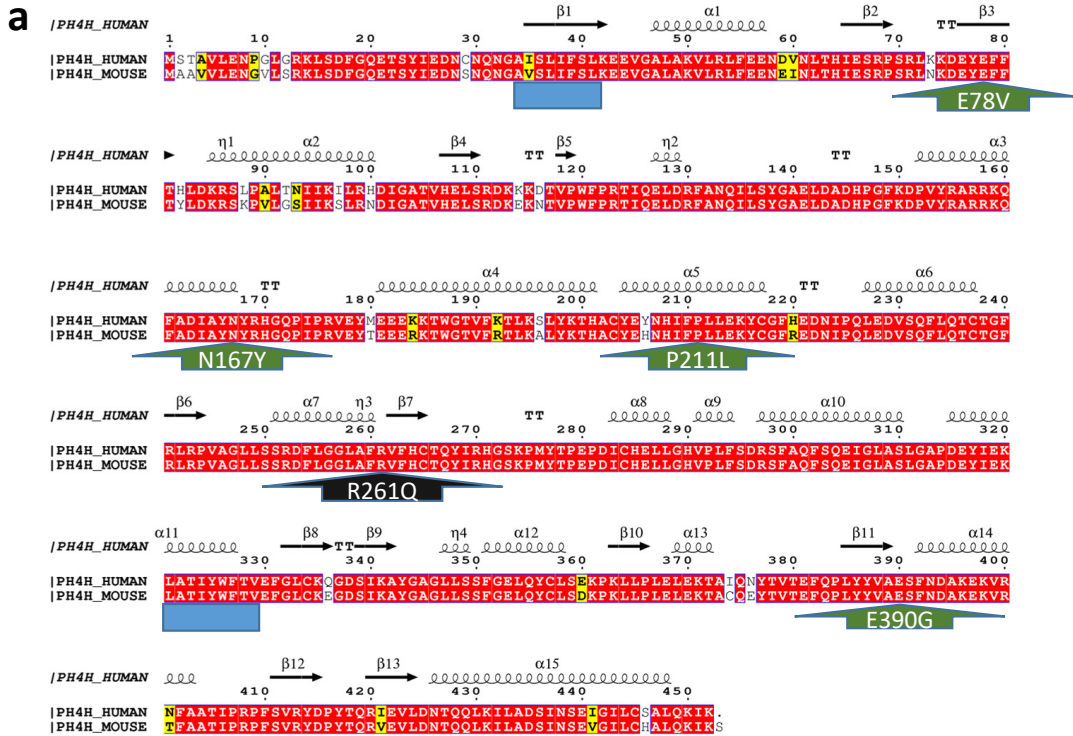
Supplementary Table 4. List of probes and primers used in the study***Quantitative RT-PCR probes***

Name	Assay ID	chromosome location	Nucleotide sequence accession code
mouse phenylalanine hydroxylase (PAH)	Mm00500918_m1	Chr.10: 87521795 - 87584137 on Build GRCm38	NM_008777.3
mouse Hsc70 (Hspa8)	Mm01731394_gH	Chr.9: 40801273 - 40805199 on Build GRCm38	NM_031165.4
mouse GTP cyclohydrolase 1 (Gch1)	Mm01322973_m1	Chr.14: 47153895 - 47189402 on Build GRCm38	NM_008102.3
mouse heat shock factor 1 (Hsf1)	Mm01201402_m1	Chr.15: 76477395 - 76500978 on Build GRCm38	NM_008296.2
mouse STIP1 homology and U-box containing protein 1 (Stub1)	Mm00490634_m1	Chr.17: 25830636 - 25833361 on Build GRCm38	NM_019719.3
mouse GTP cyclohydrolase I feedback regulator (Gchfr)	Mm00622819_m1	Chr.2: 119167788 - 119172389 on Build GRCm38	NM_177157.4
Mouse DNAJC12	Mm00497038_m1	Chr.10: 63382443 - 63408840 on Build GRCm38	NM_001253685.1
mouse sequestosome 1 (p62)	Mm00448091_m1	Chr.11: 50200152 - 50210820 on Build GRCm38	NM_001290769.1
mouse HSP70 (Hspa5)	Mm00517691_m1	Chr.2: 34772090 - 34776529 on Build GRCm38	NM_001163434.1
mouse adaptor protein complex AP-1, beta 1 subunit (Ap1b1)	Mm01187764_m1	Chr.11: 4947521 - 5042794 on build GRCm38	NM_001243043.1
mouse glyceraldehyde-3-phosphate dehydrogenase (GAPDH)	Mm99999915_g1	Chr.6: 125161338 - 125166511 on build GRCm38	NM_008084.3

Primers for genotyping

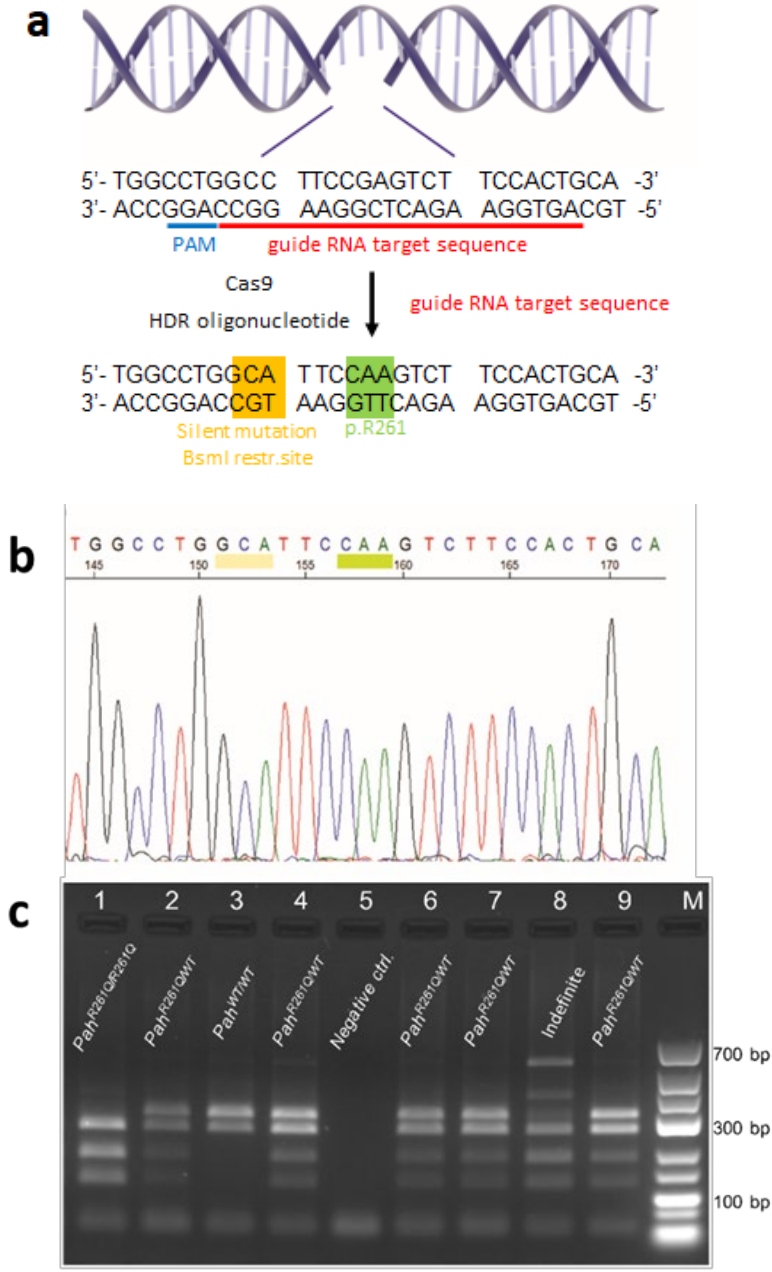
Name	Primer sequence
PAH genotype forward primer	5'-ATGCAGGATATCTAAGGTGCC-3'
PAH genotype reverse primer	5'-GAGATGCTGAGATCACTTGGC-3'

Supplementary Fig. S1



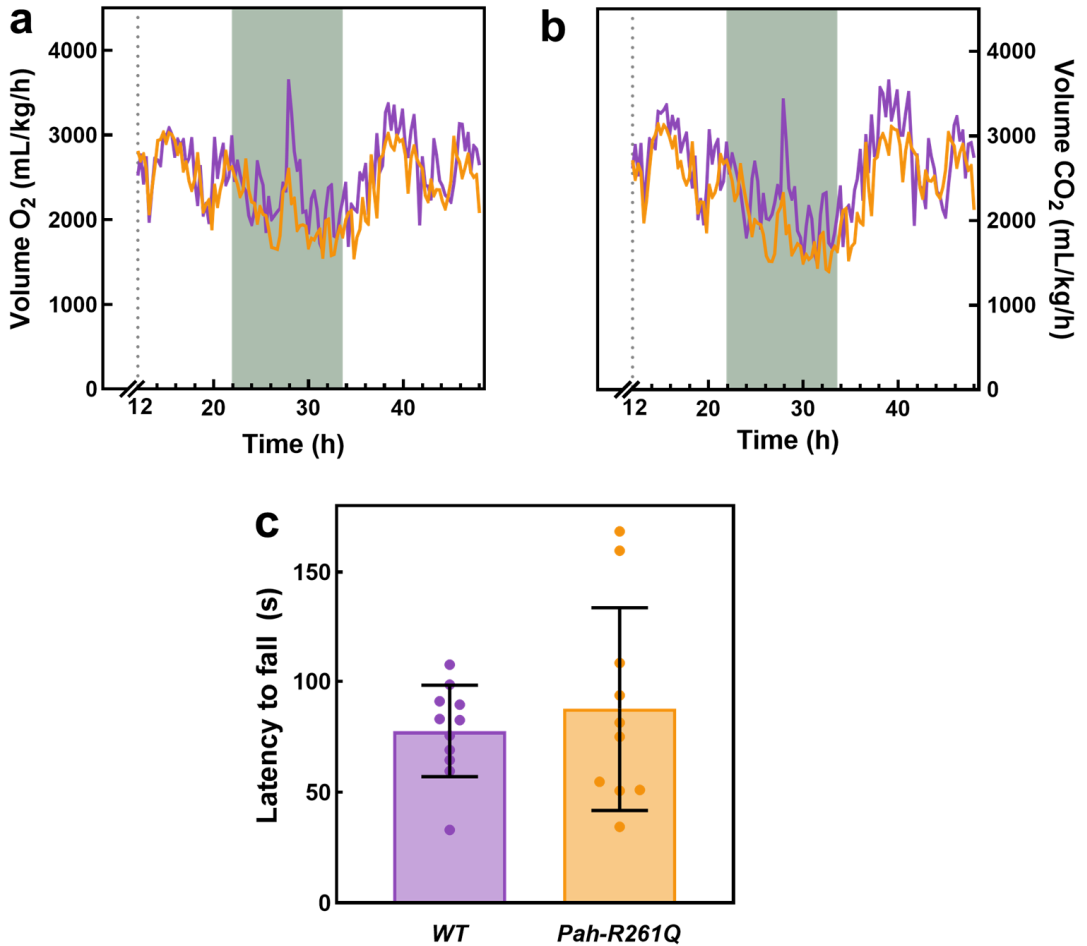
Supplementary Fig. 1. Sequence comparison and structural representation of PAH. a) Sequence alignment of human (P000439) and mouse (P16331) PAH. Identical residues (red background), conservative mutations (yellow background) and non-conservative mutations (white background) are highlighted. Prepared with ESPrnt (<http://esprnt.ibcp.fr>) with secondary structural motifs on top extracted from tetrameric human PAH (PDB 6HYC). Motifs predicted by TANGO (<http://tango.crg.es/>) to have high propensity to aggregate in a β -cross manner in the WT sequence are pointed by blue boxes, and motifs appearing in specific PKU mutant sequences are shown as broad green arrows, or as a black arrow for the R261 \rightarrow Q mutation studied here. b) Structural location of Arg261 in PAH subunits A (R261,A) and B (R261,B) (PDB 6HYC); each subunit is shown in a different color. c) Interactions of R261,A intra-subunit (with T238,A and Q304,A) and inter-subunit within one dimer (with Y417,B). The highlighted residues are shown in ball and stick representation.

Supplementary Fig. S2



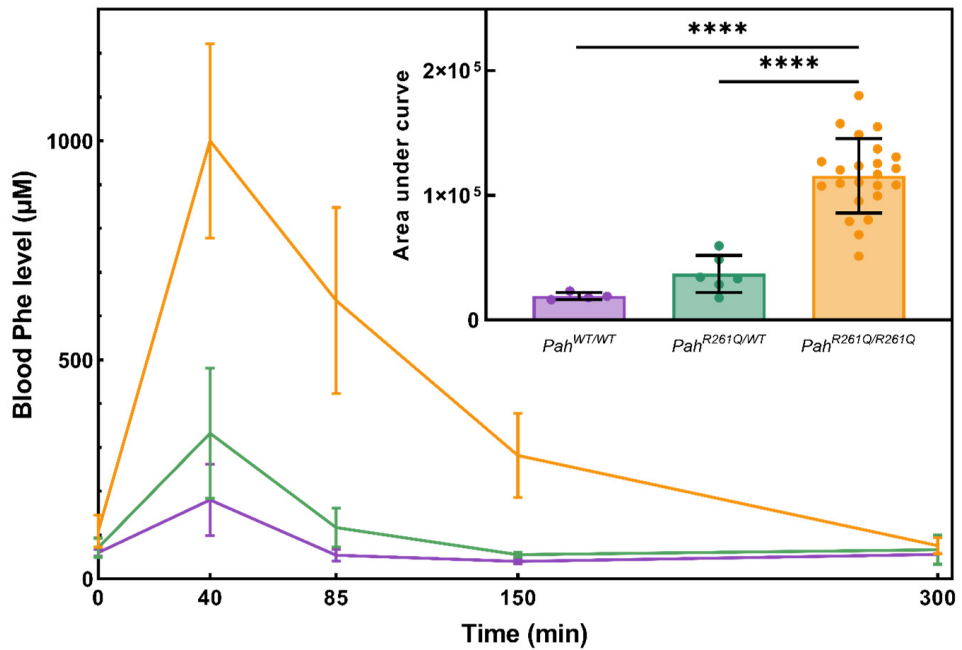
Supplementary Fig. 2. Generation and genotyping of the novel *Pah*-R261Q mouse model. a) Graphic schematic illustration of the CRISPR/Cas9 targeting strategy. The guide RNA target sequence (in red) and “PAM” (in blue) interact, complementarily, with the region of interest in exon 7 of *Pah* gene on murine chromosome 10 (NM_008777.3). The two introduced point mutations c.777C>A and c.782G>A (p.Arg261Gln) provided a successful Cas9 endonuclease action and homology-directed repair (HDR) integration, and are highlighted in ochre and green background, respectively. b) Confirmation of the germline-transmitted *Pah* mutation by evaluation of sequence chromatogram. c) Representative example of an agarose gel from a genotyping experiment. The encountered genotypes were *Pah*^{WT/WT} (2 bands), *Pah*^{R261Q/R261Q} (3 bands) and *Pah*^{R261Q/WT} (4 bands); molecular weights provided in main text. M, DNA ladder; negative ctrl., ddH₂O sample. For c) Source data are provided as a Source Data file

Supplementary Fig. S3



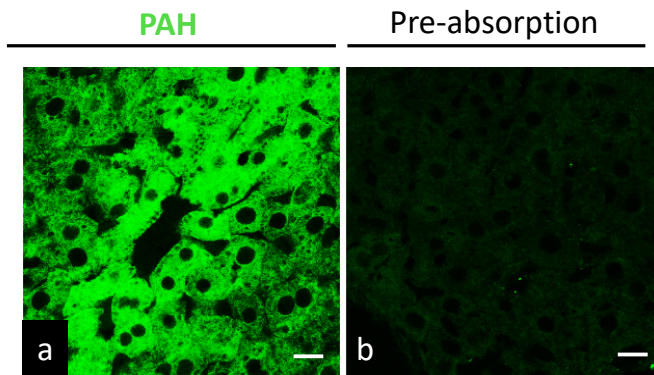
Supplementary Fig. 3. Time course of the volume of O₂ consumed and CO₂ produced and rotarod performance test. Volume of O₂ consumed (a) and CO₂ produced (b), measured in the metabolic cage. Averaged recordings with $n = 3$ *WT* and 5 *Pah-R261Q* mice in independent experiments, with one mouse per cage and 121 observations/animal. The 12 h acclimatization period was not included in the recordings. c) Motor function assessment by rotarod test. The bars express mean \pm SD ($n = 11$ *WT* and 10 *Pah-R261Q* mice, analyzed independently). The circles represent individual values for each mouse. In all panels, the data for *WT* are depicted in purple and *Pah-R261Q* in ochre. Source data are provided as a Source Data file.

Supplementary Fig. S4



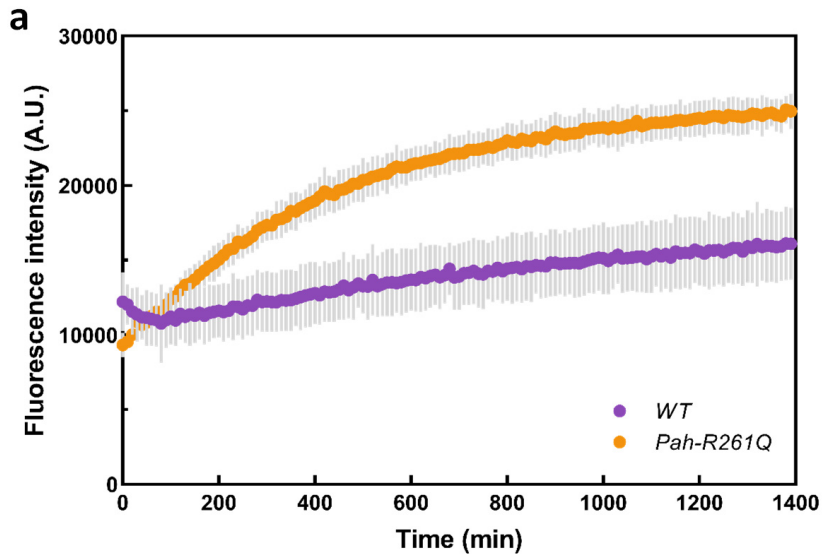
Supplementary Fig. 4. Effect of Phe challenge on blood L-Phe concentration in mice with different genotypes. At time 0, an L-Phe challenge (200 µg/g body weight) was provided by i.p. to *WT* (purple), *Pah*^{R261Q/WT} (green) and *Pah*^{R261Q/R261Q} (ochre) mice. The results represent the mean ± SD (*n*, number of animals, was 4 *Pah*^{WT/WT}, 6 *Pah*^{R261Q/WT} and 23 *Pah*^{R261Q/R261Q} mice). Inset, area under the curve (AUC) for the time dependence of L-Phe concentration between 0 and 300 min for the three genotypic groups. Data are presented as mean AUC ± SD. The circles represent the individual values for each mouse. Statistical significance between the groups was analyzed by Brown-Forsythe and Welch ANOVA test followed by Dunnett's multiple comparison test, providing *p* < 0.0001 (****) for both *Pah*^{R261Q/R261Q} vs. *Pah*^{WT/WT} and *Pah*^{R261Q/R261Q} vs. *Pah*^{R261Q/WT}. Source data are provided as a Source Data file.

Supplementary Fig. S5

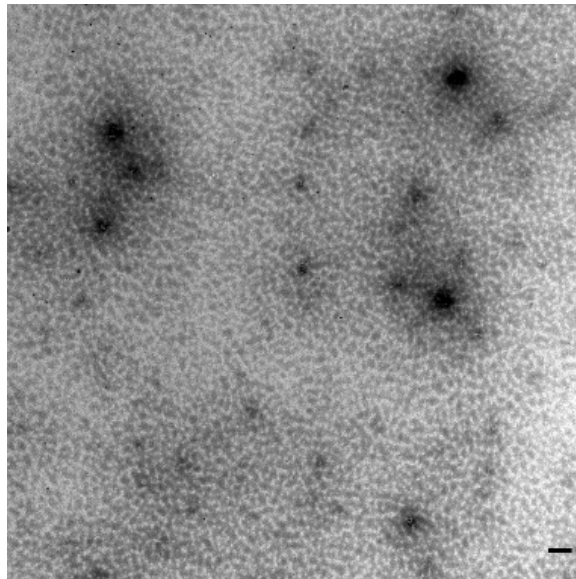


Supplementary Fig. 5. PAH immunostaining in liver of *WT* mice; specificity of the PAH antibody. a) Immunofluorescence staining reveals PAH immunoreactivity in the liver of *WT* mice. b) Disappearance of PAH staining in the *WT* liver after an antibody pre-absorption treatment with purified recombinant PAH. Scale bars are 10 μm . These are representative images based on experiments performed with two liver lysates, prepared from a different *WT* mouse each ($n = 2$), with three replicates for each preparation. Source data are provided as a Source Data file.

Supplementary Fig. S6



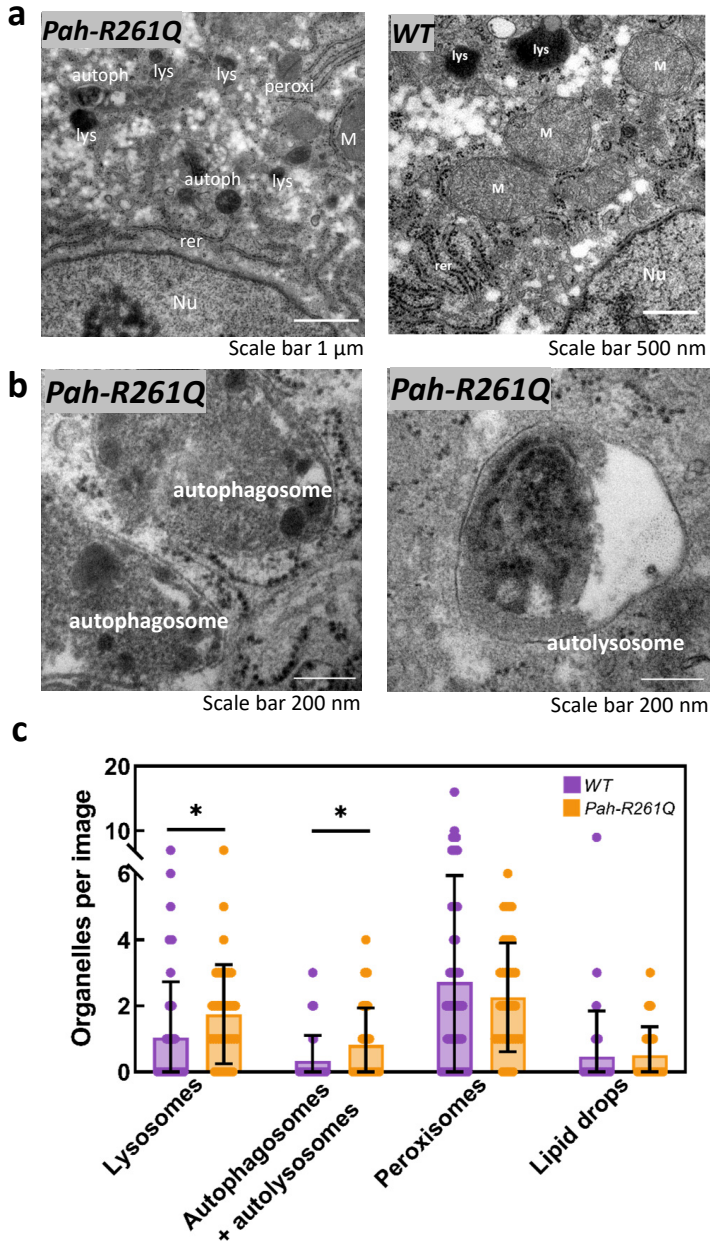
b



Scale bar 100 nm

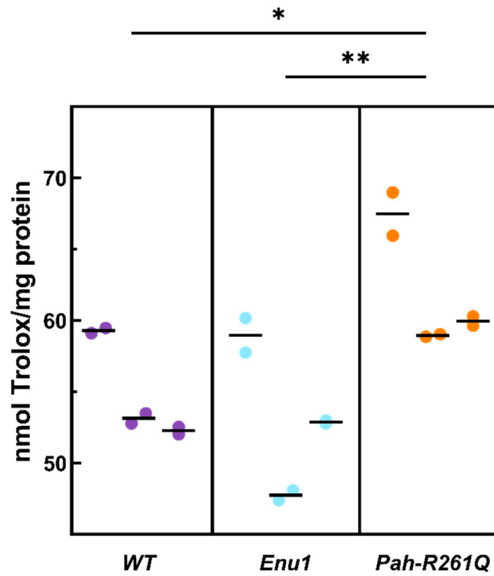
Supplementary Fig. 6. Amyloid-like aggregation of the p.R261Q-PAH protein. a) AmytrackerTM680 assay with recombinant purified proteins WT-PAH (purple) and p.R261Q-PAH (ochre), with 1 mg/ml of each protein in 20 mM Na-Hepes, 200 mM NaCl, pH 7 and incubation at 37 °C. The results represent the mean and SD (gray lines) at each time point for $n = 3$ (independent protein samples). b) Transmission electron microscopy (TEM) with negative staining for p.R261Q-PAH, after 5 h incubation at 37 °C and buffer exchange to 20 mM Na-phosphate, pH 7. The protein was applied to the grid at 0.02 mg/ml; at time 0, no particles > 20 nm in diameter are observed. Representative TEM micrograph from $n = 3$ (independent protein samples). Tetrameric PAH has a diameter of 10 nm (PDB 6HYC). Source data are provided as a Source Data file.

Supplementary Fig. S7



Supplementary Fig. 7. Transmission electron microscopy (TEM) of liver tissue. a) Representative micrographs showing normal cellular and organelle morphology in *Pah-R261Q* mice. Nu, nucleus; M, mitochondria; lys, lysosome; autoph, autophagosome; peroxi, peroxisomes; rer, rough endoplasmic reticulum. b) TEM micrographs showing two double-membrane autophagosomes and one autolysosome, representative of $n = 3$ biological replicates per mice group. c) Quantification of different organelles in images acquired in hepatocytes from both *WT* (purple) and *Pah-R261Q* (ochre) mice. 40 TEM images at 20,000 magnification were analyzed for each mice. The results represent the mean \pm SD. Statistical significance between both groups was calculated using two-tailed unpaired t-test; $p = 0.0402$ for lysosomes (*) and $p = 0.0151$ (*) for autophagosomes + autolysosomes.

Supplementary Fig. S8



Supplementary Fig. 8. Measurement of oxidative stress in liver lysates of mice models with different genotype. Total antioxidant capacity using the Trolox (6-hydroxy-2,5,7,8-tetramethylchroman-2-carboxylic acid) assay in liver lysates of *WT* (purple), *Pah^{R261Q/WT}* (blue) and *Pah^{R261Q/R261Q}* (ochre). Two independent lysates per mouse and $n = 3$ (biological replicates) per mice group were analyzed. Data are presented as means, and circles representing individual values, for each lysate. Statistical significance between the groups was calculated by one-way ANOVA followed by post hoc Tukey test, providing $p = 0.029$ (*) for *Pah-R261Q* vs. *WT* (*) and $p = 0.006$ (**) for *Pah-R261Q* vs. *Enu1*.

PAPER III

Phosphorylation at serine 31 targets tyrosine hydroxylase to vesicles for transport along microtubules.

Ana Jorge-Finnigan, Rune Kleppe, [Kunwar Jung-KC](#), Ming Ying, Michael Marie, Ivan Rios-Mondragon, Michael F. Salvatore, Jaakko Saraste, and Aurora Martinez

J Biol Chem. 292(34): 14092–14107 doi: 10.1074/jbc.M116.762344 (2017)

Abstract

Tyrosine hydroxylase (TH) catalyzes the conversion of L-tyrosine into L-DOPA, which is the rate-limiting step in the synthesis of catecholamines, such as dopamine, in dopaminergic neurons. Low dopamine levels and death of the dopaminergic neurons are hallmarks of Parkinson's disease (PD), where α -synuclein is also a key player. TH is highly regulated, notably by phosphorylation of several Ser/Thr residues in the N-terminal tail. However, the functional role of TH phosphorylation at the Ser-31 site (THSer(P)-31) remains unclear. Here, we report that THSer(P)-31 co-distributes with the Golgi complex and synaptic-like vesicles in rat and human dopaminergic cells. We also found that the TH microsomal fraction content decreases after inhibition of cyclin-dependent kinase 5 (Cdk5) and ERK1/2. The cellular distribution of an overexpressed phospho-null mutant, TH1-S31A, was restricted to the soma of neuroblastoma cells, with decreased association with the microsomal fraction, whereas a phospho-mimic mutant, TH1-S31E, was distributed throughout the soma and neurites. TH1-S31E associated with vesicular monoamine transporter 2 (VMAT2) and α -synuclein in neuroblastoma cells, and endogenous THSer(P)-31 was detected in VMAT2- and α -synuclein-immunoprecipitated mouse brain samples. Microtubule disruption or co-transfection with α -synuclein A53T, a PD-associated mutation, caused TH1-S31E accumulation in the cell soma. Our results indicate that Ser-31 phosphorylation may regulate TH subcellular localization by enabling its transport along microtubules, notably toward the projection terminals. These findings disclose a new mechanism of TH regulation by phosphorylation and reveal its interaction with key players in PD, opening up new research avenues for better understanding dopamine synthesis in physiological and pathological states.



Phosphorylation at serine 31 targets tyrosine hydroxylase to vesicles for transport along microtubules

Received for publication, October 7, 2016, and in revised form, June 13, 2017. Published, Papers in Press, June 21, 2017, DOI 10.1074/jbc.M116.762344

Ana Jorge-Finnigan^{‡§1}, Rune Kleppe^{‡§}, Kunwar Jung-KC^{‡§}, Ming Ying[‡], Michael Marie[¶], Ivan Rios-Mondragon[‡], Michael F. Salvatore^{||}, Jaakko Saraste[‡], and Aurora Martinez^{‡§}

From the [‡]Department of Biomedicine, University of Bergen, Jonas Lies vei 91, 5009 Bergen, Norway, the [§]K. G. Jebsen Centre for Neuropsychiatric Disorders, Jonas Lies vei 91, 5009 Bergen, Norway, the [¶]Department of Molecular Biology, University of Bergen, Thormøhlensgaten 55, 5020 Bergen Norway, and the ^{||}Institute for Healthy Aging, University of North Texas Health Science Center, Fort Worth, Texas 76107

Edited by Paul E. Fraser

Tyrosine hydroxylase (TH) catalyzes the conversion of L-tyrosine into L-DOPA, which is the rate-limiting step in the synthesis of catecholamines, such as dopamine, in dopaminergic neurons. Low dopamine levels and death of the dopaminergic neurons are hallmarks of Parkinson's disease (PD), where α -synuclein is also a key player. TH is highly regulated, notably by phosphorylation of several Ser/Thr residues in the N-terminal tail. However, the functional role of TH phosphorylation at the Ser-31 site (THSer(P)-31) remains unclear. Here, we report that THSer(P)-31 co-distributes with the Golgi complex and synaptic-like vesicles in rat and human dopaminergic cells. We also found that the TH microsomal fraction content decreases after inhibition of cyclin-dependent kinase 5 (Cdk5) and ERK1/2. The cellular distribution of an overexpressed phospho-null mutant, TH1-S31A, was restricted to the soma of neuroblastoma cells, with decreased association with the microsomal fraction, whereas a phospho-mimic mutant, TH1-S31E, was distributed throughout the soma and neurites. TH1-S31E associated with vesicular monoamine transporter 2 (VMAT2) and α -synuclein in neuroblastoma cells, and endogenous THSer(P)-31 was detected in VMAT2- and α -synuclein-immunoprecipitated mouse brain samples. Microtubule disruption or co-transfection with α -synuclein A53T, a PD-associated mutation, caused TH1-S31E accumulation in the cell soma. Our results indicate that Ser-31 phosphorylation may regulate TH subcellular localization by enabling its transport along microtubules, notably toward the projection terminals. These findings disclose a new mechanism of TH regulation by phosphorylation and reveal its interaction with key players in PD, opening up new research avenues for better understanding dopamine synthesis in physiological and pathological states.

Catecholamine neurotransmission disturbances are hallmarks of neurodegenerative and neuropsychiatric diseases,

such as Parkinson's disease (PD),² Alzheimer's disease, L-DOPA-responsive dystonia, or tyrosine hydroxylase deficiency (1–4). Catecholamines are stored in vesicles that originate at the Golgi complex (GC) and are transported through the classical secretory pathway (5). GC fragmentation, loss of vesicle integrity, and dysfunctional vesicular transport have emerged as pathomechanisms involved in neurodegenerative disorders, notably PD (6–8). A key enzyme in the synthesis of catecholamine neurotransmitters is tyrosine hydroxylase (TH), which catalyzes the hydroxylation of L-tyrosine into L-DOPA (L-3,4-dihydroxyphenylalanine), the rate-limiting step in the synthesis of dopamine (DA). DA is then pumped and loaded into vesicles by the vesicular monoamine transporter 2 (VMAT2) (9). The TH gene encodes one protein isoform in lower mammals, but alternative splicing gives four in humans (TH1–TH4) (10, 11). Rat TH is homologous to the TH1 human isoform, the most abundant isoform in humans together with TH2.

TH activity is controlled by catecholamine feedback inhibition and phosphorylation of its N-terminal residues 8, 19, 31, and 40 (THSer(P)-8, THSer(P)-19, THSer(P)-31, and THSer(P)-40) by different kinases (12, 13). THSer(P)-19 induces the high-affinity binding to 14-3-3 proteins, which increases TH activity and stability (14). Ser-19 increases the phosphorylation at Ser-40 in a hierarchical manner, leading to increased activity (13). On the other hand, binding of 14-3-3 to THSer(P)-19 decreases Ser-40 phosphorylation (15). THSer(P)-40 releases TH from catecholamine feedback inhibition, increasing the activity 20-fold (16). The functional implications of THSer(P)-8 are currently lacking, and a comprehensive understanding of the physiological role of THSer(P)-31 also remains unclear. Cdk5 and ERK1/2 phosphorylate TH (human isoforms 1, 3, and 4 and rodent TH) at Ser-31 (17–19), which increases TH activity about 2-fold *in vitro* (20) and *in situ* (21). In 2006, Lehman *et al.* (22) reported that for human TH1, phosphorylation at Ser-31 also produced a 9-fold increase in the rate of phosphoryla-

This work was supported by Research Council of Norway Grant FRIMEDBIO 214012 and the K. G. Jebsen Foundation. The authors declare that they have no conflicts of interest with the contents of this article.

¹Supported by the Norwegian Research Council (Yggdrasil 210731), Fundación Ramón Areces, Helse Vest, and European Union Marie Curie IF Program Grant PIF-GA-2011-299972. To whom correspondence should be addressed. E-mail: ana.jorge-finnigan@uib.no.

²The abbreviations used are: PD, Parkinson's disease; L-DOPA, L-3,4-dihydroxyphenylalanine; GC, Golgi complex; TH, tyrosine hydroxylase; DA, dopamine; VMAT2, vesicular monoamine transporter 2; NGF, neuronal growth factor; α -syn, α -synuclein; R/S, roscovitine and SL327; sytl, synaptotagmin I; PLA, proximity ligation assay; WGA, wheat germ agglutinin; CVM, chromaffin vesicle membrane.

tion at Ser-40. THSer(P)-31 is abundant at the axonal terminals of dopaminergic neurons (23), and it has been reported to increase about 3-fold in NGF-stimulated PC12 cells, whereas THSer(P)-40 is unaffected by NGF (24). Moreover, THSer(P)-31 increases TH stability in cells (25), and it may increase TH activity regardless of THSer(P)-40 under depolarizing conditions (16, 21). In the terminal fields of the central nervous system, there is a greater DA and L-DOPA content, coinciding with greater THSer(P)-31 compared with somatodendritic compartments, whereas no consistent differences in THSer(P)-40 have been reported (23, 26). Under experimental PD conditions, THSer(P)-31 stoichiometry is decreased in the striatum but increased in the substantia nigra; this pattern is also shown by DA per remaining TH; however, total amounts of TH and of THSer(P)-40 decreased in both brain areas (27). Therefore, THSer(P)-31 may affect TH activity within the range of phosphorylation stoichiometries normally seen in the central nervous system and be independent of Ser-40 phosphorylation differences. Despite the body of results, the physiological role of Ser-31 phosphorylation is still not fully understood. TH is characterized as a largely soluble and cytoplasmic tetrameric protein; however, its physiological association with membranes (28) has recently been proven to involve binding to partners, such as VMAT2 (9) and Hsc70 (29). However, the mechanism whereby TH is targeted to the synaptic vesicles still remains elusive. In this work, we investigated the functional role of Ser-31 phosphorylation, and our results indicate the association of THSer(P)-31 with the GC and the vesicular transport pathway, through VMAT2 and α -synuclein (α -syn). α -Syn is a synaptic vesicle associated-protein and a culprit in the development of PD (30). TH and α -syn are known to interact (31), but the association of both proteins at synaptic vesicles and coordinated microtubular transport is presented here for the first time. Furthermore, our results position THSer(P)-31 at sites and processes disturbed in PD and other neurodegenerative disorders, such as loss of vesicle integrity, defective vesicle trafficking, and GC fragmentation, and may contribute to explaining the early loss of striatal TH and DA that characterize PD (32).

Results

THSer(P)-31 localizes to the Golgi complex and synaptic-like vesicles

The cellular distribution of the different phosphorylated forms of TH at Ser-19, Ser-31, and Ser-40 was investigated by immunofluorescence using specific antibodies. These antibodies have been used in previous studies (26, 27, 33). Western blots of HEK293 cell extracts expressing either recombinant human V5-TH1-WT or the corresponding phospho-null (Ser \rightarrow Ala) and phospho-mimicking (Ser \rightarrow Glu) mutations for Ser(P)-19, Ser(P)-31, and Ser(P)-40, show low reactivity for the corresponding Ser \rightarrow Ala protein for the three antibodies (Fig. 1, A–C). THSer(P)-31 and THSer(P)-40 antibodies react both with the WT form (Fig. 1, B and C), phosphorylated at the corresponding site, and also with the phospho-mimicking mutants, whereas the THSer(P)-19 antibody only reacts with

Ser-19-phosphorylated WT (Fig. 1A). In undifferentiated PC12Adh (from ATCC) cells permeabilized with Triton X-100, THSer(P)-19 showed a nuclear distribution, and THSer(P)-31 as well as THSer(P)-40 showed a cytosolic distribution (data not shown), consistent with recent results (34).

To preserve TH interaction with partner proteins, we used saponin, a mild permeabilization agent, which allowed us to visualize THSer(P)-31 as punctate structures enriched in the perinuclear region, notably observed in the immense majority of PC12* cells (Fig. 1D). PC12* is an in-house clone derived from Ref. 35, which was chosen for its elevated responsiveness to NGF, leading to neurite abundance and stability (35), and has been used previously in signaling studies (36). Specific pharmacological inhibition of Cdk5 and ERK1/2 by roscovitine and SL327 (R/S) treatment (37, 38) abolished the THSer(P)-31 signal both in Western blotting and immunofluorescence (Fig. 1D), indicating that the perinuclear signal is specific. This distribution was clearly distinct from total TH, THSer(P)-19, and THSer(P)-40 (Fig. 1E, top panels), and these signals were not affected by the R/S inhibition of Cdk5 and ERK1/2 (Fig. 1E, bottom panels). Moreover, in 45% of PC12Adh cells ($n = 130$) and 35% of iCell DopaNeurons (human dopaminergic pluripotent cells) ($n = 50$), the perinuclear enrichment was also observed (Fig. 1, F and G). Because stimulation with NGF increases THSer(P)-31 (24), we investigated its effect on THSer(P)-31 distribution. Interestingly, NGF treatment led to a punctate THSer(P)-31 signal throughout the cell soma and neurites of PC12* (Fig. 1H), similar to the distribution of THSer(P)-31 in PC12Adh and iCell DopaNeurons (Fig. 1, F and G). It is well established that PC12 can give rise to specific phenotypes as described previously in depth (39–41) and illustrated here when profiling different proteins of the dopamine pathway in the presence or absence of NGF stimulation by Western blotting (Fig. 1I), where we observe that THSer(P)-31 content increases in PC12Adh by 10% after NGF treatment, whereas it increases by 2-fold in PC12*, in agreement with previous studies (24).

THSer(P)-31 signal in PC12* resembled a GC pattern, and its co-detection with the GC marker GM130 showed co-distribution in PC12Adh, iCell DopaNeurons, and PC12* cells (Fig. 2, A–C). Moreover, disassembly of the GC with brefeldin A abolished the THSer(P)-31 signal (Fig. 2C). To further investigate the punctate signal, we co-detected THSer(P)-31 and synaptic-like vesicle marker synaptotagmin I (sytl), which showed a certain signal overlapping in NGF-stimulated and unstimulated PC12Adh (Fig. 2D). Similarly, THSer(P)-31 in iCell DopaNeurons also co-distributed with sytl (Fig. 2E). Notably, fluorescence signals of immunolabeled VMAT2 and THSer(P)-31 highly overlapped in iCell DopaNeurons (Fig. 2E). Our results thus indicate that THSer(P)-31 associates with synaptic-like vesicles in rat PC12Adh cells and in a human dopaminergic neuronal model.

Phosphorylation of TH at Ser-31 is necessary for its association with vesicles

To determine whether the association of TH to vesicles is dependent on phosphorylation at Ser-31, we treated cell cultures with Cdk5 and ERK1/2 kinase inhibitors (combined ros-

TH Ser-31 phosphorylation targets TH to vesicles

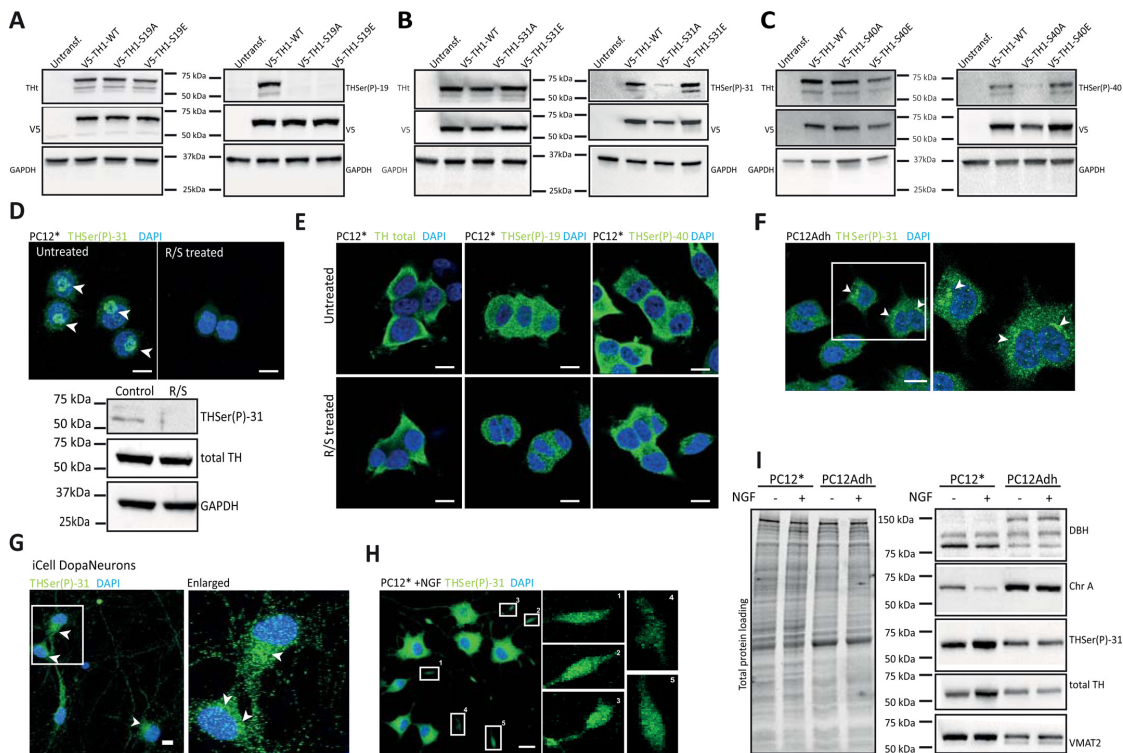


Figure 1. Distribution of TH phosphorylated forms. A–C, HEK293 cells were transfected with the WT or the phospho-null V5-TH1-S19A, V5-TH1-S31A, and V5-TH1-S40A or the phospho-mimicking V5-TH1-S19E, V5-TH1-S31E, and V5-TH1-S40E constructs. Phosphorylation at Ser-19, Ser-31, or Ser-40 was detected by Western blotting, loading equal amounts of total protein. Total TH (TH), V5 (transfection control), and GAPDH (loading control) detection was also carried out. D, immunofluorescence (top panels) of THSer(P)-31 in PC12* cells treated or not with R/S to inhibit Ser-31 phosphorylation and corresponding Western blot analysis (bottom panel), where total TH and GAPDH were also detected as controls. Arrows, perinuclear signal. E, immunofluorescence of total TH, THSer(P)-19, and THSer(P)-40 in PC12* cells treated or not with R/S. F, cellular distribution of THSer(P)-31 in PC12Adh. Arrows, perinuclear signal. G, cellular distribution of THSer(P)-31 in human pluripotent induced dopaminergic neurons (iCell DopaNeurons). Arrows, perinuclear signal. H, THSer(P)-31 distribution in PC12* stimulated with 50 ng/ml 2.5S NGF for 48 h. Insets, enlarged numbered areas. In all images, 10- μ m scale bars are shown, and all nuclei are stained with DAPI (blue). I, whole-lysate Western blot of PC12* and PC12Adh cell lines stimulated or not with NGF and detection of dopamine-related marker proteins such as DOPA β -hydroxylase (DBH), chromogranin A (Chr A), total TH, THSer(P)-31, and vesicular monoamine transporter 2 (VMAT2). Equal amounts of protein were loaded as shown in the total protein loading represented in the right panel.

covitine and SL327 treatment) and isolated the microsomal fractions (enriched in endoplasmic reticulum, GC, endosomes, and vesicles among other membranous cellular structures). We compared total TH levels of treated *versus* untreated cells to determine whether inhibition of phosphorylation at Ser-31 caused a decrease in the amount of total TH present in the microsomal fraction. Our results show that the treatment led to a large decrease of total TH in the microsomal fractions of PC12* (Fig. 3A), suggesting that phosphorylation at Ser-31 is needed for TH to associate with vesicles. Actually, a strong decrease of the signal from THSer(P)-31 was also observed in the microsomal fraction (Fig. 3A) in agreement with Ref. 25 and confirming that the treatment led to the inhibition of phosphorylation at Ser-31.

However, to rule out the possibility that the decreased observed was due an impairment of vesicle biogenesis caused by the kinase inhibition, we tested the effect of the treatment on different microsomal markers. Specifically, we treated PC12Adh cells with or without roscovitine and SL327 and

detected GC marker (GM130), endoplasmic reticulum marker (SPC25), endosome markers (clathrin and transferrin receptor), and dopamine-containing vesicle marker (VMAT2). The treatment did not lead to decreases in the signal of any of these markers (Fig. 3B).

To further confirm the role of THSer(P)-31 in this vesicle association, we performed Western blotting of cell fraction of neuroblastoma cells expressing V5-TH1-S31A and V5-TH1-S31E, which showed that V5-TH1-S31A was decreased in the microsomal fraction by 20% when compared with the wild type, whereas V5-TH1-S31E was increased by 20% (Fig. 3C). To rule out possible artifacts, we also treated V5-TH1-S31E-transfected cells with the kinase inhibitors, and then we compared the amounts of V5-TH1-S31E in the microsomal fractions, without finding significant differences (Fig. 3D). These results reinforce the specificity of the Ser-31 phosphorylation for TH vesicle association. However, compared with the large effect of the chemical inhibition of Ser-31 phosphorylation (Fig. 3A), the effect of the phospho-null mutation was less pro-

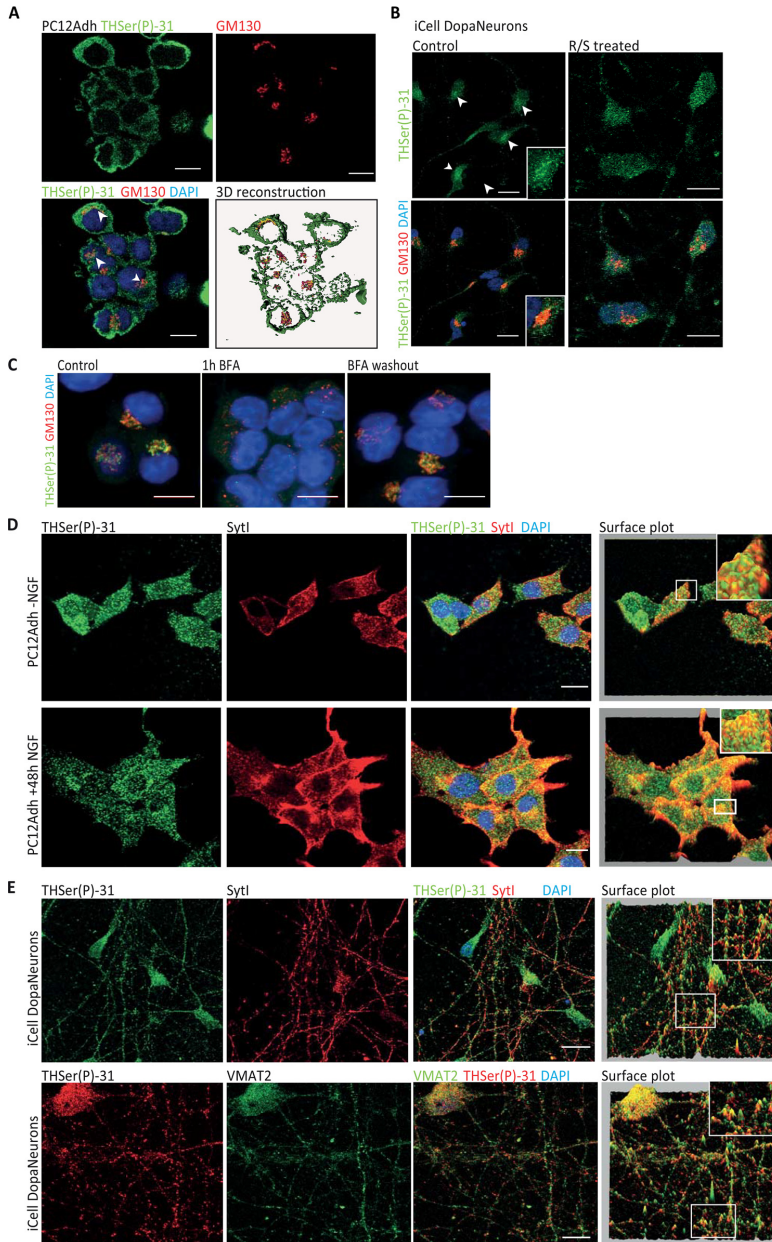


Figure 2. Endogenous THSer(P)-31 co-distribution with Golgi complex and vesicle markers. *A*, co-detection of THSer(P)-31 (green) with the Golgi marker GM130 (red) in PC12Adh (maximum projection of the confocal stack is shown) and 3D rendering of each signal and the corresponding co-localization channel in yellow. Arrows, perinuclear signal. *B*, co-detection of THSer(P)-31 (green) with the Golgi marker GM130 (red) in DopaNeurons treated or not with R/S. Arrows, perinuclear signal. *C*, GC disruption in PC12* by 30 min 5 μ g/ml brefeldin A (BFA) incubation and subsequent reassembly by drug washout. Untreated samples are presented as control. *D*, THSer(P)-31 (green) co-detection with synaptotagmin I (sytl; red) in PC12Adh cells without (top) and with (bottom) NGF treatment. *E*, THSer(P)-31 co-detection of sytl (top) and VMAT2 (vesicular monoamine transporter 2; bottom) in iCell DopaNeurons. For *D* and *E*, pixel height in the surface plot represents the pixel intensity in the confocal plane. In all images, nuclei are stained with DAPI, and 10- μ m scale bars are shown.

TH Ser-31 phosphorylation targets TH to vesicles

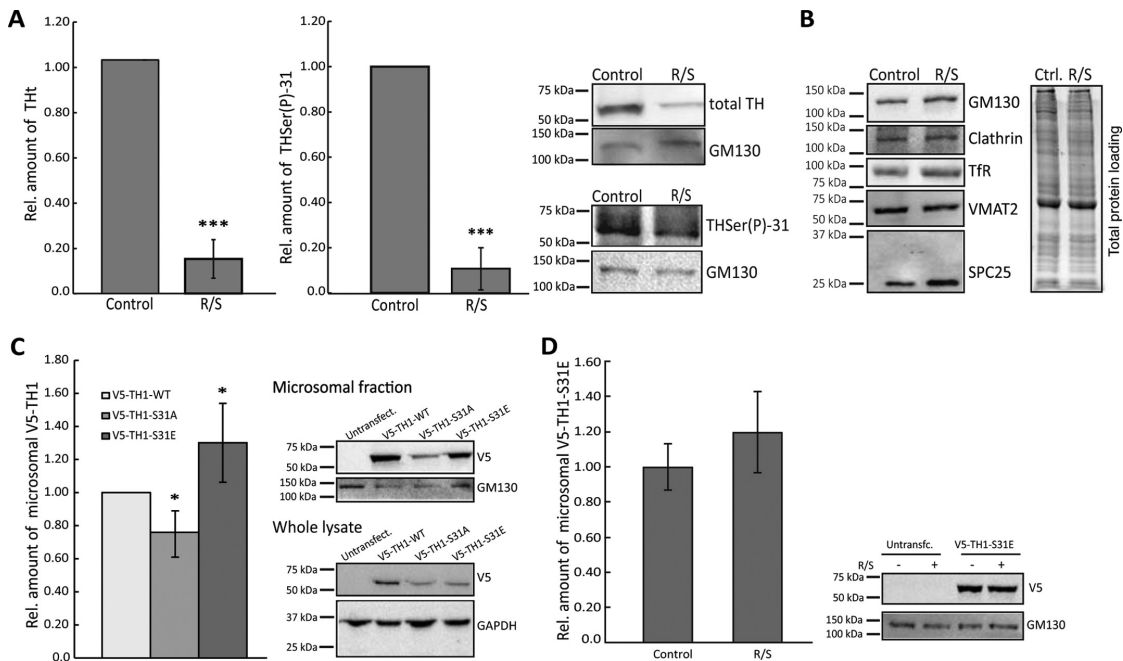


Figure 3. Requirement of TH phosphorylation at Ser-31 for interaction with vesicles. *A*, relative amount of total TH and THSer(P)-31 in PC12* microsome fractionation analyzed by Western blotting after inhibition of Ser-31 phosphorylation with 50 μ M roscovitine and 50 μ M SL327 (R/S). *Bars*, average relative amount of TH or THSer(P)-31 compared with the untreated samples (*t* test was used for statistical sample comparison; ***, $p < 0.001$; data are represented as mean \pm S.D. (*error bars*); $n = 3$). *Representative blots* are shown. *B*, relative amounts of markers to determine the vesicle biogenesis status in microsome fraction treated or not with R/S. The markers analyzed were GM130 for GC, clathrin, and transferrin receptor (*TfR*) for endosomes; VMAT2 for dopamine-vesicles; and SPC25 (signal peptidase complex 25) for endoplasmic reticulum. Equal amounts of treated and untreated samples were loaded, as shown in the total protein loading (*right*). *C*, relative amount of recombinant V5-TH1-WT, V5-TH1-S31A, or V5-TH1-S31E overexpressed in microsome fractions of neuroblastoma cells. Microsome fractions were analyzed by Western blotting using the V5 tag for detection, and mutant THs were compared with WT (*representative blots* are shown). *Bars*, relative amount of the WT construct compared with the mutant proteins (*t* test was used for statistical sample comparison; *, $p < 0.05$; data are represented as mean \pm S.D.; $n = 3$). *D*, relative amount of recombinant V5-TH1-S31E overexpressed in microsome fractions of neuroblastoma cells treated or not with R/S. Microsome fractions were analyzed by Western blotting using the V5 tag for detection, and treated samples were compared with controls (*representative blots* are shown). *Bars*, relative amount of the control samples compared with the treated samples (*t* test was used for statistical sample comparison, although no significant differences were found; data are represented as mean \pm S.D.; $n = 3$).

nounced. This may be explained by hetero-oligomerization of recombinant and endogenous monomers, as has been shown in other cases (42, 43), which would lead to a vesicular interaction of oligomers formed of phospho-null and THSer(P)-31 subunits. The phospho-variant data are consistent with the results from the chemical inhibition of Cdk5 and ERK1/2 and rule out the possibility that the observed effect would be due to either nonspecific effects of Cdk5 and ERK1/2 on other proteins directly or indirectly involved in THSer(P)-31 association with vesicles. Again, these results show that TH needs to be phosphorylated at Ser-31 to bind to vesicles.

THSer(P)-31 associates with VMAT2 and α -syn

Because TH is able to interact with negatively charged membranes (44), we investigated whether phosphorylation at Ser-31 enhances this association. To study the binding of TH to membranes, we used chromaffin vesicle membranes that had been previously trypsinized to remove any proteins that could be potential partners. Surface plasmon resonance studies using purified recombinant, non-phosphorylated human TH1 showed a certain degree of interaction with membranes (Fig. 4A), as

expected (44). However, TH1 phosphorylated at Ser-31 *in vitro* showed no difference in the interaction with trypsinized chromaffin-vesicle membranes when compared with the non-phosphorylated TH1 (Fig. 4A). It is thus unlikely that the THSer(P)-31-driven interaction involves a direct binding of the enzyme with the vesicular membrane, and the enzyme may rather interact with vesicular membrane proteins. Indeed, Torres and co-workers (9) have reported that TH can interact with the integral vesicular membrane protein VMAT2, and our immunofluorescence images of THSer(P)-31 and VMAT2 in iCell Dopamineurons showed co-distribution (Fig. 2E). To further investigate *in situ* whether THSer(P)-31 binds to vesicle proteins, we performed a proximity ligation assay (PLA), which is able to detect even weak and transient protein-protein interactions (45) with anti-V5 and either anti-VMAT2 or anti- α -syn in neuroblastoma cells expressing the phospho-variants (and GFP as transfection control). Appropriate PLA-positive and -negative controls were performed in all experiments (data not shown). PLA signals for the pair V5-TH1-S31E/VMAT2 were clearly obtained. However, for the pair V5-TH1-S31A/VMAT2, they were nearly imperceptible (Fig. 4B). Similarly, V5-TH1-S31A/

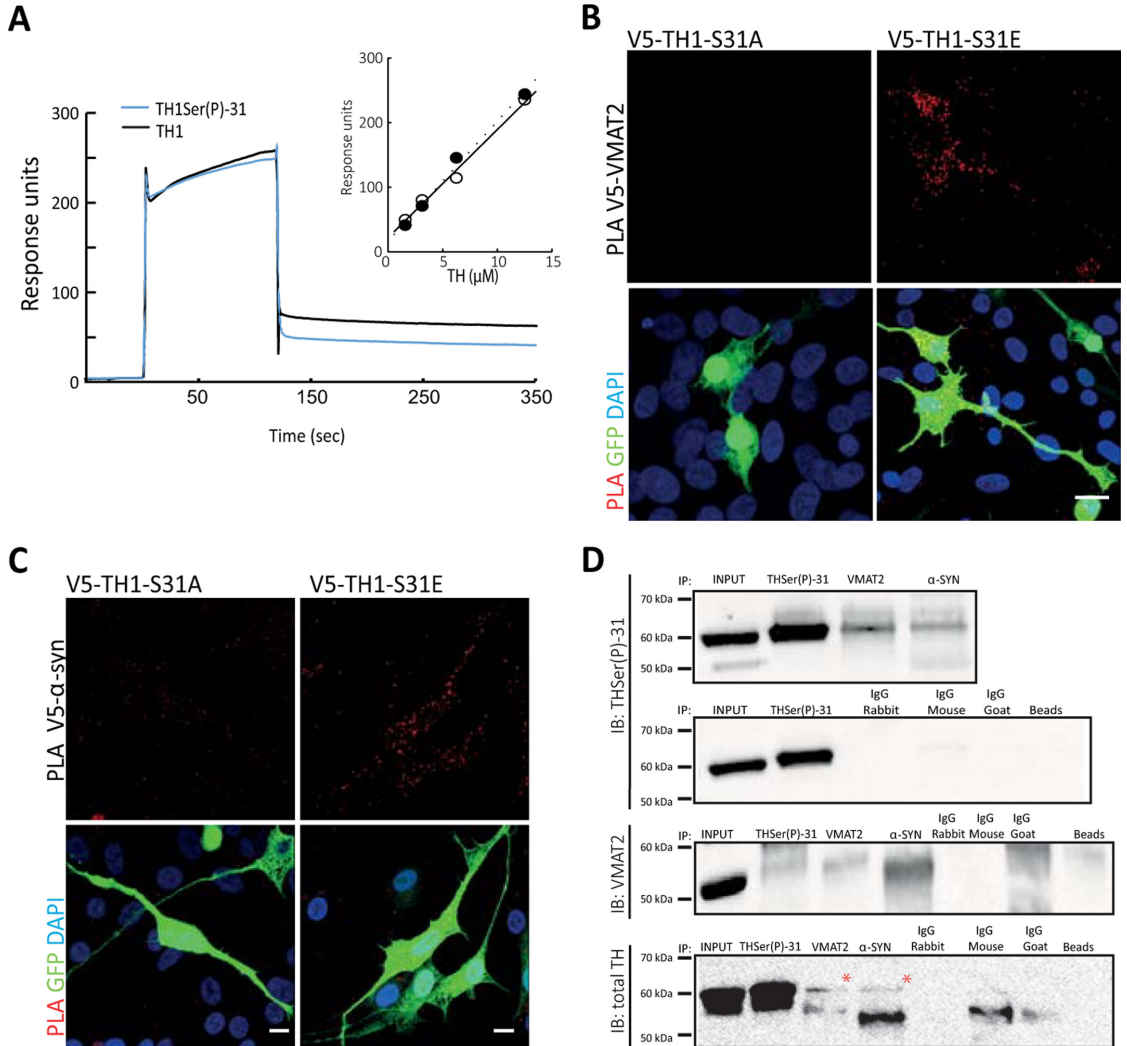


Figure 4. THSer(P)-31 interacts with VMAT2 and α -synuclein. *A*, surface plasmon resonance of TH (12.5 μM ; black trace) and THSer(P)-31 (12.5 μM ; blue trace) binding to trypsinized chromaffin vesicle membranes (trCVM). *Inset*, concentration dependence of the response of TH (\circ) and THSer(P)-31 (\bullet) binding to trCVM. *B* and *C*, PLA (signals shown in red) between V5 and either VMAT2 or α -syn antibodies in neuroblastoma cells expressing either V5-TH1-S31A or V5-TH1-S31E. Maximal projections of the whole-cell height are shown. Cells were co-transfected with GFP as a transfection control (green), and nuclei were stained with DAPI (blue). *Scale bars*, 10 μm . *D*, immunoprecipitation of THSer(P)-31, VMAT2, and α -syn from whole-mouse brain lysate and immunoblot against THSer(P)-31, VMAT2, and total TH are shown. All proteins were also detected in lysates incubated with only beads (right lane) or the different IgGs shown. THSer(P)-31 was detected in the input, as expected.

α -syn signals were significantly decreased compared with the V5-TH1-S31E/ α -syn pair (19 ± 20 versus 47 ± 24 ; $n = 15$; $p < 0.05$) (Fig. 4C).

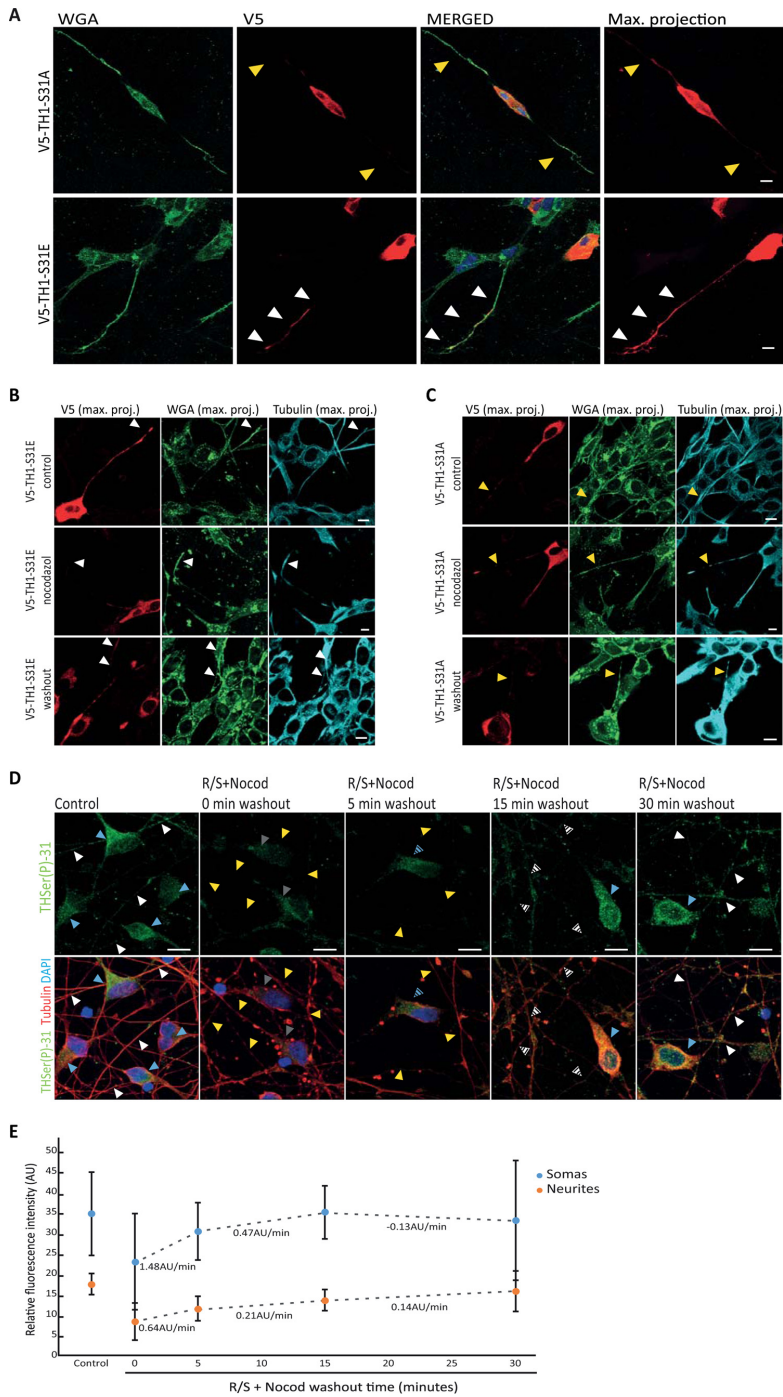
PLA results were confirmed by immunoprecipitation of THSer(P)-31, VMAT2, and α -syn from whole-brain extracts from mice, followed by immunoblotting against THSer(P)-31, total TH, and VMAT2 (Fig. 4D). Immunoblotting against α -syn did not render conclusive results, but taken together with the positive results obtained using PLA, our data suggest that the THSer(P)-31- α -syn association is weak and/or transient

because PLA allows the detection of this type of interaction, as reported previously (45). Appropriate negative controls using only beads or the different IgG were performed in parallel (Fig. 4D). Our data show the presence of THSer(P)-31 in both samples, indicating that THSer(P)-31 associates with VMAT2 and α -syn.

THSer(P)-31 is transported along the microtubules

Association of THSer(P)-31 with VMAT2 and α -syn may drive the anterograde transport of TH from GC to neurite ter-

TH Ser-31 phosphorylation targets TH to vesicles



minals. Therefore, we sought to investigate the localization and redistribution of exogenous TH phospho-mutants upon disruption of the microtubule network. First, detection of the V5 tag of recombinant V5-TH1-S31A and V5-TH1-S31E mutants showed that V5-TH1-S31A accumulates mainly in the soma of the neuroblastoma cells, whereas V5-TH1-S31E is distributed throughout the soma and neurites (Fig. 5A). The depolymerization of the microtubule network of neuroblastoma cells by nocodazole led to a decreased of V5-TH1-S31E signal in neurites compared with control samples (Fig. 5B), and drug washout recovered the V5-TH1-S31E signal in neurites. However, V5-TH1-S31A localization did not change upon microtubule disassembly (Fig. 5C). To further investigate THSer(P)-31 transport in DopaNeuron cells, we first inhibited TH phosphorylation at Ser-31 using Cdk5 inhibitors (R/S) to create an initial stage with the lowest phosphorylation levels possible, and then we depolymerized the microtubules with nocodazole. Afterward, we performed a drug washout to allow the phosphorylation of TH at Ser-31 and reassembly of the microtubule network. All samples were stained for THSer(P)-31 and tubulin to monitor the treatment and were treated in parallel, with data acquisition and image processing performed under the same conditions. As expected, R/S and nocodazole treatment (0 min of washout) showed a disrupted microtubule pattern compared with the controls, as well as a significantly decreased THSer(P)-31 signal both for the somas (34.99 ± 11.7 versus 22.81 ± 7.1 ; $p < 0.001$; $n = 50$) and for the neurites (18.85 ± 4.57 versus 8.22 ± 2.9 ; $p < 0.001$; $n = 50$) (Fig. 5, D and E). At the initial time points of the drug washout (5 and 15 min), increased THSer(P)-31 fluorescence was measured in the soma and, to a lesser extent in the neurites, the recovery rate of the signal being 2.2-fold faster in the somas than in the neurites. At the 15–30-min time lapse, an inversion of this trend was measured. At the final 30-min time point, fluorescence signals in somas and neurites were comparable with the controls with no statistical differences (somas: 32.95 ± 17.76 versus 34.99 ± 11.7 ; $p > 0.4$; $n = 50$; neurites: 15.60 ± 12.49 versus 18.86 ± 4.57 ; $p > 0.07$; $n = 50$). Therefore, our data show that THSer(P)-31 signal increases first in the somas and then gradually in the distal parts of the neurites. Thus, our results show that THSer(P)-31 trafficking depends on microtubule integrity for its transport to the neurite extensions in a human dopaminergic cell line.

The A53T mutation of α -syn (α -syn-A53T) is associated with autosomal dominant forms of PD (30), and it has been shown to hinder axonal transport in rat neurons and in neuro-

blastoma cells by fragmenting the GC and aggregating microtubuli (47, 48). Therefore, we studied whether overexpression of His- α -syn-A53T resulted in impaired distribution of V5-TH1-S31E. We co-transfected neuroblastoma cells with V5-TH1-S31E and one of the following plasmids: GFP, His- α -syn-WT, or His- α -syn-A53T, all of which are under the same promoter, CMV. To avoid comparing samples transfected only with one plasmid with samples transfected with two constructs, we used the V5-TH1-S31E/GFP co-transfection as our control and reference. We stained the cell membranes with WGA to identify the neurites of the cells. Cells transfected with V5-TH1-S31E/GFP showed the V5 signal along the whole neurite, including the more distal parts (Fig. 6A). However, cells transfected with V5-TH1-S31E and His- α -syn-WT, and especially His- α -syn-A53T, showed intense V5 signal in the cell soma but weaker signal at the distal ends of the neurites (Fig. 6A). We then quantified the intensity of the signal along the neurite length from cells transfected with V5-TH1-S31E/GFP, V5-TH1-S31E/His- α -syn-WT, or V5-TH1-S31E/His- α -syn-A53T, and we integrated the area below the plot profile. Comparing the most distal 20 μ m of the neurites, we found that the signal was significantly reduced in V5-TH1-S31E/His- α -syn-WT ($p < 0.05$) and especially in V5-TH1-S31E/His- α -syn-A53T ($p < 0.0001$) samples (Fig. 6B). Signal intensity in arbitrary units was as follows: TH1-S31E/GFP = 17.4 ± 8.1 ($n = 24$); V5-TH1-S31E/His- α -syn-WT = 12.2 ± 6.7 ($n = 16$); V5-TH1-S31E/His- α -syn-A53T = 6.9 ± 4.2 ($n = 22$). Our results indicate that overexpression of wild-type and especially mutant α -syn can affect the axonal transport of TH.

Influence of phosphorylation at Ser-31 on Ser-19 and Ser-40 sites

To better understand the previously reported multisite and hierarchical phosphorylation events in TH (13, 16, 20, 22), we studied whether phosphorylation at Ser-31 can modulate phosphorylation at Ser-19 and Ser-40, which are regulated by different signaling pathways. PLAs allow the detection of two epitopes that are in close vicinity (<100 nm (49)) and therefore were used to detect the co-existence of phosphorylation at two different sites. Anti-V5 together with anti-THSer(P)-19 or anti-THSer(P)-40 antibodies in neuroblastoma cells expressing V5-TH1-S31A developed significantly more PLA signals for both Ser-19 and Ser-40 phosphorylation compared with cells expressing V5-TH1-S31E (708 ± 442 versus 302 ± 102 , $n = 12$, $p < 0.05$ for THSer(P)-19; 1036 ± 449 versus 56 ± 65 , $n = 10$,

Figure 5. Transport of THSer(P)-31 to neurite extensions. A, distribution of V5-TH1-S31A- and V5-TH1-S31E-expressing neuroblastoma detected by V5 staining (red). Cellular membranes were stained using WGA (green). Confocal planes are presented as well as the maximum intensity projection (max. projection) of the V5 signal stack of confocal planes. Nuclei were stained with DAPI (blue). Arrows, presence (white) or absence (yellow) of V5 signal in neurites of V5-positive cells (intense red signal in the soma). B and C, detection of V5 tag in neuroblastoma cells expressing V5-TH1-S31E (B) or V5-TH1-S31A (C) after microtubule depolymerization by a cold shock and nocodazole treatment, followed by 30 min of drug washout. Control cells were processed in parallel but were not subjected to nocodazole. All samples were stained for V5 (red), tubulin (cyan), and WGA to mark the cells membranes (green) and DAPI to stain the nucleus. Maximum intensity projection of the stack of confocal planes (max. proj.) is presented. Arrows, presence (white) or absence (yellow) of V5 signal in neurites of V5-positive cells (intense red signal in the soma). D, immunofluorescence of iCell DopaNeurons detecting THSer(P)-31 (green) and tubulin (red) in samples treated first with roscovitine/SL327 for inhibition of phosphorylation of TH at Ser-31 and then subjected to a cold shock nocodazole treatment (R/S+Nocod) for microtubule disassembly before allowing drug washout. Blue and white arrows, control levels of THSer(P)-31 fluorescence in somas and neurites, respectively. Gray and yellow arrows, low levels/absence of THSer(P)-31 fluorescence in somas and neurites, respectively. Intermediate fluorescence levels are indicated with the corresponding striped arrows. In all cases, maximal projections comprehending the whole cell height are shown. E, quantification of the THSer(P)-31 signal of DopaNeuron somas or neurites in control (untreated) samples as well as in samples treated with the R/S+Nocod and subjected to drug washout. Data are shown as average \pm S.D. (error bars) (in all cases $n = 50$), and the changes in fluorescence per time (arbitrary units (AU)/min) are indicated below each pair of time points. ***, $p < 0.001$. For all confocal images, 10- μ m scale bars are shown.

TH Ser-31 phosphorylation targets TH to vesicles

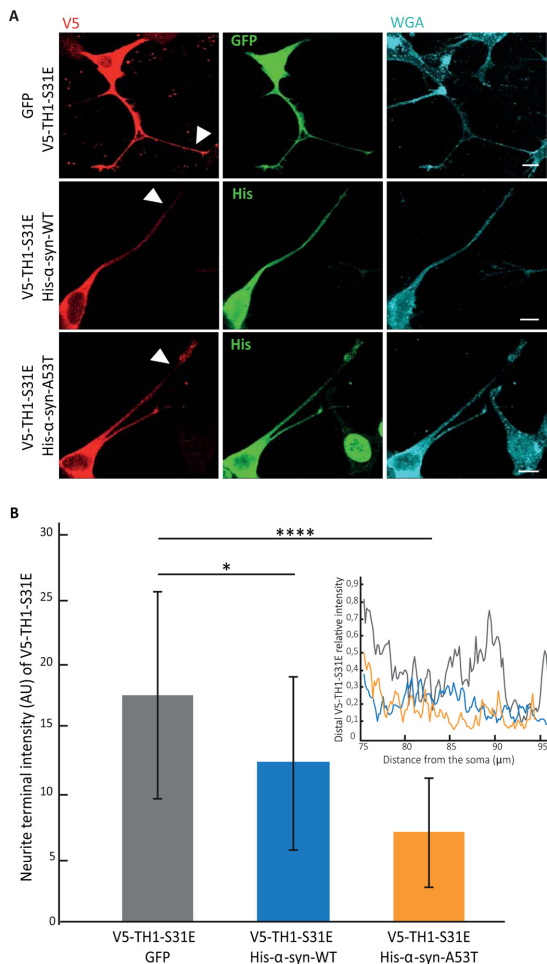


Figure 6. Effect of overexpression of α -synuclein on V5-TH1-S31E in neuroblastoma neurites. *A*, immunofluorescence of neuroblastoma cells co-transfected with V5-TH1-S31E (red) and one of the plasmids GFP, His- α -syn WT, or His- α -syn-A53T (green) and membranes stained with WGA (cyan). *B*, quantification of the signal of neurites from cells co-transfected with V5-TH1-S31E/GFP V5-TH1-S31E/His- α -syn-WT or V5-TH1-S31E/His- α -syn-A53T. Data are shown as average \pm S.D. (error bars) and are expressed in arbitrary units (AU) (left). Representative plot profiles are shown (right). For all confocal images, 10- μ m scale bars are shown. *, $p < 0.05$ and ****, $p < 0.0001$.

$p < 0.005$ for THSer(P)-40 (Fig. 7, *A* and *B*). The difference in co-distribution of Ser-19 and Ser-40 phosphorylation between V5-TH1-S31E- and V5-TH1-S31A-transfected cells was corroborated by Western blot analyses (Fig. 7C). Cells expressing V5-TH1-S31A treated or not with R/S did not show significant differences in levels of phosphorylation (Fig. 7D), further supporting our conclusions.

Taken together, our data demonstrate that phosphorylation at Ser-31 regulates TH association with vesicles and thus its transport to neurite terminals through interaction with VMAT2 and α -syn.

Discussion

TH has been described essentially as a cytosolic protein, but its membrane-associated form has recently been attracting interest (9, 29), although the regulation of the binding mechanisms remains largely unknown. Here we show that Ser-31 phosphorylation of TH regulates its association with the GC and synaptic-like vesicles. Our data also indicate that TH1Ser(P)-31 interacts, directly or indirectly, with VMAT2 and α -syn in striatal brain isolates and in cellular models. However, we observed little co-localization of TH1-S31A with α -syn and VMAT2, whereas this was prominent for the TH1-S31E mutant. It has been reported previously that α -syn interacts with, and negatively regulates, TH through activation of PP2A phosphatase, which dephosphorylates THSer(P)-40 and inactivates TH (50). In addition, it has also been shown that VMAT1/2 can be inhibited by α -syn (51). However, this work assigns to Ser-31 phosphorylation the role of controlling the association of TH to both α -syn and VMAT2. Interestingly, phosphorylation also appears to regulate the vesicular interaction of synthesizing enzymes for other neurotransmitters, such as acetylcholine and GABA. Thus, the synthesizing enzymes choline acetyltransferase and glutamate decarboxylase 65 have been found to bind to their corresponding vesicular transporter (vesicular acetylcholine transporter and vesicular GABA transporter) (52, 53), and this association seems to be phosphorylation-dependent for both glutamate decarboxylase 65 (53) and choline acetyltransferase (54). Our results thus contribute to the identification of the dopaminergic system and TH to comply with a growing class of neurotransmitter-synthesizing enzymes that couple to their transporter in a phosphorylation-dependent manner. This association may ensure an efficient packaging of the neurotransmitters into the synaptic vesicle and a proper trafficking and subcellular localization of neurotransmitter synthesis.

Based on the previous reports showing an inhibitory effect of α -syn on TH activity (50, 55), the engagement of α -syn in a vesicular complex might ensure that TH is transported most probably in an inhibited state to its destination (see below). It would also be likely that this functional transport complex contains additional regulatory or stabilizing proteins, such as Hsc70, which also has been described to interact with both VMAT2 and TH (29, 56). The DOPA decarboxylase enzyme that catalyzes the next step in DA synthesis after TH also interacts with TH, Hsc70, and VMAT2 (9, 29).

The GC enrichment of TH that we observed indicates that it associates with VMAT2 and α -syn during the vesicle formation, because VMAT2 is an integral protein that is sorted into the vesicles in the GC (57) and α -syn has been localized at the GC and dopamine-containing vesicles (58, 59), reinforcing the early stage association of these proteins. Furthermore, our data suggest that *in vivo* TH phosphorylated at Ser-31 may be transported from the GC in the cell soma to the terminals by the anterograde axonal transport. Early reports already proved fast axonal transport for TH, consistent with its association with vesicles (60–62), and additional transport of TH mRNA has more recently been described (61). Moreover, recent results from our laboratory using a knock-in mouse bearing a destabilizing TH mutation have shown the impor-

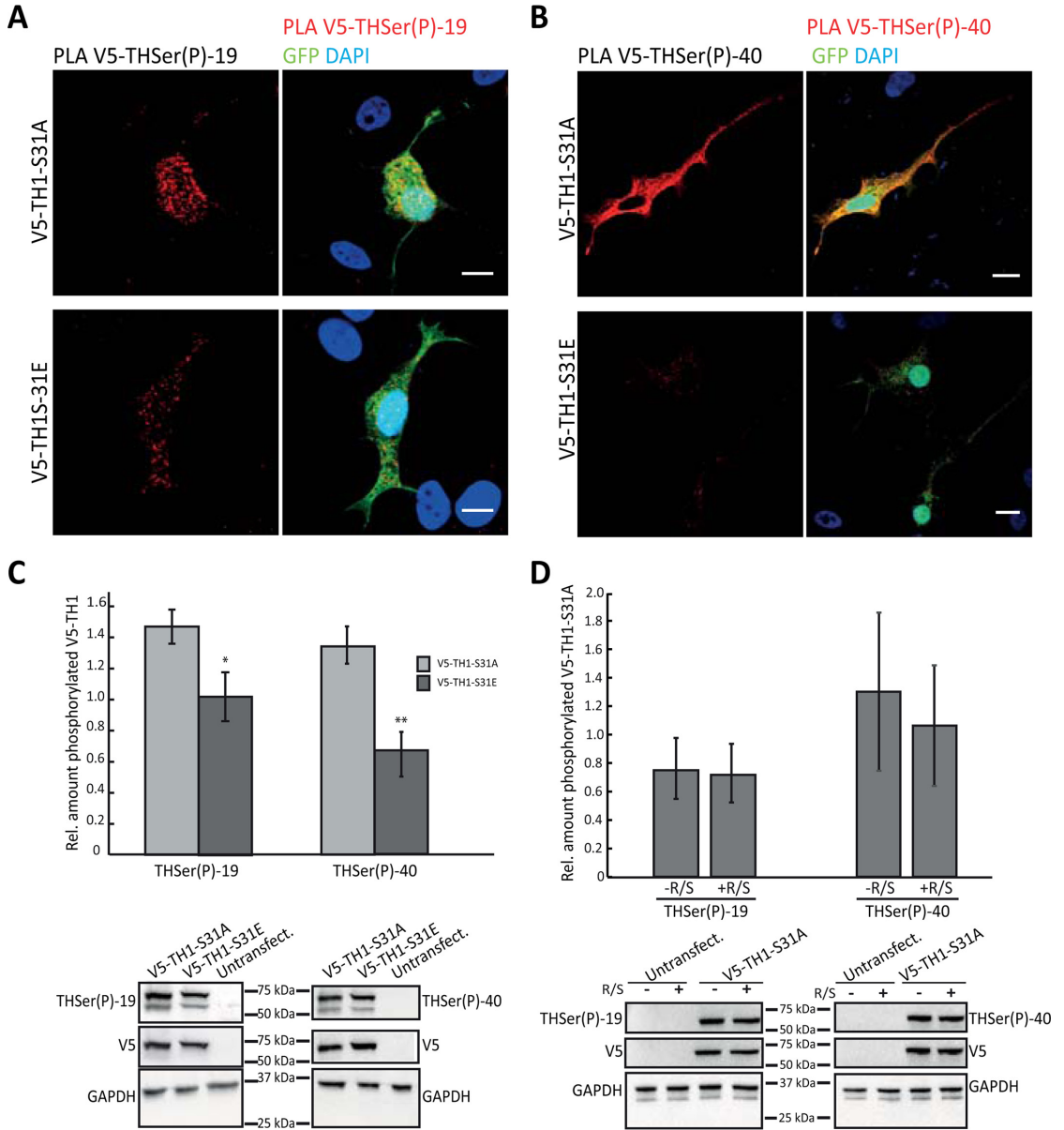


Figure 7. Effect of THSer(P)-31 on the phosphorylation of THSer(P)-19 and THSer(P)-40. *A* and *B*, PLAs (signals shown in red) between V5 and THSer(P)-19 (*A*) or THSer(P)-40 (*B*) antibodies in neuroblastoma cells expressing either V5-TH1-S31A and V5-TH1-S31E. Cells were co-transfected with soluble GFP (green) as a positive transfection control, and nuclei were stained with DAPI (blue). Scale bars, 10 μ m. *C*, THSer(P)-19 or THSer(P)-40 detection using Western blotting of whole lysates of neuroblastoma cells expressing V5-TH1-S31A or V5-TH1-S31E. Bars, relative amount of TH (t test was used for statistical sample comparison; *, $p < 0.05$; **, $p < 0.01$; data are represented as mean \pm S.D. (error bars); $n = 3$). Representative Western blots are shown. *D*, THSer(P)-19 or THSer(P)-40 detection using Western blotting of whole lysates of neuroblastoma cells expressing V5-TH1-S31A treated or not with R/S. Bars, relative amount of TH (data represented as mean \pm S.D.; $n = 3$).

tance of axonal transport of TH for proper distribution of TH in striatal terminals (63).

Effects of multisite phosphorylation events have been reported for TH, and phosphorylation at Ser-31 has been reported to stimulate the *in vitro* phosphorylation of adjacent

Ser-40 sites (22). Moreover, upon stimulation of bovine chromaffin cells, increased Ser-40 phosphorylation was observed when co-stimulating the Ser-31-targeting ERK1/2 pathways (22), but this stimulatory effect was not observed in the presence of dopamine (22). No studies have so far looked into these

TH Ser-31 phosphorylation targets TH to vesicles

hierarchical effects on phosphorylation in the brain, but our results in neuroblastoma cells suggest that localization and interaction partners of TH play a role in the phosphorylation of the different sites. Interestingly, less Ser-19 and Ser-40 phosphorylation was observed for the phospho-mimicking TH1-S31E mutant, suggesting that conformational constraints and its interaction with partners, such as α -syn or VMAT2, may affect its availability for phosphorylation. In addition, phosphorylation at Ser-31 stabilizes the enzyme, and, in addition, the decreased phosphorylation at Ser-40 would allow more binding of inhibitory catecholamines (16), which would further stabilize THSer(P)-31 (25, 64). This inhibition seems to be congruent with TH being in a stable, and probably in a non-catalytic state during its transport from the cell soma to the terminals (65). Last, further maturation of the vesicles might be accompanied by TH reactivation and increased L-DOPA synthesis upon its proper localization, probably through dephosphorylation, release from the vesicles, or interaction within different protein-protein complexes than during transport.

Synaptic vesicles are transported along the cytoskeleton to the neurites, and disruption of the cytoskeleton network is thus expected to cause the accumulation of the recombinant TH in the cells' soma, as observed here (Fig. 5B). Our results also explain previous observations showing that mice bearing a Cdk5 knock-out mutation show decreased striatal THSer(P)-31 (25). Furthermore, it has been described that the highest stoichiometry of THSer(P)-31 was found in the terminals of the nigrostriatal and mesoaccumbens pathways (23) and that Ser-31 phosphorylation was decreased in conjunction with TH loss following the 6-hydroxydopamine lesion of the nigrostriatal pathway in rats (27), also in agreement with our observation that overexpression of the PD mutant A53T α -syn decreased the amount of the V5-TH1-S31E protein in the distal regions of the neurites (Fig. 6E). Increasingly, Cdk5 and ERK1/2 have been recognized as crucial for many processes in neurodegeneration (66, 67). We therefore cannot rule out effects of these kinases on other important players in axonal transport, which could be expected to have consequences for specific transport of TH beyond Ser-31 phosphorylation.

In conclusion, our results identify a novel role for TH phosphorylation at Ser-31, controlling TH co-distribution with synaptic vesicles through association with VMAT2 and α -syn. Our results also point to the role of Ser-31 phosphorylation of TH on the transport of this enzyme from the cell soma to the terminals using the microtubule network. In addition, the distribution of THSer(P)-31 is affected when the PD mutant α -syn A53T is present. Thus, TH spatial control by Ser-31 phosphorylation implies that TH localization and DA synthesis would be directly affected by disturbances such as the loss of vesicle integrity, the defective vesicle trafficking, and the GC fragmentation described in PD (8, 68–70). Indeed, axonal transport defects correlate with decreased putamen TH levels in early PD patients, whereas in late-stage patients, TH is decreased in both putamen and substantia nigra (7, 71). Our work also points toward the potential of therapeutic avenues aimed at reverting neuronal mislocalization and transport alterations associated with PD (7, 65, 71–73).

Table 1

Sequence of primers used for site-directed mutagenesis

Primer	Forward strand sequence 5'–3'
TH1-S19A	CTTCCGCAGGGCCGTGGCGGAGCTGGACGCCAAGC
TH1-S19E	CGCAGGGCCGTGGAGGAGCTGGACGCCAAG
TH1-S31A	GGCCATCATGGCCCGCGGTTTC
TH1-S31E	CAGAGCCATCATGGAGCCCGGTTTCATTTG
TH1-S40A	CATTGGCGCGAGGCGGCTCATCGAGGACGCCCC
TH1-S40E	GGCGCAGGCAGGAATCATCGAGGAC

Experimental procedures

All reagents were supplied by Sigma except when indicated.

Constructs for transient expression in mammalian cell culture

WT human TH1 coding sequence was inserted into the pcDNA6.2/nTC-Tag-DEST vector. Mutations V5-TH1-S19A, V5-TH1-S19E, V5-TH1-S31A, V5-TH1-S31E, V5-TH1-S40A, and V5-TH1-S40E were introduced using QuikChange Mutagenesis II (Stratagene) and primers specified in Table 1. Mutations were verified by sequencing. Soluble enhanced green fluorescent protein (GFP) was purchased from Clontech. pHM6- α -synuclein-A53T mutant was a gift from David Rubinstein (Addgene plasmids 40824 and 40825) and described previously (74).

Cell culture

Rat pheochromocytoma PC12Adh cells (ATCC-CRL-1721.1) (<8 passages) were grown in RPMI 1640 medium with 10% horse serum (PAA Laboratories GmbH), 5% fetal bovine serum, 2 mM glutamine, 100 units/ml penicillin, and 100 μ g/ml streptomycin. Adherent PC12 derived from Ref. 35 underwent short-term repeat profiling and presented genetic drift, so it has been denoted PC12* to distinguish it from PC12Adh strain provided by ATCC (PC12Adh). Culture conditions for both strains were identical. When specified, cells were treated for 48 h with 50 ng/ml 2.5S NGF (Life Technologies, Inc.) in OptiMEM I (Life Technologies), leading to well-developed neurites in PC12*; however, PC12Adh cells do not develop significant projections upon NGF stimulation according to ATCC (strain specifications). Human neuroblastoma SH-SY5Y and HEK293 cells were grown in DMEM with 10% fetal bovine serum, 2 mM glutamine, 100 units/ml penicillin, and 100 μ g/ml streptomycin. Cells were profiled by short tandem repeat. Commercial midbrain dopaminergic neurons generated from human induced pluripotent stem iCell DopaNeuron cells (Cellular Dynamics) were grown following the manufacturer's indications and were analyzed 7–10 days postseeding. For immunofluorescence, PC12* or SH-SY5Y cells were grown for 48 h on poly-L-lysine or PureCol (Inamed Biomaterials) and laminin/collagen-coated coverslips, respectively. iCell DopaNeurons were grown on coverslips coated with polyornithine and laminin. For the coating of the coverslips, a final concentration of 0.1 mg/ml poly-L-lysine, 1.5 mg/ml laminin plus 1.5 mg/ml collagen or a 10 μ g/ml polyornithine plus 20 μ g/ml laminin solution was placed on the coverslips and incubated for 30 min at 37 °C and washed with PBS before seeding the cells.

Table 2
Primary antibodies used in Western blotting and immunofluorescence

Target protein	Host	Supplier	Western blot dilution	Immunofluorescence dilution
TH (total)	Rabbit	Thermo Scientific	1:1000	1:100
THSer(P)-19	Rabbit	Phosphosolutions	1:1000	1:50
THSer(P)-31	Rabbit	Phosphosolutions	1:1000	1:50
THSer(P)-31	Rabbit	Ref. 26	1:300	1:50
THSer(P)-40	Rabbit	Phosphosolutions	1:1000	1:50
GM130	Mouse	BD Transduction Laboratories	1:1000	1:100
His	Mouse	GenScript	NA ^a	1:100
Synaptotagmin I	Mouse	Abcam	1:1000	1:100
GAPDH	Rabbit	Abcam	1:1000	NA
V5	Rabbit	Sigma	1:2000	1:100
V5	Mouse	Life Technologies	1:5000	1:100
VMAT2	Rabbit	Millipore	1:1000	1:100
VMAT2	Goat	Santa Cruz Biotechnology	1:1000	1:100
α -Synuclein 3H9	Mouse	Abcam	1:1000	1:100
Tubulin	Mouse	Sigma	NA	1:1000
Clathrin	Mouse	Thermo Scientific	1:1000	NA
Transferrin receptor	Mouse	Invitrogen	1:1000	NA
SPC25	Rabbit	Gift from Stephen High	1:1000	NA
DOPA- β -hydroxylase	Sheep	Abcam	1:1000	NA
Chromogranin A	Rabbit	Novus Biologicals	1:1000	NA

^a NA, not applicable.

Transient transfection of neuroblastoma SH-SY5Y for TH overexpression

For Western blotting, SH-SY5Y or HEK293 cells were seeded on (1×10^6 cells/p60 plate) and grown overnight before transfecting with 5 μ g of DNA and Lipofectamine LTX with Plus reagent (Life Technologies), following the manufacturer's instructions. Cells were collected 48 h post-transfection. For imaging experiments, 20,000 SH-SY5Y cells seeded on coverslips were transfected with 0.5 μ g of DNA and Lipofectamine LTX with Plus reagent. 48 h post-transfection, cells were subjected to the indicated treatments and fixed with 4% paraformaldehyde. In the case of co-transfections, a 1:1 ratio of both co-transfected plasmids were used except for PLA assays where the ratio of interest/control plasmid was 3:1.

Inhibition of THSer(P)-31 phosphorylation

Cells were incubated 7 h with roscovitine (50 μ M) and SL327 (50 μ M) before being collected and frozen or subjected to drug washout by incubating with fresh medium. In the case of transfected cells treated with the inhibitors, and to ensure equal expression of the constructs in treated and untreated samples, 24 h post-transfection, cells were split into two p35 plates and were left to grow an additional day before the treatment.

GC and microtubule disassembly

GC was disrupted by incubating PC12* cells for 30 min with 5 μ g/ml brefeldin A (Epicenter Technologies). Microtubule disassembly was achieved by a 1-min 4 °C cold shock followed by 30-min 33 μ M nocodazole incubation at 37 °C. Cells were fixed in cold methanol. In all cases, drug washout was performed by replacement of drug-containing medium with fresh media for 30 min.

Immunostaining and proximity ligation assays

Samples were fixed with 4% paraformaldehyde for 30 min at room temperature, unless otherwise indicated, and permeabilized and blocked with 0.3% saponin and 5% FBS in PBS for 30 min at room temperature. When stated, a 5-min 0.1% Triton

X-100 permeabilization step was performed before blocking. Samples were incubated with specified primary and secondary antibodies in Tables 2 and 3 and, when indicated, stained with 1:200 Oregon Green or tetramethylrhodamine-labeled wheat germ agglutinin (Life Technologies) before being mounted using ProLong Gold with DAPI (Molecular Probes). PLAs were performed using Duolink® *in situ* according to the manufacturer's instructions and the primary antibody conditions stated above.

Confocal laser-scanning microscopy imaging

Confocal imaging was performed on a Leica microscope TCS SP5 in the resonant scanner mode (Leica Microsystems GmbH) using a pinhole airy 1 and a $\times 63$, 1.4 numeric aperture oil immersion objective. For each sample, a stack of images encompassing the complete height of the cell was taken, with a 130-nm step size and using the LasAF software from Leica. Each confocal plane was 512×512 pixels with a line average of 20. Stack images were processed in batch using FIJI freeware (75) and/or Photoshop Adobe with minimum adjustments of brightness and background. Single-plane surface plots and signal quantification were prepared using FIJI (75). 3D rendering of Z-stacks was performed using Imaris (Bitplane Inc.), building a co-localization channel between the green and red channels and representing all three using the surface tool. Imaris was employed to quantify the PLA signals by building a co-localization channel between the green (GFP) and red (PLA) signals to eliminate nonspecific PLA signals and set the sphere a radius of 300 nm/signal. The surpass function "spot" tool used to detect the PLA signals, and the same segmentation threshold was used for all images. The numbers of spots obtained were compared using a *t* test analysis.

For the image analysis of DopaNeuron cells, maximal projections of Z-stacks of the whole cells' height were obtained. Randomly selected cell somas and neurite sections (50–90 μ m) located $>135 \mu$ m away from their soma were manually traced on the tubulin channel using LasAF Lite software (Leica), and the mean intensity of the traced area was recorded for the

TH Ser-31 phosphorylation targets TH to vesicles

Table 3
Secondary antibodies used in Western blotting and immunofluorescence

Target protein	Host	Supplier	Conjugation	Western blot dilution	Immunofluorescence dilution
IgG Rabbit (H+L)	Goat	Invitrogen	Alexa Fluor 488	NA ^a	1:200
IgG Mouse (H+L)	Goat	Invitrogen	Alexa Fluor 555	NA	1:200
IgG Rabbit (H+L)	Goat	Invitrogen	Alexa Fluor 594	NA	1:200
IgG Rabbit (H+L)	Goat	Invitrogen	Alexa Fluor 647	NA	1:200
IgG Mouse	Goat	Santa Cruz Biotechnology	HRP	1:1000	NA
IgG Goat	Donkey	Santa Cruz Biotechnology	HRP	1:1000	NA
IgG Rabbit	Goat	Santa Cruz Biotechnology	HRP	1:1000	NA
IgG Sheep	Donkey	Santa Cruz Biotechnology	HRP	1:1000	NA

^a NA, not applicable.

THSer(P)-31 channel. Average and S.D. values were obtained for each sample set, and *p* values were calculated using a *t* test analysis. For the image analysis of the neuroblastoma neurites transfected with V5-TH1 and His- α -syn, maximal projections of Z-stacks of the first micron of the sample were obtained, neurites of a length of approximately 65–95 and 1–2 μ m were selected and manually traced on the WGA channel with a 4-pixel-wide line using FIJI, and the intensity profile was recorded for the V5 channel. Using Excel, neurite signal intensity was normalized to the cell soma intensity to minimize variations due to expression levels. The area below the curve corresponding to the most distal 20 μ m of the neurite was integrated, average and S.D. values were obtained for each co-transfection set, and *p* values were calculated using a *t* test analysis.

Cellular fractionations and chromaffin vesicle membranes

Subcellular fractionation was performed according to Ref. 76 with the only modification that for SH-SY5Y the last centrifugation step to sediment the microsome fraction was carried out for 90 min. Chromaffin vesicle membranes (CVMs) were purified from bovine adrenal medulla as described (46). The CVMs were treated with trypsin (bovine pancreas; Sigma-Aldrich) (1 mg of CVM protein, 1.5 mg of trypsin) for 2 h at 30 °C. The reaction was stopped by adding soybean trypsin inhibitor at a 1:2 ratio (mg of trypsin/mg of inhibitor).

Western blot analysis

Proteins were separated on SDS-PAGE 10% TGXTM gels (Bio-Rad) and transferred onto nitrocellulose or PVDF membranes using the TransBlot Turbo system (Bio-Rad). Membranes were incubated with the primary and secondary antibodies specified in Tables 2 and 3, developed by chemiluminescence, and visualized with a ChemiDoc instrument, and band intensities were quantified by Image Lab software (Bio-Rad). For data analysis, the intensity of target proteins was standardized with the loading control. In the case of each recombinant TH1, the microsome fraction was normalized against its corresponding whole lysate to minimize the effect of stability and transfection efficiency differences. Treated samples were referenced to untreated, which were given the arbitrary value of 1. The sample size in all cases was *n* = 3, and Microsoft Excel was used for statistical calculations. Two-way comparison was performed using the *t* test. Statistical significance was set at *p* < 0.05.

Preparation of mouse brain lysates and immunoprecipitation

Mouse whole brain was homogenized with a Tissue Lyser II (Qiagen) in IP buffer (20 mM Hepes, pH 7.4, 125 mM NaCl, 1 mM EDTA, 2 mM PMSF), containing protease and phosphatase inhibitors (Roche Applied Science). Extract was clarified by centrifugation at 16,000 \times *g* for 20 min at 4 °C. The supernatant was collected, and Triton X-100 was added to a final concentration of 1%. This sample was centrifuged at 4 °C at 20,000 \times *g* for 15 min after rotation for 1 h at 4 °C. The soluble extract was incubated with antibodies against THSer(P)-31 (rabbit; described previously (26), VMAT2 (C-20) (goat; Millipore), α -synuclein (3H9) (mouse; Abcam), control IgGs (Millipore Merck), or no antibody (only beads) with rotation overnight at 4 °C. Protein A/G PLUS-agarose beads (Santa Cruz Biotechnology, Inc.) were added to samples and rotated for 1 h at 4 °C before samples were pelleted, washed, and incubated at 37 °C for 30 min in 40 μ l of sample buffer. Samples were analyzed by SDS-PAGE and immunoblotting with anti-THSer(P)-31, VMAT2 (rabbit; Millipore), and anti-TH (rabbit; Thermo Scientific) antibodies as primary antibodies and anti-rabbit IgG light chain (HRP) (Abcam) antibodies as secondary antibodies, respectively.

TH purification and phosphorylation

Human TH1 was expressed in *Escherichia coli* (BL21 Codon Plus (DE3), Stratagene) as a His-ZZ-TH1 fusion protein (15) and purified using Talon resin (New England Biolabs) according to the manufacturer's recommendations. The fusion tag was removed by proteolytic cleavage using tobacco etch virus (1:25 (mg) tobacco etch virus/TH) in 15 mM Hepes, pH 7.4, 150 mM NaCl (HBS) for 4 h on ice before centrifugation (13,000 \times *g*, 10 min) and gel filtration (Superdex 200 HR10/30, GE Healthcare). TH1 (50 μ M) was phosphorylated for 45 min at 25 °C in HBS buffer using 500 μ M ATP, 5 mM MgCl₂, and 12.5 units/ml active p35/CDK5 (Millipore; 14-477) to a stoichiometry of 0.5 mol of phosphate/mol of TH subunits as determined by incorporation of ³²P using [γ -³²P]ATP.

Surface plasmon resonance

The Biacore 3000 system was used with L1 sensor chips and HBS-N buffer (GE Healthcare; BR-1003-69). The L1 surface was loaded with CVM (150 μ g of protein/ml, 4–6 min, 3–10 μ l/min) according to the manufacturer's recommendation by ensuring surface saturation and minimal binding of BSA. 20 mM CHAPS was used to regenerate the surface. Binding of TH

was monitored using different flow rates (5–30 $\mu\text{l}/\text{min}$) and different concentrations of TH (0.1–25 μM).

Author contributions—A. J.-F. performed all cell culture experiments, immunofluorescence assays, PLAs, and Western blots; designed experiments; interpreted the data; and wrote the paper. R. K. performed SPR experiments, purified and phosphorylated the protein, designed experiments, interpreted the data, and edited the paper. K. J. K. C. performed Western blotting and interpreted the data. M. Y. performed the IP experiments, interpreted the data, and edited the paper. M. F. S. prepared the THSer(P)-31 antibody and edited the paper. M. M., I. R.-M., and J. S. discussed experiments and edited the paper. A. M. coordinated the project, designed experiments, interpreted the data, and wrote the paper.

Acknowledgments—Prof. Clive Bramham kindly provided the SH-SY5Y cells. All imaging was performed at the Molecular Imaging Center, Department of Biomedicine, University of Bergen, Norway.

References

- Pifl, C., Rajput, A., Reither, H., Blesa, J., Cavada, C., Obeso, J. A., Rajput, A. H., and Hornykiewicz, O. (2014) Is Parkinson's disease a vesicular dopamine storage disorder? Evidence from a study in isolated synaptic vesicles of human and nonhuman primate striatum. *J. Neurosci.* **34**, 8210–8218
- Trillo, L., Das, D., Hsieh, W., Medina, B., Moghadam, S., Lin, B., Dang, V., Sanchez, M. M., De Miguel, Z., Ashford, J. W., and Salehi, A. (2013) Ascending monoaminergic systems alterations in Alzheimer's disease: translating basic science into clinical care. *Neurosci. Biobehav. Rev.* **37**, 1363–1379
- Willemsen, M. A., Verbeek, M. M., Kamsteeg, E. J., de Rijk-van Andel, J. F., Aebi, A., Blau, N., Burlina, A., Donati, M. A., Geurtz, B., Grattan-Smith, P. J., Haeussler, M., Hoffmann, G. F., Jung, H., de Klerk, J. B., van der Knaap, M. S., et al. (2010) Tyrosine hydroxylase deficiency: a treatable disorder of brain catecholamine biosynthesis. *Brain* **133**, 1810–1822
- Wijemanne, S., and Jankovic, J. (2015) Dopa-responsive dystonia—clinical and genetic heterogeneity. *Nat. Rev. Neurol.* **11**, 414–424
- Gondré-Lewis, M. C., Park, J. J., and Loh, Y. P. (2012) Cellular mechanisms for the biogenesis and transport of synaptic and dense-core vesicles. *Int. Rev. Cell Mol. Biol.* **299**, 27–115
- Alerte, T. N., Akinofolarin, A. A., Friedrich, E. E., Mader, S. A., Hong, C. S., and Perez, R. G. (2008) α -Synuclein aggregation alters tyrosine hydroxylase phosphorylation and immunoreactivity: lessons from viral transduction of knockout mice. *Neurosci. Lett.* **435**, 24–29
- Chu, Y., Morfini, G. A., Langhammer, L. B., He, Y., Brady, S. T., and Kordower, J. H. (2012) Alterations in axonal transport motor proteins in sporadic and experimental Parkinson's disease. *Brain* **135**, 2058–2073
- Nakagomi, S., Barsoum, M. J., Bossy-Wetzel, E., Sütterlin, C., Malhotra, V., and Lipton, S. A. (2008) A Golgi fragmentation pathway in neurodegeneration. *Neurobiol. Dis.* **29**, 221–231
- Cartier, E. A., Parra, L. A., Baust, T. B., Quiroz, M., Salazar, G., Faundez, V., Egaña, L., and Torres, G. E. (2010) A biochemical and functional protein complex involving dopamine synthesis and transport into synaptic vesicles. *J. Biol. Chem.* **285**, 1957–1966
- Haycock, J. W. (2002) Species differences in the expression of multiple tyrosine hydroxylase protein isoforms. *J. Neurochem.* **81**, 947–953
- Ichikawa, S., Ichinose, H., and Nagatsu, T. (1990) Multiple mRNAs of monkey tyrosine hydroxylase. *Biochem. Biophys. Res.* **173**, 1331–1336
- Haycock, J. W. (1990) Phosphorylation of tyrosine hydroxylase *in situ* at serine 8, 19, 31, and 40. *J. Biol. Chem.* **265**, 11682–11691
- Dunkley, P. R., Bobrovskaya, L., Graham, M. E., von Nagy-Felsobuki, E. I., and Dickson, P. W. (2004) Tyrosine hydroxylase phosphorylation: regulation and consequences. *J. Neurochem.* **91**, 1025–1043
- Itagaki, C., Isobe, T., Taoka, M., Natsume, T., Nomura, N., Horigome, T., Omata, S., Ichinose, H., Nagatsu, T., Greene, L. A., and Ichimura, T. (1999) Stimulus-coupled interaction of tyrosine hydroxylase with 14-3-3 proteins. *Biochemistry* **38**, 15673–15680
- Kleppe, R., Rosati, S., Jorge-Finnigan, A., Alvira, S., Ghorbani, S., Haavik, J., Valpuesta, J. M., Heck, A. J., and Martinez, A. (2014) Phosphorylation dependence and stoichiometry of the complex formed by tyrosine hydroxylase and 14-3-3 γ . *Mol. Cell. Proteomics* **13**, 2017–2030
- Harada, K., Wu, J., Haycock, J. W., and Goldstein, M. (1996) Regulation of L-DOPA biosynthesis by site-specific phosphorylation of tyrosine hydroxylase in AtT-20 cells expressing wild-type and serine 40-substituted enzyme. *J. Neurochem.* **67**, 629–635
- Gordon, S. L., Bobrovskaya, L., Dunkley, P. R., and Dickson, P. W. (2009) Differential regulation of human tyrosine hydroxylase isoforms 1 and 2 *in situ*: isoform 2 is not phosphorylated at Ser35. *Biochim. Biophys. Acta* **1793**, 1860–1867
- Haycock, J. W., Ahn, N. G., Cobb, M. H., and Krebs, E. G. (1992) ERK1 and ERK2, two microtubule-associated protein 2 kinases, mediate the phosphorylation of tyrosine hydroxylase at serine-31 *in situ*. *Proc. Natl. Acad. Sci. U.S.A.* **89**, 2365–2369
- Kansy, J. W., Daubner, S. C., Nishi, A., Sotogaku, N., Lloyd, M. D., Nguyen, C., Lu, L., Haycock, J. W., Hope, B. T., Fitzpatrick, P. F., and Bibb, J. A. (2004) Identification of tyrosine hydroxylase as a physiological substrate for Cdk5. *J. Neurochem.* **91**, 374–384
- Sutherland, C., Alterio, J., Campbell, D. G., Le Bourdellès, B., Mallet, J., Haavik, J., and Cohen, P. (1993) Phosphorylation and activation of human tyrosine hydroxylase *in vitro* by mitogen-activated protein (MAP) kinase and MAP-kinase-activated kinases 1 and 2. *Eur. J. Biochem.* **217**, 715–722
- Salvatore, M. F., Waymire, J. C., and Haycock, J. W. (2001) Depolarization-stimulated catecholamine biosynthesis: involvement of protein kinases and tyrosine hydroxylase phosphorylation sites *in situ*. *J. Neurochem.* **79**, 349–360
- Lehmann, I. T., Bobrovskaya, L., Gordon, S. L., Dunkley, P. R., and Dickson, P. W. (2006) Differential regulation of the human tyrosine hydroxylase isoforms via hierarchical phosphorylation. *J. Biol. Chem.* **281**, 17644–17651
- Salvatore, M. F., and Prueett, B. S. (2012) Dichotomy of tyrosine hydroxylase and dopamine regulation between somatodendritic and terminal field areas of nigrostriatal and mesoaccumbens pathways. *PLoS One* **7**, e29867
- Mitchell, J. P., Hardie, D. G., and Vulliamy, P. R. (1990) Site-specific phosphorylation of tyrosine hydroxylase after KCl depolarization and nerve growth factor treatment of PC12 cells. *J. Biol. Chem.* **265**, 22358–22364
- Moy, L. Y., and Tsai, L. H. (2004) Cyclin-dependent kinase 5 phosphorylates serine 31 of tyrosine hydroxylase and regulates its stability. *J. Biol. Chem.* **279**, 54487–54493
- Salvatore, M. F., Prueett, B. S., Spann, S. L., and Dempsey, C. (2009) Aging reveals a role for nigral tyrosine hydroxylase Ser31 phosphorylation in locomotor activity generation. *PLoS One* **4**, e8466
- Salvatore, M. F. (2014) Ser31 tyrosine hydroxylase phosphorylation parallels differences in dopamine recovery in nigrostriatal pathway following 6-OHDA lesion. *J. Neurochem.* **129**, 548–558
- Kuczenski, R. T., and Mandell, A. J. (1972) Regulatory properties of soluble and particulate rat brain tyrosine hydroxylase. *J. Biol. Chem.* **247**, 3114–3122
- Parra, L. A., Baust, T. B., Smith, A. D., Jaumotte, J. D., Zigmond, M. J., Torres, S., Leak, R. K., Pino, J. A., and Torres, G. E. (2016) The molecular chaperone Hsc70 interacts with tyrosine hydroxylase to regulate enzyme activity and synaptic vesicle localization. *J. Biol. Chem.* **291**, 17510–17522
- Polymeropoulos, M. H., Lavedan, C., Leroy, E., Ide, S. E., Dehejia, A., Dutra, A., Pike, B., Root, H., Rubenstein, J., Boyer, R., Stenroos, E. S., Chandrasekharappa, S., Athanassiadou, A., Papapetropoulos, T., Johnson, W. G., et al. (1997) Mutation in the alpha-synuclein gene identified in families with Parkinson's disease. *Science* **276**, 2045–2047
- Perez, R. G., Waymire, J. C., Lin, E., Liu, J. J., Guo, F., and Zigmond, M. J. (2002) A role for α -synuclein in the regulation of dopamine biosynthesis. *J. Neurosci.* **22**, 3090–3099
- Obeso, J. A., Rodriguez-Oroz, M. C., Goetz, C. G., Marin, C., Kordower, J. H., Rodriguez, M., Hirsch, E. C., Farrer, M., Schapira, A. H., and Halliday, G. (2010) Missing pieces in the Parkinson's disease puzzle. *Nat. Med.* **16**, 653–661

TH Ser-31 phosphorylation targets TH to vesicles

33. Jedynak, J. P., Ali, S. F., Haycock, J. W., and Hope, B. T. (2002) Acute administration of cocaine regulates the phosphorylation of serine-19, -31 and -40 in tyrosine hydroxylase. *J. Neurochem.* **82**, 382–388
34. Nakashima, A., Mori, K., Kaneko, Y. S., Hayashi, N., Nagatsu, T., and Ota, A. (2011) Phosphorylation of the N-terminal portion of tyrosine hydroxylase triggers proteasomal digestion of the enzyme. *Biochem. Biophys. Res. Commun.* **407**, 343–347
35. Sannerud, R., Marie, M., Hansen, B. B., and Saraste, J. (2008) Use of polarized PC12 cells to monitor protein localization in the early biosynthetic pathway. *Methods Mol. Biol.* **457**, 253–265
36. Christensen, A. E., Selheim, F., de Rooij, J., Dremier, S., Schwede, F., Dao, K. K., Martinez, A., Maenhaut, C., Bos, J. L., Genieser, H. G., and Doskeland, S. O. (2003) cAMP analog mapping of Epac1 and cAMP kinase: discriminating analogs demonstrate that Epac and cAMP kinase act synergistically to promote PC-12 cell neurite extension. *J. Biol. Chem.* **278**, 35394–35402
37. Miranda-Barrientos, J., Nieto-Mendoza, E., and Hernandez-Echeagaray, E. (2014) The Cdk5 inhibitor Roscovitine increases LTP induction in corticostriatal synapses. *ASN Neuro* 10.1042/AN20140006
38. Groblewski, P. A., Franken, F. H., and Cunningham, C. L. (2011) Inhibition of extracellular signal-regulated kinase (ERK) activity with SL327 does not prevent acquisition, expression, and extinction of ethanol-seeking behavior in mice. *Behav. Brain Res.* **217**, 399–407
39. Koike, T., and Takashima, A. (1984) Clonal variability of PC12-pheochromocytoma cells with respect to catecholamine biosynthesis. *J. Neurochem.* **42**, 1472–1475
40. Clementi, E., Racchetti, G., Zacchetti, D., Panzeri, M. C., and Meldolesi, J. (1992) Differential expression of markers and activities in a group of PC12 nerve cell clones. *Eur. J. Neurosci.* **4**, 944–953
41. Göttele, M., Burhenne, H., Sutcliffe, D., and Jinnah, H. A. (2013) Purine metabolism during neuronal differentiation: the relevance of purine synthesis and recycling. *J. Neurochem.* **127**, 805–818
42. Alvarez, D., Callejo, M., Shoucri, R., Boyer, L., Price, G. B., and Zannis-Hadjopoulos, M. (2003) Analysis of the cruciform binding activity of recombinant 14-3-3 ζ -MBP fusion protein, its heterodimerization profile with endogenous 14-3-3 isoforms, and effect on mammalian DNA replication *in vitro*. *Biochemistry* **42**, 7205–7215
43. van Rijn, R. M., Chazot, P. L., Shenton, F. C., Sansuk, K., Bakker, R. A., and Leurs, R. (2006) Oligomerization of recombinant and endogenously expressed human histamine H(4) receptors. *Mol. Pharmacol.* **70**, 604–615
44. Halskau, Ø., Jr., Ying, M., Baumann, A., Kleppe, R., Rodriguez-Larrea, D., Almás, B., Haavik, J., and Martinez, A. (2009) Three-way interaction between 14-3-3 proteins, the N-terminal region of tyrosine hydroxylase, and negatively charged membranes. *J. Biol. Chem.* **284**, 32758–32769
45. Nilsson, I., Bahram, F., Li, X., Gualandi, L., Koch, S., Jarvius, M., Söderberg, O., Anisimov, A., Kholová, I., Pytowski, B., Baldwin, M., Ylä-Herttua, S., Alitalo, K., Kreuger, J., and Claesson-Welsh, L. (2010) VEGF receptor 2/3 heterodimers detected *in situ* by proximity ligation on angiogenic sprouts. *EMBO J.* **29**, 1377–1388
46. Terland, O., and Flatmark, T. (1980) Oxidoreductase activities of chromaffin granule ghosts isolated from the bovine adrenal medulla. *Biochim. Biophys. Acta* **597**, 318–330
47. Lee, H. J., Khoshaghideh, F., Lee, S., and Lee, S. J. (2006) Impairment of microtubule-dependent trafficking by overexpression of α -synuclein. *Eur. J. Neurosci.* **24**, 3153–3162
48. Koch, J. C., Bitow, F., Haack, J., d'Hedouville, Z., Zhang, J. N., Tönges, L., Michel, U., Oliveira, L. M., Jovin, T. M., Liman, J., Tatenhorst, L., Bähr, M., and Lingor, P. (2015) α -Synuclein affects neurite morphology, autophagy, vesicle transport and axonal degeneration in CNS neurons. *Cell Death Dis.* **6**, e1811
49. Zatloukal, B., Kufferath, I., Thueringer, A., Landegren, U., Zatloukal, K., and Haybaeck, J. (2014) Sensitivity and specificity of *in situ* proximity ligation for protein interaction analysis in a model of steatohepatitis with Mallory-Denk bodies. *PLoS One* **9**, e96690
50. Peng, X., Tehrani, R., Dietrich, P., Stefanis, L., and Perez, R. G. (2005) α -Synuclein activation of protein phosphatase 2A reduces tyrosine hydroxylase phosphorylation in dopaminergic cells. *J. Cell Sci.* **118**, 3523–3530
51. Guo, J. T., Chen, A. Q., Kong, Q., Zhu, H., Ma, C. M., and Qin, C. (2008) Inhibition of vesicular monoamine transporter-2 activity in α -synuclein stably transfected SH-SY5Y cells. *Cell Mol. Neurobiol.* **28**, 35–47
52. Prado, V. F., Roy, A., Kolinsky, B., Gros, R., and Prado, M. A. (2013) Regulation of cholinergic activity by the vesicular acetylcholine transporter. *Biochem. J.* **450**, 265–274
53. Buddhala, C., Hsu, C. C., and Wu, J. Y. (2009) A novel mechanism for GABA synthesis and packaging into synaptic vesicles. *Neurochem. Int.* **55**, 9–12
54. Dobransky, T., and Rylett, R. J. (2005) A model for dynamic regulation of choline acetyltransferase by phosphorylation. *J. Neurochem.* **95**, 305–313
55. Lou, H., Montoya, S. E., Alerte, T. N., Wang, J., Wu, J., Peng, X., Hong, C. S., Friedrich, E. E., Mader, S. A., Pedersen, C. J., Marcus, B. S., McCormack, A. L., Di Monte, D. A., Daubner, S. C., and Perez, R. G. (2010) Serine 129 phosphorylation reduces the ability of α -synuclein to regulate tyrosine hydroxylase and protein phosphatase 2A *in vitro* and *in vivo*. *J. Biol. Chem.* **285**, 17648–17661
56. Requena, D. F., Parra, L. A., Baust, T. B., Quiroz, M., Leak, R. K., Garcia-Olivares, J., and Torres, G. E. (2009) The molecular chaperone Hsc70 interacts with the vesicular monoamine transporter-2. *J. Neurochem.* **110**, 581–594
57. Nirenberg, M. J., Chan, J., Liu, Y., Edwards, R. H., and Pickel, V. M. (1996) Ultrastructural localization of the vesicular monoamine transporter-2 in midbrain dopaminergic neurons: potential sites for somatodendritic storage and release of dopamine. *J. Neurosci.* **16**, 4135–4145
58. Bellucci, A., Zaltieri, M., Navarria, L., Grigoletto, J., Missale, C., and Spano, P. (2012) From α -synuclein to synaptic dysfunctions: new insights into the pathophysiology of Parkinson's disease. *Brain Res.* **1476**, 183–202
59. Cooper, A. A., Gitler, A. D., Cashikar, A., Haynes, C. M., Hill, K. J., Bhullar, B., Liu, K., Xu, K., Strathearn, K. E., Liu, F., Cao, S., Caldwell, K. A., Caldwell, G. A., Marsischky, G., Kolodner, R. D., et al. (2006) α -Synuclein blocks ER-Golgi traffic and Rab1 rescues neuron loss in Parkinson's models. *Science* **313**, 324–328
60. Brimijoin, S., and Wierma, M. J. (1977) Rapid axonal transport of tyrosine hydroxylase in rabbit sciatic nerves. *Brain Res.* **121**, 77–96
61. Gervasi, N. M., Scott, S. S., Aschrafi, A., Gale, J., Vohra, S. N., MacGibeny, M. A., Kar, A. N., Gioio, A. E., and Kaplan, B. B. (2016) The local expression and trafficking of tyrosine hydroxylase mRNA in the axons of sympathetic neurons. *RNA* **22**, 883–895
62. Wooten, G. F., and Coyle, J. T. (1973) Axonal transport of catecholamine synthesizing and metabolizing enzymes. *J. Neurochem.* **20**, 1361–1371
63. Korner, G., Noain, D., Ying, M., Hole, M., Flydal, M. I., Scherer, T., Allegri, G., Rassi, A., Fingerhut, R., Becu-Villalobos, D., Pillai, S., Wuest, S., Konrad, D., Lauber-Biason, A., Baumann, C. R., et al. (2015) Brain catecholamine depletion and motor impairment in a Th knock-in mouse with type B tyrosine hydroxylase deficiency. *Brain* **138**, 2948–2963
64. Royo, M., Fitzpatrick, P. F., and Daubner, S. C. (2005) Mutation of regulatory serines of rat tyrosine hydroxylase to glutamate: effects on enzyme stability and activity. *Arch. Biochem. Biophys.* **434**, 266–274
65. Encalada, S. E., and Goldstein, L. S. (2014) Biophysical challenges to axonal transport: motor-cargo deficiencies and neurodegeneration. *Annu. Rev. Biophys.* **43**, 141–169
66. Shah, K., and Lahiri, D. K. (2014) Cdk5 activity in the brain: multiple paths of regulation. *J. Cell Sci.* **127**, 2391–2400
67. Subramaniam, S., and Unsicker, K. (2010) ERK and cell death: ERK1/2 in neuronal death. *FEBS J.* **277**, 22–29
68. Alter, S. P., Lenzi, G. M., Bernstein, A. I., and Miller, G. W. (2013) Vesicular integrity in Parkinson's disease. *Curr. Neurol. Neurosci. Rep.* **13**, 362
69. Kurian, M. A., Gissen, P., Smith, M., Heales, S. J., and Clayton, P. T. (2011) The monoamine neurotransmitter disorders: an expanding range of neurological syndromes. *Lancet Neurol.* **10**, 721–733
70. Sun, K. H., de Pablo, Y., Vincent, F., Johnson, E. O., Chavers, A. K., and Shah, K. (2008) Novel genetic tools reveal Cdk5's major role in Golgi fragmentation in Alzheimer's disease. *Mol. Biol. Cell* **19**, 3052–3069
71. Kordower, J. H., Chu, Y., Hauser, R. A., Freeman, T. B., and Olanow, C. W. (2008) Lewy body-like pathology in long-term embryonic nigral transplants in Parkinson's disease. *Nat. Med.* **14**, 504–506
72. Lohr, K. M., Bernstein, A. I., Stout, K. A., Dunn, A. R., Lazo, C. R., Alter, S. P., Wang, M., Li, Y., Fan, X., Hess, E. J., Yi, H., Vecchio, L. M., Goldstein,

TH Ser-31 phosphorylation targets TH to vesicles

- D. S., Guillot, T. S., Salahpour, A., and Miller, G. W. (2014) Increased vesicular monoamine transporter enhances dopamine release and opposes Parkinson disease-related neurodegeneration *in vivo*. *Proc. Natl. Acad. Sci. U.S.A.* **111**, 9977–9982
73. Millecamps, S., and Julien, J. P. (2013) Axonal transport deficits and neurodegenerative diseases. *Nat. Rev. Neuroscience* **14**, 161–176
74. Furlong, R. A., Narain, Y., Rankin, J., Wytenbach, A., and Rubinsztein, D. C. (2000) α -Synuclein overexpression promotes aggregation of mutant huntingtin. *Biochem. J.* **346**, 577–581
75. Schindelin, J., Arganda-Carreras, I., Frise, E., Kaynig, V., Longair, M., Pietzsch, T., Preibisch, S., Rueden, C., Saalfeld, S., Schmid, B., Tinevez, J. Y., White, D. J., Hartenstein, V., Eliceiri, K., Tomancak, P., and Cardona, A. (2012) Fiji: an open-source platform for biological-image analysis. *Nat. Methods* **9**, 676–682
76. Ying, M., Flatmark, T., and Saraste, J. (2000) The p58-positive pre-Golgi intermediates consist of distinct subpopulations of particles that show differential binding of COPI and COPII coats and contain vacuolar H(+)-ATPase. *J. Cell Sci.* **113**, 3623–3638

Phosphorylation at serine 31 targets tyrosine hydroxylase to vesicles for transport along microtubules

Ana Jorge-Finnigan, Rune Kleppe, Kunwar Jung-KC, Ming Ying, Michael Marie, Ivan Rios-Mondragon, Michael F. Salvatore, Jaakko Saraste and Aurora Martinez

J. Biol. Chem. 2017, 292:14092-14107.

doi: 10.1074/jbc.M116.762344 originally published online June 21, 2017

Access the most updated version of this article at doi: [10.1074/jbc.M116.762344](https://doi.org/10.1074/jbc.M116.762344)

Alerts:

- [When this article is cited](#)
- [When a correction for this article is posted](#)

[Click here](#) to choose from all of JBC's e-mail alerts

This article cites 76 references, 27 of which can be accessed free at <http://www.jbc.org/content/292/34/14092.full.html#ref-list-1>



Graphic design: Communication Division, UIB / Print: Skjipes Kommunikasjon AS



uib.no

ISBN: 9788230849972 (print)
9788230844199 (PDF)